Optomechanics in hybrid fully-integrated two-dimensional photonic crystal resonators

Viktor Tsvirkun

UNIVERSITÉ PARIS-SUD XI
École Doctorale 288 : Ondes et Matière
CNRS – Laboratoire de Photonique et de Nanostructures

THÈSE DE DOCTORAT
pour l'obtention du grade de
Docteur de l'Université Paris-Sud

Domaine:
PHYSIQUE

par
Viktor Tsvirkun

Optomechanics in hybrid fully-integrated two-dimensional photonic crystal resonators

Date de soutenance : 15 Septembre 2015

Composition du jury :

Dr.	Antoine Heidmann	Université Pierre et Marie Curie / CNRS	Rapporteur
Dr.	Vincent Laude	Institut FEMTO-ST / CNRS	Rapporteur
Prof.	Jean-Jacques Greffet	Institut d'Optique Graduate School	Président du jury
Prof.	Dries Van Thourhout	Ghent University / IMEC (Belgique)	Examinateur
Prof.	Khaled Karraï	attocube systems AG (Allemagne)	Examinateur
Dr.	Rémy Braive	CNRS–LPN / Université Paris 7	Membre invité
Dr.	Isabelle Robert-Philip	CNRS–LPN	Directrice de thèse

"It doesn't matter what you do, he said, so long as you change something from the way it was before you touched it into something that's like you after you take your hands away. The difference between the man who just cuts lawns and a real gardener is in the touching, he said. The lawn-cutter might just as well not have been there at all; the gardener will be there a lifetime."

— Ray Bradbury, *Fahrenheit 451*

English abstract

Optomechanical systems, in which the vibrations of a mechanical resonator are coupled to an electromagnetic radiation, have permitted the investigation of a wealth of novel physical effects. To fully exploit these phenomena in realistic circuits and to achieve different functionalities on a single chip, the integration of optomechanical resonators is mandatory. Here, we propose a novel approach to heterogeneously integrated arrays of two-dimensional photonic crystal defect cavities on top of silicon-on-insulator waveguides. The optomechanical response of these devices is investigated and evidences an optomechanical coupling involving both dispersive and dissipative mechanisms. By controlling optical coupling between the waveguide and the photonic crystal, we were able to vary and understand the relative strength of these couplings. This scalable platform allows for unprecedented control on the optomechanical coupling mechanisms, with a potential benefit in cooling experiments, and for the development of multi-element optomechanical circuits in the frame of optomechanically-driven signal-processing applications.

Résumé en français

Les systèmes optomécaniques, dans lesquels les vibrations d'un résonateur mécanique sont couplées à un rayonnement électromagnétique, ont permis l'examen de multiples nouveaux effets physiques. Afin d'exploiter pleinement ces phénomènes dans des circuits réalistes et d'obtenir différentes fonctionnalités sur une seule puce, l'intégration des résonateurs optomécaniques est obligatoire. Ici nous proposons une nouvelle approche pour la réalisation de systèmes intégrés et hétérogènes comportant des cavités à cristaux photoniques bidimensionnels au-dessus de guides d'ondes en silicium-sur-isolant. La réponse optomécanique de ces dispositifs est étudiée et atteste d'un couplage optomécanique impliquant à la fois les mécanismes dispersifs et dissipatifs. En contrôlant le couplage optique entre le guide d'onde intégré et le cristal photonique, nous avons pu varier et comprendre la contribution relative de ces couplages. Cette plateforme évolutive permet un contrôle sans précédent sur les mécanismes de couplage optomécanique, avec un avantage potentiel dans des expériences de refroidissement et pour le développement de circuits optomécaniques multi-éléments pour des applications tels que le traitement du signal par effets optomécaniques.

Remerciements

Je remercie chaleureusement Antoine HEIDMANN et Vincent LAUDE d'avoir accepté de remplir le rôle de mes rapporteurs et de faire partie de mon jury de thèse.

I would also like to express my gratitude to Jean-Jacques GREFFET, Dries VAN THOURHOUT and Khaled KARRAÏ to kindly accept to be a part of the jury of my thesis defence and to make a long trip to LPN.

Je tiens à remercier Isabelle ROBERT-PHILIP de m'avoir offert l'opportunité d'effectuer cette thèse sous sa direction, dans une ambiance à la fois si conviviale et si riche scientifiquement ; ainsi j'ai pu profiter des connaissances, des savoir-faire, de la bonne humeur et du sens de l'humour de mon nouvel entourage pendant ces trois excellentes années. Isabelle, merci également pour nos batailles bureaucratiques et ta capacité extraordinaire à résoudre toutes sortes des problèmes en quelques mots et quelques minutes ; pour ton argot (un jour j'arriverai à le comprendre du premier coup), pour les calissons d'Aix et autres goodies, pour tes anecdotes, ta disponibilité et ta façon de voir les choses.

Je remercie Rémy BRAIVE d'avoir investi énormément de son temps sur moi et sur ce projet, de m'avoir transmis son envie de travailler en salle blanche, de m'avoir appris encore plus de choses autour de la manip et même un peu sur les relations humaines, et encore de supporter mon caractère jour après jour. Merci d'être quasiment le seul à ne pas hésiter à corriger mes erreurs de français parlé. Je te remercie pour toutes nous discussions autour de notre système 'à mille paramètres' et pour ta passion contagieuse pour la science et l'optomécanique en particulier (peut-être j'aurais pu apprendre encore plus de toi si on avait discuté d'autres sujets). En tout cas, tout cela a été particulièrement enrichissant pour moi.

Je remercie mes collaborateurs au laboratoire sans lesquels cette thèse n'aurait pas été possible. Merci à Isabelle SAGNES et Grégoire BEAUDOIN pour tous les substrats épitaxiés, pour tous les renseignements sur l'épitaxie et les gravures des substrats ; encore à Grégoire pour ton aide sur la spectroscopie FTIR et pour la découverte de 'Of Monsters and Men'. Merci à Rama RAJ et Fabrice RAINERI pour votre aide avec les reports III-V sur Si, merci d'avoir partagé un énorme savoir-faire en salle blanche, tous vos conseils, recettes et explications (et de m'avoir bien dépanné plusieurs fois en filtres et en substrats Si). Merci à Alessandro SURRENTE d'avoir partagé cette dernière année (la plus heureuse, car tout finalement fonctionnait) avec moi, de s'être beaucoup investi dans le traitement des données et dans la rédaction de l'article, mais aussi pour ta vision différente des choses,

qui m'a donné de nouvelles idées.

Je remercie Dominique MAILLY de m'avoir accueilli au sein de son laboratoire ; un grand merci à Agnès ROUX-PERRIN, Marina FERREIRA et Sandrine BOUVY pour leur aide précieuse avec des taches administratives. Mes remerciements vont aussi aux membres du service informatique : Lorenzo BERNARDI, Alain PEAN et Mehdi IDOUHAMD, pour toute votre aide avec les côtés 'soft' et 'hard' de la partie numérique de ce travail.

Merci à tout le personnel de la salle blanche d'avoir partagé leur passion et leur savoir-faire avec chaque nouvel entrant (y compris moi). Merci à Stéphane GUILET de m'avoir appris (presque) tout ce que je sais sur les gravures sèches, pour une belle initiation au nettoyage du bâti et pour ton aide précieuse pendant le développement de mes recettes. De plus, nos sorties running ensemble avec *lpn-trail* ont été des belles expériences pour moi. Merci à Lina GATILOVA pour tes conseils sur la gravure de GaAs et pour les métallisations urgentes ; merci d'avoir résisté à toutes les blagues de Stéphane et Christian et d'avoir organisé nos quelques pauses thé russophones avec Iryna ; merci en particulier de faire partie des russes ayant une vision sobre sur la vie. Merci à Christophe ROBLIN de m'avoir formé et aidé avec la lithographie optique et le bondeur. Merci à Laurent COURAUD pour les métallisations toujours bien réussies. Merci à Christian ULYSSE pour un beau sens de l'humour, ton attitude amicale et encore pour ton aide avec les échantillons pendant mon stage à l'ENS Cachan. Merci à Ahmad ITAWI pour son énergie fabuleuse, son caractère plus qu'ouvert et ses nombreux conseils.

Mes plus sincères remerciements à tous les membres du groupe NanoPhotonIQ et de ses prédécesseurs PEQ et PHOTONIQ. Merci à Avishek CHOWDHURY d'avoir brisé le climat francophone, ce qui m'as permis aussi peu à peu d'améliorer mon anglais parlé ; bon courage à toi sur notre voie de l'optomécanique intégrée. Merci à Robert KUSZELEWICZ pour les pauses déjeuners magnifiques pendant lesquelles je profitais des discussions sur la culture, la littérature, le cinéma, l'histoire etc. Merci à Sylvain BARBAY pour toutes nos discussions et ses suggestions à propos de l'optomécanique et les manips. Merci à Paul MONNIER pour toute ton aide et tes conseils sur LabVIEW, Python et mes autres jouets et en particulier d'avoir passé quelques jours ensemble pour 'craquer' le protocole de New Focus (ah oui, et pour quelques 'découvertes' dans la grande culture française). Merci à Vincenzo ARDIZZONE pour toutes les expériences PL que j'ai pu faire sur ta manip. Merci à Guillaume CROSNIER pour ton état d'esprit, pour nos pauses thé régulières et pour ton aide avec le design des nanobeams. Merci à toi et Philippe HAMEL de m'avoir fait redécouvrir le badminton. Merci à Aude MARTIN de m'avoir expliqué les particularités de la vie marseillaise et pour tes ambitions bien plus que motivantes. Merci à Alexandre BAZIN pour tes explications sur les guides intégrés et les nanobeams et pour ta thèse bien cool. Merci également à Iso ABRAM, Alexios BEVERATOS, Nadia BELABAS, Jean-Marie MOISON, Razvan NEGRU, Alejandro GIACOMOTTI, Samir HADDADI, Sébastien ALVO et Dorian SANCHEZ. Merci à Jordann GOVINDY et Carla SANNA pour leurs contributions pendant leurs stages.

Merci à tous les habitants du bureau D2-101 qui m'ont croisé pendant ces trois

années, pour une ambiance joyeuse et parfois complètement folle. Foued SELMI, Armand LEBRETON, Avishek CHOWDHURY, Iryna GOZHYK, Inah YEO et même Michel DECHENAUD – tout cela a été exclusivement possible grâce à vous. Mes remerciements particuliers à Foued d'avoir été un élément incontournable de cette atmosphère, d'avoir partagé les moments durs de la rédaction, pour nos sorties tennis et même pour tes blagues presque innocentes. Thanks to Inah for your indestructible honesty, frankness and open mind, and of course for the great Korean tea and the discovery of mouthwatering Korean food; I only regret we did it that late.

Merci à Gilgueng HWANG pour son aide avec le séchage supercritique, la micromanipulation sous MEB et l'impression 3D et d'avoir été intarissable en histoires entre temps. Merci également à Hugo SALMON pour les consultations sur l'imprimante 3D et les matériaux à y utiliser.

Merci à Mehdi ALOUINI, Goulc'hen LOAS et toute l'équipe du Département Optique et Photonique à l'Institut de Physique de Rennes de m'avoir accueilli dans les meilleures conditions, merci pour toute votre aide avec l'ampli NATIF.

Merci à Iryna GOZHYK et Nicolas CHARLES de m'avoir beaucoup aidé dès mes premiers jours en France, de m'avoir fait découvrir et initier à la cuisine française (et un peu à la culture), merci pour tous les salons du vin ensemble, des déjeuners et dîners extrêmement délicieux, pour tous vos conseils, votre convivialité et cordialité. Merci en particulier à Iryna pour ton soutien pendant ma rédaction et mon stage à Cachan, de m'avoir poussé à découvrir beaucoup plus de choses et d'endroits que je ne pouvais imaginer, merci pour ton incroyable gentillesse. Merci à Iuliia STUPACHENKO pour ton soutien pendant mes premiers pas en français, merci d'avoir partagé ta superbe passion, pour tous mes 'devoirs', nos lectures, introduction à l'argot et verlan ; et pour tous les moments vraiment agréables de cette époque-là. Merci encore à Ivan, Maksym, Iuliia, Inna, Oleksandr, Vasylyna, Dmytro, Kévin, Leonhard, Sheon, Clément, Nina ... pour les moments de ma vie en dehors de la thèse, bien que souvent on en discutait avec certains parmi vous.

I believe my life journey would not bring me to the start of this work without the support of my supervisors in National University of Kyiv – Eugene Smirnov, Yuri Pilgun, Sergiy Kolenov. I would like to express my gratitude to Oleksiy Nechyporuk for his precious help while preparing my papers for both French trips, for his attitudes and philosophy, but also for the great times with a bunch of (radio)physicists somewhere in the Crimean mountains.

I would like to thank my family and all my friends in Ukraine, France and those dispersed elsewhere around the world for their encouragements during this work and not least during its last phase. Thanks to my loveliest architect Oksana Chebina for supplying a dose of my everyday inspiration, for suggestions concerning the design part and for being around always when I need it.

Finally and foremost, I am infinitely grateful to my mother for complete freedom of choice I always had and for being such an extraordinary example of kindness.

Contents

Chapter 1

Introduction

Contents

General motivation of this PhD thesis is the development and experimentation on heterogeneously integrated optomechanical system. This system consists of an optomechanical suspended membrane, bonded over a silicon access waveguide. This hybrid three-dimensional approach can be extended to a wide variety of materials for the active device part (here III-V semiconductor), combined with compact, efficient, fully controlled and flexible optical access channel on chip. Embedding photonic crystal lattice in the optomechanical membrane brings even more versatility to our system, both from the optical and mechanical points of view. The designed system will have great scaling capabilities and can be itself easily integrated within larger circuits, paving the way towards multi-cavity and multi-resonator coupling, synchronization and further multimode optomechanical experiments. In this Introduction, we briefly describe the significance of this work and its position in the field of cavity optomechanics with micro- and nano-objects.

1.1 Optomechanics

1.1.1 Foundations

The field of optomechanics explores the interaction between light, or electromagnetic waves, with the mechanical motion. Such an interaction becomes considerable at micro- and nanoscale, where the effective mass of the mechanical oscillator can be significantly reduced. Cavity optomechanics [Kippenberg 2007; Aspelmeyer 2013] encapsulates light interactions with a mechanical resonator within a cavity (e.g., optical) in order to resonantly enhance the interaction strength.

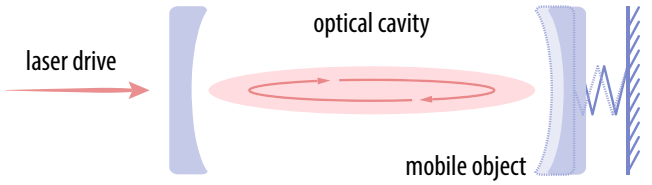

Figure 1.1: Schematic illustration of a generic optomechanical resonator in the optical domain consisting of a laser-driven Fabry-Pérot cavity, where one of the mirrors is fixed (left) and other is spring-mounted (right) and free to move.

To illustrate the simplest case of optomechanical interaction based on electromagnetic field enhancement by an optical cavity, one typically uses a model based on a Fabry-Pérot resonator where one of the mirrors is attached to a spring and free to move, as shown in Figure 1.1. Laser drive, coupled inside the cavity, may feed a confined optical mode, exerting a force on the mirrors through the radiation pressure [Lebedew 1901; Nichols 1901]. As a result, the displacement dx of the moveable mirror (along the axis of the cavity with a frequency f_{m}) modifies the length L of the resonator (the spacing between the mirrors), and thus changes the resonance frequency ($\nu_0 = c/2L$ for the fundamental mode) of the optical cavity. This in turn changes the intracavity circulating power and the radiation pressure force becomes weaker, therefore resulting in backward movement of the free mirror. The described effects are commonly referred to as dynamical backaction. The backaction cycle repeats as long as there is light inside the cavity, and can last during some period of time after the laser drive shut-off, depending on the photon lifetime τ inside the resonator.

From this simplest picture of optomechanical interaction in the Fabry-Pérot cavity involving the radiation pressure force, the field of optomechanics extends to a wide variety of systems including another types of light – matter couplings inside a monolithic cavities (e.g., via gradient force, electrostriction, photoelastic effect etc.).

1.1.2 Relevant parameters of optomechanical systems

In our example of generic optomechanical resonator (Fig. 1.1), for a given displacement dx the frequency of the optical mode will shift by $\nu_0 \cdot dx/L = d\nu_0$. In this case, in order

to maximize the effect, one should use the largest possible frequency ν_0 (while taking into account the limitations related to technical issues such as detection efficiency) and the smallest possible cavity length L. From another side, the frequency shift $d\nu_0$ of the optical cavity due to optomechanical coupling will result in a phase shift for the cavity photons, proportional to the their lifetime τ. The technique to measure the displacement involves a mixing of such phase-shifted photons from the cavity with reference photons and measuring their interference; as such, it is beneficial to maximize the accumulated phase shift as well via the increase of the photon lifetime. The quality factor Q of the optical cavity, is directly proportional to the photon lifetime $Q = 2\pi\nu_0\tau$ and, as can be seen from the formula, the Fabry-Pérot cavity lengthening increases Q (assuming no losses occur in the space between the mirrors) and cancels the induced reduction of optomechanical coupling, which makes the displacement sensitivity independent of cavity dimensions. This fact allowed the successful implementation of kilometre- (L, cavity length in free space) and kilogram-scale (m) optomechanical systems in gravitational wave interferometers (Fig. 1.2a).

Either in fundamental or applied field, general trend for the mechanical device part is for increasing its operation frequency f_m, leading to the decrease in size and switching from free space to monolithic cavities. In the case of monolithic optical resonators, which now represent the majority of optomechanical devices, another set of parameters becomes crucial. The following list summarizes the relevant optomechanical quantities for the monolithic devices in some typical experimental implementations, described in Section 1.1. These are the mechanical resonator mass m (in some cases the effective mode mass m_eff) and frequency $\Omega_\mathrm{m} = 2\pi f_\mathrm{m}$; the dissipation rates of optical ($\gamma = \nu_0/Q \propto 1/\tau$) and mechanical ($\Gamma_\mathrm{m} = \Omega_\mathrm{m}/Q_\mathrm{m}$) resonances; the "$Q_\mathrm{m} \cdot f_\mathrm{m}$" product for the mechanical resonance; the sideband suppression parameter γ/Ω_m; and the vacuum optomechanical coupling rate g_0, corresponding to the single-photon frequency shift due to the optomechanical interaction.

The reduction of the resonator mass m and increase of its vibration frequency f_m are generally achieved by shrinking its dimensions, i.e., its length L, as introduced before. Maximizing the "$Q_\mathrm{m} \cdot f_\mathrm{m}$" product, describing the device decoupling from its thermal environment, the mechanical quality factor, directly proportional to the phonon lifetime, can be increased by working on main loss channels, e.g., by designing a system with the lowest possible clamping losses or reducing the intrinsic losses by cooling the resonator down to the cryogenic temperatures. The optical (photon) dissipation rate $\gamma = \nu_0/Q$ is minimized by enhancing the quality factor of the optical resonator. Contrary to the Q independence on resonator length L in the free-space cavity, described above, the losses in monolithic cavities are usually dominated by scattering and absorption in the material where the light propagates, thus shrinking the cavity dimensions (L) can reduce the impact of these phenomena.

1.1.3 Fields of applications

The essential effect of the optomechanical coupling hence is the fact that a mechanical displacement of the cavity induces a change in the state of light. Potential fields of applications cover on one hand fundamental physics studies, eventually going beyond the regime of classical physics or combining otherwise incompatible degrees of freedom of different physical systems in a hybrid quantum device. Optomechanical systems propose a basis for the applications in quantum information processing, serving as a coherent interface between light and matter qubits. Optomechanics is also exploited in metrology for implementing high precision measurements for the optical detection of displacement, mass, force, acceleration, etc. and the use in radio frequency devices as integrated clock sources.

From the point of view of fundamental physics, several aspects of cavity quantum optomechanics were explored both theoretically and experimentally, e.g., optomechanical squeezing of light [Fabre 1994; Mancini 1994], quantum non-demolition measurements [Jacobs 1994; Pinard 1995], non-classical (i.e., with the statistics other than Gaussian) and entangled states of light and mechanical motion [Bose 1997; Mancini 1997] etc. Optical cooling of mechanical oscillators using optomechanical interaction, proposed first to cool atomic and molecular motion [Hechenblaikner 1998], was experimentally demonstrated by cavity-assisted radiation pressure cooling of a macroscopic mirror [Cohadon 1999]. Alongside with the demonstration of optomechanical couplings in numerous system from macro- to nanoscale, laser cooling of nano-optomechanical resonator has allowed to experimentally reach its quantum ground state [Chan 2011]. Such experiments in optomechanics have inspired the research on analogous effects in electromechanical systems, where the control of mechanical oscillator is achieved by capacitively coupling the mechanical motion to a microwave cavity [Regal 2008]. Almost simultaneously with optics, ground state cooling in an electromechanical system was experimentally demonstrated [Teufel 2011], for a mechanical resonator operating in MHz frequency range[1] unlike the similar optomechanical experiment [Chan 2011] for a mode at the frequency of GHz.

Another application of optomechanical interaction, exploring the radiation pressure force, is related to high-precision measurements of displacements allowing for the exquisite sensitivity, e.g., in gravitational wave detectors such as LIGO [Barish 1999] and VIRGO [Acernese 2008], with the standard quantum limit for the continuous position detection, established in [Braginskii 1977; Braginsky 1992] works.

Development of high-quality optomechanical resonators allowed as well for their implementation as on-chip integrated radio frequency (RF) oscillators with high spectral purity. Such optomechanical oscillators, featuring direct coupling to continuous-wave light field input from one side and attainable high operation frequency Ω_{m} and high quality factor Q_{m}, are good candidates for frequency reference in radio-frequency-photonic architectures.

[1] In view of measuring quantum effects one typically looks for a higher mechanical oscillation frequency, which lowers the thermal occupancy of the corresponding mode. Therefore, ground state cooling of a MHz frequency resonator becomes a more complicated procedure, when compared to a GHz frequency device.

Two different implementations exist: phase-locking to an external frequency reference and self-referenced optomechanical microwave oscillators. Already existing experimental realizations [HosseinZadeh 2008; Zheng 2013] demonstrate that the frequency and phase of an optomechanical oscillator within certain lock range can be locked to those of an external electronic oscillator, or any other signal that can modulate the power of input optical field (similar to what is done in the optical domain with lasers). Injection locking of an optomechanical to an electronic RF oscillator enables combination of the former with electronic devices and may have interesting applications in certain RF photonics and micro-opto-electro-mechanical systems. In addition, the non-electronic nature of optomechanical devices makes them insensitive to any electromagnetic interferences and good candidates for all-optical systems, also in view of experimental demonstration of such devices, compatible with CMOS platform [Luan 2014].

Optomechanical devices with coherent switching can be as well used as a non-volatile memory [Cole 2011; Bagheri 2011; Dong 2014] with the dimensions down to nanoscale, allowing for large scale integration, high speed operation and low power consumption. The potential applications of such devices cover controlled optical switches, logic gates and actuators.

1.1.4 Motivation behind micro- and nanoscale devices

From applicative point of view, the experimental realizations, listed above, show good performances in the MHz working range; most of them, however, would benefit from an extension to the GHz frequency range, where several optomechanical systems [Chan 2011; Ding 2011; Gavartin 2011; Sun 2012] have already been shown.

As an example we can state the sensing domain, where the acquisition times are limited by the device operation frequency not exceeding the MHz range. Moving to the GHz platform would open a new frontiers for such applications, e.g., in the field of bio-sensing. The same discussion holds for the on-chip signal processing and RF photonics, where the increase of the operation frequency is highly desired. Another example are the clock references, used in metrology and navigation. Current solutions with an electronic oscillator that is regulated by a quartz crystal are limited to the MHz range, and a creation of novel sources operating at GHz frequencies will lead to the considerable performance increase for the mentioned applications. In terms of more fundamental applications, increase of the frequency relaxes the requirement on the temperatures for reaching the quantum regime.

This provides the motivation behind the micro- and nanoscale devices, where the higher mechanical frequency f_{m} is attained when shrinking the resonator sizes and therefore its motional mass m. Moreover, in such devices a high optical quality factors can be attained in very small (down to diffraction limit) optical resonators. The drawback of the system size reduction is that a concomitant effect, usually observed, is the reduction of the mechanical quality factor Q_{m}, while most of the aforementioned applications require low mechanical losses. Therefore, most of the work in this context is concentrated on

the design and fabrication of high-frequency and high mechanical Q_m resonators; some of them are described in the following Sections.

1.2 Some optomechanical systems

All aforesaid shows a big impact of device mass, whose decrease generally may lead to the enhancement of several stated optimization parameters (f_m, Q, $Q_m \cdot f_m$). This Section provides a non-exhaustive large overview of the kinds of systems used in the field of optomechanics (see Figure 1.2), classified with respect to the mass m of mechanical oscillator, or to the effective motional mass m_{eff} of the mechanical mode of interest, which is one of the relevant parameters to the optomechanics experiment and can be one of the classification criteria.

1.2.1 From macro- to microscale

The largest scale – both in weight and in size – among the existing optomechanical systems is represented by the end-mirrors in the set-ups employed for the detection of gravitational waves (Fig. 1.2a). For a given example from GEO 600, the test mass silica mirror of 5.6 kg [Adams 2014] weight is suspended at the end of one arm of the Michelson interferometer. The smaller and more lightweight versions of such devices were experimented as well, going down to grams (Fig. 1.2b) and milligram (Fig. 1.2c) suspended mirrors. Shrinking dimensions of the reflective surfaces further down require micro-structuration techniques and deposition of a reflective layer or a stack of layers, creating a Bragg mirror, which allowed to achieve a few hundreds of micrograms (Fig. 1.2d) and few tens of nanograms (Fig. 1.2e) objects. This tendency ultimately resulted in significant decrease in area to be addressed by a light beam and resulted to the development of systems, that can itself confine light – optomechanical systems with monolithic optical cavities, reaching eventually the diffraction limit. One of the pioneer works was related to the use of toroidal microcavities (Fig. 1.2f), which support both high-Q optical resonances and high-Q_m radial breathing modes when held by a thin 'needle' pillar.

1.2.2 Down to nanoscale

One of the first works on nanoscale devices featuring an optomechanical interaction [Roels 2009] exploited the optical gradient forces between two partially suspended nanophotonic waveguides. Here, the light confinement was achieved only along the two directions for the propagating optical mode. In order to benefit further from light confinement, diffraction-limited optical cavities, allowing for an enhancement of the electromagnetic field, were further developed in the frame of optomechanical experiments.

Still considering a flexural vibration of frequency f_m and a fixed mechanical properties of materials (mass density ρ and bulk modulus B), the smallest system size, that still support mechanical resonance of wavelength Λ_m, is approximately $(\Lambda_m/2)^3$, where $\Lambda_m =$

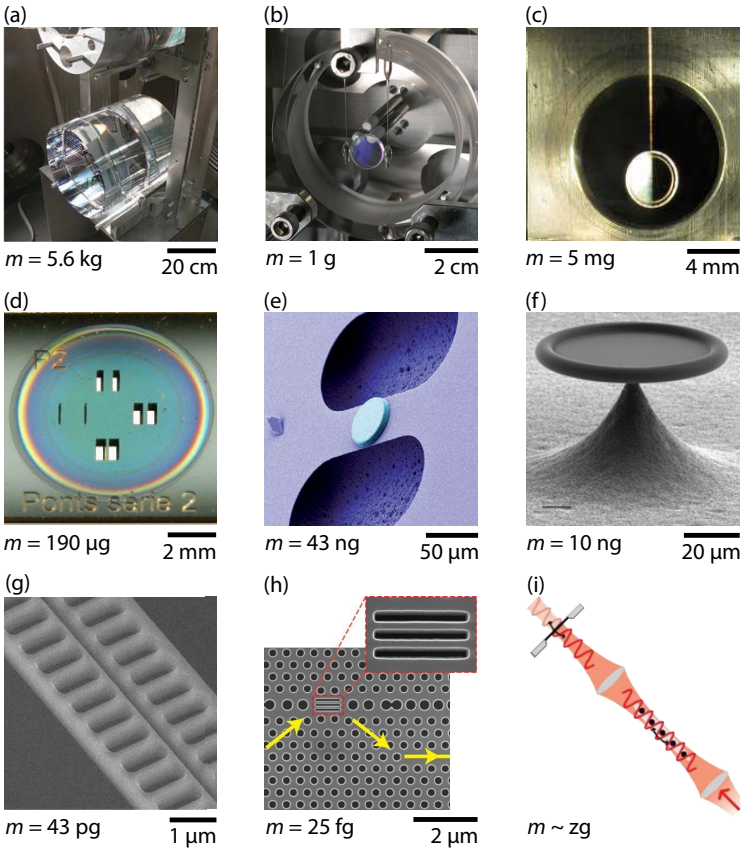

Figure 1.2: Example realizations of optomechanical devices at different weight scales, covering over 20 orders of magnitude. Indicated mass m refers to the effective motional mass (m_{eff}) of the resonator mechanical mode, used in the experiment (in the absence of such data, we provide the bulk mass of the moving device part). (a) Suspended end-mirror from GEO 600 gravitational wave detector interferometric set-up [Schnabel 2010]. (b) Gram-scale [Neben 2012] and (c) milligram-scale [Matsumoto 2013] suspended mirrors, analogous to the (a) device. (d) Double-clamped beam with mirror coating [Arcizet 2006a; Arcizet 2006b]. (e) Bragg mirror, coated on top of a doubly-clamped beam [Gröblacher 2009]. (f) Microtoroidal resonator on a thin pillar [Schliesser 2008b]. (g) 'Zipper' cavity optomechanical system, consisting of two doubly-clamped photonic crystal beams [Eichenfield 2009a]. (h) Two doubly-clamped nanobeam resonators, embedded inside a defect cavity within two-dimensional photonic crystal lattice [Sun 2012]. (i) Schematic of an optomechanical experiment with ultracold atoms [Purdy 2010; Camerer 2011]. All figures are adapted from the corresponding references.

$c^*/2\pi f_{\mathrm{m}}$, and $c^* = \sqrt{B/\rho}$ is the speed of sound in material. As for the optical part, the equivalent criterion applies: the smallest monolithic cavity volume, where an optical mode of wavelength λ_0 can exist, is approximately $(\lambda_0/2n)^3$, where n is the refractive index of material and $\lambda_0 = c/2\pi\nu_0$ with c as the speed of light in vacuum. Several diffraction-limited optomechanical systems were designed, among which photonic crystals, that allow to efficiently control the light propagation and confinement at micro- and nanoscale. An

example of picogram weight scale is a pair of one-dimensional photonic crystal nanobeams (Fig. 1.2g), or so-called 'zipper' cavity, whose high optomechanical coupling was achieved through a design insuring a high overlap between the optical mode of a defect cavity in the beam centre and its flexural mechanical modes. The same technique was used to decrease even more the size of mechanical oscillator down to few tens of femtograms weight and increase its frequency up to GHz range. Such a mechanical oscillator would no more support an optical mode in the usual working range of wavelengths (visible of near infrared), but its motion still introduces a perturbation within an optical cavity, opening a way for a new category of "NEMS[2]-in-cavity" devices, based on optomechanical interaction at the nanoscale.

The last example (Fig. 1.2i) represents mechanical object weight of the order of zeptogram (10^{-24} kg), referring to optomechanical experiments with ultracold atoms, trapped within a standing optical wave [Purdy 2010]. A cloud of such ultracold atoms can be as well coupled to the motion of a free-standing micromechanical membrane [Camerer 2011] (as shown in illustration), where both the effects of backaction of the atomic cloud on membrane motion and vice versa are observed. Such set-up can be used for sympathetic cooling of the membrane motion to quantum ground state.

In *this* work we choose to work with an optomechanical system, able to confine light within the material, in a diffraction-limited optical cavity, created inside a two-dimensional photonic crystal. In the following Section we provide a brief overview of existing photonic crystal systems for optomechanical purposes.

1.3 Photonic crystals for optomechanics

Photonic crystal (PhC) describes a natural or artificially created system being able to control locally the propagation of light [Joannopoulos 2011]. In general, they are materials which have a periodicity in dielectric constant ε in one or more dimensions. Such a variation, introduced at the optical wavelength scale, can allow to control the light propagation in such a periodic structure along chosen direction(s). In analogy to band gaps for electrons in semiconductor crystal lattice, PhC lattices can as well be designed to prohibit the propagation of photons with certain energies. These forbidden photon energies, or the corresponding wavelength range, represent a photonic band gap (PhBG) [Yablonovitch 1987; John 1987]. If a defect cavity with an optical mode, which frequency ν_0 is situated inside the photonic band gap (PhBG), is created within a PhC lattice, such mode will be highly confined and will show high lifetimes for photons, since no mode can accommodate them within the surrounding lattice. Such system has been intensively employed in various fields and applications from single photon sources [Laurent 2005] to nonlinear optics [Bazin 2014]. Only recently, in 2009, it has been used in the frame of optomechanics [Eichenfield 2009a; Eichenfield 2009b]. This concept is used in all of the

[2]Stands for Nano-Electro-Mechanical System.

systems, presented in this Section, in view of creating an optical cavity, embedded into an optomechanical device.

1.3.1 One-dimensional photonic crystal beam cavities

Several designs of one-dimensional photonic crystal optomechanical beams exist (Fig. 1.3a-d,g,i), allowing essentially to achieve a very high-Q optical resonances by introducing an adiabatic tapering for the localized defect mode. Light confinement is achieved by the refractive index periodicity along the beam direction and total internal reflection along

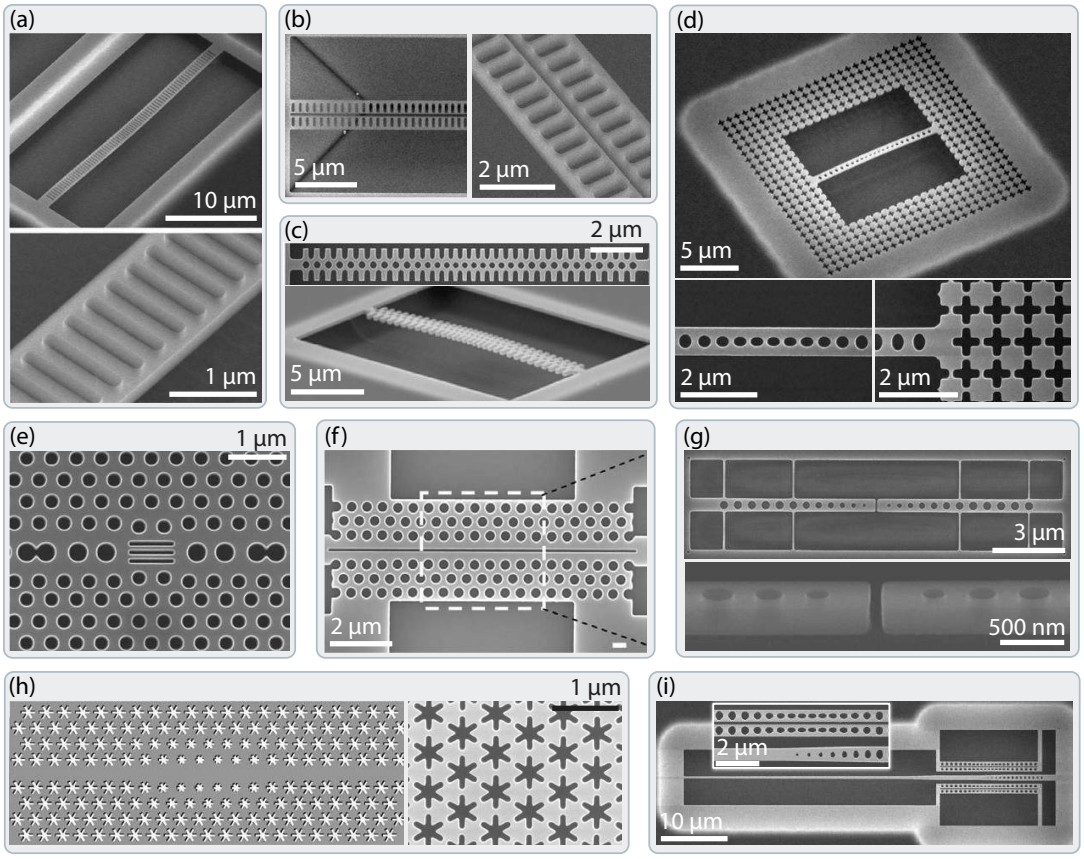

Figure 1.3: Example experimental realizations of optomechanical devices with photonic and phoxonic (combining optical and acoustic band gaps) crystals (given arrangement follows no particular order). (a) Photonic crystal beam [Eichenfield 2009b]. (b) 'Zipper' cavity, created by two adjacent doubly-clamped PhC beams [Eichenfield 2009a]. (c) One-dimensional phoxonic crystal [GomisBresco 2014]. (d) PhC beam, coupled to a photonic shield (phononic crystal lattice with complete acoustic band gap) [Chan 2011]. (e) PhC L3-nanobeam cavity [Zheng 2012]. (f) Slot-type cavity in 2D PhC lattice [Li 2010]. (g) Split-beam nanocavity, created from 1D PhC beam [Wu 2014]. (h) 'Snowflake' 2D phoxonic crystal with defect cavity in the middle [SafaviNaeini 2014]. (i) Two PhC 'zipper' cavities, coupled to a waveguide with 1D PhC mirror [SafaviNaeini 2013]. All figures are adapted from the corresponding references.

two remaining axes. At the same time, such structures exhibit some mechanical modes, localized within the beam middle (so that phonon tunnelling losses to the supporting structure are minimized) and thus often efficiently coupled to the optical mode, resulting in strong optomechanical coupling. Original ideas for further enhancement of the optomechanical coupling strength aimed at a reduction of mechanical clamping losses, strongly impacting even the vibrational modes, localized within the central part of a beam. The 'zipper' cavity [Eichenfield 2009a] as a combination of two 1D photonic crystal nanobeams [Eichenfield 2009b], allowed to create an phononic band gap (PhBG) alongside with the existing photonic one. Consequently achieved reduction of mechanical losses for a particular vibration with frequency f_{m} inside the PnBG and reduced effective motional mass of this mode (from $\sim$ 10 pg to $\sim$ 50 fg) have resulted in a dramatically increased force sensitivity of the final optomechanical system.

In addition, this made the photonic crystal systems to possess the lowest effective motional mass among the existing monolithic optomechanical devices, overcoming the performances of microtoroid realizations [Kippenberg 2007; Schliesser 2008b] (Fig. 1.2f). Following this achievement, a system combining two of such 'zipper' cavities, coupled to a tapered waveguide with PhC mirror termination [SafaviNaeini 2013], was demonstrated; such device can operate as a squeezed light source, created by the optomechanical coupling. Later, a single-beam design of 1D structure, named *phoXonic* crystal [Maldovan 2013], was proposed and implemented experimentally [GomisBresco 2014], featuring two full PnBG in the GHz range and a PhBG for TE optical polarized optical modes. Splitting a suspended beam, as in case of the 'zipper' cavity, was re-used in a transverse direction to create a split-beam nanocavity [Wu 2014]. Resulting device demonstrated a strong modification of the optical mode, confined in its middle, by the movement of each ends of the splitted beam.

Another approach for the enhancement of mechanical Q_{m} factor consists in attaching a resonant structure to the phononic shield (Fig. 1.3d) – a lattice, exhibiting a full acoustic band gap around the mechanical frequency of interest [Chan 2011]. This technique allows to perform a separate optimization of mechanical losses, while not compromising the optical properties of the defect cavity mode. In addition, such a phononic shield can be conceived for the enhancement of an arbitrary mechanical mode(s) of a nanobeam by adjusting the frequency of PnBG.

1.3.2 Photonic crystal slabs

One refers to photonic crystal slabs [Joannopoulos 2011] when considering a structure that is able to confine light in all three dimensions by a combination of two-dimensional periodicity (hence band gap) and a finite thickness in vertical direction for index guiding (via total internal reflection). Defects in such structures can be used to create optical waveguides and cavities. In optomechanics applications the hole slabs are used (contrary to rod slabs), providing the ability to suspend the resonator and optimize its clamping losses.

Both types of defects in photonic crystal slabs – cavity and waveguide – were employed in optomechanical devices. A defect L3 cavity formed inside a PhC slab membrane (three missing holes in a line) was supplemented by a nanobeam within the cavity core (Fig. 1.3e), which allowed to obtain a high-frequency mechanical resonator inside a strongly confined electromagnetic field. Such inclusion resulted in an important decrease of the cavity optical Q factor, therefore one line of holes (see Fig. 1.3e, middle line) was modified in order to restore the good optical properties (final device $Q \sim 56 \cdot 10^4$). A defect cavity inside a W1 waveguide (one line of holes missing) inside a PhC slab membrane was split in two parts along the waveguiding axis, crossing the middle of the optical mode (Fig. 1.3f), so that the mechanical motion strongly impacts its spatial distribution and therefore results in an important optomechanical coupling.

Simultaneous localization of photons and phonons in two-dimensional periodic structures with square arrangement was only demonstrated theoretically by now for L1 (one missing hole) [Maldovan 2006; Rolland 2012], for L3 (three missing holes in a line) and cross defect cavities [Jallal 2013]. Hole slabs of hexagonal arrangement with parameters suitable to obtain a PhBG in visible or infra-red ranges do not show any PnBG. The last of our examples is also based on the model of defect cavity inside a W1 waveguide, but extends to the field of phononic crystals, being designed to possess both acoustic and photonic band gaps (Fig. 1.3h). A hexagonal lattice, used in examples in Figs. 1.3e,f, origins in light confinement within the defect cavity, whereas a special type of unit cell – a snowflake – allowed to create a phononic band gap in the GHz range – first experimentally demonstrated phoxonic crystal slab device [SafaviNaeini 2013].

1.4 Integration in optomechanics: state of the art

The devices, described in the previous Section, all have an optical cavity, whose mode takes part in the optomechanical interaction. Traditionally this cavity is fed with a light coming from a probe laser, coupled to a taper fibre, which brought into the cavity evanescent field (all examples shown here, except the one in Fig. 1.3i). Such fibre requires custom preparation (central part is required to be much thinner than an ordinary fibre in order to couple to the cavity mode) and precise alignment with respect to the probed sample in three dimensions (in-plane to spatially match the cavity and vertically to achieve a proper coupling) with precision down to tens of nanometres. This complicates the experimentation of the device and adds several important restrictions: e.g., two optical cavities are hardly addressed at a time, the coupling conditions between the fibre and the cavity is unlikely to be reproduced, further integration of such devices is virtually impossible etc.

To overcome these restrictions, the existing systems use an integrated access channel, represented by an optical waveguide, which allows to efficiently address an optomechanical resonator at nanoscale. From the fabrication point of view, the easiest solution to implement was a rectangular profile waveguide with input and output grating couplers to couple to the experimental set-up scheme (Figs. 1.4a,b). All of the realizations found

in the literature demonstrate the access waveguide placed in the plane of optomechanical resonator, several examples are given in Figures 1.4a-d. The principal types of access geometries include straight (Fig. 1.4c) and curved (Fig. 1.4b) waveguide profiles at the point of coupling to the optical mode; eventually the optomechanical resonator can be designed as a part of the access waveguide (Fig. 1.4a). Taking advantage from the photonic crystal slab periodicity, one can also integrate an access defect waveguide into the PhC slab membrane (Fig. 1.4e). One or another geometry as well as the waveguide dimensions are adapted regarding the mode-matching conditions and the coupling efficiency one wants to attain.

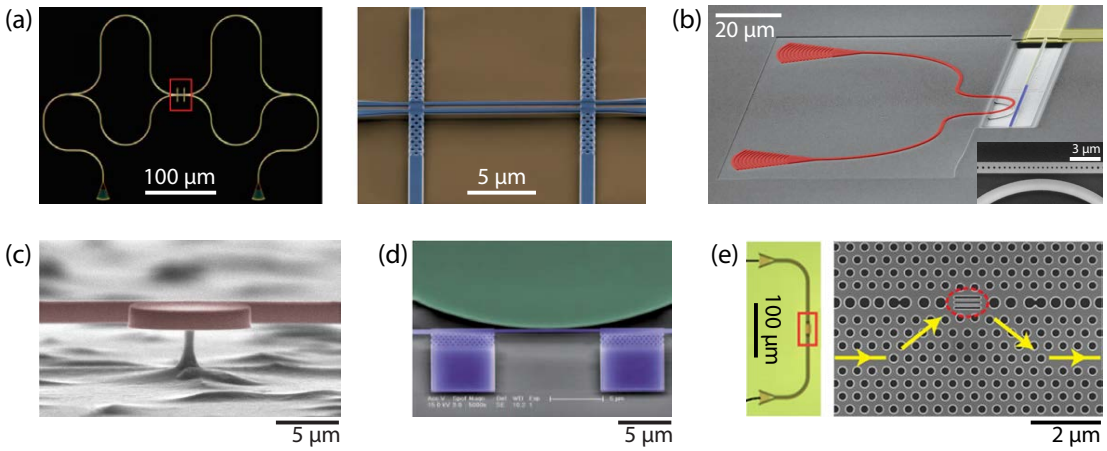

Figure 1.4: Example experimental realizations of optomechanical systems featuring integrated optical access channel. (a) Two suspended waveguides [Li 2009a]. (b) Suspended optomechanical crystal beam (blue) with photonic circuit (red, rib waveguide and grating couplers) [Bochmann 2013]. Microdisk with its suspended coupling waveguide (c) [Baker 2013]; (d) [Li 2009b]. (e) L3 – nanobeam cavity coupled to defect PhC waveguide [Sun 2012]. All figures are adapted from the corresponding references.

As a consequence of in-plane arrangement both waveguide and optomechanical resonator have to be made within the same layer, i.e., of the same material. This may induce additional optical losses due to low confinement of guided mode when using materials with low refractive index, therefore restricting the material choice for the resonator. The mode confinement in the waveguide is achieved by the index guiding principle; the simplest case is a high-index rectangle on top of a low-index substrate, e.g., silicon on SiO_2 (also known as SOI). The majority of present integrated devices are made of silicon (Figs. 1.4a,d,e), allowing to take advantage from the CMOS processing expertise. However, silicon is limited to wavelengths above 1.1 μm and does not allow device operation in the visible spectrum range where low-noise lasers are conveniently available. Moreover, its relative narrow electronic band gap also makes silicon optomechanical devices susceptible to strong two-photon absorption and free carrier absorption, which often lead to strong thermal effects that limit the device stability and cooling performance [Pernice 2011; SafaviNaeini 2011a].

Few of another materials appeared recently in the integrated optomechanical experi-

ments: these are diamond [Rath 2013] for its exceptional mechanical properties (Young's modulus of about 1 GPa) and aluminium nitride (AlN) [Xiong 2012; Bochmann 2013] (Fig. 1.4b) for low mechanical loss and high electromagnetic coupling strength, desired for electrically tunable optomechanical systems. To perform active photonic functionalities, impossible with silicon, gallium arsenide (GaAs) has in recent years found new applications in integrated optomechanical systems (Fig. 1.4c) exploiting a combination of high optical and mechanical quality factors [Ding 2011; Baker 2011]. Another III-V semiconductors like indium phosphide (InP) or gallium nitride (GaN) exist, allowing to achieve a light generation and wavelength conversion on chip, however, no integrated optomechanical devices were realized.

For the in-plane arrangement using one of the mentioned materials (diamond, AlN, GaN, etc.) important optical waveguide losses, in the material and due to fabrication imperfections (increased sidewalls roughness compared to silicon devices), make one reduce the dimensions of the waveguide, resulting in the designs like in (Fig. 1.4b).

Splitting the integrated access waveguide and the optomechanical resonator into two different levels may allow for complete flexibility when choosing the materials for each of the components. In addition it makes one more flexible when designing an optomechanical device, since the optical cavity from any resonator location can be addressed; in the same vein multiple cavities within one or several resonator can be addresses at a time using such access waveguide level, which is desirable for the development of multi-element optomechanical circuits in the frame of optomechanically-driven signal-processing applications. Designing a strongly coupled optical system using the waveguide and cavity modes, one can achieve an important optomechanical coupling of both dispersive and dissipative natures due to the modification of waveguide – cavity distance by the mechanical motion of the resonator. Having the full control over the waveguide geometry, it is then possible to control and tailor the different types of such optomechanical couplings on a single chip.

1.5 Concept of our device

Following the above-mentioned reviews in order to answer the raised questions we propose a system (Fig. 1.5) which will consist of a two-dimensional photonic crystal membrane made of InP, a III-V semiconductor material with direct band gap, allowing to embed a defect optical cavity to confine the light. Such material choice allows to have an active medium inside our device, such as quantum dots or quantum wells, for the integrated broadband light source, whose emission properties such as wavelength and linewidth can be widely tuned by the means of the optical cavity design. Mechanical motion of both the membrane and the cavity core will impact the optical properties of the defect cavity via different optomechanical effects. In order to efficiently feed the light into and from the cavity we design an integrated access waveguide in silicon-on-insulator, having all advantages of silicon photonics and much lower losses compared to the membrane material. The membrane will be vertically stacked over the waveguiding circuit, which has two principal

advantages compared to the in-plane access: first, the 'active' device part (i.e., where the optomechanical interaction occurs, in our case represented by the PhC membrane with cavity) and the access waveguide can be made of two different materials, allowing to choose the one with the optimized properties for each of these components; second, the in-plane access allows to efficiently couple to the optical modes situated in the close proximity of the waveguide, i.e., at or close to the edge of the optomechanical resonator, whereas our addressing configuration allows to address an arbitrary cavity location (or multiple locations) and gives full control over the mutual optical coupling and allows for flexible design of the 'active' device part. A sacrificial layer between the InP and SOI levels will be employed for the membrane suspension; a precise control over its thickness using the standard fabrication techniques will allow to have a full control over light coupling between the waveguide and the cavity and over the strength of the external optomechanical interactions, occurring while the latter coupling is modulated by the membrane motion.

We will rely on the hybrid integration approach, developed in the laboratory in collaboration with Ghent University [Roelkens 2008; Karle 2010], allowing for interfacing photonic crystal cavities via an integrated access channel. Such approach enabled for multiple novel applications in the field of nanophotonics. This work aims to extend its implementation to optomechanics experiments.

1.6 Organisation of the manuscript

Chapter 2 focuses on the theoretical description and simulation of optical and mechanical properties of our device alongside with the different optomechanical interaction mechanisms involved, which allows to understand and to explain the latter. It includes the designs of the photonic crystal membrane in the case of operation as a deformable end-mirror and in the integrated configuration, embedding a defect cavity. We describe the different regimes of optical coupling in the configurations with the integrated waveguide

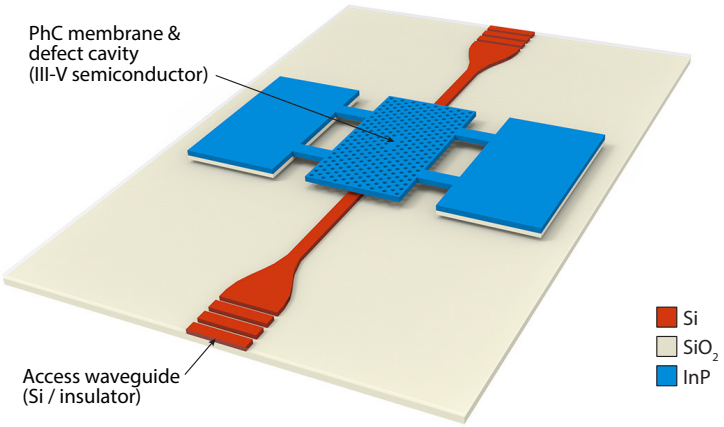

Figure 1.5: Conceptual view of proposed device architecture.

and their optimizations in view of achieving an efficient energy routing within the device. Next, the two families of mechanical modes are considered with the design proposals in order to control the mechanical dissipation in both cases. Analytical model describing the cavity response mediated by each of the optomechanical coupling mechanisms is depicted, including the intra-cavity couplings and the external ones, governed by the presence of the access waveguide, coupled to the cavity. The strengths of such couplings are simulated with the respective models with the description of tailoring mechanism for the external case. Finally, we review the obtained design characteristics in view of the possibility of optimizing the optomechanical cooling of our mechanical resonator.

Chapter 3 reviews the fabrication challenges and provides the details of device fabrication concerning its integrated configuration. It includes the heterogeneous integration of two principal layers, silicon and III-V semiconductor, for their further deterministic coupling; design of the waveguiding circuits for the efficient operation within our working wavelength range and for the efficient coupling to the experimental set-up scheme; the principal processing stages of optical and mechanical device components with the resolution of the principal encountered complexities and obstacles.

Chapter 4 describes the experimental characterization of the optical and mechanical properties of the fabricated device and of the optomechanical couplings and related effects. Two configurations are explored: suspended deformable photonic crystal mirror and integrated PhC slab cavity, coupled to the access waveguide. First allows to identify the mechanical modes, study the different mechanisms of mechanical losses for the flexural vibrations and verify the design optimizations, proposed in Chapter 2 for the reduction of the clamping losses. In the integrated configuration we perform the measurements of the dispersive and dissipative contributions to the intrinsic and external optomechanical couplings and review the limitations of such experimental identification compared to the numerical approaches. The calibration of the measured spectra of the Brownian motion is performed in order to experimentally determine the vacuum optomechanical coupling strength. Finally, we include the studies on system operation in non-linear optical regime in the presence of the optomechanical transduction mechanism, allowing for the system preparation to the bi-stable mechanical regime.

Chapter 5 gives general conclusions on the performed work and describes the potential system evolution and targeted future experiments.

In Appendix A we propose a development of another optomechanical membrane device, combining the tailored mechanical properties (an additional tensile strain, induced by a lattice mismatch between the membrane and host substrate materials) with light mass of the few hundred nm thick suspended layer. We investigate the alternative materials for such a system, combining the advantages of planar dielectric membrane resonators (i.e., low optical losses in near infrared range, ability to tune the resonator stress state [Sankey 2010]) and the electro-optic properties of compound semiconductors [Liu 2011] (allowing the use of embedded light emitters, photothermal, photoelastic effect) in order to be exploited for quantum optical control of massive mechanical systems.

Chapter 2

Simulation of photonic crystal slab structures for optomechanics

Contents

This chapter presents the main concepts and the theoretical studies that were carried out on the optical and optomechanical couplings within the heterogeneously integrated PhC defect cavity – SOI waveguide system. The system optical and mechanical designs are discussed together with the corresponding approaches for their numerical simulation. Then we study the optomechanical coupling occurring in the chosen architecture and the nature of the various involved interaction mechanisms. This system enhances both the dispersive and dissipative couplings; their respective contributions are evaluated in view of reaching an optimal ground state cooling implementation.

2.1 Optical properties of photonic crystals for optomechanics

2.1.1 External and embedded cavities using photonic crystal

Let's consider a photonic crystal lattice, which represents a 2D periodic medium with a high-contrast variation of the refractive index between a dielectric material and the surrounding air. This variation can be described by a spatial distribution of the dielectric constant $\varepsilon(\vec{r})$. If we trace the solutions for the wave vector values along all directions within the crystal (following the Γ–M–K–Γ trace in the reciprocal space, see Fig. 2.1), we obtain a so-called photonic band structure, describing the dispersion of eigenmodes for the structure under study. The shaded band structure area in Fig. 2.1, called the light cone, is the projection of all states that can radiate in the air [Joannopoulos 2011]. With the analogy to an electronic band gap, our crystal has a photonic band gap (highlighted in dark grey), where at certain frequencies light is not allowed to propagate.

By making use of photonic band structure and some of the crystal Bloch modes, we can design it for a specific application in optomechanics, where it can become a highly reflective end-mirror for an external cavity or hold a defect cavity, which confines the optical mode within a small volume inside the PhC slab. The example band structure given in Figure 2.1 represents a particular 2D PhC lattice with equilateral triangular (hereinafter triangular) arrangement, but the concepts we describe below can be applied generally to any type of lattice and any crystal dimensionality.

Using the two superposed modes with flat dispersion at Γ point (Fig. 2.1a), we can make a PhC mirror, operating at normal incidence, with very high reflectivity at the corresponding mode wavelength (e.g., $R > 99.8\%$ for 50 nm band around 1064 nm for a rectangular lattice 2D PhC slab membrane from [Makles 2015]). From another hand, we can use the photonic band gap and design inside it a mode of an embedded cavity (Fig. 2.1b), created by introducing a defect in our perfect lattice (e.g., by removing or

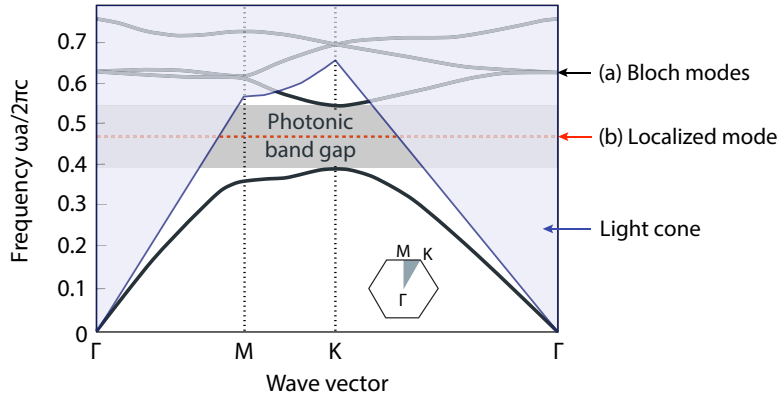

Figure 2.1: Example of a photonic band structure of infinite triangular PhC slab with lattice period a. Inset shows the corresponding irreducible Brillouin zone and its special Γ, M and K points. (a) Two optical eigenmodes with a flat dispersion at Γ point; (b) Example of a mode, localized inside the defect cavity. Shaded area represents the light cone, where the slab modes can couple to the radiative ones.

changing the size of one or several holes). In this latter case, the interference effects on the surrounding media with a periodic refractive index for the cavity eigenmode will allow to get an important electromagnetic field enhancement inside the defect optical resonator, leading to high optical Q factor.

If this cavity is integrated inside a suspended PhC membrane, one gets in addition a high refractive index contrast along the direction perpendicular to the membrane plane and thus a high mode confinement in the vertical direction. This mode confinement due to the total internal reflection on the interfaces between membrane dielectric and air not only allows for the engineering of high-Q cavities with ultimate volume ($V \sim (\lambda/n)^3$ with λ for wavelength and n for the refractive index of dielectric material), but also for high-reflectivity of a PhC mirror for a plane wave at normal incidence. According to the chosen optical cavity type, the PhC device will be probed in a different ways. If a suspended PhC mirror is considered, its mechanical motion can be read out in the interferometric (e.g., Michelson interferometer) set-up, or with an external Fabry-Pérot resonator [Makles 2015], where a highly-reflective PhC membranes serves as one of the mirrors. When optically addressing a defect PhC cavity, one can employ an access waveguide brought in its evanescent field [Aspelmeyer 2014], in either a taper fibre or integrated configuration.

2.1.2 Photonic crystal slab mirror

As it was introduced above, the two-dimensional photonic crystal lattice of a finite thickness (i.e., PhC slab) can be addressed in two distinct ways in order to probe the device mechanical motion. In the first case, the probe light is being reflected from PhC lattice at normal incidence.

This section is focused on the optical design and simulation of such a device – a photonic crystal slab membrane employed as a high-reflectivity mirror ($R > 99\%$) for the

wavelengths around 1064 nm and at normal wave incidence.

In our study the PhC hole slab membrane is made of InP, with the main geometrical parameters described in Fig. 2.2. The square lattice is defined by a hole radius r, a slab thickness t (along z direction) and a lattice period a, which corresponds to the distance between the centres of two adjacent holes. Main optical property of the structure – its refractive index (RI) $n = \sqrt{\varepsilon}$, is taken to be $n_{\mathrm{InP}} = 3.3$ at 1064 nm [Fox 2001], whereas the RI of air for the etched holes as well as for the space above and below the membrane is $n_{\mathrm{air}} = 1$.

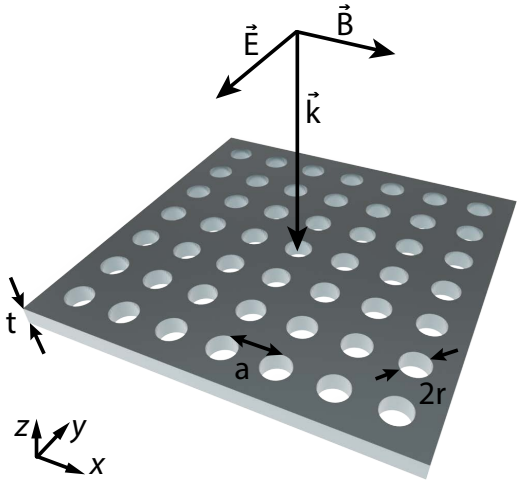

Figure 2.2: Schematic view of a photonic crystal slab with a rectangular lattice.

Discontinuities in the spatial distribution $\varepsilon(\vec{r})$ of the dielectric constant make impossible to solve analytically the Maxwell's equations for electromagnetic wave propagation in such kind of system. The numerical methods, that have been developed to find the solutions, can be classified into frequency-domain (FD) and time-domain (TD) categories. One of the pioneers in FD simulations was the Plane Wave Expansion (PWE) method, which comes from the studies of crystals in solid state physics. One of the popular implementations of the PWE method is realized in free *MIT Photonic Bands* (MPB)[1] software, which is used for calculations of photonic band structure for PhC systems. The solutions in this method realization are obtained using preconditioned block-iterative eigensolvers in a planewave basis [Johnson 2001], in this way the eigenmode frequencies and states of the wave vector can be found.

Another FD method, called Scattering-Matrix Method (SMM) [Yasumoto 2005] or S-Matrix method, is one of the most efficient for solving the problem of scattering in a periodic systems. In this work, we make use of its realization through a freely available S^4 package (Stanford Stratified Structure Solver) [Liu 2012], for simulations of electromagnetic propagation through given 3D structures with 2D periodicity. In brief, the implementation is the frequency domain code to solve the linear Maxwell's equations. It

[1] http://ab-initio.mit.edu/wiki/index.php/MIT_Photonic_Bands

considers the unit cell with the Bloch boundary conditions (BC), which corresponds to the simulation of an infinite structure along the directions where the corresponding BC were applied (axes x and y on Fig. 2.2). For the direction of wave propagation (z in the same Figure), a multi-layer structure is described via a spatial distribution of a relative permittivity $\varepsilon = n^2$. The structure transmittance and reflectivity (Fig. 2.3) are then evaluated as the Poynting vector flux through the last and the first layer in the simulation stack (air above and below the membrane in our case), normalized to the incident one, correspondingly.

Our structure is operating in the regime of a near-wavelength diffraction grating (NWDG) [Karagodsky 2012], or a thin slab of material with refractive index with periodicity a slightly smaller than the incident optical wavelength λ. The diffraction properties of an NDWG element are strongly different when comparing to usual diffraction gratings. Such properties result from a combination of special conditions: $a < \lambda$ would imply that all diffracted beams of non-zero order are evanescent in the surrounding air. Besides this, when $\lambda/n_{\text{eff}} < a$ (where n_{eff} is an effective refractive index of the PhC slab membrane), several propagating modes will exist inside the dielectric slab. Then, for some particular values of membrane thickness t, the boundary conditions at the dielectric/air interfaces will result in a destructive interference for the transmitted zero-order of the incident plane wave. Consequently, by conservation of the optical flux, such a phenomenon is associated with a reflectivity close to unity for the incoming beam.

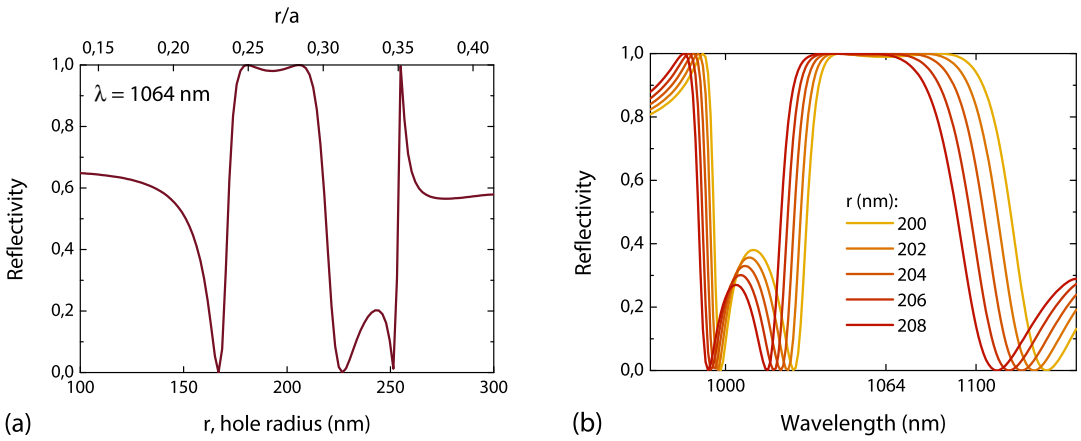

Figure 2.3: Reflectivity spectra of an InP photonic crystal slab structure with the parameters $t = 260$ nm and $a = 725$ nm for varying hole radius r.

With the above-mentioned conditions and for the design wavelength $\lambda = 1064$ nm, the crystal lattice period was chosen as $a = 725$ nm. Next, for a hole radius of $r = 200$ nm a study of the reflectivity of our NWDG was performed while varying the membrane thickness t, which revealed a large high-R plateau around 1064 nm wavelength for the value of $t = 260$ nm. In the technological realization of our devices the lattice parameter a fidelity is controlled better than the hole radius r, therefore we are looking next for the

range of r, where the reflectivity of our PhC mirror will exhibit a plateau of high values. In this purpose, for the given layer thickness $t = 260$ nm and a constant lattice parameter $a = 725$ nm we analyse the reflectivity R dependence on the hole radius (see Fig. 2.3a), which shows a relatively large high-R plateau for the radii between 180 and 210 nm. We further explored the given parameter span to simulate the spectral reflectivity dependence (see Fig. 2.3b), which for $r = 202$ nm gives about 50 nm large region with $R \geq 0.99$ centred at 1064 nm. Analysis of the structure design tolerance to the fabrication imperfections (the designed and fabricated holes r mismatches) shows that up to 6 nm mismatch the reflectivity at 1064 nm will remain as high as for the optimal parameters set.

Presented results are valid in assumption of a perfect plane wave, incident on an infinite PhC lattice. The realistic scenario of a laser beam requires taking into account the angular spread in the wave vector associated with the beam waist on the membrane plane. In the same time this allows to examine the angular dependence of the PhC mirror reflectivity for the angles close to normal incidence. The corresponding simulations, performed in [Makles 2015], show that it is still possible to obtain reflectivities $R > 99\%$ for a beam waist of 4.2 μm, however, over a reduced wavelength span > 20 nm. Concerning the angular dispersion of an incident wave at 1064 nm wavelength, the PhC membrane reflectivity does not degrade for the angles span up to 5°, and reaches $R = 99\%$ value at incidence angle close to 9°.

2.1.3 Photonic crystal L3 defect cavity strongly coupled to external waveguide

In a second configuration, allowing for full integration of the optomechanical platform, the optical cavity is embedded in the photonic crystal slab membrane. In that case the probe light is coupled to the cavity mode via an external waveguide. As it was introduced before, a tapered fibre or an integrated waveguide with the input-output couplers can be used for this scheme. Our solution includes a SOI access waveguide, positioned nearby the cavity in a way to couple light between the waveguide and the cavity via the evanescent field tail.

2.1.3.1 SOI waveguide optical mode

The single waveguide on the SOI circuit used in this work (Fig. 2.4) is a silicon ridge of width W_{wg} (along y axis), height h_{wg} (along z axis) and few hundreds microns long (along x axis, which is the direction of wave propagation). Hereinafter the height h_{wg} is set constant to 220 nm (unless otherwise stated), corresponding to the real ridge height in our fabricated devices. The insulator layer below the waveguide comprises $h_{\mathrm{SiO_2}} = 2$ μm of silicon dioxide, which corresponds to the height shown in Figure 2.4. The refractive indices used in electromagnetic simulation at 1.55 μm, are $n_{\mathrm{Si}} = 3.4777$ for silicon [Salzberg 1957] and $n_{\mathrm{SiO_2}} = 1.4442$ for silicon dioxide [Malitson 1965].

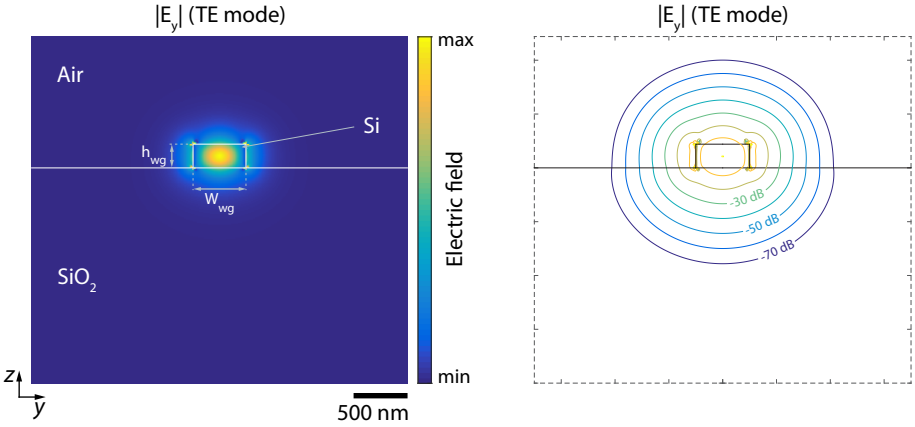

Figure 2.4: Simulated E_y field component (absolute value) distribution for the fundamental optical quasi-TE mode of a ridge Si waveguide at 1.55 μm with $W_{\mathrm{wg}} = 500$ nm, $h_{\mathrm{wg}} = 220$ nm, $h_{\mathrm{SiO_2}} = 2000$ nm. (Left) colour plot with adapted mapping; (right) isolines showing mode decay in $y - z$ plane, with 10 dB difference between two adjacent curves (distance between two ticks on both axes is 500 nm).

We simulated the fundamental quasi-TE waveguide mode, where the main electric field component is perpendicular to the propagation direction and lies in the plane of the Si core. Mode wavelength was chosen to be $\lambda = 1550$ nm. The obtained E_y distribution (Fig. 2.4) at 1.55 μm shows a good mode confinement within the waveguide core due to high refractive index contrast and perfect ridge isolation from the host Si substrate. The mode effective index is $n_{\mathrm{eff}} = 2.39$. As can be seen, the field decays to -70 dB at 1 μm depth in SiO_2, whereas the total waveguide – substrate separation is 2 μm.

Simulation of the fundamental waveguide quasi-TM mode (the main magnetic field component is perpendicular to the propagation direction and lying in the plane of the core layer) at 1.55 μm gives a similar field distribution to the quasi-TE one (Fig. 2.4), but with a much lower effective index $n_{\mathrm{eff}} = 1.60$. The phase constant $\beta_{\mathrm{wg}} = 2\pi n_{\mathrm{eff}}/\lambda$ is thus smaller as well, corresponding to a lower field confinement within the waveguide core and consequently more losses for the propagating mode. For the latter reason it was chosen to work in the TE-like configuration.

2.1.3.2 Photonic crystal slab with TE-like band gap around 1.55 μm

As introduced in Section 2.1.1, light confinement inside a photonic crystal can be achieved by creation of a defect cavity: lattice periodicity is locally broken by introducing a point defect (a hole removed or replaced with one whose size, shape or dielectric constant is different than the original). The resonant cavity mode would only exist if its frequency lies inside a photonic band gap of the host lattice. At these forbidden frequencies the interference effects on the surrounding periodic medium result in a high electromagnetic field confinement within a defect. Considering the wave propagation directions in the plane of the PhC slab, the TM-like (transverse magnetic, no magnetic field in the wave

propagation direction) and TE-like (transverse electric, no electric field in the wave propagation direction) gaps can be achieved with rectangular rod slab and triangular hole slab (Fig. 2.5a), respectively [Joannopoulos 2011]. Full band gaps (any wave polarization is prohibited) cannot be achieved within the photonic crystal slab lattices.

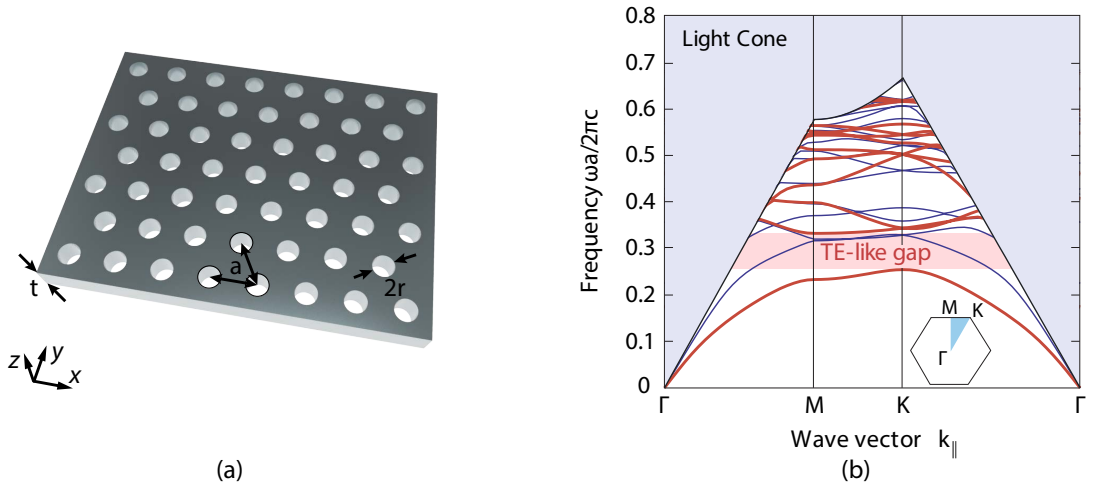

Figure 2.5: (a) Schematic view of a photonic crystal slab with a triangular lattice. (b) Band diagram for photonic crystal slab from (a) with following parameters: $r = 0.3a$ and $t = 0.6a$ (adapted from [Joannopoulos 2011]). Red and blue lines represent TE and TM-polarized in-plane guided modes, respectively. The corresponding Brillouin zone with its special points is given in inset.

Although the successful realizations of defect cavities in a rectangular PhC slab (as one that we studied in Section 2.1.2) were demonstrated [Hennessy 2003; Sar 2011], the electric field maximum in such devices is localized in the air holes surrounding the cavity. Among different existing defect cavity realizations in triangular lattice, we chose a line defect (i.e., one or few missing holes in a line), which was extensively studied over last decade [Akahane 2003; Sauvan 2005; Akahane 2005]. They allow to confine optical modes within the dielectric medium, which is the preferred configuration for our optomechanical device, as it promotes light-matter interaction.

According to the chosen access waveguide mode properties (see Section 2.1.3.1), we designed the PhC slab in view of opening a band gap for TE-polarized mode (Fig. 2.5b) around 1550 nm wavelength. For the given InP refractive index ($n = 3.16$ at 1550 nm at room temperature [Pettit 1965]) and membrane thickness $t = 260$ nm, we obtain about 100 nm large TE-like band gap, centred at 1.54 μm with the lattice parameters $a = 420$ nm and $r = 90$ nm. The small changes (within ± 10 nm from the designed one) in hole radius would shift the band gap of approximately 5 nm per 1 nm of Δr (with respect to its sign).

2.1.3.3 Optical mode of defect PhC cavity

Optical microcavities, created in a PhC lattice slab with triangular hole arrangement, by a point defect (one missing hole) or few of them in a line, are commonly designated in literature as Lx cavities (where x equals the defect length in number of missing holes). Standard L3 cavity, compared to L1 and L2, has better optical quality factor [Sauvan 2005] (up to one order of magnitude higher) and possesses very low mode volume ($V \simeq 0.7$ cubic wavelengths), limited by diffraction. These cavities have already been implemented in various applications (PhC lasers [Painter 1999; Ellis 2011], cavity quantum electrodynamics (cQED) experiments [Yoshie 2004], drop filter [Takano 2004]). We extended here their use to cavity optomechanics. For higher x value ($x > 3$) the PhC cavity becomes multimode and the optical Q factor of its resonances degrades [Okano 2010].

Fine-tuning of such L3 cavity optical losses was demonstrated [Akahane 2003] by displacing two air holes at both edges by an optimal value dx_A (cf. Fig. 2.6). Such displacement allows for high Q factor while the mode volume remains virtually unchanged. Such procedure, applied to silicon structures, demonstrated an experimental Q factor enhancement from 10^3 to 4.5×10^4. This value can be even increased by shifting the neighbouring external holes, located in the same line with the ones displaced by dx_A, as described in [Akahane 2005], leading to the cavity Q factor increase up to 10^5 (experimentally measured value; the simulated one is 2.6×10^5). This kind of optimization procedure, though, requires more computational effort in order to inspect the additional shifting distances, moreover, an obtained cavity geometry would be more complex in terms of understanding it mechanical and optomechanical operation.

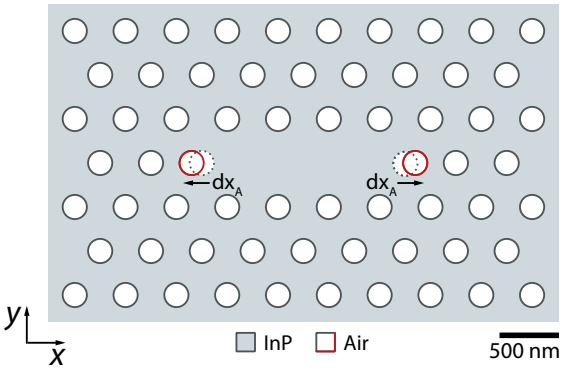

Figure 2.6: Schematic top view of investigated L3 defect cavity (incomplete plot, lattice of real device continues in both x and y directions). Two first holes (dotted circles) are displaced for dx_A outwards from the cavity along x axis.

The simulations of the optical properties of our devices were performed using two types of methods. Widely employed numerical method from time-domain category is the Finite-Difference Time-Domain (FDTD) technique [Courant 1928; Yee 1966]. FDTD is a versatile modelling technique and calculates the electric and magnetic fields everywhere in the computational domain as they evolve in time. A broadband pulse (such as a Gaus-

sian pulse) is used as the source, then the response of the system over a wide range of frequencies is obtained with a single simulation. Therefore it is useful for the cases where resonant frequencies are not exactly known, or any time when a broadband result is desired. Together with these advantages, FDTD method requires the entire computational domain to be gridded with spatial discretization sufficiently fine to resolve both the smallest electromagnetic wavelength and the smallest geometrical feature in the model. For complex models, very large computational domains can be easily developed, which results in very long computational times. The FDTD software, used in this work, is the commercially available package *FDTD Solutions* by Lumerical[2]. We used this software for the calculations of PhC defect cavity modes, with and without the evanescently coupled waveguide (optical Q factors, modal volumes, spatial electromagnetic field distributions and their temporal evolution).

Some part of numerical modelling of the optomechanical interaction in our devices was accomplished with a Finite Element Analysis (FEA) software and its particular realization in *COMSOL Multiphysics*[3] software platform. It implements advanced numerical methods for modelling and simulating various physics-based problems through particular modules, which can interact between them, providing standalone solution for multiphysics simulations. The RF (radio frequency) Module[4] was used for computing the electromagnetic field distribution of the cavity optical mode. In COMSOL implementation of this module, Maxwell's equations are solved using the finite element method with numerically stable edge elements. Cluster computing is also supported, as the large computational domains with high resolution for electromagnetic field studies are required in order to correctly model the studied characteristics.

Both 3D FDTD and FEA methods were employed and gave consistent solutions for cavity optical eigenmodes. The fundamental optical cavity mode at 1.54 μm (Fig. 2.7b, 2.8) was simulated by placing one or more electric dipole sources (TE-polarized) in the cavity medium and examining the time evolution of the field (in the case of FDTD simulation, cf. Fig. 2.7a) or the stationary solutions (in FEA simulation). A short pulse duration, i.e., its broad spectrum, allows to examine the broadband cavity response with a single simulation run. The time decay monitor for the electromagnetic field is also placed inside the cavity, allowing to examine its temporal evolution. An example of such a trace is shown on Figure 2.7b, where the electric field decays very slowly (compared to the launched dipole pulse of few tens of fs), attesting the presence of one or more high-Q cavity resonances.

The Fourier transform of the E_y time domain trace allows to reveal and identify the existing optical cavity modes (Fig. 2.7b), if the simulation time is long enough to achieve a frequency resolution better than the spectral linewidth of the cavity resonance. Corresponding field distributions inside the cavity can be seen in Fig. 2.8 for the resonance at 1.54 μm and will be used later for the simulation of optomechanical coupling.

[2] http://www.lumerical.com
[3] http://www.comsol.com/comsol-multiphysics
[4] http://www.comsol.com/rf-module

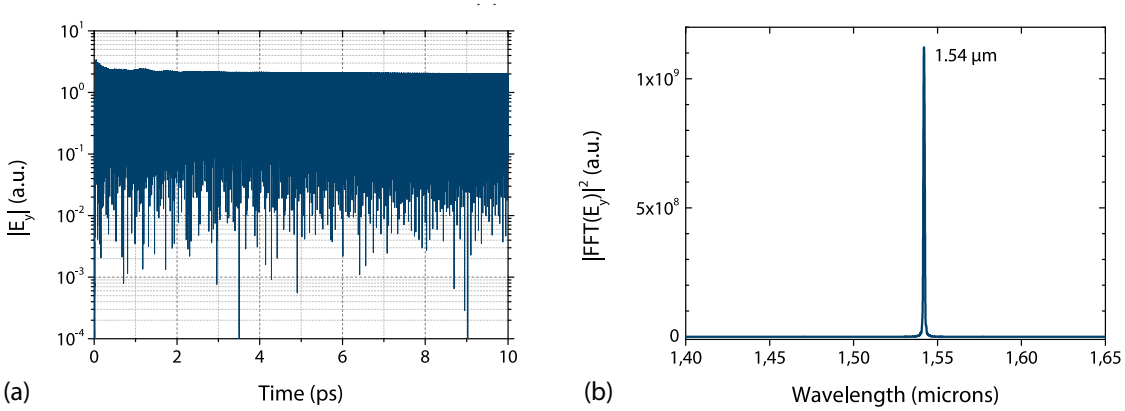

Figure 2.7: (a) 3D FDTD simulation of the E_y electric field decay (absolute value in logarithmic scale) inside a defect L3 PhC cavity over the simulation time. The flat aspect of such trace over 10 ps generally indicates the presence of a high-Q cavity mode(s). (b) Fourier transform of the E_y field component, showing the cavity mode at 1.54 μm.

The study was performed on a lattice having 31 period along x axis and 21 along y axis (directions shown in Fig. 2.6). InP slab has refractive index $n = 3.16$ at 1550 nm[5] at room temperature [Pettit 1965], thickness $t = 260$ nm and surrounded by $5t$ thick air layers from both sides along z direction. Symmetric Bloch boundary conditions (BC) are applied at $y = 0$ and $z = 0$ planes; asymmetric BC – at $x = 0$ plane, considering the symmetry properties of fundamental optical mode, that has been first simulated without any BC except the absorbing PML (perfectly matched layers) [Berenger 1994] at the outer boundaries of the entire computational cell. The symmetry conditions reduce the simulation time eightfold, corresponding to the reduction of the computational domain.

The technique used to identify the optical resonance, however, does not allow to properly retrieve the quality factor of the revealed modes, as in general the spectral resolution is not high enough. For its correct estimation in the current version[6] of Lumerical *FDTD Solutions*, the time domain trace of electric field evolution inside the cavity (Fig. 2.7, left) is decomposed in Fourier space as a sine function and a decaying exponential, therefore allowing for both the identification of the eigenmode frequencies and their respective decay times. Optical Q factor optimization according to the technique used in [Akahane 2003], gave $dx_A = 0.2$ result, corresponding to simulated optimal Q of about 10^5 for the mode shown in Fig. 2.7b.

2.1.3.4 Mutual optical coupling

In our platform, light is coupled into the cavity via the integrated SOI waveguide. The optical coupling between two layers (SOI and PhC) has been examined in order to optimize

[5]Lumerical *FDTD Solutions* software package provides an internal material database (including InP, Si and silicon dioxide present in the simulated devices) with the wavelength-dependent refractive index, which was used in our studies instead of constant n values.

[6]The versions used during this work cover 8.5 through 8.11.

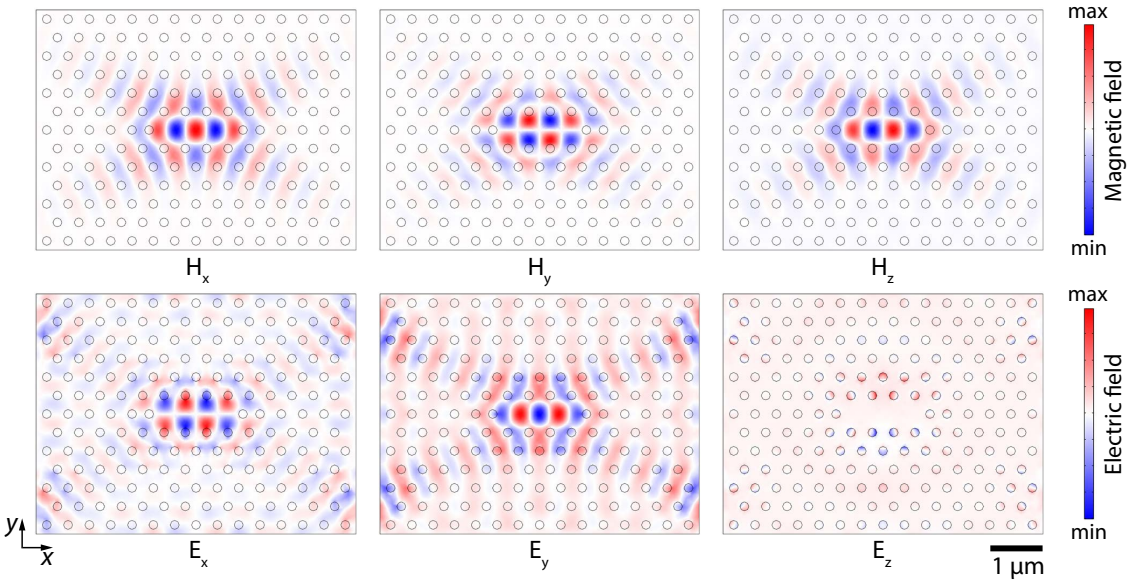

Figure 2.8: Simulated electric and magnetic field distributions for the fundamental optical TE mode of L3 PhC cavity at 1.55 μm with $t = 260$ nm, $a = 420$ nm, $r = 90$ nm, $dx_A = 0.2$. The maximum/minimum values of E_i scale are about 10 times bigger than the ones of H_i.

the energy transfer efficiency within the final device. The coupling of a III-V PhC cavity to a SOI waveguide at short distances is based on the side-evanescent coupling mechanism. In this mechanism, the mode of each optical component is weakly perturbed by the presence of the other one, positioned nearby. The waveguide is centred in $x - y$ plane with respect to the defect cavity, whereas the cavity is suspended few hundreds of nanometres above (see Fig. 2.9).

For the defect L3 PhC cavity (cf. Section 2.1.3.3), the electric field envelope decays exponentially (Fig. 2.9) in the direction towards the Si waveguide (z axis). The same behaviour is also observed for the designed SOI waveguide (Fig. 2.4). The overlap of the evanescent tail, or the exponentially decaying part of electromagnetic field, with the field inside the core of the coupled optical device will determine the mutual coupling strength [Haus 1984]. Such coupling mechanism can be highly efficient; it is widely employed in directional waveguide couplers [Marcatili 1969] as passive devices for optical power splitting and modulation [Taylor 1973].

In the following part, we exploit a similar approach than the one developed in [Bazin 2013] to explain and estimate the coupling efficiency within cavity-waveguide system.

Coupling efficiency between the integrated waveguide and the PhC cavity is one of the principal figures of merit considering the energy routing within the hybrid system. A stationary geometric state of the system, when all the components are fixed at pre-defined distances, can be designed in the way to precisely control the amount of light, coupled from the cavity to the interfacing circuit. We consider two main loss channels in the hybrid

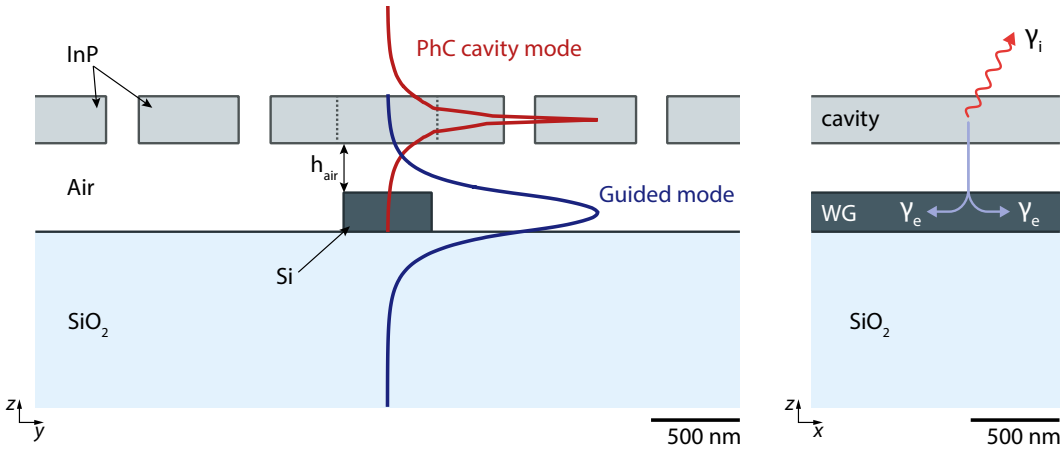

Figure 2.9: Transverse schematic of the hybrid structure (two cutting plane pass through the PhC cavity middle, cf. Fig. 2.6). Red and blue lines correspond to the normalized amplitudes of E_y field along the middle line ($y = 0$) of the respective optical component, simulated separately and superimposed at $h_{\text{air}} = 500$ nm (the SOI waveguide (WG) parameters are the same as in Fig. 2.4. For reference, the inner cavity border along x axis (left pane) is represented with a dotted line. Right pane illustrates the two main loss channels in the coupled system: radiative (γ_i) and coupling to the backward- and forward-propagating waveguide modes (γ_e).

system (Fig. 2.9) – PhC cavity emission due to the coupling to the radiative modes (which defines the intrinsic losses γ_i) and the evanescent coupling to the guided SOI waveguide mode (represented be the external losses $2\gamma_e$). By proper design, the cavity field coupled to radiative modes can be considerably reduced, concomitantly with a preferential tunnelling of the cavity mode energy into the integrated circuit. In turn, the signal propagating in the waveguide can be coupled with a desired ratio inside the connected cavity. The coupling efficiency value η, is thus defined as follows:

$$\eta = \frac{\text{Rate of optical losses from the cavity into the waveguide}}{\text{Total amount of cavity optical losses}} \tag{2.1}$$

If each of the loss mechanisms is characterised by a corresponding electromagnetic field decay time τ, we can as well attribute a respective quality factor Q, expressed as $Q = 2\pi\nu_0\tau$, where ν_0 is the cavity resonance frequency. Then, it can also be written that

$$\eta = \frac{\frac{1}{\tau_c}}{\frac{1}{\tau_c} + \frac{1}{\tau_0}} = \frac{Q_0}{Q_0 + Q_c} = \frac{\frac{Q_0}{Q_c}}{1 + \frac{Q_0}{Q_c}}, \tag{2.2}$$

where τ_0 (τ_c) and Q_0 (Q_c) are the field decay times and quality factors related to the radiative losses (respectively to the evanescent coupling into the propagating waveguide mode). The corresponding relations with the cavity loss rates, or linewidths, are $Q_0 = \omega_0/\gamma_i$ and $Q_c = \omega_0/2\gamma_e$.

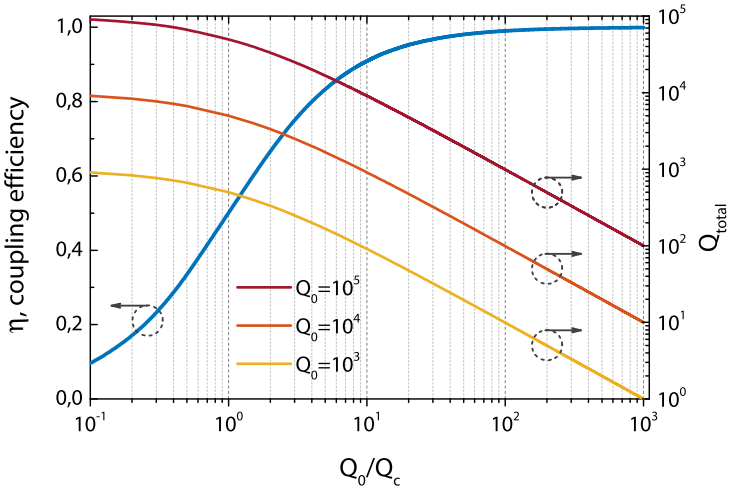

Figure 2.10: Coupling efficiency η as a function of the ratio Q_0/Q_c and total optical quality factor Q_{total} for several values of Q_0, as computed with the coupled mode theory.

Equation 2.2 holds if assuming that the perturbation of the PhC cavity mode by the waveguide is small enough that Q_0 and resonance frequency ν_0 can be considered constant. This holds the designs in which the distance between the waveguide and the cavity h_{air} (Fig. 2.9) remains large enough, i.e., for the evanescent coupling. The unloaded cavity quality factor Q_0, is considered constant ($Q_0 = 10^5$) in the following discussion.

The coupling efficiency dependency from Eq. 2.2 is plotted in the Figure 2.10 (blue trace) for Q_0/Q_c ratios, that cover the range of theoretically achievable ones with different designs of our device (via the variation of coupling losses from cavity to waveguide mode). In general, when distance h_{air} increases, the overlap between cavity and waveguide evanescent field tails will be superimposed, leading to the increase of the coupled field decay time factor τ_c (and the associated quality factor Q_c). With the constant Q_0, as assumed above, the Q_0/Q_c ratio thus decreases. In another words, $Q_0/Q_c \propto 1/h_{air}$.

For the cases where the Q_0/Q_c ratio exceeds 9, the coupling efficiency η is higher than 90%, thus an efficient energy exchange can establish. From another side, a considerable decrease of the coupled quality factor Q_c leads to an important decrease in the total cavity $Q_{\text{total}} = 1/(Q_0^{-1} + Q_c^{-1})$. For example, the yellow trace in Figure 2.10 (the case of the constant $Q_0 = 10^3$) shows a total cavity Q decrease when its coupling efficiency to the waveguide η rises.

High Q_{total} factors would lead to more efficient optomechanical interactions within the resonator because of the longer photon lifetimes, whereas high coupling efficiency η guarantees an important photon flow from the cavity to the access waveguide. As these two conditions can not be simultaneously maximized, a trade-off between sufficient optical coupling within the integrated circuit and sufficient photon lifetime inside the PhC cavity has to be found. The latter could be enhanced without additional impact on coupling efficiency by the optimization of intrinsic and radiative optical cavity losses Q_0, leading

to higher Q_{total} values (orange and red traces in Fig. 2.10) and thus achieving stronger optomechanical interaction.

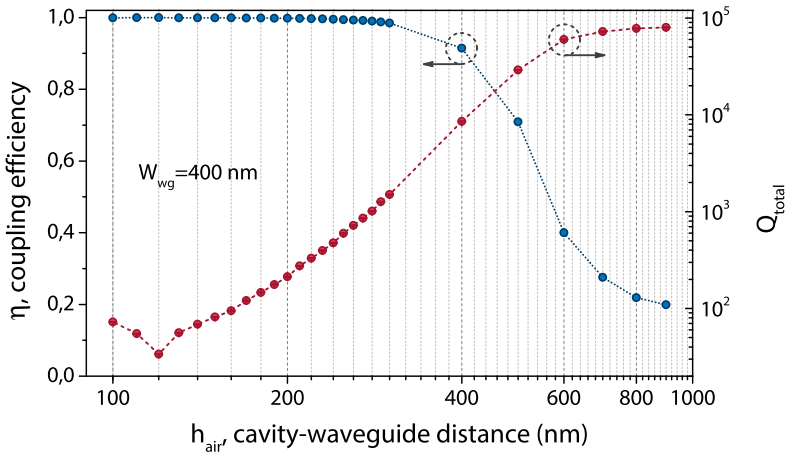

Figure 2.11: FDTD simulation of optical quality factor Q_{total} (dark red) and coupling efficiency η (dark blue) as a function of the cavity – waveguide distance h_{air}.

Maximization of the coupling efficiency η requires the accurate design of the field overlap in real space as well as the wave vector overlap in the reciprocal space. In the real space, this overlap would depend on the relative positioning of two corresponding optical components – cavity and the waveguide, in the reciprocal space – on the phase matching between their modes, impacted by the waveguide dimension W_{wg}.

By performing a 3D FDTD simulation of the coupled system (and not of the two levels separately, as it was done for the studies represented in Fig. 2.8, 2.4 and 2.9) it is possible to retrieve a Q_{total} factor and a resonance wavelength of a defect PhC cavity in its coupled regime of operation. The simulated dependences of η and Q_{total} follow the corresponding trends given in Fig. 2.10, with the inverse proportionality on x-coordinate, confirming the $Q_0/Q_c \propto 1/h_{\text{air}}$ relation derived above.

Obviously, these numerical studies would require much longer running times due to two factors: larger simulation volume with the same fine meshing and the lower number of symmetry planes; it is not straightforward to predict the order of magnitude of Q factor of a coupled system, therefore, the simulation time can not be strongly reduced and should still ensure good resolution in frequency domain in order to correctly evaluate the extracted Q and wavelength values.

2.1.3.4a Coupling efficiency in real space: fields overlap

Let us first consider the impact on the coupling efficiency of the thickness of intermediate air layer, h_{air}, measured from the top of the SOI waveguide to the bottom of the defect cavity. As seen above in this section, cavity and waveguide modes exhibit similar transverse field profiles (cf. Fig. 2.9), then, assuming their relative alignment to be per-

fect, the vertical separation change (along z direction) will directly modulate the overlap between the two fields.

Figure 2.11 shows the Q factor and coupling efficiency η evolution as the air band thickness h_{air} changes, for the fixed waveguide dimensions $W_{\mathrm{wg}} = 400$ nm and $h_{\mathrm{wg}} = 220$ nm. When the cavity is placed far from the waveguide, its total Q factor value reaches the one calculated in Section 2.1.3.3 for the uncoupled cavity, namely about 10^5. As can be seen in Fig. 2.11, the total Q decreases as h_{air} decreases, which can be simply explained by the enhancement of the penetration of the cavity mode evanescent tail inside the waveguide. In good agreement with the previous calculations (cf. Fig. 2.10) it shows (Fig. 2.12) that near 90% coupling efficiency is achieved with reduction by a factor of 10 in Q factor compared to the intrinsic one (Q_0) for $W_{\mathrm{wg}} = 400$ nm. Loaded cavity Q factor can drop by about three orders of magnitude from its initial value, corresponding to uncoupled operation (equivalent to a cavity – waveguide pair with the vertical separation starting from $\sim$1 μm thickness). Of course, the Q factor of the real device will generally be much lower than the one predicted by simulations (due to the fabrication imperfections), however, its relative dependency on the separation distance change will remain the same. It should be taken into account that for $h_{\mathrm{air}} < 300$ nm the mutual coupling starts to affect the PhC cavity resonance wavelength. This effect becomes more important as the layer separation decreases and will be discussed later.

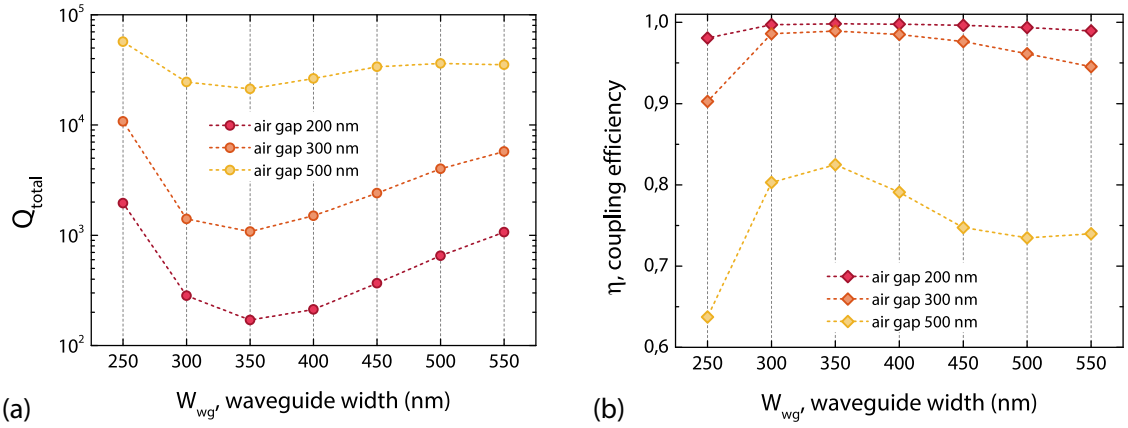

Figure 2.12: 3D FDTD simulation of optical quality factor Q_{total} (a) and coupling efficiency η (b) as a function of the SOI waveguide width W_{wg} for several cavity – waveguide distances h_{air}. Uncoupled cavity quality factor Q_0 (in the absence of the waveguide) is about 10^5.

Another geometric property in the hybrid system is the SOI waveguide width W_{wg}. Figure 2.12 shows how the Q_{total} factor (a) and corresponding coupling efficiency η (b) vary with the waveguide width for several air gaps h_{air} between the two levels. It can be clearly seen that these two quantities are also strongly dependent on W_{wg}, as expected due to the modification of the coupling conditions. The tendencies for their evolution as a function of h_{air} can be also found and in general apply for all the W_{wg} values examined. The optical mode of the waveguide is centred at the wavelength of the L3 cavity resonance;

for the invariant cavity field distribution a different field confinement may be achieved within a waveguide when its geometry (width) changes (cf. Fig. 2.12). In the same way the wave vector of the waveguide mode will change while changing W_{wg}. In consequence, the overlap of the fields in real space and the wave vectors in reciprocal space will change accordingly to the chosen waveguide geometry, modulating the coupling efficiency. For certain waveguide dimensions (e.g., $W_{\mathrm{wg}} = 350$ nm) a drop in total Q factor of more than 2 orders of magnitude can be observed together with a coupling η decrease from 99% down to 82% for h_{air} values varying from 500 nm to 200 nm. Such high coupling efficiency values spring from the fulfilment of the two above-mentioned conditions: a high spatial mode profile overlap and a good phase-matching (high wave vectors overlap in k-space) are achieved.

2.1.3.4b Coupling efficiency in reciprocal space: phase matching

In order to give a good description of the Q factor and thus the coupling efficiency trends when the waveguide width W_{wg} vary, we examined the overlap between the wave vectors of two optical modes in the reciprocal space. To quantify this phenomenon, we extract the wave vector magnitude along PhC in-plane (x–y) directions for the simulated E_y electric field component (cf. Fig. 2.8) of an uncoupled L3 PhC cavity. To do so, a Chirp Z-transform (CZT), a generalization of the discrete Fourier transform [Bluestein 1970; Rabiner 1975], which provides more realistic results comparing to a standard FFT, is employed in order to calculate the k_x and k_y vectors for the cavity optical mode, represented in Figure 2.13a. Then, according to the waveguide – cavity mode matching conditions, we consider the k_x wave vector distribution along the $k_y = 0$ axis (grey dotted line in Fig. 2.13a), which takes into account the fact of cavity alignment along the x axis.

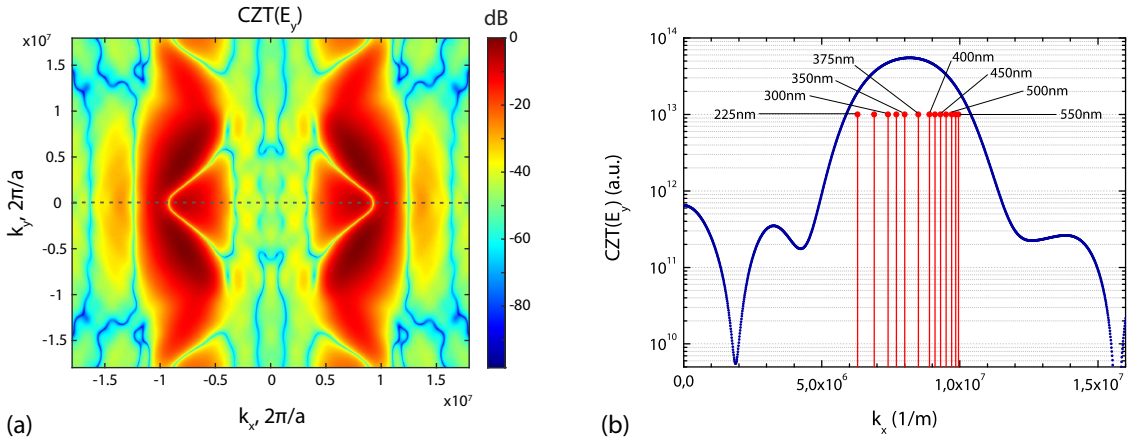

Figure 2.13: (a) Fourier transform of the simulated (FDTD) E_y electric field component of L3 PhC cavity (normalized to its maximum value, logarithmic scale). (b) Its extracted profile (blue) along $k_y = 0$ line (grey dashed on the left figure) with the wave vectors of SOI waveguides of different W_{wg} (red).

In Figure 2.13b, the positive values of k_x amplitude along $k_y = 0$ line (in blue) are superimposed with the waveguide wave vectors β_{wg} (in red), calculated for different widths W_{wg} from 225 to 550 nm (the ones in our device cover the range from 250 to 550 nm with a step of 50 nm). The k_x values for different waveguide geometries are calculated with Lumerical *Mode Solver* giving the effective index n_{eff} at the cavity resonance wavelength (see Section 2.1.3.1) using the relation $\beta_{\mathrm{wg}} = 2\pi n_{\mathrm{eff}}/\lambda$. The best phase-matching conditions are achieved for the width of $W_{\mathrm{wg}} = 350$ nm (limited by a W_{wg} stepping). It can be noticed that the value of β_{wg} decreases more rapidly as W_{wg} does below 350 nm value; for this reason the phase is increasing faster for $W_{\mathrm{wg}} < 350$ nm, leading in turn to faster Q factor growth and η worsening (see Fig. 2.12). For the waveguides larger than 350 nm, β_{wg} is increasing smoothly with W_{wg}, giving the shallow growth to the Q_{total} (and Q_c) and explaining the asymmetric shapes of the corresponding parameters in the Fig. 2.12.

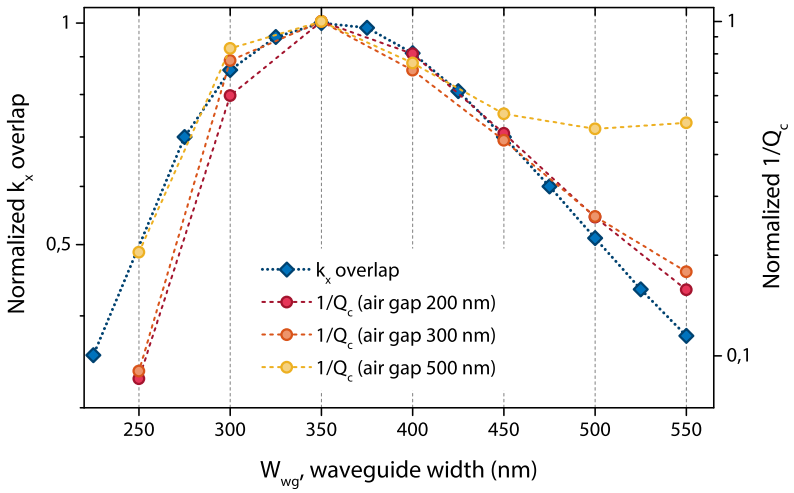

Figure 2.14: A comparison of k_x mode overlap (diamonds) and coupled cavity Q_c quality factor (for different air gaps h_{air}, circled), normalized to their maximum values.

Using this data, we calculated the integral of the wave vector overlap in the k_x direction. Considering that the guided modes are described by a Dirac functions in the corresponding space, the integral would be equal to the FFT of the cavity mode, evaluated at each of β_{wg}.

Figure 2.14 shows a comparison of the above-mentioned integral (denoted as k_x overlap) with the inverse coupling factor $1/Q_c$, or the cavity losses due to the presence of a waveguide in its vicinity, evaluated for different waveguide – cavity separation distances h_{air} (corresponding to the data in Fig. 2.12). Both quantities are normalized to their maximum values. As it can be seen, the coupling loss and the wave vector overlap exhibit a very similar trends while the W_{wg} is varied. The overlap is calculated exclusively along the $k_y = 0$ line, not taking into account the transverse spatial overlap (cf. Fig. 2.13a for the area of $k_y \neq 0$). This could be an origin of the remaining discrepancies between two parameters investigated on Fig. 2.14.

In summary, we studied the optical properties of two main parts of the hybrid system – SOI waveguide and L3 PhC cavity, taken either apart or coupled together via overlapping evanescent tails of their fundamental optical modes. The dependence of the cavity coupled quality factor Q_c and coupling efficiency η to the waveguide were examined as a function of two main opto-geometric parameters: the air gap h_{air} between the waveguide and membrane layers and the waveguide width W_{wg}, considering the mode overlap in the real and reciprocal spaces. Optimized high coupling efficiency $\eta \geqslant 98\%$ between the optical modes of the waveguide and the cavity across the whole range of waveguide geometries in our samples (W_{wg} from 250 nm to 550 nm) is achieved for the membrane suspension heights $h_{\text{air}} \leqslant 200$ nm, leading to the total cavity Q factors of the order of 10^2 – 10^3.

2.2 Mechanical properties of photonic crystal slab membranes

The suspended PhC slab not only sustain optical modes but also mechanical vibrations. The mechanical eigenmodes in our PhC slab system can be separated into two distinct families: low-frequency modes of the entire suspended membrane block and localized modes, which appear in the case where a defect PhC cavity is embedded inside the membrane. Along with the conventional eigenfrequency studies a numerical spectroscopy of these modes (both flexural motion of the suspended PhC slab ensemble and the vibrations localized within the cavity volume) has been performed taking into account the constraints of some real-world experimental configurations.

The mechanical dissipation is also reviewed for some modes of interest. It can be optimized while taking into account the main loss channels for each of the two mode families – flexural motion of the suspended PhC membrane ensemble or the confined vibrations inside the defect cavity body. We propose the corresponding solutions, that will be further implemented in the design of our mechanical resonators, potentially allowing for an enhancement of the optomechanical interaction via the high-Q mechanical resonances and/or the longer phonon lifetimes.

2.2.1 Flexural membrane modes

Suspended membrane resonator in the investigated device (cf. Fig. 2.15) consists of a rectangular plate of m_x by m_y lateral dimensions, patterned with either a triangular photonic crystal lattice including a defect cavity in its middle or with a square lattice, presented in the previous Sections. The same mechanical geometry will be used in both cases associated to the two different lattice arrangements. In each configuration the membrane is suspended over a layer of air using two pairs of bridges from two opposite sides. These bridges are identical and have lateral dimensions denoted b_x and b_y and leave the membrane anchored to the suspension pads. The thickness of all these elements is denoted t,

corresponding to the one of InP layer. As can be seen in Fig. 2.15, the membrane and all the connected bridges are suspended, whereas the support pads are assumed fixed.

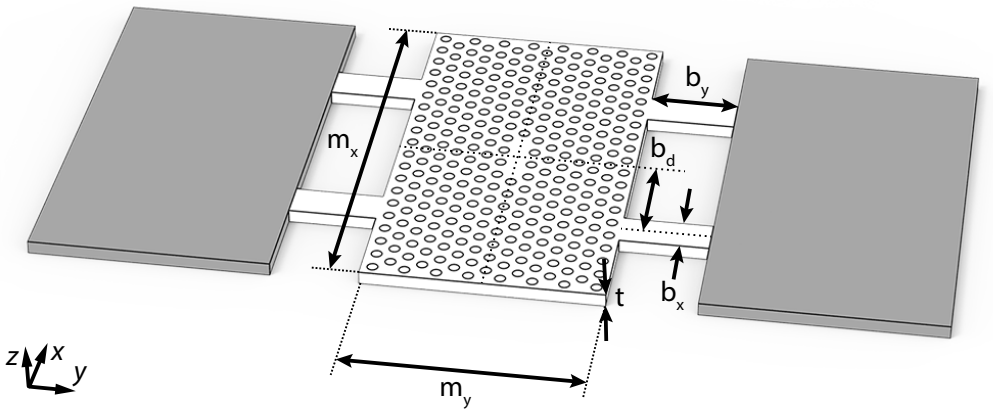

Figure 2.15: Schematic view of a suspended photonic crystal slab membrane with an embedded defect PhC L3 cavity. The white part of structure is free to move, the grey one is assumed fixed.

Simulations of the flexural modes of such a suspended membrane were carried out using the Structural Mechanics module[7] of COMSOL *Multiphysics* software package. Material properties of InP for the simulation of mechanical eigenmodes are set as follows: bulk density is $\rho = 4810$ kg/m^3, Poisson's ratio $\nu = 0.36$, Young's modulus $E = 40$ GPa, considered to remain equal along all the crystalline directions. The above-mentioned parameters were obtained by taking the ones from [Gavartin 2011] and further adapting to best fit our experimentally obtained eigenfrequencies. In [Gavartin 2011], the good agreement between the experimentally measured and the simulated mechanical frequencies of a doubly-clamped PhC membrane resonator made of InP were found for the Young's modulus of InP equal to 20 GPa. We found that this value, however, would fit well the experimental data obtained from doubly-clamped membranes, whereas the four-bridge type clamped membranes are simulated more accurately by taking $E = 40$ GPa.

The simplified geometry, corresponding to the one shown in Fig. 2.15 but excluding the holes, is set up for the simulation. To take this modification into account, a corresponding approximation introduced in this work, the effective material density ρ_{eff} for a bulk membrane is a substitute to a PhC slab one, pierced by holes. This quantity takes into account the filling factor ζ of the real membrane by computing the volumes of a bulk and patterned plates, so that $\rho_{\text{eff}} = \rho\,\zeta$, where $\zeta = \left(a^2\sqrt{3} - 2\pi r^2\right) / \left(a^2\sqrt{3}\right)$ for the cylindrical holes. The membrane is thus simulated as a plate of bulk InP with the effective density ρ_{eff}, while the remaining structure is set to have the density ρ. The fixed constraints in the simulation are imposed on the bottom planes of the two suspension pads. This allows to mimic a piezo actuation from the bottom of the sample, which is one of the possible techniques employed during the readout of the membrane motion.

[7] http://www.comsol.com/structural-mechanics-module

The middle of each of the four bridges is displaced by a distance $\pm b_d$ from the membrane middle line (along x axis), as visualized in Fig. 2.15. This choice of this distance was made according to the optimized mechanical dissipation for one of the membrane flexural modes and is discussed in detail in Section 2.2.1.2. Following this optimization, this distance in our structure is equal to $b_d = \pm 0.295\, m_x$.

2.2.1.1 Numerical mode spectroscopy in MHz range

The example shown in Figure 2.16 considers a membrane with a following set of parameters (see Fig. 2.15): $m_x = 20$ μm, $m_y = 10$ μm, $t = 260$ nm, $b_x = 1$ μm, $b_y = 2$ μm, $b_d = \pm 5.9$ μm, $E = 40$ GPa; ρ_{eff} for the PhC slab part is calculated taking into account the lattice parameters $a = 430$ nm and $r = 100$ nm (for L3 PhC defect cavity). In the case of square lattice used to create a PhC mirror from the membrane, the effective density ρ_{eff} will change and this will consequently shift the frequencies $\Omega_m/2\pi$ of the eigenmodes, however, the discussion remains the same.

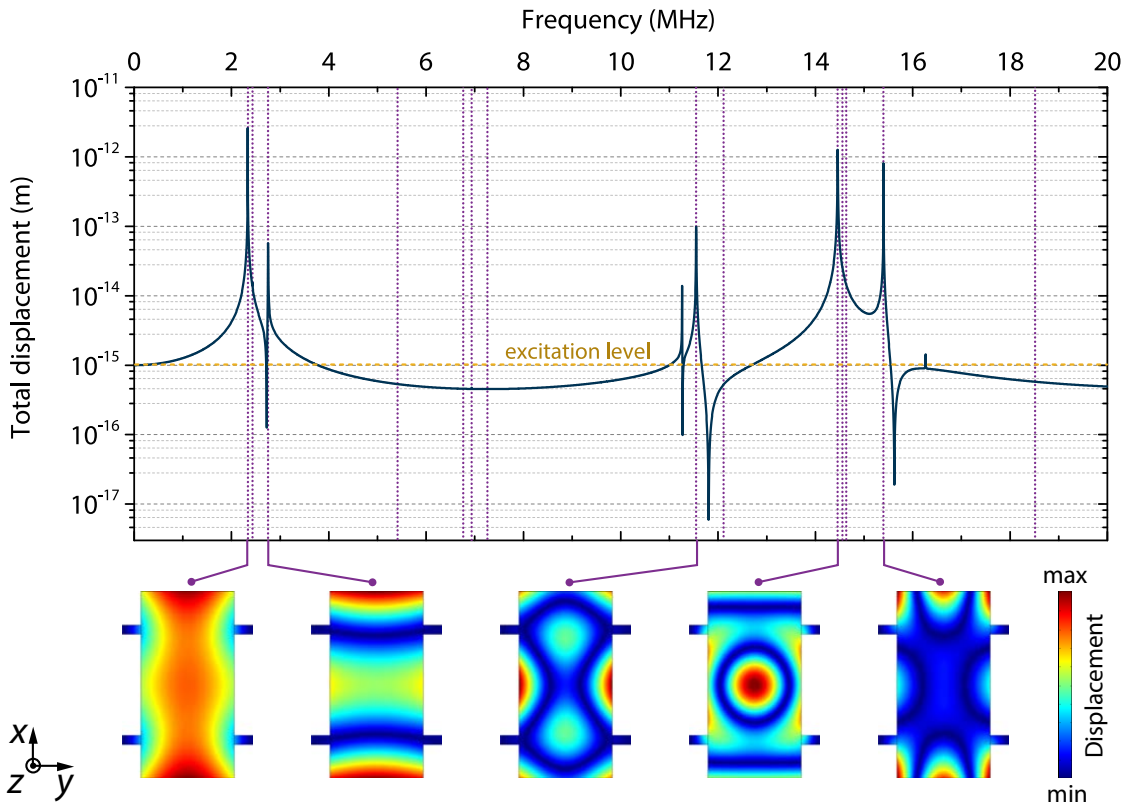

Figure 2.16: (Solid dark blue) Simulated low-frequency mechanical response in the middle of a suspended membrane with a displacement of 10^{-15} m in z direction (refers to yellow dashed line) of the suspension pads. (Dashed violet) Simulated eigenfrequencies $\Omega_m/2\pi$ of the same system without excitation. Mechanical mode profiles with the colour-coded normalized displacement field for the corresponding coincidences are given at bottom.

We estimate the strength of mechanical response for different eigenfrequencies of a

suspended membrane. The dark blue curve in Figure 2.16 represents the total displacement of a point taken on the top membrane boundary in the middle of the membrane block, while a displacement of 1 fm in vertical (z) direction is applied to both of support pads. We also performed the simulation of the eigenfrequencies for the same system excluding the displacement condition, and the corresponding values are represented by violet dashed lines.

As can be seen, only few among the present eigenmodes can be resonantly excited by an out-of-plane displacement excitation. Since only the membrane displacement along z axis can be probed efficiently with either a PhC mirror configuration or a PhC cavity one (due to the geometrical considerations), the present simulation gives only a qualitative estimation of possible resonant modes of the membrane, probed within one of the above-mentioned configurations. Moreover, the total displacement is probed with a discrete step in frequency domain (equal to 5 kHz for the data presented in Figure 2.16, aiming to provide enough resolution on resonance linewidths). It gives only qualitative estimation of amplitude modulation in z direction.

For each coincidence between the eigenfrequency and probed membrane displacement the displacement field $\vec{Q}(\vec{r})$ distributions are shown in Figure 2.16 (bottom) for the most prominent modes. It should be noticed that total displacement has only non-zero component, corresponding to the one along z direction $w \equiv Q_z$, which follows the excitation vector. Corresponding mode profiles in most have important $\vec{Q}(\vec{r})$ field value in the membrane middle (see Fig. 2.16), confirming the observed strong impact on the modulation of membrane position compared to its stationary state.

2.2.1.2 Control of mechanical dissipation: geometry tuning

One of the geometrical parameters we first mentioned in Section 2.2 is the parameter b_d, describing the position of attachment for the suspension bridges (cf. Fig. 2.15). In fact, this parameter can have an important impact both on the mechanical mode spatial profile and on the associated clamping losses [Cole 2011]. The evolution of three first eigenmodes of the suspended PhC slab membrane has been studied numerically.

Membrane geometry is chosen to be consistent with the one studied in Section 2.2.1.1[8] with only b_d parameter that may vary. First three modes in the default device configuration $b_d = \pm 5.9$ μm are mapped in frequency domain as M1*, M2* and M3*. Given that bridge width is $b_x = 1$ μm and the membrane one is $m_x = 20$ μm, b_d is swept from 0.5 to 9.5 μm (hereinafter we omit the $\pm$ notation since the structure is assumed symmetric with equal length for all four bridges); displacement field distributions for studied modes and for different b_d values are shown in Figure 2.17c. The change in clamping geometry via b_d parameter at first impacts the frequency of mechanical modes, making it vary in different ways (Fig. 2.17a).

[8] Membrane: $m_x = 20$ μm, $m_y = 10$ μm, $t = 260$ nm; bridges: $b_x = 1$ μm, $b_y = 2$ μm; material: $E = 40$ GPa; ρ_{eff} for the the lattice parameters $a = 430$ nm and $r = 100$ nm.

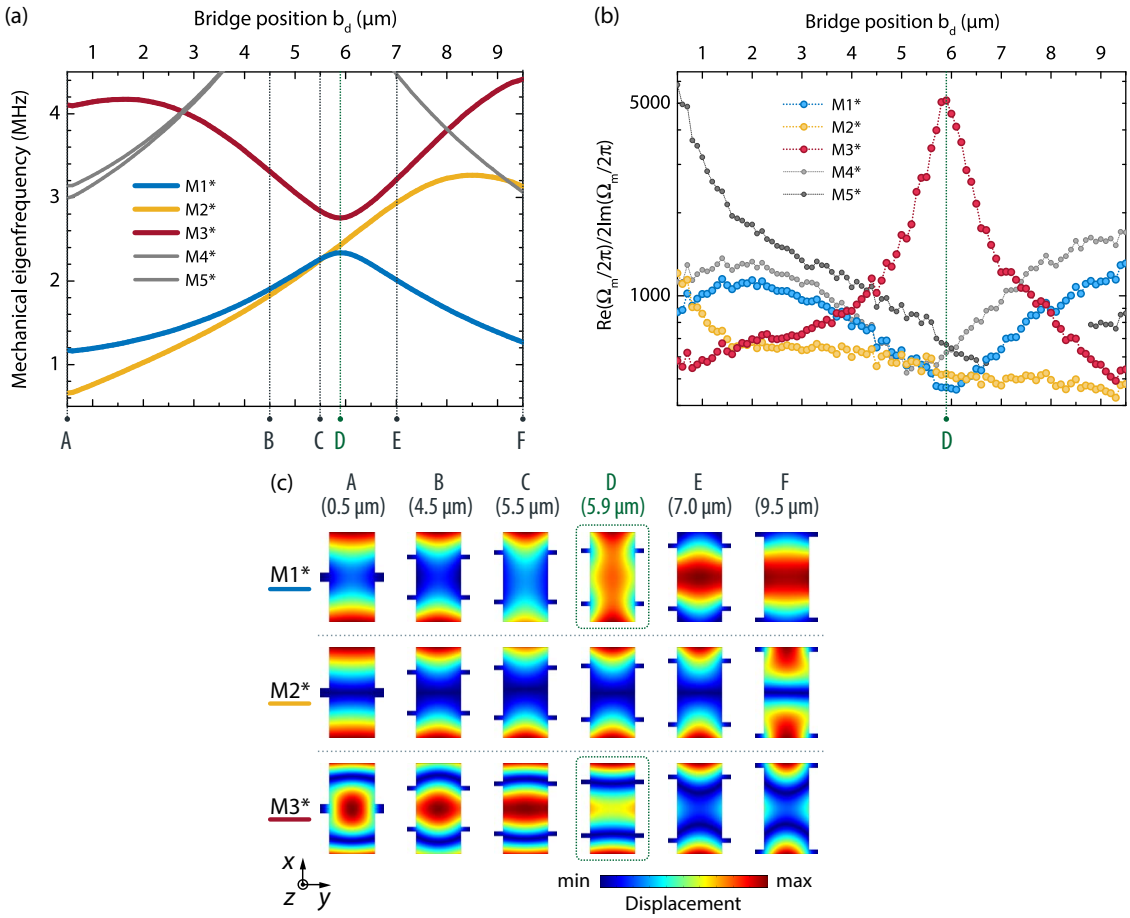

Figure 2.17: Simulated mechanical eigenmodes of the PhC membrane of dimensions 10×20 μm versus suspension bridge attachment position b_d (for a constant bridge dimensions $b_x = 1$ μm and $b_y = 2$ μm). (a) Evolution of the eigenfrequency $\Omega_\mathrm{m}/2\pi$ of the first three modes is considered and illustrated at different b_d values. (b) Mechanical quality factor, estimated as $Q_\mathrm{m} = \mathrm{Re}(\Omega_\mathrm{m}/2\pi)/2\,\mathrm{Im}(\Omega_\mathrm{m}/2\pi)$ (logarithmic scale). Corresponding mode profiles (normalized displacement field $\vec{Q}(\vec{r})$) are shown (c). Chosen optimal b_d distance of 5.9 μm for the mode M3* is highlighted in green (point D).

The present study considers mainly modes M1* and M3*: these modes show important displacement around membrane centre (Fig. 2.17c), which is essential for their optical addressing both in PhC mirror and defect cavity configuration. In optimization of bridge position we will focus on the reduction of mechanical losses for these two modes, mainly examining the simulated mechanical quality factor (Fig. 2.17b), defined as $Q_\mathrm{m} = \mathrm{Re}(\Omega_\mathrm{m}/2\pi)/2\,\mathrm{Im}(\Omega_\mathrm{m}/2\pi)$, and the displacement field $\vec{Q}(\vec{r})$ distribution through some characteristic b_d values (Fig. 2.17c). In order to obtain both real and imaginary part of the simulated eigenfrequencies, we introduced the perfectly matching layers (PMLs), absorbing the acoustic energy. They are represented by two blocks of InP bulk material, attached from below to the suspension pads, which allows to mimic the phonon losses and also to take into account the undercut depth influence on the membrane mechanical

eigenfrequencies, present in real devices. Absolute values of mechanical quality factor, obtained with such numerical estimation, will depend on the configuration of used PMLs (position, geometry) and therefore do not pretend to give a precise characterization of clamping losses in the simulated system. We use this approach to obtain rather a qualitative description for the evolution of the clamping losses of different modes throughout the investigated changes in clamping geometry.

From the current study we found that at the point D, where $b_d = 5.9$ μm or $b_d = 0.295\, m_x$, the mode M3* shows the maximum of simulated quality factor Q_m (Fig. 2.17b) and a corresponding optimized spatial profile allowing for maximum reduction of clamping losses. Mode M3* displays a node of the displacement field at exactly the clamping point of each bridge (Fig. 2.17c), thus minimizing phonon tunnelling towards the suspension pads. Fundamental M1* mode at $b_d = 5.9$ μm acquires the $\vec{Q}(\vec{r})$ field distribution, demonstrating maximally possible uniformity for the given bridge dimensions. That is, the whole membrane would oscillate along z direction with the minimized bending when compared to other possible clamping positions. However, the simulated quality factor Q_m shows local minimum for this mode. For this type of displacement field distribution the clamping losses through the suspension bridges can be then further reduced by their elongation, that is, by increasing b_y distance.

The clamping losses for the fundamental flexural mode M1* (cf. Fig. 2.16, 2.17) can also be further reduced by designing longer suspension bridges while $b_d = 0.295\, m_x$. Theoretical study of this phenomenon is presented in Figure 2.18. The same first three flexural modes of a suspended PhC membrane are considered both in frequency domain, in terms of mechanical quality factor Q_m and regarding their spatial profile distribution. It can be observed (Fig. 2.18a), that the eigenfrequencies of the first two modes – M1* and M2* – are strongly dependent on the clamping geometry and decrease rapidly as the suspension bridge length b_y increases. Mode M3*, in turn, was designed so that it presents antinodes at the points of bridge connections, which results in a smaller dependence on the b_y parameter. To get a better insight into the change of mechanical quality factor of different modes, we normalize its value Q_m, as introduces in the previous study, by the reference value at $b_y = 2$ μm (denoted as $Q_{\mathrm{m},0}$ in the following) and plot for the first three modes in Figure 2.18b. Although the real part of eigenfrequency for all three modes decreases with b_y increase (Fig. 2.18a), our estimate for the quality factor $\mathrm{Re}(\Omega_\mathrm{m}/2\pi)/2\,\mathrm{Im}(\Omega_\mathrm{m}/2\pi)$ shows stable enhancement for each mode (Fig. 2.18b). While for mode M3* the normalized Q_m trend shows a saturation around $b_y = 11$ μm value and reaches about a factor of 12, the trend for the fundamental M1* (as well as for the M2*) mode displays a monotonic increase, reaching $Q_\mathrm{m}/Q_{\mathrm{m},0}$ ratio of about 4 for the maximum considered b_y parameter value. Considering the evolution of the spatial profiles (Fig. 2.18c), which can also be used for the estimation of mode energy leaking towards the substrate, the M3* mode with full correspondence to the quality factor simulations shows virtually no change when compared to the reference clamping geometry with $b_y = 2$ μm. Fundamental mode M1*, essentially targeted by this study, demonstrates a significant $\vec{Q}(\vec{r})$ field profile evolution towards a

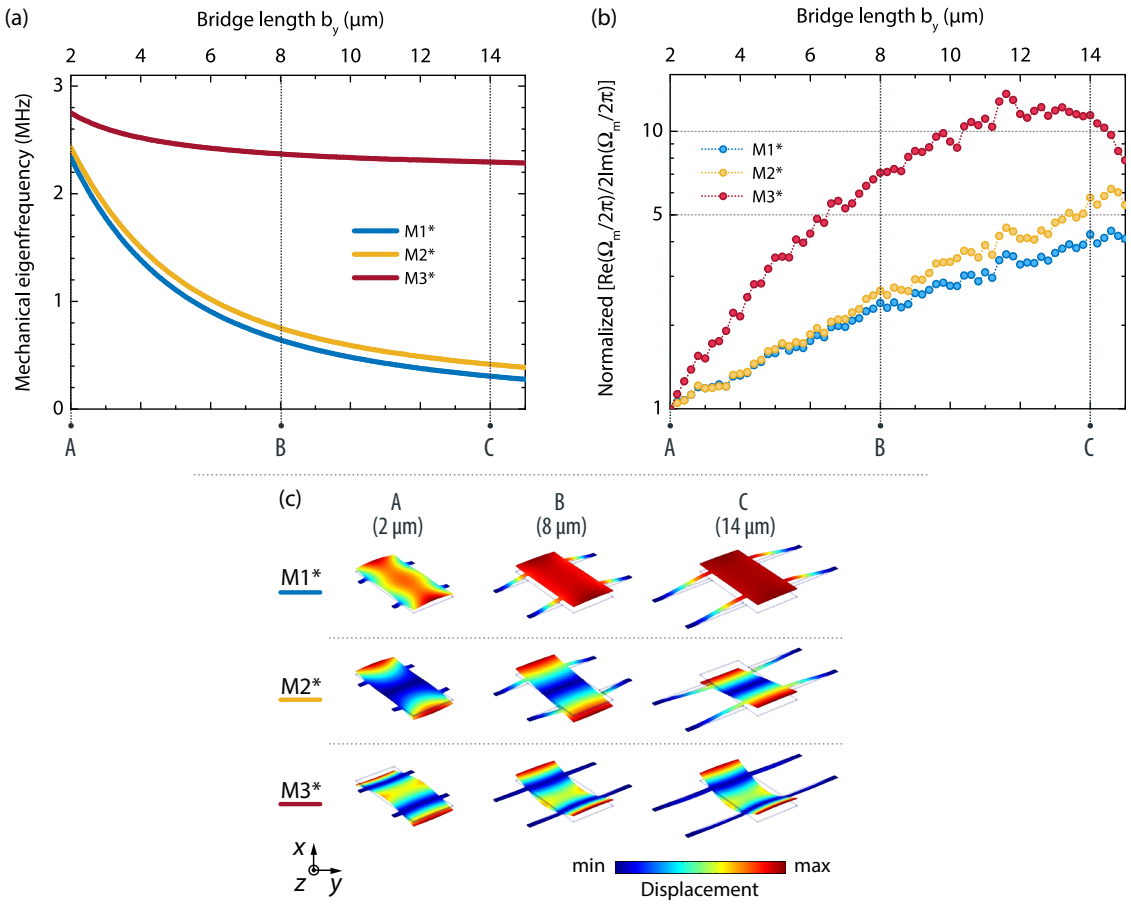

Figure 2.18: Simulated mechanical eigenmodes of the PhC membrane of dimensions 10×20 μm versus suspension bridge length b_y (for a constant bridge position $b_d = 5.9$ μm and width $b_x = 1$ μm). Evolution of the first three modes is considered and illustrated at different b_y values by the corresponding eigenfrequencies (a), normalized mechanical quality factor (b) and (c) mode profiles (normalized displacement field $\vec{Q}(\vec{r})$).

uniform distribution across the membrane block together with zero-displacement regions close to the attachment points bridge – suspension pad, which also corresponds to low phonon tunnelling probability and higher mechanical quality factors when the b_y value increases (by analogy with [Cole 2011]). This technique of clamping loss optimization is experimentally confirmed in Section 4.1.2.

Another interesting observation concerning the mechanical band diagram in Figure 2.17a, is that close to the point C the modes M1* and M2* are degenerate. Mode M1*, when decreasing b_d from the optimum point D, corresponds to an in-plane motion of the membrane edges in x direction, while M2* corresponds to an anti-phase motion. This explains the degeneracy point close to C and can be eventually used to experimentally implement the phenomenon of mode crossing or anti-crossing by exploiting these two modes with small eigenfrequency difference close to the C point and further fine-tuning one of the mechanical modes frequencies towards another by making use of optical spring

effect [Kippenberg 2007; Shkarin 2014].

2.2.2 Localized modes within the L3 defect cavity

2.2.2.1 Numerical mode spectroscopy in GHz range

The second family of mechanical modes sustained by the membrane are the high-frequency vibrations, exclusively observable in PhC defect configuration and localized inside the core of the defect, which were experimentally demonstrated in [Gavartin 2011].

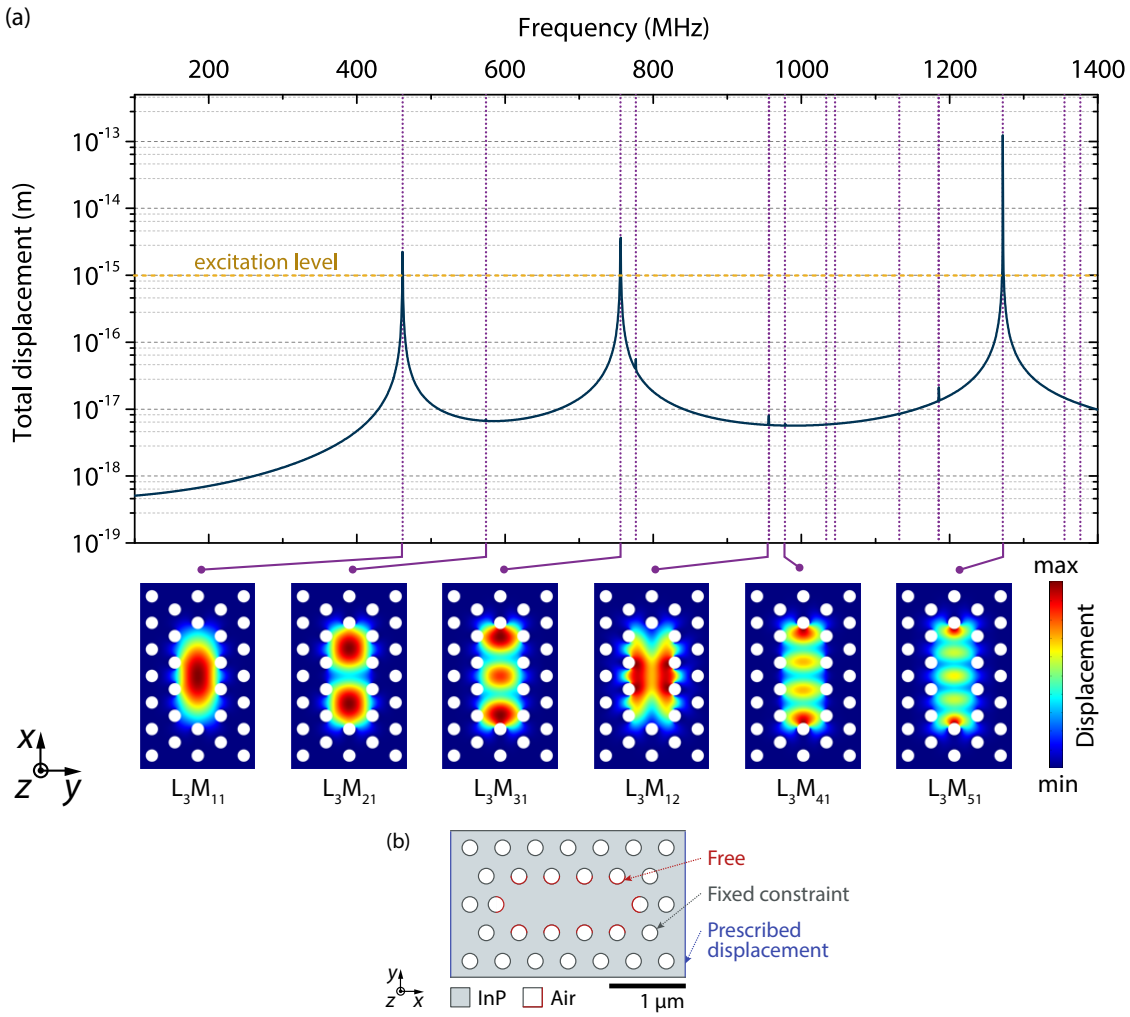

Figure 2.19: (a) [Solid dark blue] Simulated high-frequency mechanical response in the middle of a suspended L3 defect cavity with a prescribed displacement of 10^{-15} m in z direction of the lateral sides (see below). [Dashed violet] Simulated eigenfrequencies of the same system without excitation. Mechanical mode profiles with the colour-coded normalized displacement field for the same eigenfrequencies are shown. (b) Boundary conditions used in the given simulations.

Figure 2.19a presents the same type of study, as for the membrane flexural modes, but

this time considers the mechanical resonances, confined within the defect PhC cavity. For this study the PhC slab structure was explicitly simulated, thus excluding the needs for introduction of an effective density. The Young's modulus was taken $E = 20$ GPa, according to the fitting results from [Gavartin 2011] for the same type of mechanical resonances. According to the same article, special boundary conditions were introduced in order to obtain the eigenfrequencies that would correspond to the experimentally measured ones (see Fig. 2.19b). The inner half-circles of the holes (Fig. 2.19b, in red) that form the outer limits of the defect L3 cavity were left as free, i.e., these boundaries are allowed to move. All the remaining holes boundaries as well as the two outer simulation volume limits were set as fixed constraints (Fig. 2.19b, in grey), which allowed to introduce the sufficiently high meshing precision. The two opposite lateral sides of the simulation volume (Fig. 2.19b, in blue) were used as the excitation planes by introducing a prescribed displacement condition of 1 fm along z axis (the same as for the flexural membrane modes). The fact of choosing either two planes parallel to x axis or to y would only change the absolute value of the probed mechanical response (total displacement) in the cavity middle, whereas the frequency domain trend remains unchanged. Moreover, it allowed us to reduce the simulation volume down to only few holes surrounding the defect cavity, while still giving the converging results. The discretization step in frequency domain, discussed above, for the given high-frequency study was 500 kHz.

From Figure 2.19a it can be seen that the most prominent modes are the localized modes of the $\{n,1\}$ type, where n is odd, meaning that there will be always a mode antinode in the cavity middle. High spatial overlap of such mechanical mode displacement field with the electromagnetic field of the optical mode could lead to the enhancement of their mutual interaction. These modes are potential candidates for the high intrinsic optomechanical coupling to the localized cavity optical mode: for example, E_y electromagnetic field component (cf. Fig. 2.8) and $\{5,1\}$ mechanical mode (L_3M_{51} in Figure 2.19a).

2.2.2.2 Control of mechanical dissipation: phoNonic crystal

In recent years a new trend in cavity optomechanics emerged, studying the interaction of localized defect optical and mechanical modes, created inside a so-called phoXonic lattices. This structure, if considered without defects, provides band gaps for both electromagnetic and elastic waves. Simultaneous existence of these two types of gaps, leading to an enhanced interaction between elastic and optical modes with strong spatial overlap, were demonstrated theoretically and experimentally for a phoxonic nanobeam cavity [Oudich 2014] and for a two-dimensional phoxonic crystal cavity, conceived inside a square lattice slab [Rolland 2012; Jallal 2013].

The particularity of our hybrid device is the use of triangular lattice for the creation of defect optical cavity. As it can be seen from Figure 2.20a, it gives no complete phononic band gap even at high filling factors ($r = 0.45\,a$) The study of the phononic band structure (cf. Fig. 2.20a) was carried out for a wide range of filling factors, or the corresponding r/a ratios, in order to reveal possible complete band gaps for acoustic waves. However, it

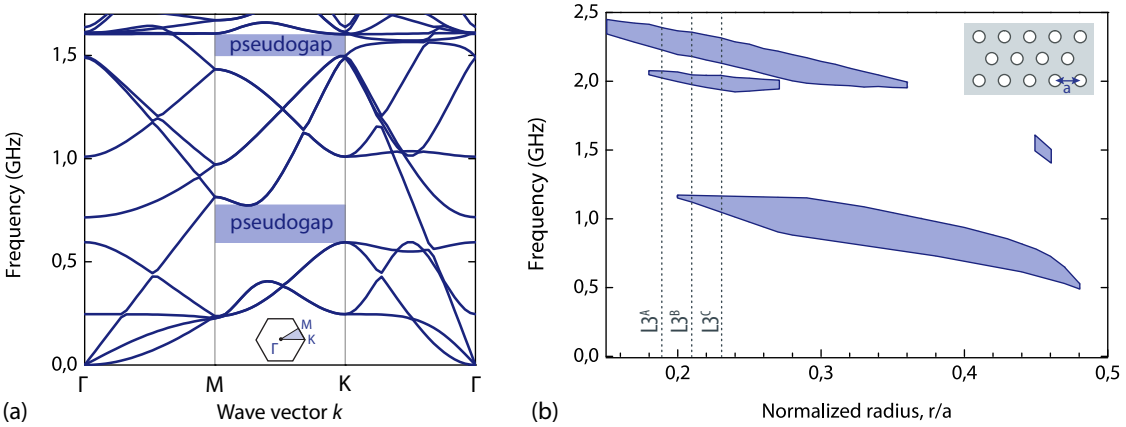

Figure 2.20: (a) Simulated mechanical band structure for an infinite triangular PhC slab made of InP (thickness $t = 0.62\,a$, hole radius $r = 0.45\,a$, $E = 20$ GPa). Phononic pseudogaps along M–K wave vector direction are highlighted in light blue. (b) Pseudogap dependence on normalized hole radius r/a, the filled areas represent the corresponding gap frequencies. Dashed lines indicate lattice geometries for three defect L3 variations included within a real device: $L3^A$ corresponds to the lattice parameters $t = 260$ nm, $a = 430$ nm, $r = 80$ nm; $L3^B$ and $L3^C$ – to the lattices of same t and a with $r = 90$ nm (B) and $r = 100$ nm (C).

showed that only a pseudogap may exist within such structures, covering the wave vectors between special points M and K of the first Brillouin zone (see Fig. 2.20a,b). The evolution of these pseudo-gaps along MK is monitored with respect to r/a ratio. For r/a values required for the phoTonic structure (dashed lines in Fig. 2.20b) the pseudogap reduces and goes to the higher frequencies. This study indicates that it will not be possible to rely on the opening of a phononic band gap to reduce the mechanical losses for the localized modes described in previous Section. The localized defect cavity modes (cf. Section 2.2) can be generally described as standing waves along x and y axes, as visualized in Figure 2.19. These directions in real space correspond to ΓM path in reciprocal space, where no band gap exist at any frequency, according to this study.

One solution in order to reduce the mechanical losses combines two types of arrangements: a triangular one with a defect L3 cavity in the middle of the slab, surrounded by a crystal with a full phononic band gap around a mechanical frequency of interest. In this way a loss reduction for one or more of the cavity localized mechanical modes could be achieved. Several phoNonic crystal lattices exist; the two commonly used are honeycomb and square types. The preference is given to the honeycomb lattice over the square one, as in case of PhC slab membranes [Mohammadi 2010] the first provides a broader phononic band gap which can spread along a wider range of normalized radii r/a. Such tunability permits to match more easily the phoNonic band gap with the eigenfrequency of our localized mechanical modes. It should be taken into account, however, that high r/a lattice designs are more demanding concerning fabrication precision of the real device.

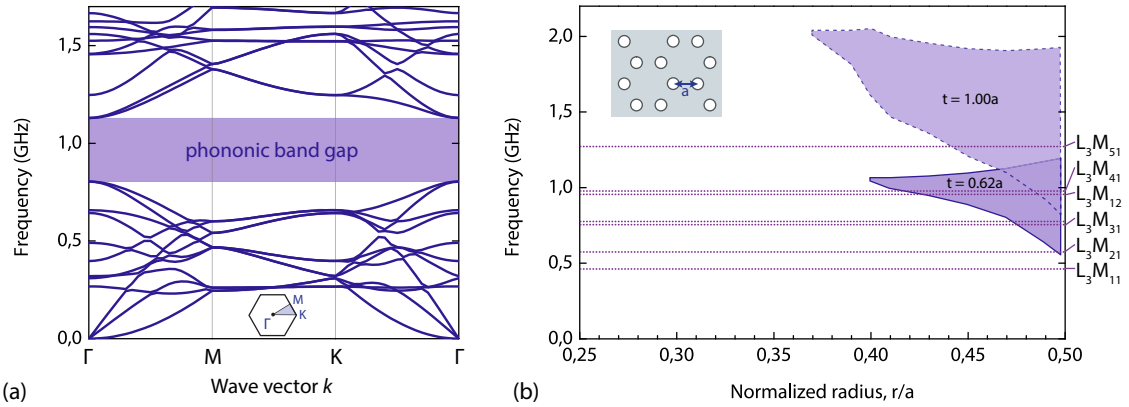

Figure 2.21: (a) Simulated mechanical band structure for an infinite honeycomb PhC slab made of InP (thickness $t = 0.62\,a$, hole radius $r = 0.47\,a$, $E = 20$ GPa). Full phononic band gap is highlighted in light violet. (b) Band gap dependence on normalized hole radius r/a for two different lattice parameters a; the filled area represents the corresponding gap frequencies. Dashed lines indicate the eigenfrequencies of several prominent mechanical modes within a defect L3 cavity (from triangular lattice), as described in Figure 2.19a.

Figure 2.21a shows a simulation of a honeycomb lattice that can fit our current hybrid structure, still preserving the same thickness to lattice parameter ratio $t = 0.62a$. Slab thickness and mechanical properties are the same as used in the first part of this Section for the simulation of phononic band structures of a triangular PhC lattice. At high filling factors, e.g., when $r = 0.47\,a$ (see Fig. 2.21a), the band gap covers an important range of frequencies, eventually allowing to decrease losses even for several modes at a time. In Figure 2.21b we trace the evolution of band gap opening versus normalized hole radius r/a with the significant gap increase towards the higher radii. Considering that the honeycomb lattice will be used as a surrounding pattern around the central membrane part with a PhC cavity, we are free to choose the r value to best fit our expected phononic mirror properties. Several localized modes of interest (Fig. 2.19a) are given as dashed lines in Fig. 2.21b for the direct comparison with band gap frequencies.

As suggested in [Mohammadi 2010], increasing the t/a ratio to unity may lead to further band gap widening. Given that all the previous studies for the phoNonic part of our device were conducted for a fixed slab thickness $t = 260$ nm, we decreased the lattice constant without changing t in order to reach $t = 1a$ condition. The obtained results (Fig. 2.21b) confirm the band gap widening, although its frequency range shifts towards higher values.

The drawback when choosing a lattice with high r/a ratio in order to increase the band gap range, is that the physical gap between two adjacent holes becomes thin and thus puts higher requirements on the device fabrication. The devices that we were able to successfully fabricate for the studied thickness to lattice period ratio $t = 0.62\,a$ cover r/a range up to 0.43 (up to 0.41 for $t = 1.00\,a$ design).

2.3 Dispersive and dissipative optomechanical couplings

Up to now, the optical and mechanical properties of our devices were simulated and studied separately. Current section reviews different optomechanical interaction mechanisms, that occur in our hybrid coupled system between optical and different mechanical resonances. Very recently the experimentation of few optomechanical systems was demonstrated, exhibiting the simultaneous presence of two types of optomechanical couplings – dispersive (modulation of refractive index) and dissipative (losses modulation) [Wu 2014; Sawadsky 2015]. These effects will be introduced in the frame of our integrated devices and then investigated in details.

2.3.1 Optomechanical coupling strengths

Optomechanical coupling in our hybrid system shows a mutual existence of both types of effects – dispersive and dissipative. More interestingly, these effects can be produced by two distinct mechanisms. External effects, governed by the presence of an evanescently coupled SOI waveguide in the vicinity of a PhC cavity, as well as intrinsic couplings, that rely exclusively on the processes occuring within the PhC membrane body, will be studied. Changes in external coupling strength and intra-cavity effects generally have different impacts. Mechanical motion of the flexural membrane modes modifies the cavity – waveguide gap h_{air}, that would effectively change the mutual optical mode overlap (when the gap is small enough to introduce a sufficient mode perturbation by a presence of waveguide). As it was seen previously (cf. Fig. 2.11), a change in h_{air} modifies cavity optical loss due to external coupling (corresponding quality factor Q_c and decay rate γ_e), resulting in external dissipative optomechanical coupling [Elste 2009; Xuereb 2011] (Fig. 2.22b). This effect originates in the modulation of the overlap of the evanescent field tails – between cavity and waveguide optical modes (Fig. 2.9); this modulation arises when the membrane moves and displaces the embedded cavity with respect to the fixed waveguide. A second important coupling component for the PhC cavity is the modulation of its resonance frequency ω_0 (Fig. 2.22a) due to the changing surrounding dielectric environment, resulting in external dispersive optomechanical coupling [Kippenberg 2008]. Resonance frequency ω_0 of the cavity mode depends on the dielectric tensor ε distribution inside the membrane, but also in its vicinity. Therefore the modulation of the membrane – waveguide separation h_{air} will affect ω_0 by changing the ε distribution in the mode evanescent field.

Additional two coupling mechanisms arise when the deformation of the membrane during its mechanical motion impacts the cavity optical parameters, such as its intrinsic photon decay rate γ_i (corresponding to the quality factor Q_0) (Fig. 2.22d) and its resonance frequency ω_0 (Fig. 2.22c). These two effects are referred to as intrinsic dissipative and dispersive optomechanical couplings, respectively. As it can be concluded from Figure 2.22a,c, the impact of external and intrinsic coupling mechanisms on cavity transmission is the same, therefore it can not be experimentally detected separately, contrary to the

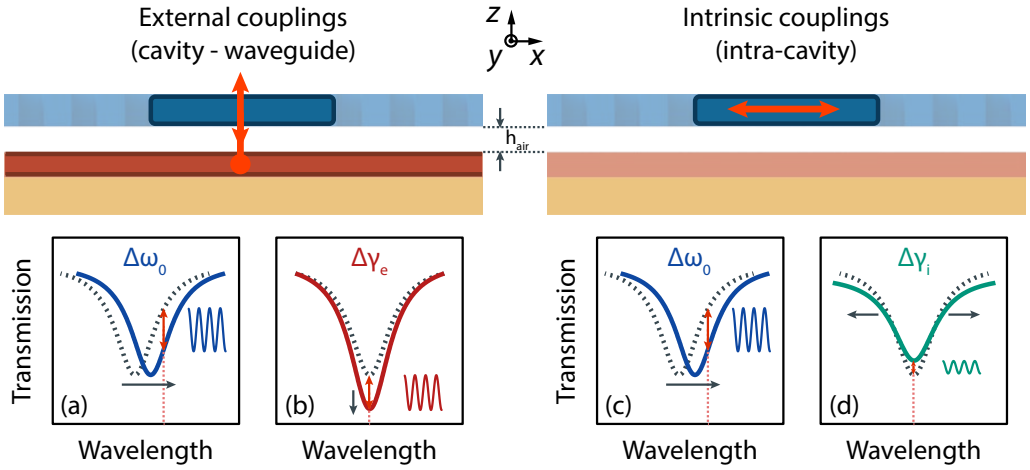

Figure 2.22: Illustration of the effect of mechanical displacement on the optical response of a PhC cavity (highlighted in blue) coupled to a SOI waveguide (highlighted in red), after a half-period of mechanical oscillation. Change in the resonance line shape, as detected via waveguide transmission, for external (a) dispersive and dissipative (b), and equivalent intrinsic (c,d) optomechanical couplings.

simulations given later in this chapter. By putting a laser probe as shown in Figure 2.22 for each of the coupling types, its intensity will be modulated with the corresponding amplitude shown on graphs. We next introduce a model, which allows to describe the cavity transmission spectrum while taking into account all the previously described mechanisms.

2.3.2 Wavelength dependence of hybrid optomechanical response

This Section presents the equations describing the wavelength dependence of the optomechanical response of a PhC cavity evanescently coupled to a SOI waveguide. This model takes into account dissipative and dispersive optomechanical coupling and considers both external and intrinsic interaction mechanisms.

The total optical cavity loss rate is given by

$$\gamma_t\left(h_{\mathrm{air}}, W_{\mathrm{wg}}\right) = \gamma_i\left(h_{\mathrm{air}}, W_{\mathrm{wg}}\right) + 2\gamma_e\left(h_{\mathrm{air}}, W_{\mathrm{wg}}\right), \tag{2.3}$$

where γ_i describes the intrinsic cavity loss including absorption or emission into modes other than the fundamental waveguide mode, e.g., scattering into radiation modes (this parameter may also include the light coupling to the waveguide modes other than the fundamental one, however, here we consider a monomode operation); γ_e denotes the external coupling rate into the forward (or backward) propagating mode of the waveguide, dependent on the opto-geometric parameters h_{air} and W_{wg}.

For the optomechanical system consisting of a waveguide coupled to a defect cavity, designed as described in previous Sections, the transmission will show a Lorentzian-like deep at the cavity resonance ω_0. From coupled mode theory, it can be shown [Wu 2014]

that the transmission spectrum $T(\Delta)$ of a microcavity evanescently coupled to an access waveguide has the form:

$$T(\Delta) = \frac{\Delta^2 + (\gamma_i/2)^2}{\Delta^2 + (\gamma_t/2)^2}, \tag{2.4}$$

where $\Delta = \omega - \omega_0$ is the detuning with respect to the cavity resonance frequency ω_0. Equation 2.4 holds for the particular case of the hybrid system studied in this work, where no coupling to any optical waveguide modes other than the fundamental one is considered.

The figure of merit, describing the efficiency of the coupling mechanisms introduced above, is commonly referred to as an optomechanical coupling strength g. It equals the frequency shift of the involved optical parameter (cavity resonance frequency ω_0 or linewidth γ) with respect to the mechanical displacement $d\vec{r}$ (in three spatial directions), induced by a particular mechanical resonator mode. The external optomechanical couplings, governed by the flexural modes in MHz range (see Section 2.2.1.2, Fig. 2.16), rely mainly on the mechanical resonator displacement along out-of-plane membrane direction (z axis in Fig. 2.22). Consequently, two coupling strengths can be assigned: $g_{\omega,e} = d\omega_0/dz$ for the external dispersive, and $g_{\gamma,e} = d\gamma_e/dz$ for the external dissipative component. The intrinsic couplings may generally occur for any of above-mentioned mechanical mode type (Figs. 2.16 and 2.19) and along all the three axes, therefore the corresponding coupling strengths are given as $g_{\omega,i} = d\omega_0/d\vec{r}$ and $g_{\gamma,i} = d\gamma_i/d\vec{r}$ for dispersive and dissipative intrinsic components, respectively.

The optomechanical response of our coupled PhC cavity can be modelled by considering the dependence of the parameters from Eq. 2.4 on the mechanical state of the mechanical resonance of interest, given essentially by its coordinates $\vec{r}$. In the unresolved-sideband regime, i.e., when the mechanical resonance frequency Ω_m is small compared to the optical linewidth $\Omega_m \ll \gamma_t$ the waveguide transmission T would adiabatically follow the mechanical oscillations [Aspelmeyer 2013]. Then, the amplitude of the optical oscillations with respect to the detuning Δ for a given complex mechanical displacement amplitude $d\vec{r}$ can be written as

$$dT(\Delta) = \left| g_{\omega,e}\frac{\partial T}{\partial \Delta} + g_{\gamma,e}\frac{\partial T}{\partial \gamma_e} \right| dz + \left| g_{\omega,i}\frac{\partial T}{\partial \Delta} + g_{\gamma,i}\frac{\partial T}{\partial \gamma_i} \right| d\vec{r}, \tag{2.5}$$

when taking into account the preferential axis for the external coupling. The respective derivatives for the terms in Eq. 2.5, found from the Eq. 2.4, are

$$\frac{\partial T}{\partial \Delta} = \frac{2\Delta(1-T)}{\Delta^2 + (\gamma_t/2)^2}, \tag{2.6}$$

$$\frac{\partial T}{\partial \gamma_i} = \frac{\gamma_i - T(\gamma_i + 2\gamma_e)}{\Delta^2 + (\gamma_t/2)^2}, \tag{2.7}$$

$$\frac{\partial T}{\partial \gamma_e} = \frac{-2\gamma_t T}{\Delta^2 + (\gamma_t/2)^2}. \tag{2.8}$$

Three principal optical coupling regimes between the PhC cavity and the waveguide are examined, as illustrated in Fig. 2.23. The influence of each of the partial derivatives from Eqs. 2.6 – 2.8 is then depicted in Figure 2.24.

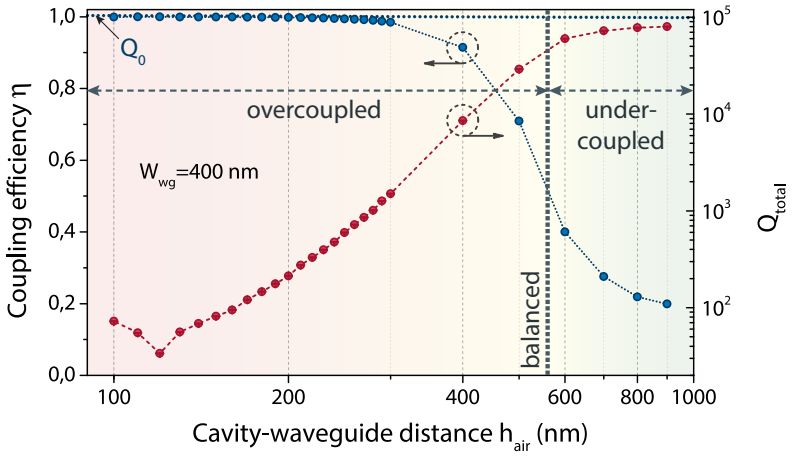

Figure 2.23: FDTD simulation of coupling efficiency η (dark blue) and optical quality factor Q_{total} (dark red) as a function of the cavity – waveguide distance h_{air} for the particular waveguide width $W_{\text{wg}} = 400$ nm; with the corresponding optical coupling regimes. $\eta = 0.5$ and the bold grey dotted line correspond to the balanced regime. Q_0 line corresponds to the cavity quality factor in the absence of the waveguide (10^5).

The undercoupled regime corresponds to the $\gamma_i \gg \gamma_e$ condition, and in particular case of Fig. 2.24a represents a slight cavity Q factor change from intrinsic $Q_i = 10^5$ to the total coupled $Q_{\text{total}} = 9 \times 10^4$. Such coupling regime can be reached by suspending the PhC membrane in our device at a height of $h_{\text{air}} \geqslant 600$ nm (Fig. 2.23). As it can be concluded, the external dissipative coupling has a dominant influence on the line shape due to the fact that the decay rate ($\gamma_e/2\pi \approx 0.1$ GHz) to the waveguide is much smaller compared to the cavity linewidth ($\gamma_i/2\pi \approx 2$ GHz). In this configuration it is possible to exploit optomechanics at resonance, given that the other coupling strengths (g_ω and g_{γ_i}) remain relatively small or comparable to the external dissipative, according to Eq. 2.5. As can be derived from coupled mode theory, at cavity resonance $T(\omega_0) \to 1$ when $\gamma_i \gg \gamma_e$, hence the coupling efficiency from the waveguide into the cavity is weak, which complexifies the implementation of high photon fluxes through the device active part.

In balanced coupling regime $T(\omega_0) = 0.25$ when $\gamma_i = 2\gamma_e$, giving the coupling efficiency of $\eta = 0.5$, marked by a bold grey dotted line in Fig. 2.23. For the particular choice of waveguide width for this Figure ($W_{\text{wg}} = 400$ nm), the balanced coupling region corresponds to the air gap distances $h_{\text{air}} \approx 500 - 600$ nm. For a set of different W_{wg} widths, present in our sample, it is thus possible to shift the position of this boundary due to the variation of phase matching conditions with W_{wg}. Consequently, within one sample with a fixed membrane suspension height h_{air} a certain degree of tunability between different coupling regimes may be achieved. In this operating regime for $\gamma_i \approx 2\gamma_e$ the three

contributions show comparable contributions to the cavity transmission and now depend almost equally on all the g coupling strengths, as shown in Fig. 2.24b.

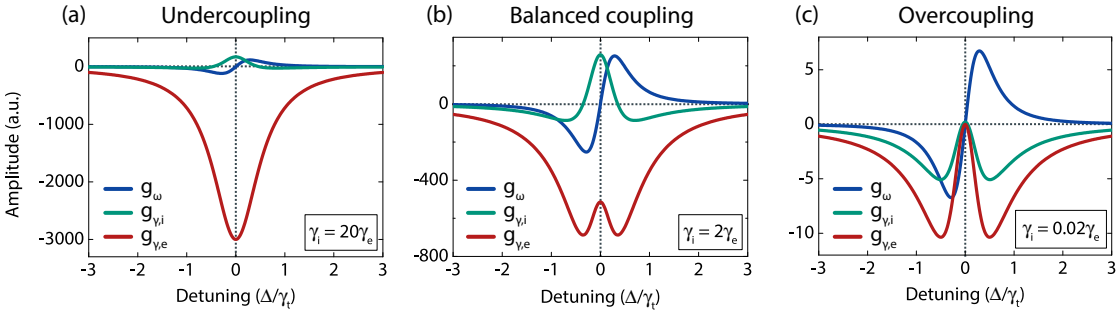

Figure 2.24: Relative strengths of the three optomechanical coupling contributions: g_ω – dispersive, $g_{\gamma,i}$ – dissipative intrinsic and $g_{\gamma,e}$ – external dissipative, plotted versus normalized detuning. Different regimes of cavity – waveguide optical coupling are considered: (a) undercoupling, where $\gamma_i \gg \gamma_e$, (b) balanced coupling, where $\gamma_i \approx 2\gamma_e$ and (c) overcoupling, where $\gamma_i \ll \gamma_e$.

Finally, for the case when $\gamma_i \ll \gamma_e$, the waveguide transmission at cavity resonance $T(\omega_0) \to 0$, corresponding to coupling efficiencies η close to unity, allowing to ensure high phonon fluxes through the cavity for the resonant injection ($\omega = \omega_0$). In this regime the three optomechanical couplings show comparable strengths (Fig. 2.24c), much like for the balanced configuration. The important difference, however, is that for the high mutual optical coupling strengths $\eta \lesssim 1$ it will be not possible any more to exploit optomechanical response at resonance ($\Delta = 0$), as all the three contributions tend to zero amplitude at this point even with a strong g_ω coupling coefficient (like in the case of a purely dispersive coupling with $g_\gamma = 0$, $g_\omega \to \infty$).

The last two regimes (balanced and overcoupling) can be employed as a starting point for the optomechanical system where, by carefully mixing the coupling rates, as suggested in [Weiss 2013], one can efficiently implement an optomechanical cooling of the mechanical modes down to their ground state even in the sideband-unresolved regime ($\Omega_m \ll \gamma_t$). Experimental realization for current device design is ensured with the PhC membrane suspension heights of $h_{\text{air}} \leqslant 500$ nm with finer optical coupling strength η control within one sample via the waveguide width W_{wg} (cf. Fig. 2.12b).

In the following sections different numerical simulations are performed in order to predict the dispersive g_ω and dissipative g_γ coupling strength coefficients for both external and intrinsic interaction mechanisms.

2.3.3 Numerical simulation of external optomechanical couplings

Simulations of the external optomechanical couplings were performed using both the perturbative theory approximation and the FDTD method. As it was introduced above, the two external coupling strengths are written as $g_{\omega,e} = d\omega_0/dz$ and $g_{\gamma,e} = d\gamma_e/dz$, as we assume that the in-plane membrane motion can be neglected. Perturbative theory provides

a fast way of estimation of these parameters, considering the local perturbation of the cavity field and dielectric tensor by the presence of the waveguide in close proximity. For this approximation, fields $\vec{E}(\vec{r})$ and dielectric tensors $\varepsilon(\vec{r})$ are calculated (once) separately using FDTD or FEA, and then used in the overlap integrals. Complete FDTD approach involves the simulation of the entire coupled system, as described in Section 2.1.3.4, with different z values with subsequent numerical derivation of $g_{\omega,e}$ and $g_{\gamma,e}$. This requires considerably greater computing times, but allows to account for phase-matching between two coupled optical parts, which can not be done by perturbative theory. We restricted the studied air gaps h_{air} region to $100 - 300$ nm, where coupling efficiency is very high $\eta \lesssim 1$.

2.3.3.1 Perturbative theory approximations

As proposed in [Hryciw 2014], the perturbative theory approximation for Maxwell's equations with shifting material boundaries [Johnson 2002] may allow to gain insight into the physical mechanisms that govern the impact of the waveguide on both dispersive and dissipative external coupling values inside an optomechanical system.

The estimation of the dispersive coupling strength $g_{\omega,e}$ requires the knowledge of the electric field $\vec{E}_c(\vec{r})$ distribution for the PhC cavity fundamental optical mode, which was already calculated using 3D FDTD simulation in Section 2.1.3.3 (cf. Fig. 2.8). The dielectric mode profile of the PhC structure $\varepsilon_c(\vec{r})$ is also extracted from this simulation, assuming the mirror symmetry with respect to the $x = 0$, $y = 0$, $z = 0$ planes. Using this data, the first-order correction to the resonance frequency ω_0 of an electromagnetic cavity due to a change in permittivity of its surrounding medium may be calculated using [Johnson 2002]

$$\Delta\omega_0 = -\frac{\omega_0}{2}\frac{\left\langle \vec{E}_c \middle| \Delta\varepsilon_{wg} \middle| \vec{E}_c \right\rangle}{\left\langle \vec{E}_c \middle| \varepsilon_c \middle| \vec{E}_c \right\rangle}, \tag{2.9}$$

where ω_0 corresponds to the resonance frequency of an unperturbed cavity, $\Delta\varepsilon_{\text{wg}}$ is the perturbation of the local dielectric environment due to the waveguide. For the waveguide geometry studied in this work, $\Delta\varepsilon_{\text{wg}} = \varepsilon_{\text{wg}} - 1$, with the integral restricted to the region inside the waveguide. The used notation $\langle\vec{a}|b|\vec{c}\rangle$ represents integration over all space $\langle\vec{a}\,|b|\,\vec{c}\rangle = \int \vec{a}\,(\vec{r}\,) \cdot b\,(\vec{r}\,) \cdot \vec{c}\,(\vec{r}\,)\,d\vec{r}$, with $\int d\vec{r} = \iiint dx\,dy\,dz$.

The obtained $g_{\omega,e}$ values are traced in Figure 2.25a (violet solid line with diamonds at the evaluated points). From this trace as well as from the expression for $\Delta\varepsilon_{\text{wg}}$, we see that the change in the cavity resonant frequency with W_{wg} scales with the intensity of the evanescent cavity field overlapping with the waveguide. Basically, the more material with $\varepsilon > 1$ is introduced within the cavity evanescent field, the larger is the perturbation, thus $g_{\omega,e}$ decays with the decreasing waveguide width W_{wg}.

One should consider the additional correction to the Eq. 2.9, if the permittivity contrast at the perturbation boundary is high. This is the case for silicon waveguide block,

surrounded by air, thus we used the corresponding perturbative theory derivation from a limit of system with smoothed boundaries [Johnson 2002], resulting in the derivative of the dispersion with respect to a small displacement being equal to

$$\frac{d\omega_0}{d\alpha} = \frac{\omega_0}{2} \frac{\int dA \frac{dh}{d\alpha} \left[\Delta\varepsilon_{wg} \left| \vec{E}_{c,\parallel} \right|^2 - \triangle \left(\varepsilon_{\mathrm{wg}}^{-1} \right) \left| \vec{D}_{c,\perp} \right|^2 \right]}{\int dV \varepsilon_c \left| \vec{E}_c \right|^2}, \tag{2.10}$$

where $h(\alpha; \vec{r})$ is the parametrization of a surface deformation, including the boundary initial position with a small displacement α perpendicular to the surface of the structure; dA represents a small area where surface is locally flat, $\int dV$ refers to a volume integral; $\Delta\left(\varepsilon_{\mathrm{wg}}^{-1}\right) = \varepsilon_{\mathrm{wg}}^{-1} - 1$; $\vec{E}_{c,\parallel}$ is the in-plane electric field, and $\vec{D}_{c,\perp}$ is the out-of-plane component of the cavity mode electric displacement field.

Using now the Eq. 2.10, the obtained corrected $g_{\omega,e}$ values are traced in Figure 2.25a (blue line with diamonds at the evaluated points). As can be seen from this Figure, the ε tensor correction effectively reduces the dispersive coupling coefficient (by about a factor of 5), since only the part of cavity field is now being considered, additionally substracting the out-of plane $\vec{D}$ field contribution. We obtain values of $g_{\omega,e}$ of about 1 GHz/nm, varying monotonically with the increase of $\Delta\varepsilon_{\mathrm{wg}}$, corresponding to the amount of waveguide material in the cavity evanescent field (in the same way as for non-corrected approximation).

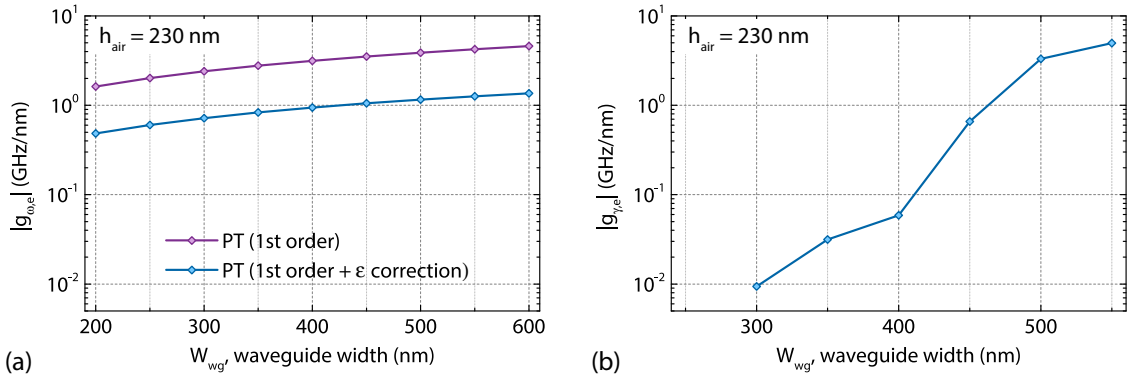

Figure 2.25: External dispersive $g_{\omega,e}$ (a) and dissipative $g_{\gamma,e}$ (b) optomechanical coupling strengths, obtained with the perturbative theory (PT) for $h_{\mathrm{air}} = 230$ nm membrane suspension height.

We next estimate the dissipative optomechanical coefficient $g_{\gamma,e}$ using the perturbative theory. It states that an approximation for the cavity loss rate into the external waveguide, γ_e, can be obtained from coupling-mode analysis for a generalized waveguide – resonator system [Manolatou 1999]. Neglecting dispersion, the loss rate into either the forward- or backward- propagating waveguide mode is

$$\gamma_e = \left| \frac{\omega \varepsilon_0}{4} \int_{z_1}^{z_2} dz \iint dx\, dy\, (\varepsilon_c - 1)\, \vec{E}_c^{\,*} \cdot \vec{E}_{\mathrm{wg}} e^{-i\beta z} \right|^2, \tag{2.11}$$

where ε_c is the relative permittivity of the cavity media, $\vec{E}_c(x, y, z)$ is the unperturbed cavity electric field distribution, normalized to unit energy; $\vec{E}_{\mathrm{wg}}(x, y)$ is the unperturbed waveguide electric field mode profile, normalized to unit power; β is the propagation constant of the propagating waveguide mode (cf. Section 2.1.3.3). The integrals in x and y are restricted to the region inside the cavity dielectric.

The unperturbed cavity $\vec{E}_c$ and waveguide $\vec{E}_{\mathrm{wg}}$ fields were simulated independently using FDTD method, as described in Section 2.1.3.3. Obtained dependence of the external dissipative coupling strength on the waveguide geometry is shown in Figure 2.25b (solid blue line with diamonds at the evaluation points). This $g_{\gamma,e}$ trend shows a monotonic dependence, and in the same way as for the external dispersive contribution $g_{\omega,e}$, we can state that the change in the coupled cavity linewidth γ_e versus the increase of the waveguide dimension W_{wg} scales with the intensity of the evanescent cavity field overlapping with the waveguide.

In conclusion, this theory allows for the estimation of the corresponding coefficients $g_{\omega,e}$ and $g_{\gamma,e}$ over a large span of opto-geometric parameter variation using considerably lesser computational powers and times when compared to a 3D FDTD simulation, which requires re-running a complete study of a coupled structure at each point of parameters grid. Nevertheless, for the evaluation of the dispersive coupling strength in our system the perturbative approximation does not take into account the difference in phase-matching conditions for different waveguide geometries. This phenomenon, however, shows a major influence on the coupling strength in the system (cf. Section 2.1.3.4) and thus has to be considered when evaluating the optomechanical coupling, which is accomplished in the following Section.

2.3.3.2 Complete FDTD simulation

FDTD simulation of the entire coupled structure gives us access to the total PhC cavity quality factor Q_{total} and to its respective resonance wavelength λ_0. By converting this data into the frequency domain and making use of Eq. 2.3, where γ_i is taken from the cavity mode simulation in the absence of the waveguide, we return to the dependencies of ω_0 and γ_e on the parameters of interest, namely h_{air} and W_{wg}.

The displacement field pattern of a specific mechanical mode is hardly introduced into the FDTD simulation using the software packages that were available during this work. We thus implement this simplified model by investigating the above-mentioned parameters (λ_0 – Fig. 2.26a and Q_{total} – Fig. 2.26b) of the optical system while varying the separation h_{air} between the flat membrane and the access waveguide (Fig. 2.22) for different waveguide widths W_{wg}. These trends are subsequently fitted by a suitable function (we choose exponential dependence for γ_e both for ω_0, which in the case of strong coupling regime between waveguide and cavity optical modes is well explained by the exponential character

of decay of the evanescent field tail) around the z value (which appears in this case for the h_{air} distance), corresponding to the equilibrium position of the membrane, where the g will be estimated (shaded areas in Fig. 2.26a,b). Finally the two derivatives for $g_{\omega,e}$ and $g_{\gamma,e}$ are calculated and used in Figs. 2.27a and b, respectively. In this way the external coupling coefficients were obtained for a set of different access waveguide widths W_{wg} and two air gaps h_{air} (150 nm and 230 nm). As can be seen, the small h_{air} difference of 80 nm in membrane position results is considerable change of both external coupling coefficients.

The cavity resonance frequency displays a more important shift as the waveguide approaches (see Fig. 2.26a); consequently gap h_{air} modulation induces an important $\Delta\omega_0$ shift and the dispersive optomechanical coupling strengthens considerably. For a given waveguide width, $g_{\omega,e}$ increases at least by a factor of 3 (Fig. 2.26a). Furthermore, the evolution of the external dispersive coupling strength $g_{\omega,e}$ shows the similar trends across the waveguide width W_{wg} variation for the two considered h_{air} distances.

External dissipative coupling strength $g_{\gamma,e}$ values (see Fig. 2.27b) shows an overall increase when the separation distance h_{air} shortens, while this effect is more pronounced around W_{wg} values close to $350-400$ nm. It can be explained by the better phase-matching conditions (see Fig. 2.14) between the waveguide and the defect cavity modes.

Imprecision of the simulated $g_{\omega,e}$ coefficients (Fig. 2.27a) comes from the numerical simulation error, which can be observed in Fig. 2.26a, where the cavity resonance wavelength curve appears more noisy that the linewidth curve in Fig. 2.26b. This is explained by the use of different methods for the evaluation of these two quantities, as described in details in Section 2.1.3.4, where the Q factors and thus the linewidths γ are extracted with the higher precision. The resonance wavelength λ_0 evaluation, in contrary, shows strong dependence on the meshing quality. Although the used simulation package (Lumerical *FDTD Solutions*) employs an adaptive mesh refinement within the zones where the

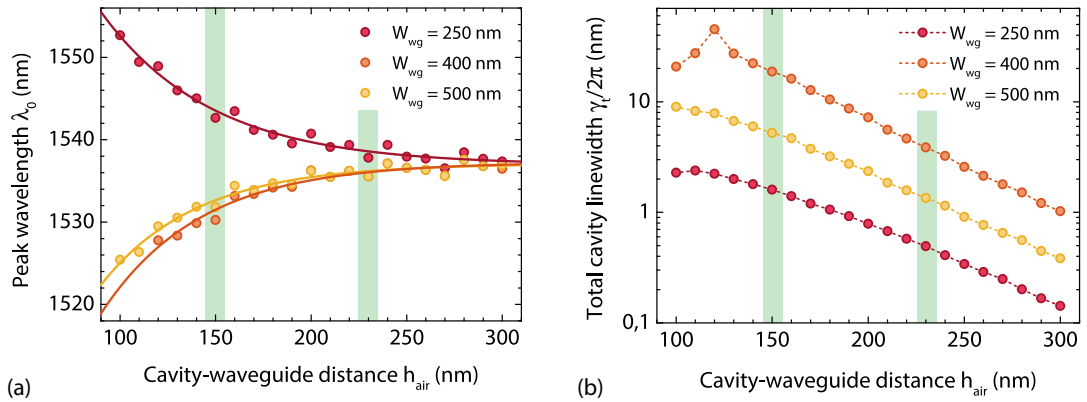

Figure 2.26: Numerical 3D FDTD simulation of resonance wavelength λ_0 (a) and total cavity linewidth γ_t (b) as a function of the cavity – waveguide separation h_{air} for several waveguide widths W_{wg}. Wavelength trends are fitted with simple exponential, given as solid lines in (a). The shaded areas correspond to the two air gaps h_{air} (150 and 230 nm), where the coupling strengths ($g_{\omega,e}$ and $g_{\gamma,e}$) are next evaluated.

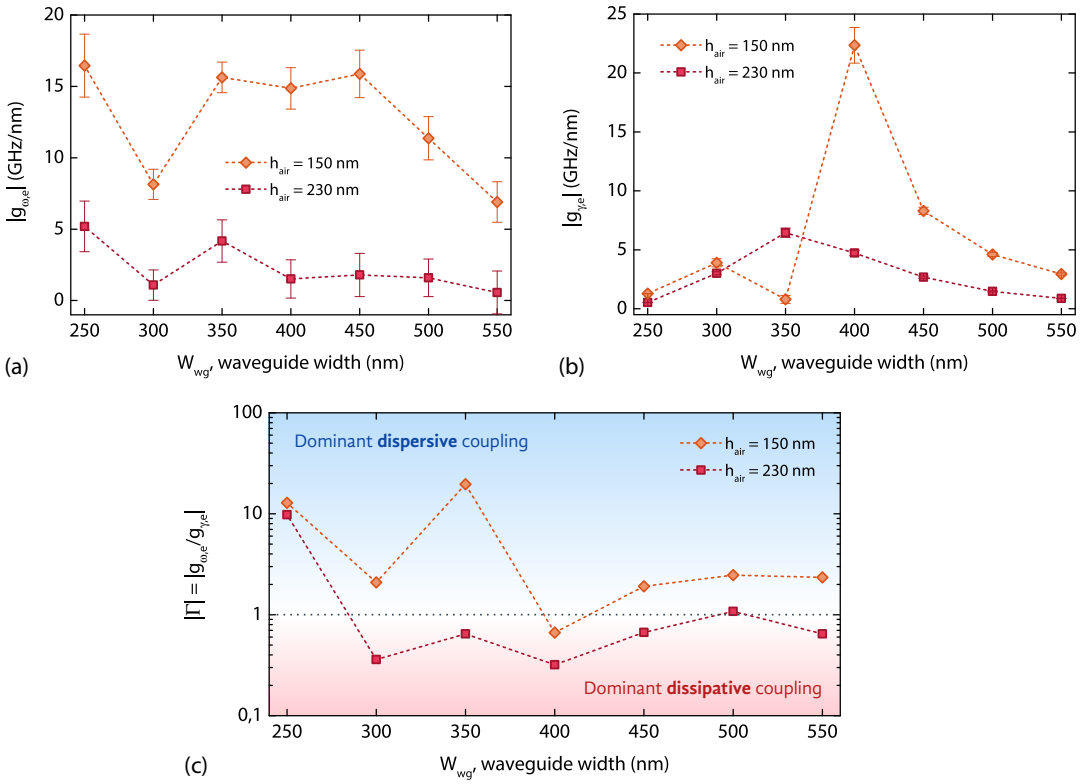

Figure 2.27: External dispersive $g_{\omega,e}$ (a) and dissipative $g_{\gamma,e}$ (b) optomechanical coupling strengths, obtained with the numerical simulations, as a function of access waveguide width W_{wg} and for two different membrane – waveguide gaps h_{air}. (c) Extracted from (a,b) ratio Γ between the dispersive to dissipative contributions for the same set of two geometry parameters W_{wg} and h_{air}.

dielectric tensor undergoes an abrupt change (i.e., on every boundary between the membrane dielectric and air), with the finest mesh achievable by the means of our computing resources ($20 \times 20 \times 20$ nm^3 unit cell) it was not possible to completely suppress the evaluated λ_0 fluctuations for the simulated z discretization step of 10 nm, which resulted in the imprecision for $g_{\omega,e}$ values given in Fig. 2.27a.

An important quantity, characterizing the coupling in optomechanical system with both non-zero dispersive and dissipative components, is the ratio $\Gamma = g_{\omega,e}/g_{\gamma,e}$ between the corresponding coupling strengths. Figure 2.27c shows the evolution of $|\Gamma|$ parameter, obtained from simulations performed for Figs. 2.26a,b. While for shorter suspension height of $h_{\mathrm{air}} = 150$ nm the overall optomechanical coupling strength for the two components increases, the dispersive interaction becomes more pronounced compared to the dissipative one. This leads to a system where the dispersive coupling regime is dominant. The tuning of the ratio Γ at this fixed value of h_{air}, on the other hand, can be realized over more than one order of magnitude by switching between different access waveguide geometries (Fig. 2.27c), introducing an additional degree of freedom for the optomechanical experimentation of our system.

To sum up, when comparing the two results from the first-order perturbative theory (Fig. 2.25a,b) with the corresponding numerical derivatives, obtained from 3D FDTD simulations (Fig. Fig. 2.27a,b for h_{air} = 230 nm), the theoretical trends fall approximately within the error bars of the simulated ones. However, the FDTD simulation, contrary to both perturbative theory results, does not show a monotonic behaviour, featuring local maxima and minima along W_{wg} variation axis. The perturbative theory can be still employed as a quick way to estimate a coupling strength variation for the same cavity – waveguide pair, while changing the separation distance. Such study showed some consistent results with the FDTD simulation for the coupled cavity – external fibre system presented in [Hryciw 2014], when the change in coupling was examined versus the spatial separation of these two elements.

2.3.4 Numerical simulation of intrinsic optomechanical couplings

Simulation of the intrinsic optomechanical couplings is a subject of multi-physics study, involving the knowledge of different perturbations caused by each of the mechanical resonator modes to some of optical system parameters, therefore, the correct estimation of these effects requires a FEM simulation. Commercially available *COMSOL Multiphysics* software package was used for this purpose, providing a direct way to perform a coupled simulations between different physics types (e.g., structural mechanics and electromagnetic waves). The two types of interactions, dissipative and dispersive, are described using the perturbative theory approximations (Section 2.3.3.1), adapted to the specific optomechanical effects occurring inside a moving PhC slab membrane. In this case, 3D FDTD simulation cannot be used since it is not possible to model displacement field distribution for mechanical model with this technique. Simulation of the dissipative intrinsic interaction was not performed in the framework of these studies, as it requires finer meshing of the computational domains while introducing the displacement field $\vec{Q}(\vec{r})$ patterns for each of the modes of interest. This procedure, however, was not achievable using our available computational means. Therefore the following Sections review two principal contributions to the dispersive intrinsic coupling, given by moving boundaries and photoelastic effects.

2.3.4.1 Moving interfaces contribution

A deformation of the optical resonator boundaries, related to a displacement field profile of a particular mechanical mode, affects the dielectric tensor at the frontier between different materials. This effect is explained by the shift of the high-contrast step profile of $\varepsilon(\vec{r})$ across a boundary because of the deformations of the structure. By relating such deformation to a change in the dielectric constant ε, we can use Equation 2.10 to calculate the optomechanical coupling for the intrinsic case. In [Johnson 2002] paper a robust expression for this shift in frequency was derived, which, when adapted to an optomechanical interaction [Eichenfield 2009c], gives an optical frequency shift per displacement

unit length, or, the dispersive coupling strength due to the effect of moving interfaces, as follows:

$$g_{\omega,\mathrm{MI}} = -\frac{\omega_0}{2}\frac{\int dA\left[\vec{Q}\left(\vec{r}\right)\cdot\hat{\vec{n}}\right]\left[\Delta\varepsilon_c\left|\vec{E}_{c,\parallel}\right|^2 - \triangle\left(\varepsilon_c^{-1}\right)\left|\vec{D}_{c,\perp}\right|^2\right]}{\max\left(\left|\vec{Q}\right|\right)\int dV\varepsilon_c\left|\vec{E}_c\right|^2}, \tag{2.12}$$

where $\Delta\left(\varepsilon_c^{-1}\right) = \varepsilon_c^{-1} - 1$ is a difference permittivity tensor between the cavity dielectric and surrounding medium (including the holes in the PhC lattice), $\hat{\vec{n}}$ is the outward facing unit normal vector on the surface of the unperturbed cavity and $\int dA$ represents the integration over all the available cavity boundaries while taking into account the proper normal vectors.

Considering the permittivity tensors from Eq. 2.12 and their relation to the refractive index, one generally writes $\varepsilon = \varepsilon_1 + i\varepsilon_2 = (n + ik)^2$, where ε_1 and n refer to real parts of dielectric constant and refractive index, whereas ε_2 and k – to the corresponding imaginary parts. In our simulation we assume $\varepsilon_2, k = 0$, therefore $\varepsilon = \varepsilon_r\varepsilon_0$, where ε_r is the relative material permittivity and ε_0 is the vacuum permittivity $\varepsilon_0 = 8.75 \times 10^{-12}$ F/m. For our case of the isotropic permittivity tensor, one thus gets for Eq. 2.12: $\varepsilon_c = n^2\varepsilon_0$, $\Delta\varepsilon_c = \left(n^2 - 1\right)\varepsilon_0$ and $\Delta\left(\varepsilon_c^{-1}\right) = \left((1/n)^2 - 1\right)/\varepsilon_0$.

2.3.4.2 Photoelastic contribution

The photoelastic contribution to the intrinsic optomechanical coupling arises from local changes in the refractive index due to strain in the structure, created by the displacement field distribution for a given mechanical mode. For a particular vector displacement field $\vec{Q}(\vec{r})$, the induced dielectric perturbation is given by

$$\overline{\overline{\delta\varepsilon}}\left(\vec{r}\right) = \bar{\bar{\varepsilon}}\cdot\frac{\bar{\bar{p}}\cdot\overline{\overline{S}}}{\varepsilon_0}\cdot\bar{\bar{\varepsilon}}, \tag{2.13}$$

where $\bar{\bar{\varepsilon}}$ is the permittivity tensor of the unperturbed structure and double overline $\overline{\overline{\square}}$ notation is employed to distinguish between tensor and scalar variables; $\overline{\overline{S}}$ is the strain tensor, corresponding to the chosen mechanical mode via its $\vec{Q}(\vec{r})$ distribution:

$$S_{ij} = \frac{1}{2}\left(\frac{dq_i}{dx_i} + \frac{dq_j}{dx_j}\right) \tag{2.14}$$

with $\vec{q}(\vec{r}) = \vec{Q}(\vec{r})/\alpha$ being a mode profile (displacement), as introduced in Eq. 2.25.

Equation 2.13 in our case of isotropic medium [Chan 2012] reduces to

$$\frac{d\varepsilon_{ij}}{d\alpha} = -\varepsilon_0 n^4 p_{ijkl}S_{kl}, \tag{2.15}$$

The fourth-rank $\bar{\bar{p}}$ tensor with components p_{ijkl} is called the photoelastic tensor. For a material of cubic lattice symmetry (e.g., Si, InP, GaAs), a reduced tensor with elements p_{ij} can be used:

$$\overline{\overline{p}} = \begin{bmatrix} p_{11} & p_{12} & p_{12} & 0 & 0 & 0 \\ p_{12} & p_{11} & p_{12} & 0 & 0 & 0 \\ p_{12} & p_{11} & p_{11} & 0 & 0 & 0 \\ 0 & 0 & 0 & p_{44} & 0 & 0 \\ 0 & 0 & 0 & 0 & p_{44} & 0 \\ 0 & 0 & 0 & 0 & 0 & p_{44} \end{bmatrix} \tag{2.16}$$

In Cartesian coordinate system the strain tensor is written as

$$\overline{\overline{S}} = \begin{bmatrix} S_{xx} & S_{xy} & S_{xz} \\ S_{yx} & S_{yy} & S_{yz} \\ S_{zx} & S_{zy} & S_{zz} \end{bmatrix} \tag{2.17}$$

Next, using the fact that $S_{ij} = S_{ji}$ for $i \neq j$, we can introduce a contracted index notation ($xx \to 1$; $yy \to 2$; $zz \to 3$; yz, $zy \to 4$; xz, $zx \to 5$; xy, $yx \to 6$) and write

$$\overline{\overline{S}} = \begin{bmatrix} S_1 & \frac{1}{2}S_6 & \frac{1}{2}S_5 \\ \frac{1}{2}S_6 & S_2 & \frac{1}{2}S_4 \\ \frac{1}{2}S_5 & \frac{1}{2}S_4 & S_3 \end{bmatrix} = \begin{bmatrix} S_{xx} \\ S_{yy} \\ S_{zz} \\ 2S_{yz} \\ 2S_{xz} \\ 2S_{xy} \end{bmatrix} = \begin{bmatrix} S_1 \\ S_2 \\ S_3 \\ S_4 \\ S_5 \\ S_6 \end{bmatrix} \tag{2.18}$$

This notation allows now to calculate a matrix product $\overline{\overline{p}} \cdot \overline{\overline{S}}$ for Equation 2.13, with the notations from Eqs. 2.16, 2.18:

$$\overline{\overline{p}} \cdot \overline{\overline{S}} = \begin{bmatrix} p_{11}S_1 + p_{12}S_2 + p_{12}S_3 \\ p_{12}S_1 + p_{11}S_2 + p_{12}S_3 \\ p_{12}S_1 + p_{12}S_2 + p_{11}S_3 \\ p_{44}S_4 \\ p_{44}S_5 \\ p_{44}S_6 \end{bmatrix} \tag{2.19}$$

By reversing our contracted notation with Eq. 2.18, we come back to Cartesian coordinate system indices:

$$\overline{\overline{p}}\cdot\overline{\overline{S}} = \begin{bmatrix} p_{11}S_{xx}+p_{12}S_{yy}+p_{12}S_{zz} & p_{44}S_{xy} & p_{44}S_{xz} \\ p_{44}S_{xy} & p_{12}S_{xx}+p_{11}S_{yy}+p_{12}S_{zz} & p_{44}S_{yz} \\ p_{44}S_{xz} & p_{44}S_{yz} & p_{12}S_{xx}+p_{12}S_{yy}+p_{11}S_{zz} \end{bmatrix} \tag{2.20}$$

At this point a simple volume integral from perturbative theory approximation, such as the one shown in Eq. 2.9, can be used to find the intrinsic dispersive optomechanical coupling strength, coming from to the photoelastic effect:

$$g_{\omega,\mathrm{PE}} = -\frac{\omega_0}{2}\frac{\int dV\,\vec{E}_c\cdot\overline{\overline{\delta\varepsilon}}\cdot\vec{E}_c}{\max\left(\left|\vec{Q}\right|\right)\int dV\,\varepsilon_c\left|\vec{E}_c\right|^2}, \tag{2.21}$$

where the $\vec{E}_c\cdot\overline{\overline{\delta\varepsilon}}\cdot\vec{E}_c$ product in numerator with Equations 2.15 and 2.20 is given by:

$$\begin{aligned}\vec{E}_c\cdot\overline{\overline{\delta\varepsilon}}\cdot\vec{E}_c = -\varepsilon_0 n^4 \big[&2\,\mathrm{Re}\left\{E_x^*E_y\right\}p_{44}S_{xy} + 2\,\mathrm{Re}\left\{E_x^*E_z\right\}p_{44}S_{xz} + 2\,\mathrm{Re}\left\{E_y^*E_z\right\}p_{44}S_{yz} + \\ &+\left|E_x^2\right|\left(p_{11}S_{xx}+p_{12}\left(S_{yy}+S_{zz}\right)\right) + \left|E_y^2\right|\left(p_{11}S_{yy}+p_{12}\left(S_{xx}+S_{zz}\right)\right) + \\ &+\left|E_z^2\right|\left(p_{11}S_{zz}+p_{12}\left(S_{xx}+S_{yy}\right)\right)\big].\end{aligned} \tag{2.22}$$

Refractive index of InP at 1550 nm wavelength and at room temperature is taken $n = 3.16$ [Pettit 1965]. The components of the reduced photoelastic tensor, used in Eq. 2.22, were taken as $(p_{11}, p_{12}, p_{44}) = (-0.05, -0.02, 0.0546)$. None of these values are explicitly given in the literature for 1.55 μm wavelength, thus the used ones are the results of extrapolations of data found in [Canal 1979; Rönnow 1998] using the relations from [Adachi 1992].

2.3.4.3 Total intrinsic coupling

The optomechanical coupling ratio g, introduced before, is a parameter which depends on the displacement of the resonator. It is even difficult to estimate for three-dimensional displacement as for more complicated mechanical normal modes (see the discussion in [Aspelmeyer 2013]). Another figure of merit, the vacuum optomechanical coupling strength

$$g_0 = g\,x_{\mathrm{ZPF}}, \tag{2.23}$$

expressed in frequency, is used instead for the description of the optomechanical interaction and evaluating its strength. Such figure of merit also allows for comparison between various resonators of unequal geometries and even more different displacement patterns. It quantifies the interaction strength between a single photon and a single phonon and

corresponds to the frequency shift; induced by the zero-point fluctuation of the mechanical motion. The multiplier for g in Eq. 2.23, x_{ZPF}, is indeed the zero-point fluctuation amplitude[9] of the mechanical oscillator, or, its maximum single-phonon displacement:

$$x_{\mathrm{ZPF}} = \sqrt{\frac{\hbar}{2m_{\mathrm{eff}}\Omega_m}}, \tag{2.24}$$

where m_{eff} is the effective mass of the mechanical mode (see below) and $\hbar$ is the reduced Planck constant.

Definition of the effective mass of a mechanical mode comes from the introduction of the effective mode volume, $m_{\mathrm{eff}} \equiv \rho V_m$ with ρ being the resonator's material density. From the analogy to the modal volume of an optical mode,

$$m_{\mathrm{eff}} = \frac{\int d\vec{r}\,\vec{Q}^*(\vec{r}) \cdot \rho(\vec{r}) \cdot \vec{Q}(\vec{r})}{\max\left[\left|\vec{Q}(\vec{r})\right|^2\right]} = \rho \int dV \left(\frac{\left|\vec{Q}\right|}{\max\left|\vec{Q}\right|}\right)^2, \tag{2.25}$$

where ρ is the material density, which is considered isotropic; $\vec{Q}(\vec{r})$ is the vector displacement field, describing perpendicular displacements of the boundaries of volume elements. It can be decomposed as $\vec{Q}(\vec{r}) = \alpha\,\vec{q}(\vec{r})$, where α is the mechanical vibration amplitude and $\vec{q}(\vec{r})$ is a mode profile (displacement), so that $\max(|\vec{q}|) = 1$.

Mode	$\Omega_m/2\pi$ (MHz)	m_{eff} (pg)	x_{ZPF} (fm)	$g_{\omega,\mathrm{MI}}$ (MHz/nm)	$g_{\omega,\mathrm{PE}}$ (MHz/nm)	$g_{0,i}$ (Hz)
M_1	2.34	117.2	5.54	134.4	-0.27	1858.5
M_2	2.75	61.8	7.14	110.1	0.24	1967.8
M_3	11.54	21.7	5.90	39.8	0.24	590.6
M_4	14.45	32.9	4.28	169.5	0.49	1818.5

Table 2.1: Simulated intrinsic dispersive optomechanical coupling sthengths and characteristic parameters for several flexural modes of a suspended 10×20 μm^2 InP membrane.

Values of simulated intrinsic dispersive coupling components, using Eqs. 2.12 and 2.21, for the two families of mechanical modes (cf. Section 2.2) – the flexural ones of the whole membrane and the ones localized inside the L3 PhC cavity, are illustrated in Figs. 2.28, 2.29, while the data including characteristic optomechanical parameters are given in Tables 2.1 and 2.2. Top plots in Figs. 2.28, 2.29 include the simulated (cf. Section 2.2) mechanical response of the suspended membrane and the L3 defect cavity to an external excitation, read out in their middle, allowing to compare the relative amplitude of different modes. Using this criterion, several eigenmodes from the two families were selected for

[9] Zero-point fluctuation amplitude equals the spread of the coordinate in the ground-state of a mechanical oscillator, i.e., $\langle 0 | \hat{x}^2 | 0 \rangle = x_{\mathrm{ZPF}}^2$, where $|0\rangle$ denotes the mechanical ground state and $\hat{x} = x_{\mathrm{ZPF}}(\hat{b} + \hat{b}^\dagger)$ with the respecting phonon creation ($\hat{b}^\dagger$) and annihilation ($\hat{b}$) operators.

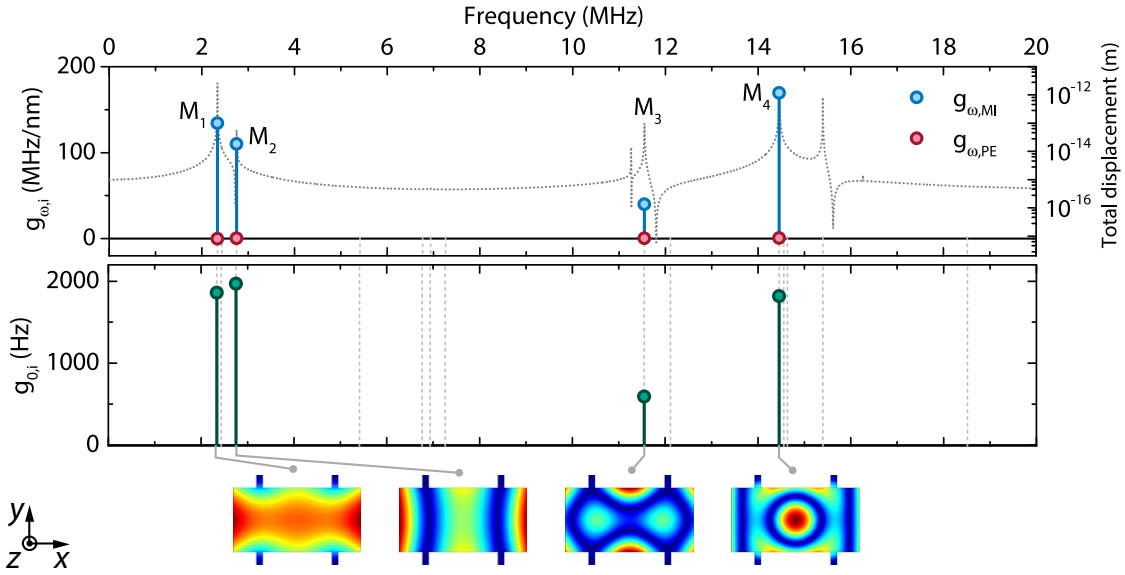

Figure 2.28: Simulated intrinsic dispersive optomechanical coupling $g_{\omega,i}$ components (moving interfaces and photoelastic effects) and characteristic parameters for several flexural modes of a suspended InP membrane with dimensions $m_x = 20$ μm, $m_y = 10$ μm, $b_x = 1$ μm, $b_y = 2$ μm. Dotted grey curve (top plot) represents a mechanical response to the external membrane actuation, measured in the cavity middle, as given in Fig. 2.16; the modes of interest are mapped with the corresponding $\vec{Q}$ profiles (bottom).

the estimation of coupling coefficients $g_{\omega,i}$ and total intrinsic vacuum coupling rate $g_{0,i}$, as given in Tables 2.1, 2.2. The zero-point fluctuation amplitude x_{ZPF} and effective mode mass m_{eff} are also included, according to Eqs. 2.24 and 2.25.

Mode	$\Omega_m/2\pi$ (MHz)	m_{eff} (fg)	x_{ZPF} (fm)	$g_{\omega,\mathrm{MI}}$ (MHz/nm)	$g_{\omega,\mathrm{PE}}$ (MHz/nm)	$g_{0,i}$ (Hz)
L_3M_{00}	462	439	6.43	4.31	-0.82	21.7
L_3M_{10}	574	483	5.50	51.25	-13.88	201.8
L_3M_{20}	756	437	5.04	-22.37	22.02	-1.7
L_3M_{30}	978	339	5.03	-85.82	27.91	-256.59
L_3M_{40}	1272	264	5.00	52.22	26.15	354.54

Table 2.2: Simulated intrinsic dispersive optomechanical coupling strengths and characteristic parameters for several localized L3 PhC cavity mechanical modes.

For the flexural membrane modes (Fig. 2.28) the major contribution to the intrinsic coupling comes from the effect of moving interfaces, whereas the photoelastic effect is about 2–3 orders of magnitude weaker. The two mechanisms, however, become comparable for the family of localized cavity mechanical modes, where the displacement and electromagnetic fields show a very high spatial overlap.

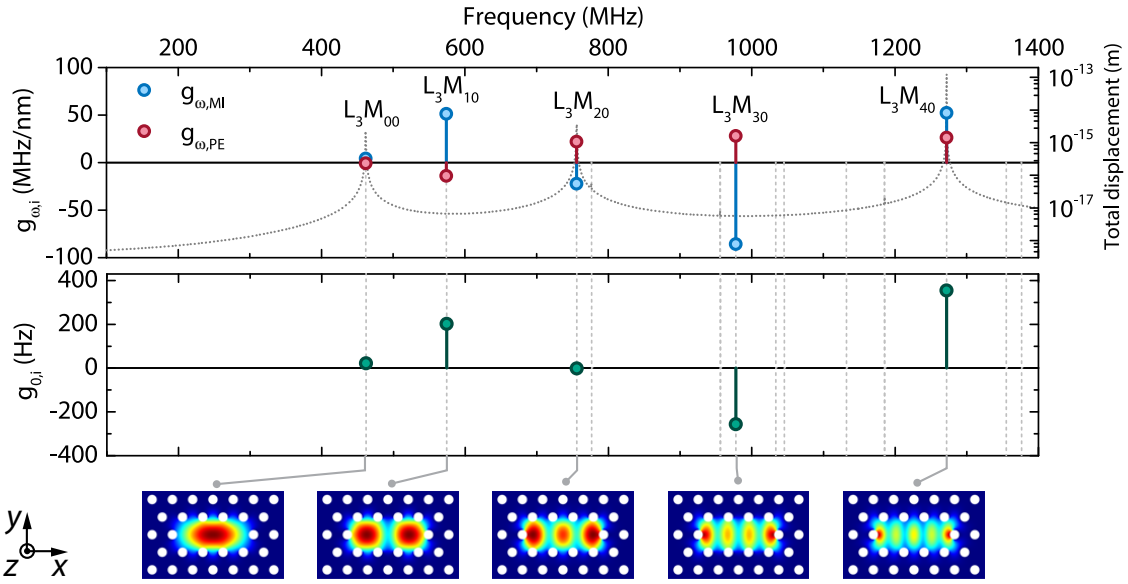

Figure 2.29: Simulated intrinsic dispersive optomechanical coupling $g_{\omega,i}$ components (moving interfaces and photoelastic effects) and characteristic parameters for some of localized mechanical modes of the L3 PhC cavity. Dotted grey curve (top plot) represents a mechanical response on the external actuation, measured in the cavity middle, as given in Fig. 2.19; the modes of interest are mapped with the corresponding $\vec{Q}$ profiles (bottom).

In general conclusion, the strength of intrinsic optomechanical coupling is much lower compared to the external dispersive component $g_{\omega,i} \ll g_{\omega,e}$. Moreover, as discussed in Section 2.3, the two dispersive-type interactions in their external and intrinsic realization can not be experimentally distinguished, therefore, the total g_ω value will be either a sum or a difference of these two terms, depending on the phase of the mechanical mode taken into account for the simulations of $g_{\omega,i}$ and $g_{\omega,e}$ parts. For the MHz range modes it can be assumed that $g_\omega \sim g_{\omega,e}$. For the localized modes family (GHz range), even if $g_{\omega,i}$ is weak, the displacement in z direction will be very small, thus the prominent coupling will be still governed by the intrinsic effects. It should be noted that the simulation of photoelastic coupling strength depends directly on the values of the photoelastic tensor components $(p_{11}, p_{12}, p_{44}) = (-0.05, -0.02, 0.05)$, which were not yet precisely measured for InP at our working wavelength, thus the extrapolated data taken into account in our calculations can be a considerable source of error for the overall $g_{\omega,i}$ value.

2.4 Towards optimized optomechanical cooling

Optomechanical cooling of a mechanical resonator and eventually reaching its ground state, was first introduced and achieved [Chan 2011] for the optomechanical system with dominant dispersive coupling, operating in the sideband-resolved regime ($\Omega_\mathrm{m} \gg \gamma_t$). Removing thermal phonons from the mechanical element can be implemented by exploiting

the intracavity radiation pressure, the force due to momentum transfer associated with photon scattering [Aspelmeyer 2012]. In the sideband-resolved limit, a pump laser of frequency ω, coupled to the cavity resonance $\omega = \omega_0$, will be modulated by the mechanical frequency Ω_m and form sidebands at frequencies $\omega \pm \Omega_\mathrm{m}$. From a quantum mechanical point of view, this process is analogous to the generation of Stokes and anti-Stokes sidebands in Raman scattering. The upper sideband $\omega + \Omega_\mathrm{m}$ is a result of pump-laser photons acquiring energy by annihilating thermal phonons in the mechanical element; the lower sideband $\omega - \Omega_\mathrm{m}$ results from photons creating phonons and reducing its own energy.

By carefully detuning the frequency of the pump field relative to a specific cavity resonance, one can resonantly enhance one of the processes. In particular, red-detuning from the cavity resonance to $\omega = \omega_0 - \Omega_\mathrm{m}$ enhances the upper sideband and promotes extraction of energy from the mechanical mode at Ω_m. As long as the up-converted photons leave the cavity sufficiently fast, carrying with them their newly acquired energy, the process can cool the motion of the mechanical element to well below the temperature of its surroundings.

Using this technique, the authors in [Chan 2011] cooled the resonator from the surrounding bath temperature of $T_b \approx 20$ K to its mechanical ground state with a mean phonon occupancy of $\bar{n} < 1$. For a given mode at $\Omega_\mathrm{m}/2\pi$ of a mechanical oscillator in a thermal bath of temperature T_b, the phonon occupancy is $n_b = k_\mathrm{B} T_b/\hbar\Omega_\mathrm{m} \gg 1$. For a quantum-limited drive laser, it can be reduced to $\bar{n} = n_b/(1+C) + \tilde{n}$, where k_B is Boltzmann's constant and $C \equiv \gamma_\mathrm{m,OM}/\gamma_{\mathrm{m},i}$ is the cooperativity, the ratio of the optically induced $\gamma_\mathrm{m,OM}$ and intrinsic $\gamma_{\mathrm{m},i}$ mechanical damping rates. In the weak-coupling regime ($\gamma_\mathrm{m,OM} \ll \gamma_t$), this damping is given by $\gamma_\mathrm{m,OM} = 4g_0^2 n_c/\gamma_t$, where n_c is the average number of drive-laser photons stored in the cavity and g_0 is the vacuum optomechanical coupling rate, as given by Eq. 2.23. The residual scattering of drive photons into the lower-frequency sideband limits the cooled phonon occupancy to $\tilde{n} = (\gamma_t/4\Omega_\mathrm{m})^2$, which is determined by the level of sideband resolution.

From the discussion above, assuming the drive laser is placed at optimal detuning $\omega_0 - \Omega_\mathrm{m}$, the minimum reached phonon occupancy of the mechanical mode $\bar{n}_\mathrm{min}$ will depend on the vacuum optomechanical coupling rate g_0 and the laser drive power, coupled into the cavity ($\propto n_c$). The bath temperature T_b, cavity optical linewidth γ_t and intrinsic mechanical mode damping rate $\gamma_{\mathrm{m},i}$ are assumed constant. This means that the device optimization in order to reach lower $\bar{n}_\mathrm{min}$ would essentially require increasing the optomechanical coupling g_0.

Optomechanical systems in the sideband-unresolved regime ($\Omega_\mathrm{m} \ll \gamma_t$) are not suitable for the implementation of such cooling scheme when dispersive coupling is dominant ($g_\omega \to \infty$, $g_\gamma \to 0$). However, it was demonstrated recently [Weiss 2013], that the cooling can be realized by putting such a system into purely dissipative coupling regime ($g_\omega \to 0$, $g_\gamma \to \infty$). The optimal cooling condition is, nevertheless, not simply $g_\omega \to 0$ and $g_\gamma \to \infty$, but is related to the ratio Γ between these two, as introduced before in in Section 2.3.3.2.

We studied the theoretically predicted optimal ratios for dispersive and dissipative

optomechanical coupling strengths with the currently achievable values for our system (see Fig. 2.27c). When an optomechanical system in the sideband-unresolved regime features both dispersive and dissipative interactions, the minimum reachable phonon number $\bar{n}_{\mathrm{min}}$ (in another words, the maximum possible cooling of the mechanical mode) can be achieved for a given optimal $\Gamma^{\dagger}$ ratio

$$\Gamma^{\dagger} = g_{\omega}^{\dagger}/g_{\gamma_t}^{\dagger} = -\frac{3}{2}\frac{\Omega_{\mathrm{m}}}{\gamma} \tag{2.26}$$

The optimal detuning Δ of the cooling laser in this case coincides with the one for the dispersive cooling: $\Delta^{\dagger} = -\Omega_{\mathrm{m}}$. The optimal $\Gamma^{\dagger}$ mixing ratio for both types of couplings is plotted from the Eq. 2.26 in Figure 2.30 as a function of the mechanical resonator frequency $\Omega_m/2\pi$ and the optical cavity linewidth $\gamma_t/2\pi$ in the range including the currently achieved and theoretically achievable values of both parameters with our system under study.

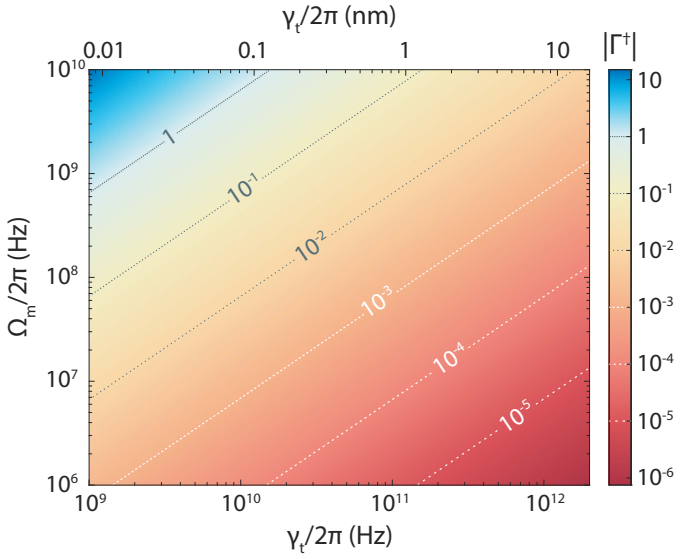

Figure 2.30: Optimal ratio $\Gamma^{\dagger}$ (absolute value) between dispersive and dissipative optomechanical coupling strengths versus mechanical mode frequency $\Omega_{\mathrm{m}}/2\pi$ and total cavity linewidth $\gamma_t/2\pi$ in view of achieving the minimal mean phonon number via the laser cooling for an optomechanical system in sideband-unresolved regime.

To put some characteristic numbers, for the fundamental flexural mode at few MHz with the coupled cavity linewidth $\gamma_t/2\pi = 1$ nm, the optimal coupling ratio equals $\Gamma^{\dagger} \approx -10^{-5}$, whereas for a localized cavity mode at $\Omega_{\mathrm{m}}/2\pi \approx 1$ GHz it increases to $\Gamma^{\dagger} \approx -10^{-2}$. When comparing to Fig. 2.27c, the further optimization of our actual device design in order to reach the optimal cooling conditions would require an improvement of the loaded linewidth γ_t towards smaller values, meaning a reduction of the intrinsic cavity losses γ_i from one side, and/or the passage to higher frequency Ω_m of the mechanical modes being cooled from another side, where the localized cavity modes in the GHz range appear to be a good candidates for reaching an optimum $\Gamma^{\dagger}$ cooling condition.

It should be taken into account, that in the case where the two parameters mentioned above (Ω_{m} and γ_t) start to approach the passage to the good cavity, or sideband-resolved limit ($\Omega_{\mathrm{m}} \gg \gamma_t$), which corresponds to the upper left graph corner in Fig. 2.26, the minimum phonon number n_{min} will become independent of the sideband parameter Ω_m/γ_t. However, in the current system design even the condition $\Omega_{\mathrm{m}} \approx \gamma_t$ is yet hardly achievable and thus not considered in view of implementation of optomechanical cooling.

2.5 Summary

This chapter introduced the optical and mechanical designs together with the complete simulation, including optical, mechanical and optomechanical characteristics of our hybrid system, either formed by a PhC slab membrane acting as a deformable mirror or containing a defect L3 photonic crystal cavity embedded inside it and heterogeneously integrated with a SOI waveguide. In the latter case, two types of simultaneously existing optomechanical couplings – dispersive and dissipative – were studied both in case of intra-cavity interaction mechanisms ('moving interfaces' and photoelastic effects) and in case of interaction with the external waveguide, coupled optically by an evanescent tail of a propagating mode. Overall dispersive intrinsic interaction strength showed to be less pronounced comparing to the external coupling effects at small membrane suspension heights ($\leqslant 300$ nm).

Dependence of the external couplings on different opto-geometric parameters of the integrated system, such as the membrane – waveguide vertical separation and the waveguide width were studied, and the possibility to achieve a tailoring of both effect strength and relative weight via these parameters was demonstrated. The implementation of an optimized ground state cooling of our mechanical resonator was examined by bringing the system into the regime of dominance of dissipative coupling while introducing different relative strengths of the dispersive optomechanical interaction.

Chapter 3

Fabrication of III-V photonic crystal membranes on SOI circuit

Contents

The previous Chapter detailed the design and realization of the photonic crystal membrane resonators, integrated in our experiments on a network of Silicon-On-Insulator (SOI) waveguides. Current chapter provides a detailed description of the fabrication process of such hybrid structures, which principally consist of a III-V photonic crystal membrane on top of SOI waveguide for an integrated and controlled optical access. From an optomechanical point of view, this integration creates a strong interaction loop with the in-plane

optical cavity, embedded in the membrane. This loop induces two pronounced types of optomechanical couplings, which can be tailored via a control over a waveguide geometry.

Main fabrication challenges during this work are twofold. First challenge consists in the obtention of high optical quality (Q) factor defect PhC cavities made of III-V material, which must be aligned to a SOI waveguide circuit with a precision (within a few nanometres); secondly, each of these cavities is a part of large (50 to 200 μm^2 in-plane dimensions) and thin (260 nm) membrane, whose proper suspension over a thin air gap (few hundreds of nm) must be achieved systematically on a chip scale. The strategies we used to tackle the aforesaid challenges are explained in the following.

Except the SOI circuit wafers, realized through the ePIXfab European network in IMEC facility (Leuven, Belgium), all the fabrication steps were implemented at LPN.

3.1 Fabrication challenges

The overall process flow in regard of its main constituents involve four main steps (Fig. 3.1).

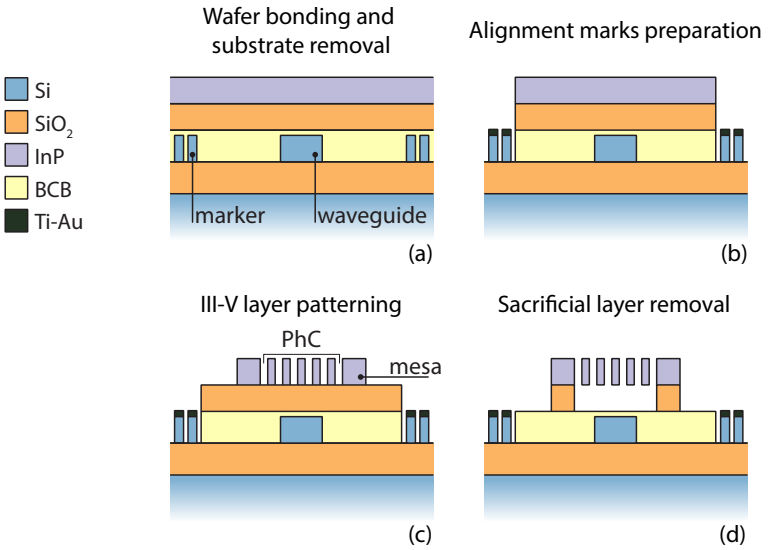

Figure 3.1: Main fabrication steps for the processing of the suspended III-V photonic crystal slab membrane integrated on a SOI waveguide circuit.

In a first step, a Si wafer holding a SOI waveguide circuit, as presented previously, is bonded with a III-V wafer containing the InP membrane (260 nm thick) with a monolayer of quantum dots. Once adhesive bonding is done, chemical substrate removal of the III-V wafer leaves solely the membrane on the SOI substrate (Fig. 3.1a). The membrane can then be further processed. In a second step, alignment marks used in the electron beam lithography runs are prepared. An enhanced contrast is obtained by additional metal covering (Fig. 3.1b). These markers allow to align the PhC cavities etched in the InP layer with respect to the access SOI circuit; we routinely achieve a mutual positioning precision

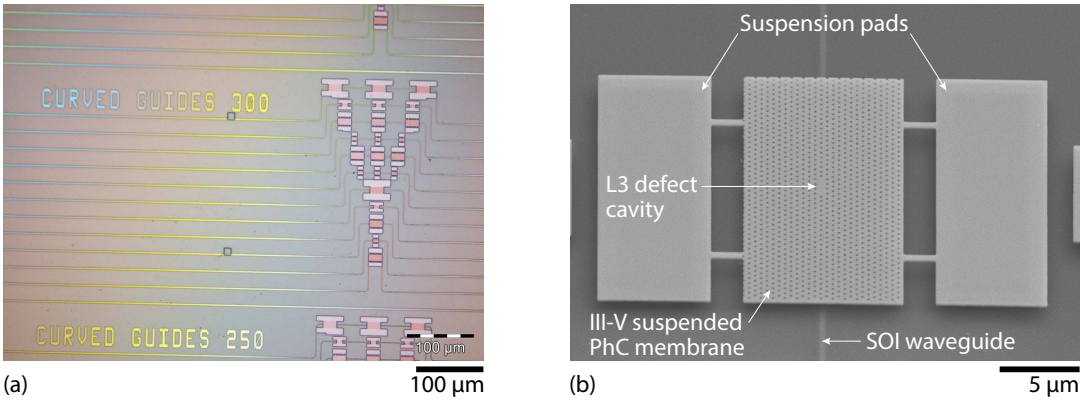

Figure 3.2: Fabricated devices at their final stage. (a) Top view of the sample revealing part of the SOI waveguide network in the middle of tapered section allowing to address the suspended membranes. (b) Scanning electron microscope (SEM) image of a single suspended PhC membrane.

of < 40 nm. In a third step, the InP layer is patterned by electron beam lithography and subsequent dry etching processing (Fig. 3.1c). This step imprints on the InP membrane the photonic crystal, defect cavity and their surrounding mesa structures (used to anchor the suspended membrane to the substrate). Last, the PhC membranes are underetched and dried via a critical point drying technique (Fig. 3.1d), creating an air gap between the waveguide an PhC membrane of a few hundreds nanometres with a controlled membrane – waveguide distance. This control is crucial for tailoring the strengths of both optical and optomechanical effects.

These four steps will be discussed in details is in the following sections.

3.2 Heterogeneous bonding of the III-V and SOI substrates

This heterogeneous bonding technique is aimed at taking advantage of both silicon (implementing low loss waveguides) and III-V material (with optical and mechanical properties, crucial for our optomechanical resonator, but also allowing to implement an integrated light source). Such heterogeneous integration was first developed for other purposes than optomechanics, in particular for advanced nanophotonics circuitry combining active and passive functionalities. In our case, we additionally use a quantum dots as active medium (Section 3.2.1), these dots are embedded within the InP membrane (Fig. 3.3a,b and Fig. 3.6a, right). This membrane will form our optical and mechanical element. The main goal of this part is to ensure an integrated coupling to the optical cavity, via a low-loss optical waveguide made of silicon (cf. Section 3.2.2). It comprises three steps: growth of the III-V membrane (Section 3.2.1), patterning of the SOI substrate (Section 3.2.2) and adhesive bonding (Section 3.2.3).

3.2.1 Active material layer

Unlike silicon, III-V materials have a direct band gap, which is usually employed for a fabrication of efficient semiconductor light sources. Suitable alloys and heterostructures permit to obtain radiative transitions at desired wavelengths ranging from 200 nm to 20 μm. Furthermore, with the vast growth experience of these materials a variety of heterostructures from bulk to quantum confined structures, such as quantum dots [Yoshie 2002; Braive 2009], dashes [Gosset 2006] and wells [Merghem 2008] can be grown (given references cover the devices operating at wavelengths around 1.55 μm).

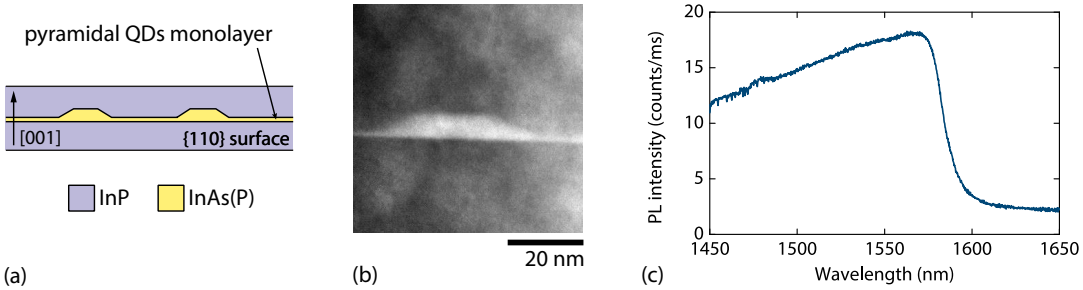

Figure 3.3: (a) Schematic of the embedded InAs(P) quantum dots monolayer (not to scale), (b) scanning transmission electron microscope (STEM) image of the {110} surface section of InAsP and (c) corresponding photoluminescence spectrum (taken at room temperature under continuous wave laser pumping: $\lambda_{\text{pump}} = 532$ nm, $P_{\text{pump}} = 400$ μW).

We took advantage of these developments and incorporated a single layer of self-assembled InAs(P) quantum dots (QDs) in the middle of a 260 nm thick InP membrane layer (Fig. 3.3). Starting from a 350 μm thick host InP(100) substrate (Fig. 3.6a, right), an intermediate layer of InGaAs (1 μm) is grown by metalorganic chemical vapour deposition (MOCVD), followed by the InP membrane with embedded QDs. The InGaAs layer will be used as etch-stop during the III-V substrate removal right after its bonding on the silicon wafer holding the passive part of our device.

The photoluminescence spectrum of the InAsP QDs at 300 K covers our wavelength of interest (1550 nm) with a very large spectral width of several hundreds of nanometres (cf. Fig. 3.3c; cut-off around 1600 nm is due to the limitations of spectrograph operation range).

3.2.2 SOI waveguide circuitry

As it was introduced before (cf. Sections 1.5, 2.1.3.4), the integration of SOI waveguides within our sample allows for efficient and fully controlled light input and extraction to and from the devices under study.

We start the fabrication with a standard SOI sample which consists of 1000 μm thick silicon (Si) substrate and a network of parallel Si waveguides, separated by a 2 μm thick cladding layer of Buried Oxide (BOx) made of SiO_2. For the optical mode propagating in

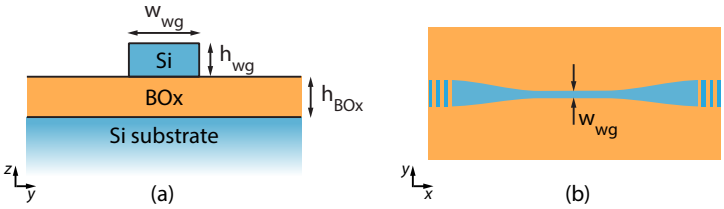

Figure 3.4: Schematic representation of a single waveguide within the SOI circuit: (a) y–z projection (cutting plane passes through the waveguide middle), (b) x–y projection.

the SOI waveguide, good lateral confinement is ensured due to the high refractive index contrast between the SiO_2 ($n_{SiO_2} = 1.45$) and Si core ($n_{Si} = 3.46$) [Taillaert 2002]. A thick cladding layer of SiO_2 prevents any optical couplings between two Si layers – waveguide and substrate (see Fig. 3.4a,b) and thus ensures optical confinement within the waveguide with respect to the vertical direction.

Each waveguide is tapered from 10 μm (side dimension of the grating coupler, cf. Fig. 3.5) to few hundreds of nm width (w_{wg}) in the middle (500 μm long section of constant w_{wg}). A single waveguide has a length of 6 mm and is terminated on both sides with shallowly etched grating couplers [Emmons 1992] for light coupling and extraction to and out of the chip (Fig. 3.5). Our standard waveguide array consists of series of $h_{wg} = 220$ nm thick waveguides with w_{wg} (ridge width in the coupling region, see Fig. 3.4b) varying from 250 to 550 nm with a step of 50 nm, which makes them single-mode for transverse electric (TE) polarization[1] and additionally allows for different strengths of optical coupling with the optical cavity in the waveguide evanescent field (cf. Fig. 2.12b).

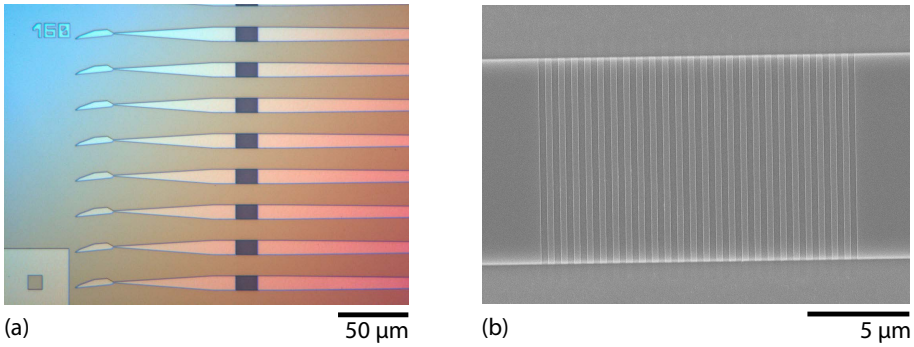

Figure 3.5: Optical microscope (a) and SEM (b) pictures of the SOI waveguide terminations with the grating couplers.

Waveguide optical losses are typically around 2.4 dB/cm mainly due to light scattering on imperfections brought by fabrication. Both grating couplers and waveguides are designed to have a transmission band centred at 1550 nm with a 1 dB bandwidth of around 40 nm large. The grating couplers are conceived to work with a standard cleaved single-

[1] The electric field in such propagating wave would be parallel to the wafer surface and perpendicular to the waveguide sidewalls.

mode optical fibre (SMF), brought into the coupler's vicinity, and show [Taillaert 2006] best coupling efficiency of -5.1 dB (input to output fibre) within the designed bandwidth and a fibre to substrate's normal angle[2] of (10±3)°.

SOI photonic circuit contains also two lines of alignment markers (see Section 3.3 for more details), which are necessary to perform successive electron beam lithography runs and achieve correct alignment of a PhC membrane with respect to the corresponding access waveguide. This procedure and its limitations is one of the key point of this fabrication process and will be described below.

SOI wafers are fabricated in a CMOS line at IMEC facility with a SmartCut technique (developed originally in CEA-LETI [Bruel 1997]) and deep UV lithography [Selvaraja 2009]; the complete procedure is discussed in detail in [Bazin 2013]. Main steps are presented in the next Section.

3.2.3 Bonding of III-V on SOI

Heterogeneous integration of a III-V membrane resonator with a SOI waveguide requires an adhesive bonding of the two respective wafers via an intermediate layer. Our scientific application imposes two main requirements on this step. First, the bonding layer should ensure the planarization of the Si waveguide circuit while preserving control over the overlaying thickness, as we want to obtain a pre-defined gap between the waveguide and the III-V membrane as small as possible. Second, it should be transparent in our operating wavelength band (1.5 – 1.6 μm) and the refractive index contrast for the propagating optical mode in the encapsulated waveguide should be kept high for tight mode confinement.

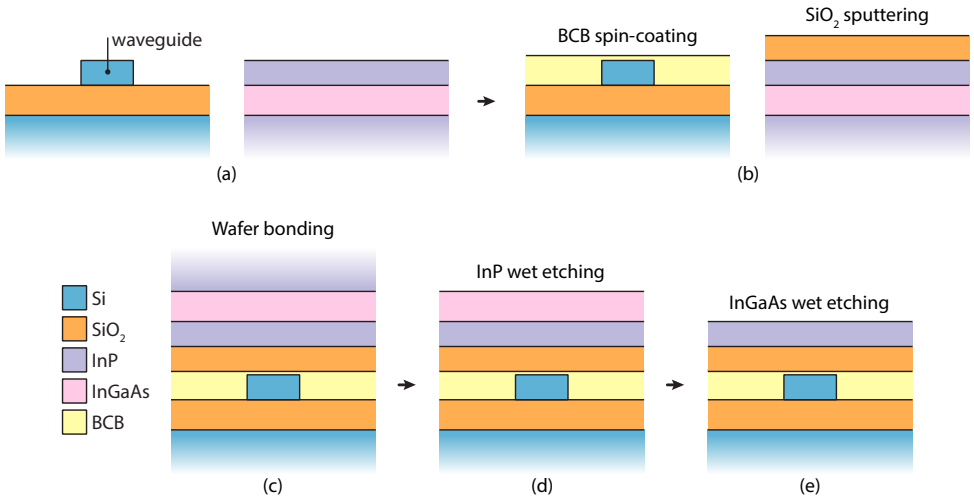

Figure 3.6: Process flow of InP membrane preparation and bonding on a SOI waveguide wafer.

[2]Grating couplers usually designed for slightly deviated from normal incidence input beam in order to avoid direct reflection. Optimal angle between the fibre and the normal incidence is 10° for our samples.

Recently an adhesive bonding technique was developed for the fabrication of InP / InGaAsP dies integrated on the patterned silicon-on-insulator wafers [Roelkens 2006]. The employed polymer, divinylsiloxane-benzocyclobutene (DVS-BCB), fulfils both of our requirements. Its thickness during fabrication (Fig. 3.6b, left) can be as low as few tens of nanometres [Keyvaninia 2013] when working with its dilution in mesitylene (C_9H_{12}, derivative of benzene).

To obtain the maximum success rate during the bonding process, we employ a layer of amorphous SiO_2 as an interface between the InP membrane and the DVS-BCB layer. In general, only few nanometres of silica are sufficient for successful bonding; in our case the thickness of this sacrificial layer is of the order of few hundreds nanometres to adjust the distance between the Si waveguide circuit and the InP membrane (Fig. 3.6b, right). This thickness has been chosen as a compromise solution between two aspects: if the silica layer is too thin, underetching and correct release of the membrane become difficult, whereas thicker sacrificial layers reduces strongly the optical coupling efficiency between the PhC cavity and the addressing waveguide. The optimal working range for our objectives (cf. Section 2.1.3.4) lies between 100 and 400 nm approximately.

Before the bonding, a cleaning procedure of the surface of SOI wafer is performed in order to optimize the bonding quality and efficiency. The protecting resist (coated prior to the shipping of processed SOI wafers) is removed from the sample surface in an acetone ultrasonic bath (5 min, 80 Hz, 100 % nominal power), followed by isopropyl alcohol (IPA, C_3H_7OH) rinse and N_2 flow drying. It is followed by 2' O_2 plasma cleaning[3] for removal of the remaining resist; thus leads to the creation of the native oxide layer on silicon, which improves adhesion during bonding.

Then a DVS-BCB[4] solution, mixed with mesytilene (2:1.5 by volume), is spin-coated (5000 rpm speed, 2000 rpm/s acceleration, 30 sec) on the SOI wafer. This coating is followed by a 15' post-bake on a hotplate at 80 °C in order to outgas the remaining solvent (Fig. 3.6b, left). These parameters result in 250 nm thick DVS-BCB layer, leaving a 30 nm thick (cf. Section 3.5.2) film over the Si waveguide top surface. The exact distance between the InP and Si levels is then adjusted during the SiO_2 coating on the InP membrane, which is controlled in more precise manner.

At the same time the InP wafer is cleaned with 2' O_2 plasma prior to the deposition of the sacrificial SiO_2layer. The latter procedure is accomplished in two steps. The first 25 nm of SiO_2 are deposited by plasma-enhanced CVD (PECVD), which does not involve target wafer bombardment by ions. Thus the surface quality of the underlying InP layer is not degraded. The remaining SiO_2 thickness, typically 175 nm, is deposited by sputtering to improve adhesion compared to PECVD-deposited silica.

Once both dies are prepared, they are put in contact and the bonding is performed in a high precision wafer bonder (SÜSS MicroTech SB6): the ensemble is heated up

[3] Reactive-ion etching, RIE.

[4] Commercially available solution from *Dow Chemicals*, Cyclotene 3022-35, is the partially polymerized DVS-BCB oligomers mixed with mesitylene.

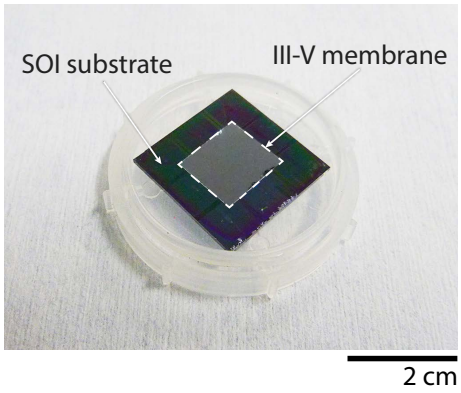

Figure 3.7: InP membrane (highlighted with a dashed line) bonded on a silicon substrate with the SOI circuit. The picture is taken after the III-V substrate removal – the InP is still covered with the InGaAs etch-stop layer.

and maintained at 320 °C for 30 minutes in vacuum ($P \leqslant 5 \cdot 10^{-3}$ mbar) to reach full polymerization of the BCB. At the same time, a constant force is applied to the entire structure via an internal press (with a pressure equivalent of $P = 500$ mbar[5]), which ensures the homogeneous flatness of the polymer surface and thus constant interlayer distance across the whole sample.

Resulting structure (Fig. 3.6c) subsequently goes through the substrate removal procedure. The InP substrate's surface is first cleaned by dipping it into a H_2SO_4:H_2O_2:H_2O solution (3:1:1 by volume) during 1 min. This cleaning insures enhancement of substrate removal speed and etching homogeneity. Wet etching in a HCl acid solution (40 %) during approximately one hour (Fig. 3.6d) then completely removes the InP substrate.

The etching stops at InGaAs layer interface, which is removed after in a H_2SO_4:H_2O_2:H_2O solution (same ratio as above; etching time is approximately 1 min for 1 μm thick layer) (Fig. 3.6e).

3.3 Processing of high-contrast alignment markers for electron beam lithography

After the bonding of the two wafers and InP substrate removal, the top InP membrane is ready to be patterned with successive electron beam lithography and dry etching steps. However, we need a relative positioning of the PhC patterns with respect to the underlying waveguides smaller than 40 nm. This strong requirement can be fulfilled with the help of alignment markers already present on the SOI waveguide level.

First issue is the presence in the bonded structure of a high number of layers (see Fig. 3.8a) that cover the SOI circuit. Thus the markers are not detectable by an electron

[5]Some samples were successfully bonded at 250 mbar setting, which, however, will result in different BCB layer thickness.

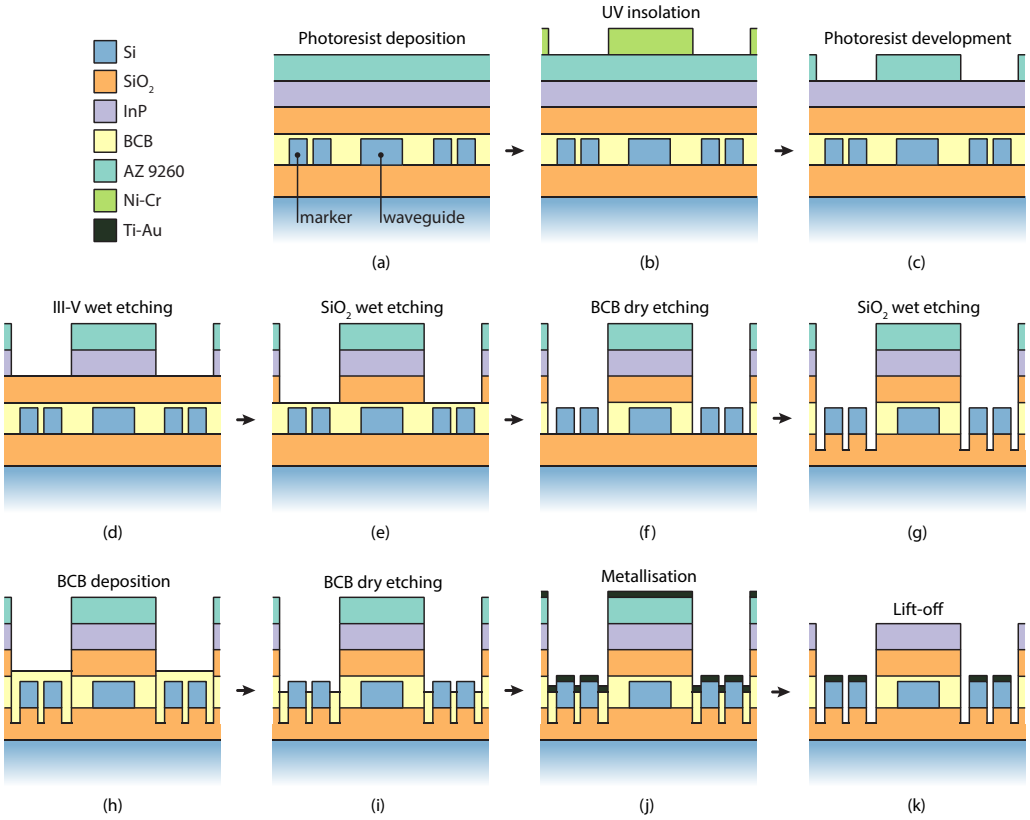

Figure 3.8: Process flow of high contrast markers preparation for electron beam alignment.

beam. The problem can be solved by selectively etching openings through these top layers in order to restore access to the markers arrays.

Each sample contains two lines of markers, that is, 100 × 100 μm Si pillars with 10 × 10 μm openings in the middle (Fig. 3.9a). These markers are processed during the SOI substrate patterning (Section 3.2.2).

The process flow of the markers openings is shown in Figure 3.8. Two trenches are etched above each of markers lines. To do so, a layer of AZ 9260 photoresist[6] is spin-coated on top of the InP layer (4000 rpm speed, 4000 rpm/s acceleration, 30 sec, 7–8 μm thick after the bakeout) and then baked for 7' on a hot plate at 120 °C (Fig. 3.8a). Ultraviolet (UV) photolithography is performed through a metallic slit mask with a broadband UV source (310–450 nm, mercury vapour lamp, 2' exposure) (Fig. 3.8b). Next, the photoresist is developed in AZ 400K developer[7] (diluted in H_2O as 1:4 by volume) until the resist is completely cleared from the exposed areas (8' approximately). In such manner the 500 μm wide trenches are defined in the AZ 9260 layer (Fig. 3.8c).

The InP membrane layer is removed (Fig. 3.8d) inside these trenches by wet etching in a HCl (40 %) solution (10 sec for 260 nm thickness); then the SiO_2 sacrificial layer is wet

[6] http://www.microchemicals.com/products/photoresists/az_9260.html
[7] http://www.microchemicals.com/products/developers/azr_400k_developer.html

etched (Fig. 3.8e) in an ammonium fluoride (NH_4F, 40 % in H_2O) solution (3' for 200 nm thickness). Finally, the Si level is revealed by RIE etching the cured BCB in a SF_6/O_2 plasma (Fig. 3.8f). In Figure 3.9a, the InP membrane (still recovered by protective AZ 9260 photoresist layer) and marks in Si can be seen (cf. colour-coded legend) together with the few neighbouring waveguides.

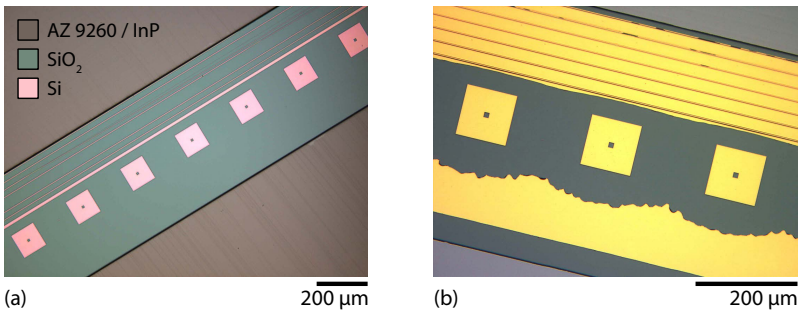

Figure 3.9: Line of alignment markers at the SOI level after InP wafer bonding and selective removal of the InP substrate and InGaAs etch-stop layer (a); after the metallisation and lift-off (b).

Second issue is related to the particularity of electron beam lithography operation exploiting the marker detection. The backscattered signal of an electron beam is directly related to the atomic number of the material in which the marker is defined. Our markers consist of Si pillars on SiO_2 areas, – two materials with little contrast seen by electrons. To overcome this problem and considerably enhance the contrast between an internal marker square (silicon dioxide) and its surroundings (silicon), we employ a metal coating on top of outer silicon pillar.

Metal patterns are generally fabricated with a lift-off technique. First, a negative pattern is created in a sacrificial resist layer, deposited on the surface of the substrate (or the layer of interest). The target metal is then deposited over the whole area of the wafer, so that it reaches the surface of the substrate in the etched regions. When the resist layer is removed, the metal on its top is lifted-off and washed away as well. As a result, the target metal remains only in the regions where it had a direct contact with the substrate.

For this purpose, we use a new layer of BCB as a sacrificial layer, since the already present cured BCB layer cannot be lifted-off any more because of its complete polymerization. The underlying silica layer is partially wet-etched (Fig. 3.8g) in ammonium fluoride (AF) solution for 10', which results in about 800 nm gap. The new layer of BCB is then spin-coated (3000 rpm speed, 2000 rpm/s acceleration, 30 sec) and post-baken for 3' at 120 °C. BCB is a planarizing resist, thus the hollows around and within the silicon pillars are filed up, while the top surfaces of markers are covered with a much thinner resist layer (cf. Fig. 3.8h). We remove it with 5' in SF_6/O_2 plasma, additionally etching around 500–700 nm of sacrificial layer outside of the markers, which assures correct lift-off behaviour (the etching liquid thus will be able to penetrate within the interior marker opening and interact with the BCB resist, Fig. 3.8i). A metal double-layer of Ti/Au (100/1000 Å)

is deposited by EBPVD (electron beam physical vapour deposition) and finally lifted-off (Fig. 3.8j,k) by stripping the BCB sacrificial layer in EBR (Edge Bead Remover) PG solution[8] at ultra-sound bath (25% nominal power, 2' or until complete metal removal from the markers interior). Metal layer from the remaining part of the sample (outside trenches) is lifted-off by stripping the AZ 9260 photoresist with acetone and IPA rinse.

As a result we obtain high-contrast negative markers (see Fig. 3.9b), which will serve for the alignment during subsequent electron beam lithography runs.

3.4 III-V membrane layer patterning

SOI waveguide and InP membrane are bonded with a controlled separation distance of about 200 nm. Alignment markers are now visible by an electron beam and allow for standard processing of the InP membrane. The basics of techniques used for patterning the III-V membrane are first briefly introduced and then used in the frame of the work.

3.4.1 Basic techniques for membrane patterning

3.4.1.1 Electron beam lithography

Electron beam lithography is a common tool for patterning structures with minimum dimensions down to nanometre scale. The InP layer patterning is realized through two main stages: first, the etching mask is written in an electron-sensitive resist layer by a focused scanning electron beam; second, the mask pattern is transferred by dry etching techniques into the underlying layer.

During this work, two types of electron-sensitive layers were employed – positive tone photoresist [Reichmanis 1989], PMMA (polymethyl methacrylate[9]) and negative tone one, HSQ (hydrogen silsesquioxane[10]).

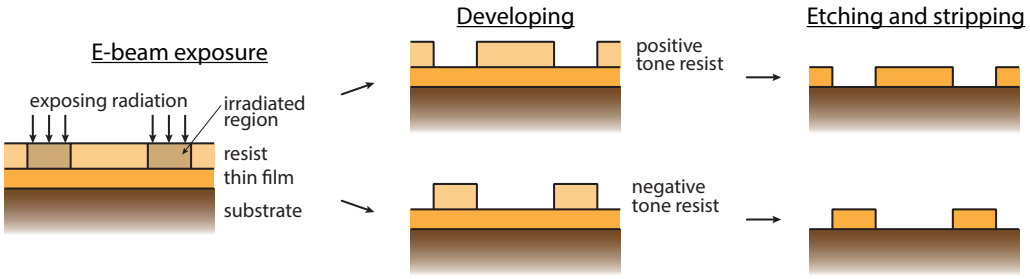

Figure 3.10: Schematic of the lithographic process with the resists of two tones.

Difference between these two types of resists (Fig. 3.10) lies in the effect produced by the electron beam on their chemical structure. Depending on tone, either the exposed area (positive tone) or everything but this area (negative tone) is removed during resist

[8] http://www.microchem.com/pdf/ebr.pdf
[9] http://www.microchem.com/pdf/PMMA_Data_Sheet.pdf
[10] http://www.dowcorning.com/content/publishedlit/XR-1541_E-Beam_resist.pdf

development. We take advantage of these two types of resists to simplify the process of mask transfer into the InP membrane layer. Subsequent etching and stripping then reproduce the obtained pattern into the thin semiconductor layer.

This lithography technique requires relatively long exposure times in order to get nanometric resolution. The particularity of the structures being studied in this work is that from one side, they contain photonic crystal lattices requiring high mask writing resolution, and from another side, each PhC lattice has in its surrounding mesa structures, composed of μm-scale blocks, which can be processed with a lower resolution since this doesn't influence the device characteristics required for our application. These particularities are taken into account and the lithography is thus split into two runs.

The PhC lattice – optical component of our device – is exposed and further etched with the PMMA positive tone resist. The processing of the surrounding mesa structures is more advantageous with another kind of resist – a negative tone one, HSQ [Namatsu 1998; Olynick 2010], which can be used directly as a hard mask for dry etching. Fabrication of these two parts (PhC lattice and mesa) is described in more detail in two following Sections (3.4.2 and 3.4.3).

3.4.1.2 Dry etching with CCP-RIE and ICP-RIE plasma

Another technique required for patterning the InP membrane, is the dry plasma etching. The transfer of layout patterns into a membrane layer has to fulfil some requirements, such as low roughness of etched material, high verticaliy of sidewalls, high fidelity of pattern dimensions etc.

The plasma used in this process consists of a partly ionized gas, in which the ionization rate is maintained through a constant supply of energy. The plasma is being created by a radio frequency (RF) field and contains the ionic species together with some radicals that chemically react with the material one wishes to etch.

RF field is created between two electrodes, in consequence, it exists a continuous difference of potential between them. This difference of potential will constantly accelerate reactive ion species towards the surface of the sample. The etching process consists thus in a chemical reaction between active species and the material to etch, while ion bombardment enhances or promotes this reaction (Fig. 3.11, middle). By adjusting the chamber pressure, densities and ratios of species, the bias voltage, coil power etc., these two actions can lead to an optimal combination of two distinct mechanisms – purely physical and purely chemical one. These two mechanisms could also be employed independently for the etching purposes, however, they present alone considerable disadvantages.

From one hand, for a purely physical etching (Fig. 3.11, left) the ion energy mechanically ejects substrate material. This process is highly directional along the axis of ion acceleration and is thus anisotropic, nevertheless, it is little selective between different materials and typically has low etching rates. Low selectivity corresponds to comparable etching rates for mask and membrane layers. The mask layer is quickly removed and thus the major process drawback is that it does not allow to obtain high aspect etching ratios.

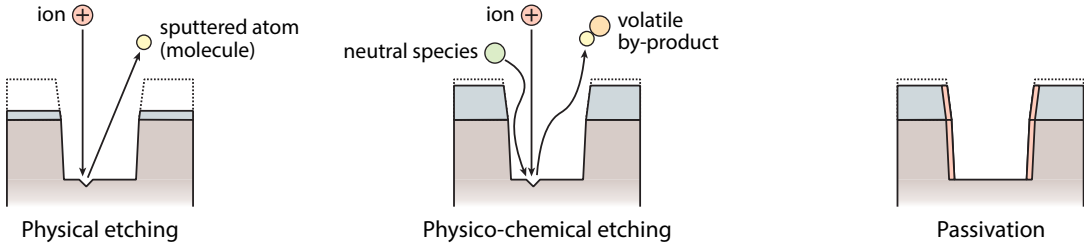

Figure 3.11: Mechanisms involved in the dry plasma etching.

From another hand, a purely chemical etching is, in contrast, highly selective and has high etching rates. Its drawback is the highly isotropic etched profiles, thus making impossible the fabrication of high-quality periodic structures with vertical sidewalls. The combined use of these two basic mechanisms, known as physico-chemical (Fig. 3.11, middle), or ion induced etching, conversely benefit from the high anisotropy of physical etching and good material selectivity of chemical etching. We will also make use of an optional mechanism to ensure anisotropic etch profiles: the sidewalls can be passivated (Fig. 3.11, right) by a deposition of thin protective layer during the etching process. This permits to limit the chemical reaction with the etched material only at the bottom of the openings, while the flanks being protected by the passivation layer.

Dry plasma etching systems can be divided into two process types -corresponding to low and high ($> 10^{11}$ cm^3) densities of ion species. In a basic low density set-up, the plasma is created between two electrodes and the sample is placed on the bottom one. In such system, named capacitively coupled plasma reactive ion etching (CCP-RIE), the density and the energy of ions both depend on the RF power. As a consequence, they can not be controlled independently. The advantage of this kind of reactor is the possibility to etch a wide range of materials, such as dielectric, silicon-based, III-V, sputtered metals and more. For this reason we employ it for all the dry etching processes during the fabrication of our samples, excluding the patterning of III-V layer. However, in order to obtain relatively high ion flow and gas concentrations, an important bias value is required. This high voltage accelerates efficiently the charged particles towards the surface, leading to a rapid mask degradation (as the contribution of physical etch is high).

In order to operate within a high ion density, another technique is used, namely inductively coupled plasma RIE (ICP-RIE). In such technique the density and the energy of ion species can be tuned independently via ICP and RF power setting, respectively. The ion acceleration is achieved, as in the CCP-RIE system, via the capacitive coupling between two separated electrodes. Ion density is controlled by an inductive coupling mechanism, which offers an additional degree of freedom.

3.4.2 Photonic crystal lattice fabrication: optical component

3.4.2.1 Pattern transfer by e-beam lithography

Fabrication of the optical component of our device demands high quality transfer of an array of circular shapes (with diameter of about 200 nm and period about 400 nm) into the active layer. It should satisfy the main requirements for achieving the expected optical characteristics (resonant wavelength and optical losses): high positioning resolution is needed for keeping constant the lattice period, hole radius and shape over the whole device. These requirements apply both to the electron beam lithography and to the dry etching stages; moreover, they should be fulfilled at the level of all involved intermediate layers (electrosensitive layer, hard masks and semiconductor membrane).

First main stage in the pattern transfer to a sensitive resist through an electron beam insolation (Fig. 3.13a–c). To achieve a high quality transfer, particular attention is given to several aspects of electron beam insolation.

First crucial point in this path is the resolution of a written pattern. The mask layouts, created by use of a specialized software (Tanner EDA *L-Edit*[11]) and suited for the e-beam lithography, are essentially composed of arrays of vector shapes with the infinitely high resolution of the latter. The electron beam, in turn, can only move along the defined rectangular grid during the pattern insolation, hence the vector mask is rasterized on a given mesh. An example of such a discretization is given on Fig. 3.12. The circle of 100 nm radius, which is typical for our optical components, is translated onto a square mesh of different sizes. As can be seen, with the resolution of about 100 pm – 1 nm the mask layout rasterization does not limit the quality of the fabricated device in case of equal or higher internal resolution of electron beam system.

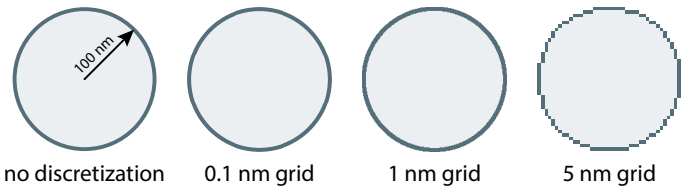

Figure 3.12: Discretization of a 100 nm radius circle with different rectangular grids.

Second important point concerns the electron beam displacement procedure during the insolation process. Usual field-emission systems [Stepanova 2011] employ a magnetic deflection coil to position the electron beam spot on a defined stationary location; this is done within a field area depending on the particular system design. The e-beam system used during this work (Leica/Vistec EBPG 5000+) has a working field with dimensions of 160 × 160 μm^2 at its highest accessible writing resolution (1.25 nm). As it holds for every Gaussian beam, its in-plane cross-section (spot) will change from circular in the centre of the working field to elliptical in its corners. This, in turn, will lead to distorted

[11] http://www.tannereda.com/l-edit-pro

pattern writing closer to the exposure field borders, which is strongly undesirable as it decreases the homogeneity of holes dimensions and shapes in the PhC lattice. With these considerations we reduce the exposure field to the dimensions of a single PhC lattice within our sample (typically $10 \times 20\ \mu m^2$ maximum). Thus, the stage sample holder would move to match the exposure field centre with the one of each of the PhC lattice, ensuring a high reproducibility of the resulting patterns within the sample.

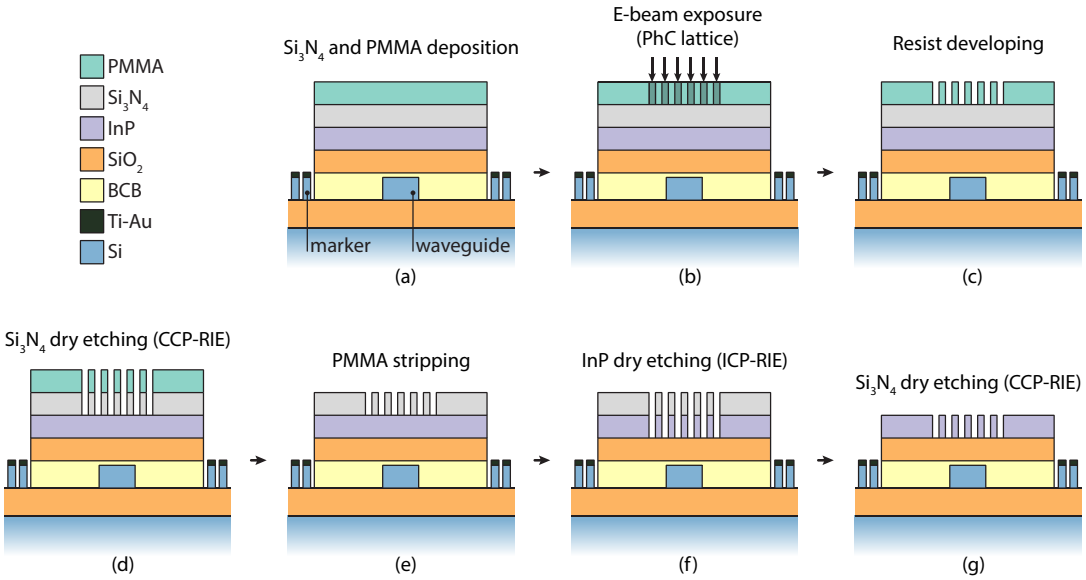

Figure 3.13: Process flow for patterning of the InP layer with a 2D photonic crystal lattice using positive PMMA resist.

Last issue is related to the alignment precision between the patterns insolated during two or more different electron beam lithography runs. During each run, the positioning system aligns the set-up to the same relative reference points using the special markers (discussed in Section 3.3). These markers permit us to correct for the rotation, shift, and scaling between the SOI and InP layers; however, positioning errors still exist due to the imperfections of the employed system (e.g., the finite precision on the detection of a marker dimension and absolute position). It was demonstrated [Karle 2010], that for the markers size of $10 \times 10\ \mu m^2$ (as the ones used in this work) in our lithography system, the mean statistical alignment offset between a pattern in InP and a Si waveguide is (26 ± 19) nm. The work also shows that tight mutual lateral positioning control between the Si waveguide and the PhC cavity is required on a scale of about 100 nm for ensuring the designed optical coupling performances between these two elements. In consequence, this issue is not a limiting factor with the alignment and positioning system employed in this work.

The whole process flow schematic is represented in Figure 3.13. Once every aspect of electron beam lithography presented above is mastered, we insolate the photonic crystal structure of the future device (Fig. 3.13b). A PMMA A7 resist is spin-coated (4000 rpm

speed, 4000 rpm/s acceleration, 30 sec time, resulting thickness 450 nm) and soft-baked for 15' in the oven at 160 °C (Fig. 3.13a). With the use of positive resist only the holes area is exposed to the electon beam and will be further removed. The PMMA layer is developed in 1:4 solution of MIBK (methyl isobutyl ketone) in IPA by full immersion for 30 sec and followed by 15 sec IPA rinse, which efficiently cleans the obtained openings. Such a low concentration of MIBK solvent allows to preserve maximal resolution with the PMMA resist[12] (Fig. 3.13c).

3.4.2.2 Pattern transfer by dry etching

The pattern transfer between the PMMA layer and the InP thin film is accomplished through an intermediate 300 nm thick Si_3N_4 layer, deposited by PECVD (Fig. 3.13a). This Si_3N_4 layer is necessary because the PMMA layer is not hard enough to be used as etching mask in the ICP-RIE process. The photonic crystal lattice pattern is transferred (Fig. 3.13d) into the underlying Si_3N_4 layer by CCP-RIE dry etching in SF_6 gas atmosphere at low gas flow rate and at low RF power, which ensures proper etched profile (Fig. 3.14a) within the 300 nm thickness of silicon nitride. After this step, the PMMA layer is removed with an O_2 plasma (CCP-RIE etching); its remaining thickness is being constantly monitored with the built-in interferometry system, hence the etching process is stopped exactly when we reach the Si_3N_4 layer (Fig. 3.13e).

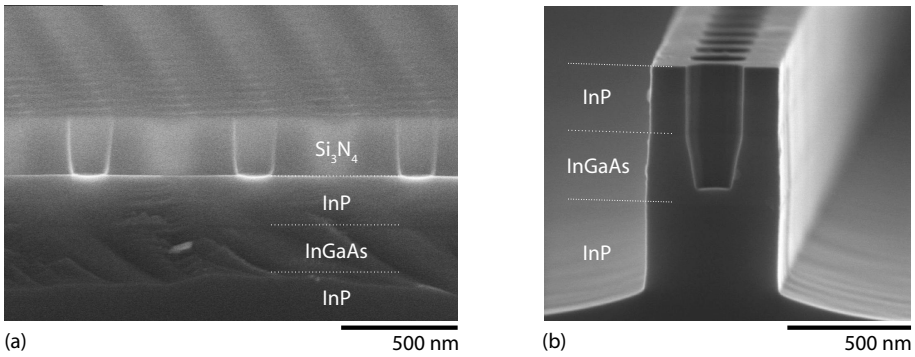

Figure 3.14: SEM picture of a photonic crystal lattice cross-section after its transfer into a Si_3N_4 mask (a) and into a InP layer (b).

The process allowing for etching high-quality photonic crystal structures in the InP membrane (Fig. 3.13f, 3.14b) was developed for the ICP-RIE reactor. The mixture of three gases – HBr, O_2 and He – is used at low pressure, which results in a long mean free path of the volatile by-products and thus speeds up their evacuation away from the etched surface. The III-V semiconductors family is generally effectively etched with halogen gases (F, Cl and Br). Bromine that displays the highest atomic mass, was chosen as it simply provides more energy for the physical component during etching. Oxygen is added in order achieve the sidewall passivation (Fig. 3.11, right) during the etching process; the

[12] http://www.microchem.com/pdf/pmma.pdf

lightweight He gas allows for the dilution of the gas mixture to the chosen ratios. The used ICP-RIE parameters are the following: ICP power 600 W, RF power 60 W, working pressure 0.5 mTorr, the gases ratio $HBr/O_2/He$: 10/0.6/30. The mask used during the etching of InP is a Si_3N_4 mask, which is subsequently removed by dry etching in SF_6 plasma (CCP-RIE) with the interferometric monitoring, as mentioned above (Fig. 3.13g).

3.4.3 Fabrication of mesa structures: mechanical component

Fabrication of the mesa structures upholding the membrane is less challenging, as it requires lower resolution. Nevertheless, it still needs the same high precision on its relative positioning with respect to the waveguide and photonic crystal.

The use of negative electron sensitive resist is here more suitable, thus the HSQ flowable oxide is employed (see Fig. 3.16). It allows for considerable reduction of electron beam exposure time comparing to the positive tone resists and moreover does not require any intermediate layer (as Si_3N_4 for the PMMA process, mentioned above). Furthermore, the HSQ resist is fully compatible with our process for III-V dry etching and hence there is no more need in the intermediate Si_3N_4 layer. The process flow (Fig. 3.15) is thus considerably simplified comparing to the one used for photonic crystal (Fig. 3.13).

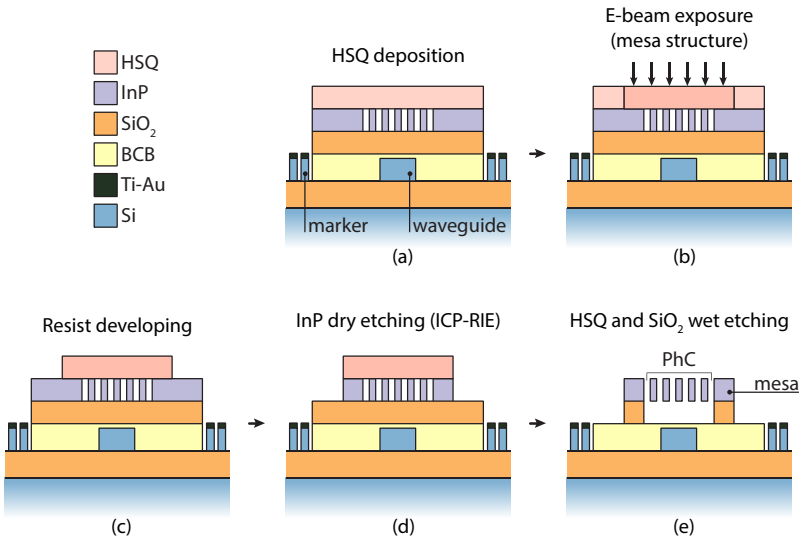

Figure 3.15: Process flow for one-step patterning of the III-V layer with mesa structure using HSQ resist.

To ensure a good adhesion of the resist on the InP layer, a dedicated surface preparation is required. It relies on a 2 min RIE O_2 plasma cleaning and subsequent dehydration prior to the resist deposition by soft-baking for 5 min in the oven at 160 °C. The HSQ layer (FOx–12 flowable oxyde, Dow Corning) is then spin-coated (1000 rpm speed, 1000 rpm/s acceleration, 30 sec, resulting thickness around 160 nm) on top of InP and baked for 30 sec at 90 °C on the hotplate (Fig. 3.15a). Next (Fig. 3.15b), the electron beam insolates

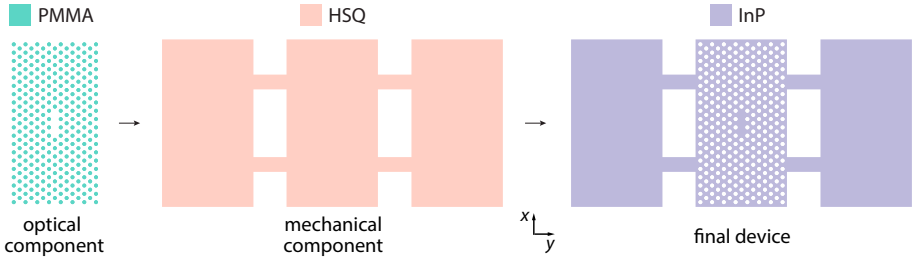

Figure 3.16: Schematic of the insolation patterns used for optical and mechanical components with the corresponding materials, as sdescribed in Sections 3.4.2 and 3.4.3.

the HSQ layer with a pattern of corresponding to the mesa structures. After exposure the resist is developed in an AZ 400K : H_2O solution (1:4 by volume) for 1 min (Fig. 3.15c). Subsequent InP layer dry etching with HSQ mask follows the same ICP-RIE process as described in previous section for silicon nitride mask (Fig. 3.15d). Finally, the resist is stripped by wet etching in diluted AF (1:9 with H_2O). This solution etches also the silica sacrificial layer below InP (Fig. 3.15e) and thus the structures get suspended, assuming 10' of etching time per 200 nm of SiO_2 layer thickness.

In addition to simple mask fabrication and transfer to InP layer, the HSQ resist also allows to obtain the low sidewall roughness and good verticality, which in turn ensures high sidewalls quality in the InP layer and can as well be employed for the fabrication of photonic components with high optical qualities [Bazin 2014].

3.5 Control of membrane – waveguide distance

3.5.1 Critical point drying

The following step, after etching of the membrane, consists in the sample drying after the InP layer underetching step. This final step is used to suspend membranes by removing the sacrificial layer of silicon dioxide. However, the effect of capillary adhesion, occurring during natural water drying after wet etching, made it impossible to ensure correct suspension of the membranes.

When a fluid passes through the transition from liquid to gaseous state, this happens at a finite speed, while the amount of fluid decreases. When this happens in a heterogeneous environment, the surface tension in the liquid induces traction on any solid structure with which the fluid is in contact, that is to say with the membrane one wants to suspend. During the removal of the gas-liquid mixture, the membrane tends to deteriorate and bend, even to collapse onto the SOI wafer under the surface tension (see Fig. 3.17a).

To avoid this phenomenon, the sample can be dried via an alternative way without crossing the liquid-gas transition. We used the critical point drying[13] (CPD) technique [Cleland 2002]. Right after the structured InP layer gets suspended with the removal of

[13]Sometimes also referred as supercritical drying.

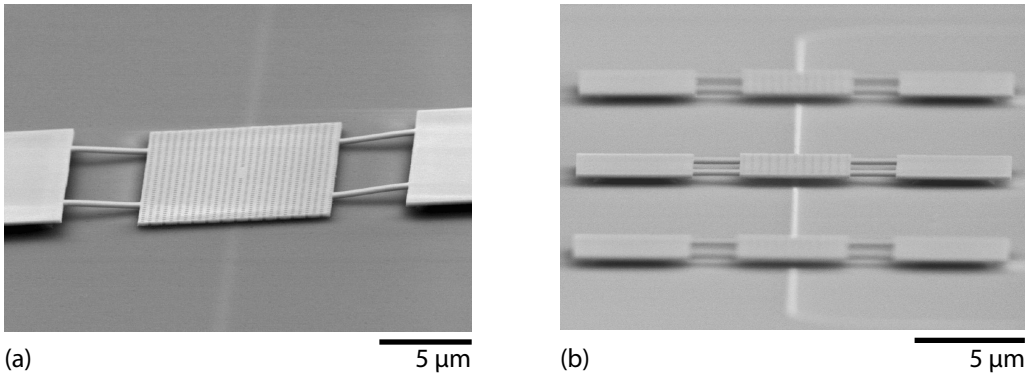

Figure 3.17: An example of membranes underetched with a wet etching and dried normally (a) and with the critical point drying technique (b).

silica sacrificial layer, the sample is soaked in water to remove the eventual residuals of etching solution (and thus completely stop it) and is immediately transferred into a IPA bath, so that the fluid in between the membrane and the substrate is always conserved. The critical point drying is performed next in an automated environment.

The critical point (see Fig. 3.18) of a liquid/gas system (e.g. water/steam, liquid CO_2/gaseous CO_2) is associated with a critical temperature and pressure, where the liquid and vapour phases coexist (in the same way, all three phases do at the triple point). Above the critical temperature, the system is always gaseous and cannot be liquefied by the application of pressure. The transition from liquid to gas at the critical point takes place without an interface because the densities of liquid and gas are equal at this point. If the sample is totally immersed in a liquid below its critical point and if the liquid is then taken to a temperature and pressure above the critical point, the sample ends up

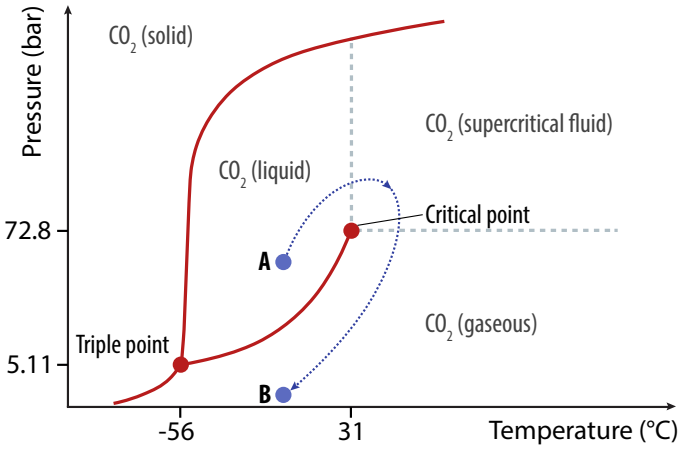

Figure 3.18: Phase diagram for CO_2 showing the triple and critical points. Adapted from [Pandithage 2012] and [Cleland 2002]. The CPD procedure follows the A–B curve for pressure-temperature conditions to avoid direct passage from liquid to gas state.

immersed in gas (i.e., dried) without being exposed to damaging surface tension forces.

The temperature and/or pressure of critical point for water and the solvents like acetone or IPA are much higher than the ones for carbon dioxide, which explains its common use in the CPD systems. Isopropyl alcohol can still be used as an exchange fluid (to bring a sample after the wet etching step inside a CPD machine), while the liquid carbon dioxide is used as a working fluid. A sample is thus dried by submerging it into pressurized CO_2 liquid at room temperature (point A in Fig. 3.18), heating and pressurizing the transitional liquid so that it passes around the critical point (dotted blue line), and then cooling and releasing the pressure to return the sample to room temperature and atmospheric pressure in the vapour phase of CO_2 (point B). In such manner we could make the InP membranes suspended at a height of about 200 nm above the SOI waveguide circuit (Fig. 3.17b).

3.5.2 Experimental determination of cured BCB layer thickness

As seen in Chapter 2 (see Section 2.1.3.4), a precise control of distance between waveguide and membrane is required for obtaining the desired optomechanical coupling. In our experiments, the uncertainty on this distance mainly comes from the thickness of BCB layer on top of waveguide.

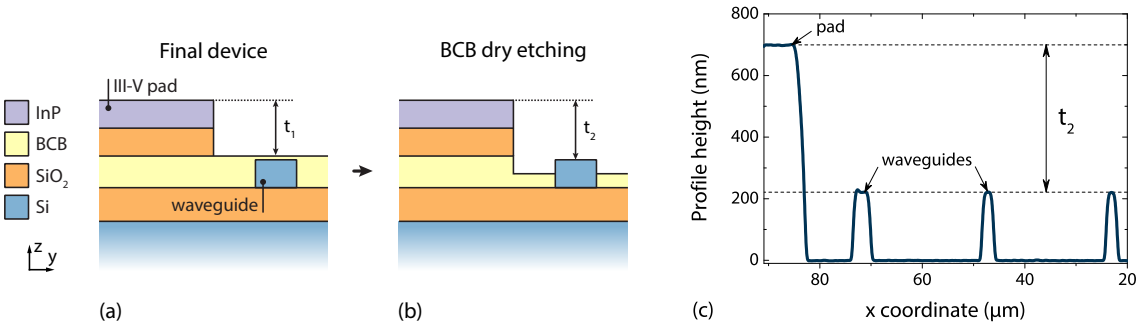

Figure 3.19: Experimental determination of the BCB layer thickness after wafer bonding.

The measurement of the added thickness of cured BCB layer after the wafer bonding is carried out in the following manner (Fig. 3.19). After the complete processing procedure, the sample contains an array of InP membranes, each of them being anchored to two suspension pads. The InP layer has been removed on most of the sample surface, uncovering the Si waveguides outside the mechanical InP pads. Moreover, the BCB glue layer is not removed during the SiO_2 wet etching, leaving the thin film on top of each waveguide.

Hence, the total height of the suspension pad (Fig. 3.19a) is the sum of InP and sacrificial silica layer thicknesses (260 and 200 nm, respectively). By measuring with a profilometer (Dektak 8) the difference between two areas (t_1 on (Fig. 3.19a)), we can estimate the pad height. Next, the cured BCB is dry etched for 1 min in RIE SF_6/O_2 plasma in order to partly uncover the Si waveguide circuit (this gas mixture does not etch the InP membrane). Another profile measurement (t_2 on (Fig. 3.19b,c)) is performed in

order to determine the wanted quantity $t_{\mathrm{BCB}} = t_2 - t_1$, typically giving a value of about 30 nm for the BCB dilution ratio and bonding process parameters described in Section 3.2.3.

3.6 Summary

In summary, this chapter provides the description of the fabrication of our InP optomechanical platform heterogeneously integrated on SOI circuit. Principal steps include adhesive bonding of the SOI and III-V semiconductor substrates, preparation of high-contrast alignment markers for electron beam lithography, patterning of optical (photonic crystal lattice) and mechanical (mesa structures) device components and removal of the sacrificial layer in order to suspend the PhC membrane. Many features have been implemented into the process flow in order to solve the major issues, including the obtention of high-Q optical cavities, aligned to the circuit of access waveguides, and the proper suspension of the PhC membranes over an air gap of few hundreds of nanometres. The achieved precision of alignment of the InP suspended PhC cavities with respect to SOI circuit is $\leqslant$ 40 nm. Standard deviation of the resonant wavelength between PhC cavities with the same geometrical parameters is about 2 – 3 nm on the whole sample (typically several hundreds of devices). The InP layer patterning was optimized by making use of positive tone PMMA and negative tone HSQ resists, allowing to satisfy different requirements for the optical and mechanical device parts, correspondingly. The critical point drying technology has allowed us to achieve the suspension yield 100 % for the air gaps about 200 nm high and for the PhC slab membranes of 10×20 $\mu\mathrm{m}^2$ lateral dimensions.

Embedded active layer allows next to experimentally verify the operating wavelength of the fabricated cavities, whose luminescence will be used to align the dedicated set-up for evidencing optomechanical coupling effects. This set-up will be described in details in the following chapter.

Chapter 4

Experimental characterisation of hybrid platform

Contents

In this Chapter we describe the experimental characterisation of the optical and mechanical properties of our device, as well as the optomechanical couplings and related effects. Two geometries have been experimentally explored: suspended photonic crystal mirrors and integrated PhC slab cavities over a SOI waveguide. In the first, non-integrated – photonic crystal mirror – configuration and without an external cavity, mode mapping is accomplished through the measurements of the low-frequency mechanical spectra, further

compared to the simulations detailed in Chapter 2. The impact of the suspension bridges geometry on the clamping losses is also investigated alongside with the low-temperature studies of intrinsic losses. Next, we present the experimental investigation of the hybrid integrated platform, which includes a defect cavity, embedded into a suspended PhC slab membrane and evanescently coupled to an access SOI waveguide. In particular, the measurements of intrinsic and external contributions to the dispersive and dissipative optomechanical coupling mechanisms are performed, revealing the experimental limitations for their differentiation compared to the numerical approaches. We perform a calibration of mechanical displacement spectra using an external reference, which is used as well to experimentally determine the total optomechanical coupling strength. Finally we show some preliminary results on the operation of such integrated platform in the non-linear optical and mechanical regimes, and on the transduction from optical to mechanical bi-stable behaviour.

4.1 Identification of mechanical modes

Current Section reviews the experimental methods for assigning the mechanical modes to the corresponding simulated mode profiles in the system with multiple eigenmodes whose relative frequency splitting changes with minor changes in clamping geometry. In this study, first three modes in order of their apparition in the mechanical spectrum are considered; the method can be then extended to an arbitrary number of resonances in the similar system. For this purpose we fabricate a device, consisting of a suspended PhC membrane, designed as a high-reflectivity mirror at normal incidence around 1064 nm wavelength, as described in Section 2.1.2. The mode identification and mapping is based on the simulated eigenfrequency evolution when changing one parameter of the clamping structure at a time, given in Section 2.2.1.2.

Mode assignment to its corresponding displacement field $\vec{Q}$ spatial distribution is performed by experimentally measuring the frequencies of the mechanical modes. Quality factor Q_{m}, relative to the phonon lifetime inside our mechanical oscillator, is also measured in order to estimate the clamping and intrinsic losses for each particular vibrational mode.

Mechanical eigenmodes of the highly reflective membranes were probed in a conventional Michelson-like interferometric set-up, as illustrated in Fig. 4.1. The sample containing a set of suspended PhC mirrors with varying dimensions of clamping bridges is mounted onto the piezoelectric actuator stack (PI Ceramic, operation frequencies up to $0 - 3$ MHz). The ensemble is then put inside a cryostat chamber with an optical access, able to work with Helium-4 (^{4}He) filling, which gives us access to a working temperatures range from about 4 to 300 K and working pressures down to $\lesssim 10^{-5}$ mbar. PhC membrane is used as a moving end-mirror in one of the optical arms of Michelson interferometer, the another arm being terminated with a high-reflectivity fixed mirror, acting as a local oscillator.

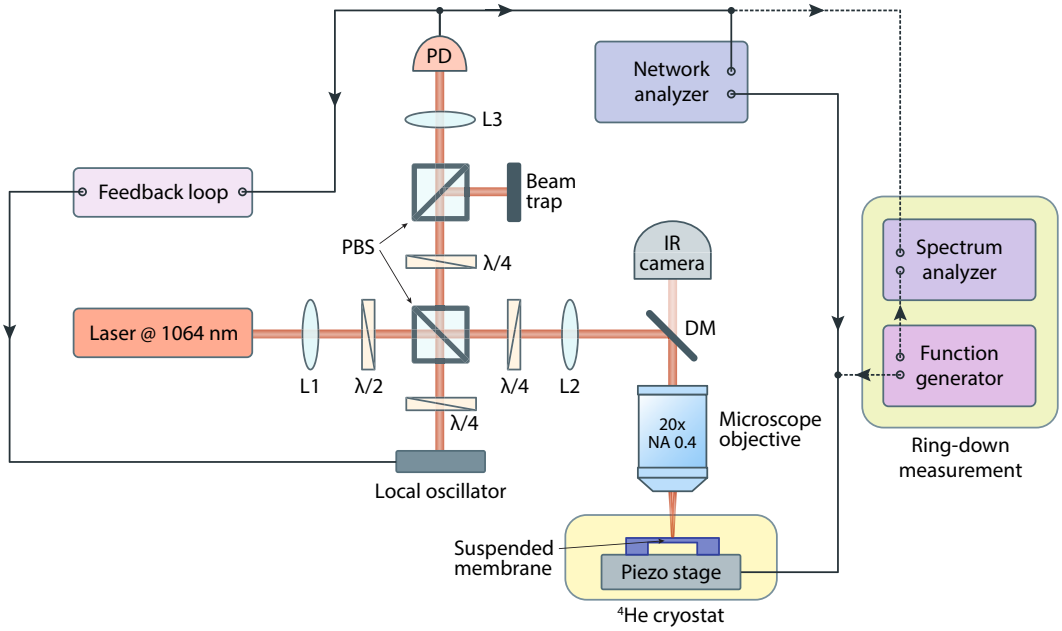

Figure 4.1: Schematic view of the experimental Michelson-like interferometric set-up for optical readout of mechanical motion. Light path is represented in red, electrical wiring is represented in black. (PBS – polarizing beamsplitter, PD – photodiode, DM – dichroic mirror, IR – infra-red, L – lens, NA – numerical aperture.)

A light beam of neodymium-doped YAG laser operating at 1064 nm wavelength is sent in the interferometer. It is split into two orthogonal linear polarizations by a half-wave plate and a polarizing beamsplitter (PBS)[1].

Therefore, the light reflected by the PBS is directed to the local oscillator, whereas the transmitted part is focused with the help of a microscope objective on the surface of chosen PhC mirror within the sample. In each of the arms the light is reflected from the respective end-mirror and acquires a phase shift of $\pi/2$ while propagating in each arm due to the presence of a quarter-wave plate. Yet, their interference can not be achieved while emerging from the interferometer since their polarizations are still orthogonal. An additional quarter-wave plate and a second PBS are employed to overcome this mismatch, and the interference pattern is finally recorded on a photodiode (Thorlabs PDA36A-EC, DC to 10 MHz bandwidth). The choice of the membrane to address and the corresponding beam alignment are verified by means of infra-red (IR) imaging. An IR camera (Allied Vision Goldeye P-008 SWIR) is placed in front of the microscope objective. A point broadband (partially covers visible and near infra-red ranges) light source is placed in the close proximity of the sample (not shown in Fig. 4.1), covering a sufficiently large working area with diffused light, subsequently imaged with an IR camera. A small part of the laser beam intensity passes through the dichroic mirror after being reflected from the substrate

[1] A PBS would only transmit light with linear vertical polarization while the linear horizontal one is being reflected.

surface, allowing to control the laser alignment on the sample surface with respect to the studied membranes array.

Readout of the membrane mechanical spectrum is performed with a network analyzer (Agilent E5061B), which drives the piezoelectric stack and reads out the response from the PD. The need for external actuation of the membrane motion is imposed by the sensitivity of the employed interferometric technique, which showed the ability to measure the mirror displacements starting from about few tens of nanometres. Additional drawback of a free-space interferometer set-up consists in its high sensitivity to any mechanical vibrations, which may induce spurious variations of the optical path of the same order of magnitude as the displacement of the actuated membrane. In order to exclude this noise contribution from our measurements a feedback loop is introduced. The local oscillator mirror (Fig. 4.1) was mounted on another piezoelectric stack, driven by the feedback electronics. An error signal from the photodiode output is fed to the mirror actuator to compensate the optical path discrepancy caused by the spurious mechanical vibrations. The local oscillator is thus locked to record the interferences on the photodiode at their maximum contrast and reach the ultimate set-up sensitivity, allowing to detect the displacements of about nanometre.

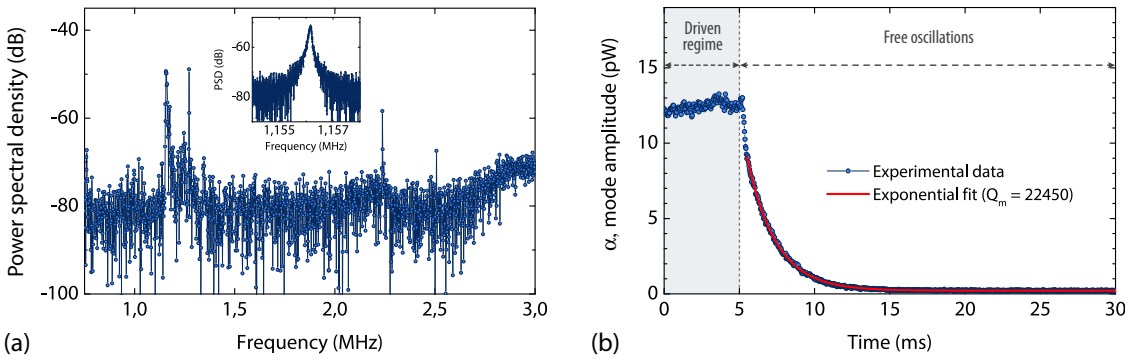

Figure 4.2: (a) Example of a low-frequency mechanical spectrum, recorded on a 20×10 μm^2 membrane, suspended with four 1×4 μm bridges, read out in the Michelson interferometer set-up within the actuation range of the piezoelectric stack. Inset: close-up on the fundamental mechanical mode, recorded at lower driving power (0 dB at the exit of the network analyser). (b) Example of a ring-down measurement of the mechanical quality factor Q_m for a fundamental membrane mode from (a) at $T_b = 4.4$ K with the exponential fit using Eq. 4.1. The external membrane excitation has been switched off at $t = 5$ ms on the shown time scale.

Figure 4.2a illustrates a typical example of the membrane low-frequency mechanical spectrum under external actuation, captured by the depicted interferometric set-up. Variation of the background level along the scanning frequency range is explained by a variable response of the used piezoelectric stack. The membrane under study has dimensions of 20×10 μm^2 and is suspended by four lateral 1×4 μm bridges (displaced from the mem-

brane middle by $b_d = 5.9$ μm, see Fig. 2.15). The experiment is carried out at low pressure ($P < 10^{-3}$ mbar) to avoid air damping of membrane motion. The working temperature for the data, provided in Figs. 4.2a,b, is $T_b = 4.4$ K. A close-up of the fundamental mode spectrum (inset in Fig. 4.2a), recorded at lower driving power (-30 dB compared to the full spectrum, taken with 0 dB output power from network analyzer, cf. Fig. 4.1), shows a Lorentzian-like shape, as it can be expected for the mechanical response of a harmonic oscillator.

As introduced before, the mechanical quality factor Q_m quantifies the dissipation of vibrational resonance and is directly related to the decay time of free membrane oscillations. Alongside with the conventional fitting of the recorded Lorentzian shape at the mechanical resonance frequency, another method for Q_m estimation exploits the forced oscillations regime. This method, so-called ring-down technique [Nawrodt 2008], is particularly suited for the high-Q resonances, giving more precise values of the measured quantities. The membrane is excited resonantly via the piezoelectric stack inducing an inhomogeneous sinusoidal electrical field oscillating at the resonant frequency of the mechanical mode of interest Ω_m. These measurements imply to work in the linear regime of excited mechanical oscillations, which corresponds to a low driving power of the used piezoelectric stack (approximately at 0 dB or below).

During a ring-down measurement the network analyzer is removed and the piezo stage driving is performed with a high-frequency function generator (Agilent 81150A), providing a sine modulation at the resonance frequency $\Omega_\mathrm{m}/2\pi$. Readout of the membrane response is now performed by a spectrum analyzer, set to zero span at $\Omega_\mathrm{m}/2\pi$ frequency (Fig. 4.1). A low-frequency square signal is used as an envelope for the sine modulation in order to switch between free running and forced oscillation regimes; the duration of free run is chosen so that the oscillations have enough time to fade out before the excitation is switched on again. At the same time this square signal is fed to the spectrum analyzer, allowing to start the acquisition at the beginning of free oscillation period by a negative edge triggering (corresponds to a grey dashed line in Fig. 4.2b). After reaching a sufficiently high amplitude α_0, the excitation is switched off and the subsequent ring-down is recorded for the free-running amplitude α at the resonance frequency, recorded in the interferometry set-up. The free-decaying amplitude $\alpha(t)$ follows an exponential law

$$\alpha(t) = \alpha_0 \times \mathrm{e}^{-t/\tau}, \tag{4.1}$$

where τ is the characteristic ring-down time, so that $Q_\mathrm{m} = \pi\tau \cdot \Omega_\mathrm{m}/2\pi$. For linearly scaled recorded power spectral density (PSD) of the mechanical mode amplitude α an exponential fit of the experimental ring-down data is performed as shown in Fig. 4.2b for the fundamental mode from Fig. 4.2a, measured at cryogenic temperature $T_b = 4.4$ K, that gives $Q_\mathrm{m} = 22450$.

The two described procedures for measuring the mechanical mode eigenfrequency Ω_m and the corresponding quality factor Q_m will be next used through the mode identification procedures, described in the following Sections.

4.1.1 Impact of suspension bridge position

The positions of the suspension bridges b_d, relative to the membrane middle along x axis (see Fig. 2.15), as discussed in Section 2.2.1.2, impacts the spatial displacement field distribution of the flexural modes and eventually may reduce the clamping losses for the specific mode. Eigenfrequencies of first three membrane modes in the MHz range follow different trends according to b_d parameter change, as predicted by simulations and traced in Fig. 4.3a (solid lines). The device, considered here, consists of membranes with the dimensions that correspond to ones used in experiments throughout previous Section (4.1), i.e., 20×10 μm^2 $\times$ 260 nm, however, with changing parameters for the position of suspension bridges.

Using the experimental set-up described above, we can trace this evolution and assign the corresponding mode profile to the different detected peaks in frequency domain.

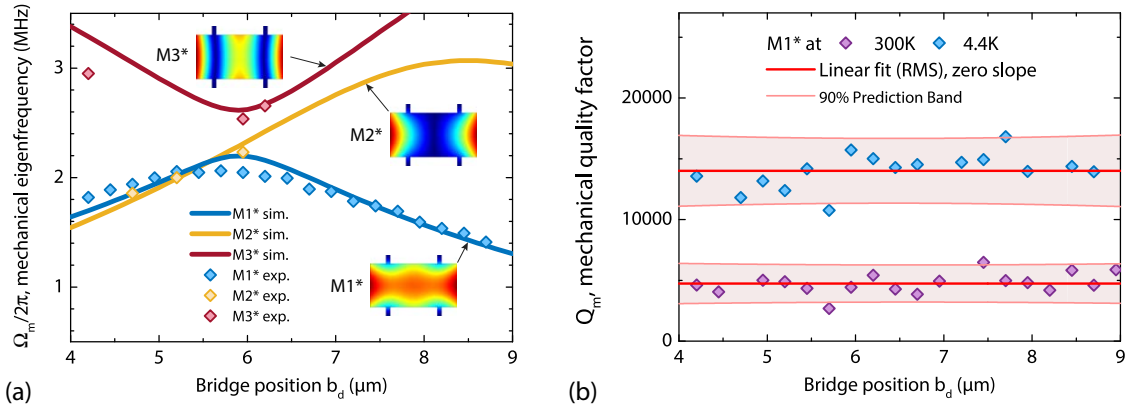

Figure 4.3: (a) Experimentally measured (diamonds) versus simulated (solid lines) eigenfrequencies $\Omega_\mathrm{m}/2\pi$ of the first three flexural modes of the suspended PhC membrane (parameters: $m_x = 20$ μm, $m_y = 10$ μm, $b_x = 1$ μm, $b_y = 2$ μm). Insets – simulated displacement field profiles of the corresponding modes for bridge position $b_d = 5.9$ μm. (b) Mechanical quality factors Q_m of M1* mode, measured at T_b of 300 K (violet diamonds) and 4.4 K (blue diamonds) with the corresponding linear fits (solid lines).

The interferometric detection technique relies on the PhC membrane operation as an end-mirror, therefore the best displacement sensitivity is achieved for the fundamental membrane mode M1* – as its displacement profile $\vec{Q}(\vec{r})$ is almost homogeneous across the membrane surface (cf. inset in Fig. 4.3a), which in turn introduces the same phase difference across the cross-section of the reflected probe beam. Flexural modes at higher frequencies, considered in the above-mentioned simulation, which possess stronger $\vec{Q}(\vec{r})$ inhomogeneity (cf. Fig. 2.17), are less likely to be detected. As a result, we were able to collect trustworthy data for the eigenfrequency evolution of M1* (blue diamonds in Fig. 4.3a) for all of the clamping bridge positions b_d from the studied sample (from 4 to 9 μm), whereas the unambiguous identification of the modes M2* and M3* (yellow and red diamonds, correspondingly) was possible for only few of the investigated devices.

Simulations of the mechanical eigenfrequency in Section 2.2.1 considered both of the suspension pads (cf. Fig. 2.15) as fixed constraints, whereas in the real samples they are partially under-etched, so that few microns of the pad from each side are suspended. This impacts the resonance frequency of the flexural membrane modes, which depend on the clamping configuration, hence the above-mentioned undercut has to be and was taken into account for mechanical simulations in the present Sections. Comparison of the simulations, taking into account the mechanical properties of InP, as detailed in Section 2.2.1, the parameters a, r of PhC lattice and the undercut of suspension pads of real devices, with the measured data confirms that the fundamental flexural mode as well as the higher order ones follow the predicted trends and therefore can be distinguished by their frequencies. The discrepancies with the simulations can be explained by fabrication imperfections as well as by the deviation of undercut depth and shape (the suspended pad part in our simulations is considered as a rectangular block of length m_x (the one of membrane) and given depth, whereas in reality it may take arbitrary distorted shapes due to under-etching anisotropy of the sacrificial layer from one device to another). Nevertheless, for the optimum bridge attachment position $b_d = 5.9$ μm (cf. Section 2.2.1.2) the modes in the displacement spectrum can be unambiguously assigned to their corresponding profiles. We suppose that in the region where M1* and M2* frequencies are close (b_d values from 4 to 6 μm in Fig. 4.3a) the experimentally determined counterparts would obey the same spectral order. The attribution of experimentally measured frequencies in Fig. 4.3a was implemented using this assumption.

Optimization of the clamping losses for M3* mode, carried out in Section 2.2.1.2, could not be verified using this detection scheme due to the actuation bandwidth limitation of piezoelectric stack in current experimental set-up. To take advantage of good signal-to-noise ratio of the fundamental mode across all b_d variations, we studied instead the impact of b_d parameter and the sample environment temperature T_b on the intrinsic mechanical losses. The obtained tendency should generally apply for any of present mechanical modes of the device. Experimentally measured quality factors via ring-down technique for the fundamental M1* mode are represented in Fig. 4.3b for the bridge dimensions $b_x = 1$ μm (width) and $b_y = 2$ μm (length). Two characteristic regimes of operation were examined: room temperature $T_b = 300$ K (violet diamonds) and base temperature of a ^{4}He cryostat $T_b = 4.4$ K (blue diamonds). At lower temperature the intrinsic frictional mechanical losses decrease, following the phonon energy, which increases the measured total quality factors. This trend can be well observed in Figure 4.3b. If for fixed temperature we consider Q_m independent from the bridge position and perform the experimental data fitting, the deduced mean quality factor at room temperature is about 5000, whereas at 4.4 K it raises up to 14000, confirming the decrease of intrinsic losses. This value could be further increased, since in analogy with similar experiments [Schliesser 2009] we did not observe the saturation of Q_m curve when approaching the lowest temperature attainable with current set-up ($\sim$ 4 K), but requires making use of a dilution cryostat, allowing to reach lower bath T_b temperatures (few tens of mK).

4.1.2 Impact of suspension bridge length

Length b_y of the suspension bridges was also one of the optimization factors, identified in order to decrease mechanical clamping losses for the fundamental mode M1*, as described in Section 2.2.1.2. As seen in previous Section, the fundamental mechanical mode is the easiest one to detect using current interferometric set-up. Hence experiments on the Q_m dependence on bridge length b_y have been carried out on this mode M1*.

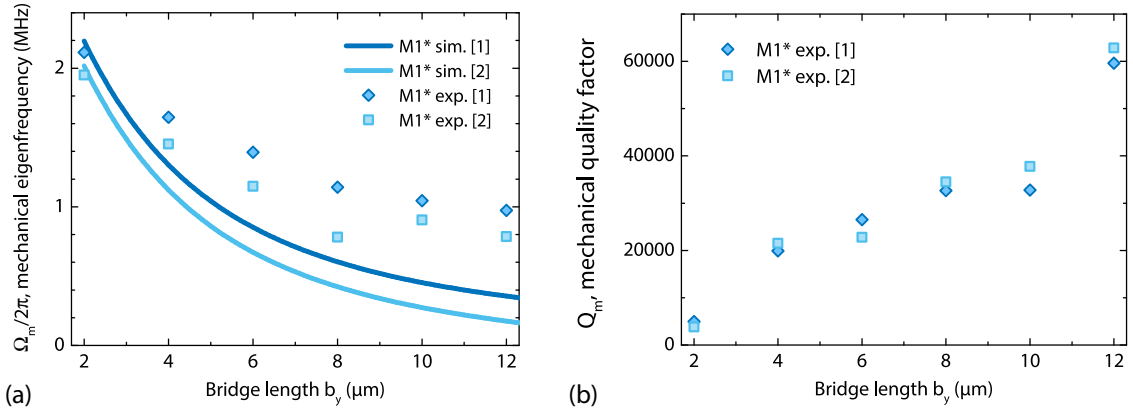

Figure 4.4: (a) Experimentally measured (points) versus simulated (solid lines) eigenfrequencies $\Omega_\mathrm{m}/2\pi$ of the fundamental flexural mode M1* of the suspended PhC membrane (parameters: $m_x = 20$ μm, $m_y = 10$ μm, $b_x = 1$ μm, $b_d = 5.9$ μm; PhC lattice filling factors: $\zeta = 0.97$ [1] and 0.90 [2]). (b) Corresponding mechanical quality factors Q_m of M1* mode, measured at $T_b = 4.4$ K.

Fabricated sample includes membranes with suspension bridges covering b_y length range from 2 to 12 μm, for which membrane suspension was technologically achieved. Standard InP membrane could not be suspended using bridges of more than 4 μm length. To complete this study, an InGaAs layer (of 10/20 nm thickness) was inserted in the middle of the membrane to increase its mechanical stiffness. This samples generation was not processed with critical point drying technique (cf. Section 3.17), but instead dried conventionally under atmospheric pressure. Measurements were carried out using the previously described ring-down technique at an environment temperature $T_b = 4.4$ K on devices with the identical membrane and bridges dimensions, but featuring two different PhC filling factors $\zeta = 0.97$ and 0.90 ([1] and [2] series in Fig. 4.4, respectively); these filling factors were as well taken into account for the mechanical simulations of the corresponding devices by representing a PhC slab membrane as a solid rectangular block with effective material density $\rho_\mathrm{eff} = \rho\zeta$, where $\zeta = a^2 - \pi r^2$ for the rectangular lattice arrangement (as it was also introduced in Section 2.2.1). Experimentally measured eigenfrequency Ω_m comparison with the corresponding simulated trends (Fig. 4.4a) reveals for both device series a good qualitative agreement, yet a quantitative underestimation of simulated Ω_m while increasing the bridge length b_y. Additional error can come from the approximation of the suspension pads undercut geometry, implemented for the mechanical eigenfrequency

simulation. Such a tendency can indicate that a more rigorous model should be used in the simulations, including an intermediate InGaAs layer with the corresponding mechanical properties and eventually suppressing the effective density while introducing the PhC fine structure. Implementation of this model, consequently, would increase the computational means required for simulation.

Characterization of the mechanical Q factor was performed via the ring-down technique on both device series. Obtained data (Fig. 4.4b) demonstrates an increase from about $Q_\mathrm{m} = 5 \times 10^3$ for $b_y = 2$ μm long suspension bridge to more than $Q_\mathrm{m} = 6 \times 10^4$ for $b_y = 12$ μm, i.e., more than an order of magnitude improvement. Eigenfrequency decreases by about a factor of 2, therefore the $Q_\mathrm{m} \times f_\mathrm{m}$ product, a figure of merit for a mechanical resonator in optomechanics[2], improves in the devices with longer bridges. As indicated by the measured trends (Fig. 4.4b), a further bridge b_y elongation could potentially enhance the membrane decoupling from the substrate, but is limited for the moment by fabrication constraints. Use of other materials with better mechanical properties could be also a possibility, since higher Young's modulus [Burek 2014] or additional induced tensile stress [Verbridge 2008] would allow for suspension of larger structures (up to few hundreds of microns experimentally demonstrated in both cases for the doubly-clamped resonators).

The identification of the mechanical modes alongside with the study of associated clamping and intrinsic losses allowed for a full understanding of the mechanical behaviour of our mechanical structures. In a second stage, such study has been extended to hybrid integrated devices. Consequently, the working bridge length of $b_y = 2$ μm was chosen. Another constraint comes from the design of SOI circuit: the distance between two adjacent waveguides is 25 μm, that is, from the middle of one membrane to the one of another. Assuming the membrane width $m_y = 10$ μm, the remaining length for suspension structure is 7.5 μm, which should include the bridges of length b_y and a suspension pad. For the above-mentioned reasons, we use 2 μm long bridges in the integrated configuration.

4.2 Optical and mechanical spectroscopy on the integrated platform

Current Section describes the experimentation of optomechanical devices comprising a suspended PhC membrane with an embedded defect cavity, coupled to an integrated SOI waveguide. Optical and mechanical spectroscopy of the corresponding types of resonances is first introduced and subsequently used for more complex optomechanical measurements. In such latter devices, the suspension bridge was fixed to 2 μm length for the main reason: the membrane did not include the InGaAs thin layer in view of increasing its stiffness.

Two series of experiments have been implemented: first, the cavity resonance wavelength λ_0 is measured by photoluminescence (PL) spectroscopy and confirmed by measure-

[2]The "$Q \times f$" product is a direct measure for the degree of optomechanical system decoupling from its thermal environment. Specifically, $Q_\mathrm{m} \times f_\mathrm{m} = Q_\mathrm{m} \times \Omega_\mathrm{m}/2\pi > k_\mathrm{B} T_b/\hbar$ is the condition for neglecting thermal decoherence over one mechanical period of mechanical oscillation [Aspelmeyer 2013].

ment of the SOI waveguide transmission around λ_0. Having established an optical access to the defect cavity via the waveguide link, we exploit the resonance deep for probing the Brownian motion modes of the membrane and the defect cavity itself by examining the transmitted laser probe signal.

4.2.1 Micro-photoluminiscence spectroscopy of defect cavity

As it was introduced in Section 3.2.1, a single layer of self-assembled InAs(P) quantum dots is incorporated into our InP membrane. Their emission wavelength range largely covers our working bandwidth around $1.5 - 1.6$ μm (dark blue curve in Fig. 4.5c). Quantum dots photoluminescence spectrum will be filtered by the PhC cavity embedded within the membrane at a cavity resonance ω_0 (corresponding wavelength λ_0) and with its linewidth $\gamma_t = \gamma_i + 2\gamma_e$, including the intrinsic losses and the coupling to the forward- and backward-propagating waveguide optical mode (see Section 2.3.2 for more details). This approach adds few advantages to our system. By performing a micro-photoluminescence (μPL) spectroscopy on the cavities fabricated in such a way, we check the correspondence of the designed optical properties of our resonators (resonance wavelength, which can vary due to technological imperfections) with the obtained samples.

Experiment schematic is given in Figure 4.5a. A pump laser (Lumix LU808M100 diode with ILX Lightwave LDC-3724C controller and LDM-4980 module) is used for the non-resonant pumping of the quantum dots layer at 800 nm, which is below the InP band gap. Their emission, filtered by the cavity, is radiated back and subsequently read out by the spectrometer with 0.09 nm spectral resolution (Princeton Instruments Acton SP-2500 with PyLoN-IR cooled CCD camera, operating at -90 °C). In such a way the cavity mode together with the band-edge modes of the PhC lattice can be characterized (light blue curve in Fig. 4.5c; dark blue trace represents a reference for the QDs emission in the absence of PhC lattice, recorded from a suspension pad). The present scheme (Fig. 4.5a) includes a CCD camera (Thorlabs DCU223C) for sample imaging in visible range and pump laser alignment to a chosen device. Typical CCD camera image of the central part of the sample, containing an array of membrane devices, is shown in Fig. 4.5b.

4.2.2 Waveguide transmission measurement

On the other hand, the PhC cavity emission, coupled to the underlying SOI waveguide and to free space via the grating couplers, allows for simple alignment procedure between the sample and the input/output optical channels in the set-up scheme. If the active medium inside the cavity is non-resonantly pumped (orange arrow in Fig. 4.5a and Fig. 4.6a) in the presence of access waveguide the cavity emission will not only be radiated from cavity in the direction, normal to the membrane (B′ in Fig. 4.6a), but will also be coupled to the waveguide and radiated to free space from its ends via the grating couplers (in A′ and C′ directions).

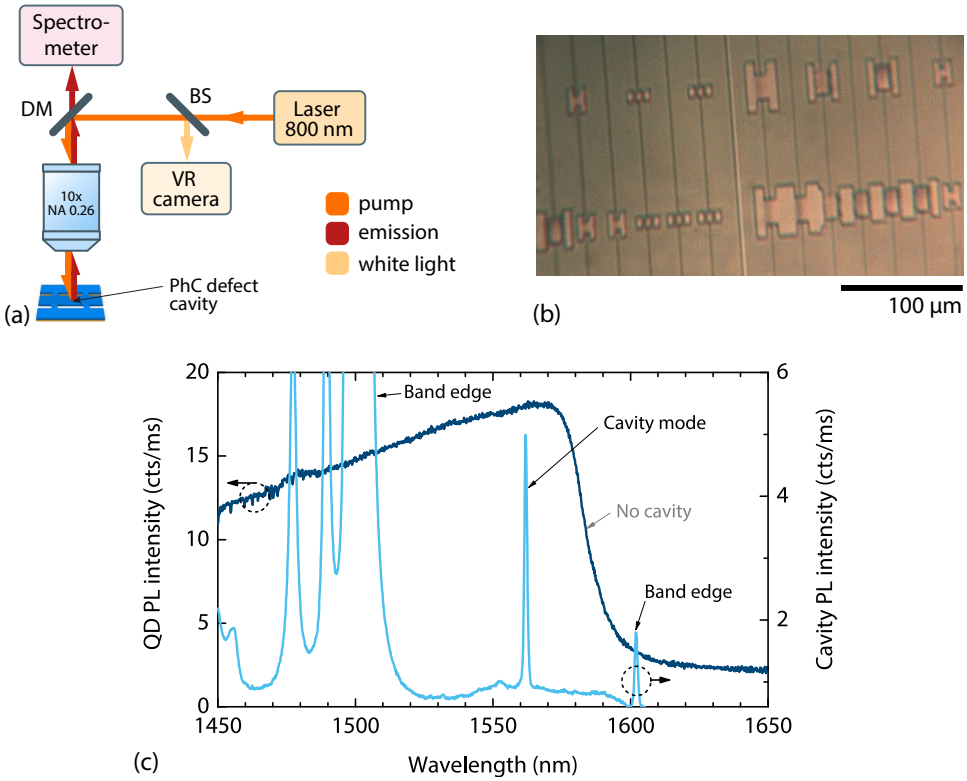

Figure 4.5: (a) Schematic view of the experimental set-up part dedicated to photoluminescence (PL) measurements. (BS – beamsplitter, DM – dichroic mirror [wavelengths lower 1000 nm are reflected, higher – transmitted], VR – visible range, LD – laser diode, NA – numerical aperture.) (b) Example picture of the central sample part with PhC membranes, taken by VR camera. (c) PL spectra: emission of quantum dots (QD) monolayer from unpatterned InP membrane (dark blue); same emission, filtered by a L3 defect cavity (light blue).

Our InP resonator is suspended over a host substrate made of silicon, which possesses low optical absorption around 1.55 μm wavelength, and thus the emitted cavity mode is also transmitted through the substrate and can be seen from the sample backside. Therefore, the three additional emission directions (A, B and C in Fig. 4.6a) are accessible in our set-up. These emission directions are observed with an infra-red (IR) camera (VDS Vosskühler NIR-300PGE) placed in the backside of the vacuum chamber, through an aperture allowing for light transmission from sample. As shown in schematic in Fig. 4.6a, the IR camera with the suitable objectives set is adjusted for imaging of all three emission directions (A, B, C).

This IR imaging is first used to identify the position of the two grating couplers, as shown in Fig. 4.6b. QDs in the membrane are pumped from the frontside of the sample (B′ in Fig. 4.6a) with a 800 nm laser, and cavity emission, seen from the backside, shows a bright spot at B and two spots at A, C directions, indicating the positions of the waveguide gratings. Next, a probe laser at $\lambda \approx 1.55$ μm is sent from the frontside C′ direction on the

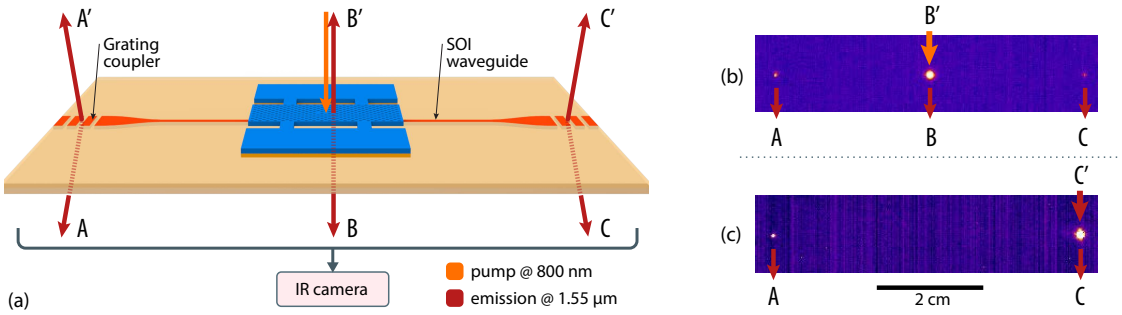

Figure 4.6: (a) Schematic view of the QDs/cavity emission (red arrows), outcoupled from the waveguide gratings (A, A′ and C, C′ directions) and the cavity itself (B, B′). (b) IR camera capture of the sample backside, showing a cavity emission, radiated directly (B) and from the waveguide gratings (A, C), while the QDs are non-resonantly pumped (from frontside, B′ direction). (c) An external laser, non-resonant to the cavity ($\lambda \approx 1.55$ μm, $\lambda \neq \lambda_0$), aligned by emission spot at C from (b) procedure, and thus coupled to a waveguide. Transmitted laser is outcoupled from grating at A direction (QDs pump is off).

grating coupler so that it matches the corresponding emission point at C (it is possible to match these two spots by aligning them with the IR camera imaging, as the 1.55 μm laser is also partly transmitted through the Si substrate). The subsequent alignment between the laser and the grating coupler is performed with the 800 nm pump from B′, turned off. When the laser is non-resonant with the cavity ($\lambda \neq \lambda_0$), it will only be spotted by IR camera at A and C directions. By changing the input spot position and focalization we maximize the light output from A spot, which corresponds to a better laser-to-waveguide coupling. Once this alignment is completed, the same procedure is repeated for another grating coupler by shining 1.55 μm laser from A′ direction and optimizing the waveguide throughput. Eventually the two couplers are used as input and output ports for addressing the device in the set-up scheme, as described in the following.

Figure 4.7 shows the schematic of the experimental set-up which is used for waveguide transmission measurement and further for the spectroscopy of the Brownian motion of our optomechanical device. As a result of alignment procedure, described above in the Section, we use two microscope objectives aligned with respect to the input and output grating couplers of the chosen waveguide. It should be noticed that the used grating couplers are designed for efficient operation at light incidence angle $\theta = 10°$ (with the angular acceptance of 3° within 3 dBm bandwidth), with respect to the normal line to substrate plane [Taillaert 2006]. Taking this particularity into account, each of the objectives was equipped by 6 degrees of freedom (6DoF) positioning system, including rotation (θ change) and two tilt controls alongside with the conventional 3-coordinate translation stage. In such manner the two optical access paths to and from the waveguide can be aligned independently from each other and from the sample positioning stage. Once their alignment is done, the vacuum chamber with the sample can be simply translated in order to switch

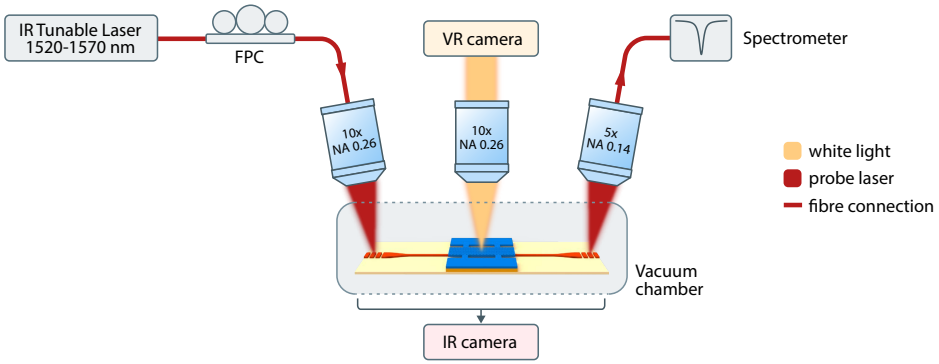

Figure 4.7: Schematic of the set-up for experimentation of integrated optomechanical device. Corresponding free space and fibred light paths are indicated. (IR - infra-red, FPC – fibre polarization controller, VR – visible range, NA – numerical aperture)

between different access waveguides, which considerably simplifies the alignment routine, e.g., compared to the taper fibre coupling technique.

In our experimental scheme the detected optical signal consists of the output field in the fundamental mode of an optical SOI waveguide positioned in the near field of the PhC cavity, as described above. The polarization of this mode and therefore of the probe laser coupled to it is chosen to maximize the coupling to the cavity (cf. Section 2.1.3.4). The probe laser is a continuous wave (CW) tunable infra-red source (New Focus Velocity TLB-6728-P-D fibre coupled external cavity diode with TLB-6700 controller), covering $\lambda = 1520 - 1570$ nm wavelength range, which approximately correspond to the transmission band of the SOI waveguide and grating couplers system. Its polarization is adjusted with a fibre polarization controller (Thorlabs FPC561) prior to injecting into the access waveguide (Fig. 4.7).

In order to avoid air damping effects, the sample is placed inside a vacuum chamber (pressure of $< 10^{-4}$ mbar). Our vacuum chamber has two optical access windows at its frontside and backside, and a sample chamber can host a few mm thick 1-inch wafer. However, out-of-plane grating couplers in our devices are designed to work with a fibre whose end is brought in the proximity of grating (so fibre and sample are almost touching). With the vacuum chamber the minimal distance from a grating coupler to a fibre end would be not less than $3-4$ mm, taking into account the thickness of optical access window glass and the separation between it and the sample. All of these makes impossible to implement the fibre access unless designing a bigger vacuum chamber, which is foreseen for the next generation of the set-up. Consequently, we employed two microscope objectives with sufficient numerical apertures (NA) to cover the acceptance angles of the gratings and with the longest possible working distance in order to have three focused spots (Fig. 4.7) in the middle of the sample and at each of the grating couplers while resolving the issue of objectives congestion.

Two cameras are used in this set-up: a visible range one (frontside) for the visual

control allowing to identify the device to address and an infra-red one (backside) for the alignment of the two objectives to the grating couplers, as discussed above. The probe laser light with optimal polarization (matching the one of waveguide fundamental TE mode) is injected into the waveguide and collected from its opposite side for the further analysis (Fig. 4.7).

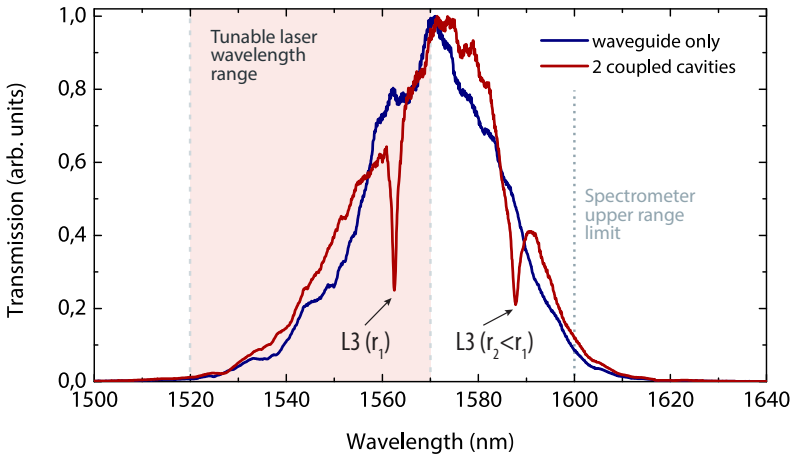

Figure 4.8: Normalized transmission spectra of two SOI waveguides: (blue) without coupled cavity and (red) with two coupled cavities from the PhC lattices with different radii (r_1 and $r_2 < r_1$). Highlighted region corresponds to the tuning range of the probe laser. Cut-off wavelength of the used spectrometer is about 1.6 μm.

Part of the transmitted light can be directed to the spectrometer in order to check the waveguide and cavity mutual coupling and the alignment of the objectives with respect to grating couplers (as the change in light incidence angle θ from optimum on a grating coupler shifts the transmission band). Conventional approach for recording a transmission curve over a large wavelength span consists in sweeping the probe laser across its working range and measuring the output intensity at different wavelengths. In our set-up we established a more rapid way of this procedure, allowing to monitor the transmitted signal spectrum over a large span with a typical frame rate of the order of 10^3 full spectra per second. To do so, the probe laser is set to operate in the amplified spontaneous emission (ASE) regime, which for the used laser diode is achieved by setting the output power just below the threshold (0.3 mW) at the minimum possible wavelength ($\lambda = 1520$ nm). In such a way the laser output contains a spectrally wide signal with sufficient power to be detected by the spectrometer at high acquisition rates (milliseconds). Moreover, this technique allows to characterize the transmission of waveguide – cavity systems over a large span, limited in our case by the cut-off wavelength of the spectrometer.

Figure 4.8 shows two characteristic spectra captured by this technique. Blue curve corresponds to the transmission spectrum of a single waveguide without any coupled cavity, thus characterizing the intensity distribution across the bandwidth with respect to the chosen laser polarization and angle of incidence $\theta \pm \Delta\theta$ within the light cone at the objective

output. Using this real-time feedback, it is possible to adjust the position and central angle θ of the input and output objectives in order to shift the transmission maximum to a desired wavelength (i.e., the one of the coupled cavity λ_0) and maximize the overall transmission by optimizing the objective stage position relative to the sample holder. As characterized in [Taillaert 2006], a 1° change in central angle θ would shift the maximum of waveguide transmission region by approximately 20 nm to the blue side of the spectrum.

Red curve corresponds to a transmission spectrum of a waveguide, coupled at a time to two PhC L3 cavities with different hole radii r. The alignment of the coupling objectives was performed in a way to include two resonances of these cavities inside the non-zero transmission range. It shows that, for instance, multiple cavities embedded inside one or several mechanical resonators can be addressed using one integrated waveguide, maintaining comparable coupling strengths (defined by the resonance deep depth and cavity linewidth γ_t, both of which can be compared using the discussed spectrum in Fig. 4.8). These two cavities, coupled to the same waveguide, were designed within the lattices of different radii r_1 and $r_2 < r_1$, which generally separates their resonance wavelengths by about $\Delta\lambda = 2|r_1 - r_2|$. In the case shown in Figure 4.8, the working range of our probe laser is highlighted in light red, indicating that solely one of these cavities can be addressed in the laser regime. In the following Section we will use this resonance deep in transmission in order to perform a mechanical spectroscopy of the cavity host membrane. This allows, for example, to selectively address each of multiple mechanical resonators, coupled to a common access waveguide, by designing the respective embedded cavity resonances to spread across a range of wavelengths, covered by the probe laser source.

4.2.3 Optical readout of Brownian motion

This Section describes the experimental implementation of the mechanical spectroscopy of the optomechanical device under study. In these experiments we launch a probe laser signal into the SOI waveguide, the laser beam is coupled to the optical resonance of an embedded PhC cavity, transmitted through the access SOI waveguide and collected in the same manner as for the transmission measurement (see Section 4.2.2).

However, instead of using full spectrum of the tunable laser, we employ a sharp probe ($\sim$ 200 kHz linewidth) at fixed wavelength, as depicted in Fig. 4.9. The collected light first gets selectively amplified by a two-stage erbium doped fibre amplifier (EDFA[3]). First stage of the EDFA is followed by one of two (100 MHz and 20 GHz bandwidths) spectral filters, which, once locked on the probe laser resonance, can automatically follow it over all the working wavelength range. The locking is controlled visually and in real-time mode on the optical signal analyser (OSA; Anritsu MS9740A), to where a part of the amplified signal is directed (Fig. 4.9). This functionality allows us to perform experiments with

[3]This amplifier was custom-made at Département Optique et Photonique in Institut de Physique de Rennes in collaboration with the group of Mehdi Alouini. Such amplifier allows for low input powers ($1 - 10$ nW) and low noise figure [Noise figure (NF) for an optical amplifier is calculated as a ratio between the output and input signal-to-noise ratios (SNR): $\mathrm{NF} = \mathrm{SNR}_{\mathrm{out}}/\mathrm{SNR}_{\mathrm{in}}$]. In our experiment, NF < 4 dBm and the high amplification gain is ~ 50 dBm.

the sweeping probe laser while still ensuring stable signal amplification with high signal-to-noise ratios (SNR) and noise figure at the level of state of the art EDFAs. Following the second path (Fig. 4.9), after amplification, the probe signal power gets adjusted by a variable optical attenuator (VOA; Thorlabs VOA50) in order to match the working range of the detector input power. This probe signal is additionally filtered by the tunable (spectrally with variable linewidth) bandpass filter (BPF; Yenista WSM-160), which allows to reduce the noise in the detection scheme, related to the modulation of the laser carrier at the wavelength other than the one of the sharp probe (e.g., background of amplified spontaneous emission). Electrical signal from the fast photodiode (New Focus 1592, DC to 3.5 GHz) is read out by the electric spectrum analyzer (ESA; Rohde&Schwarz FSV7, 9 kHz – 7 GHz).

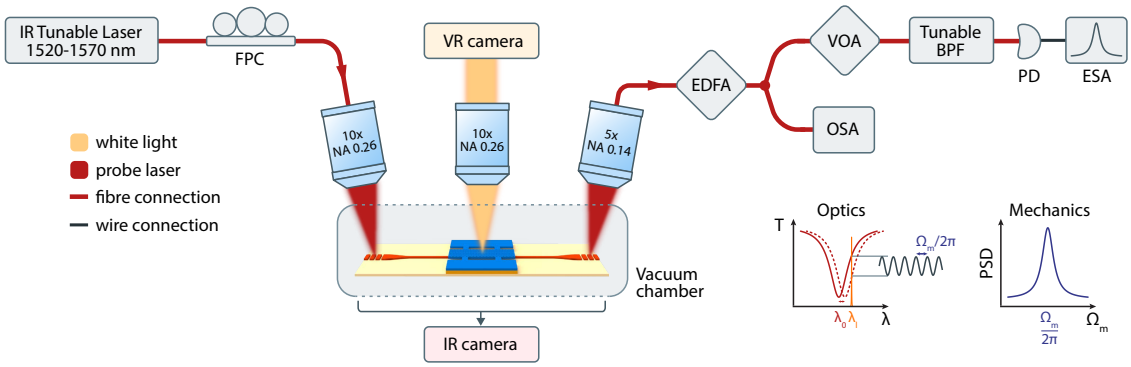

Figure 4.9: Schematic of the set-up for measuring the mechanical spectrum of the integrated optomechanical device. Corresponding free space, fibred and wired signal paths are indicated. Transduction scheme of the mechanical motion via the fixed laser probe is illustrated on two spectra, showing waveguide transmission with the coupled cavity [$T(\lambda)$] and the power spectral density of the transmitted probe laser [$PSD(\Omega_m)$], as measured by the ESA. (IR - infra-red, FPC – fibre polarization controller, VR – visible range, NA – numerical aperture, EDFA – erbium doped fibre amplifier, VOA – variable optical attenuator, OSA – optical spectrum analyzer, BPF – bandpass filter, PD – photodiode, ESA – electric spectrum analyzer.)

This experimental set-up allows to perform the so-called "side of the fringe" technique for the detection of mechanical motion, as illustrated in Figure 4.9. If we first look at the cavity transmission close to its resonance λ_0, we typically found a Lorentzian shape, e.g., as the one in Fig. 4.8. The mechanical resonator, oscillating at its eigenfrequency $\Omega_m/2\pi$, modulates the cavity resonance wavelength via dispersive or dissipative coupling mechanisms (see Section 2.3.1). Therefore, such modulation of the cavity Lorentzian optical response gets imprinted onto the probe laser (in the case when its linewidth is much sharper comparing to the cavity linewidth $\gamma_l \ll \gamma_t$), slightly detuned from the resonance wavelength to one of the sides, as shown in Figure 4.9. In this configuration, the probe intensity is modulated at the frequency of the resonator mechanical oscillation, which holds also for any mechanical mode impacting the optical resonance. By looking at

the noise of the transmitted probe with an ESA, one retrieves the mechanical mode(s) of host membrane in the recorded PSD spectrum (Fig. 4.9).

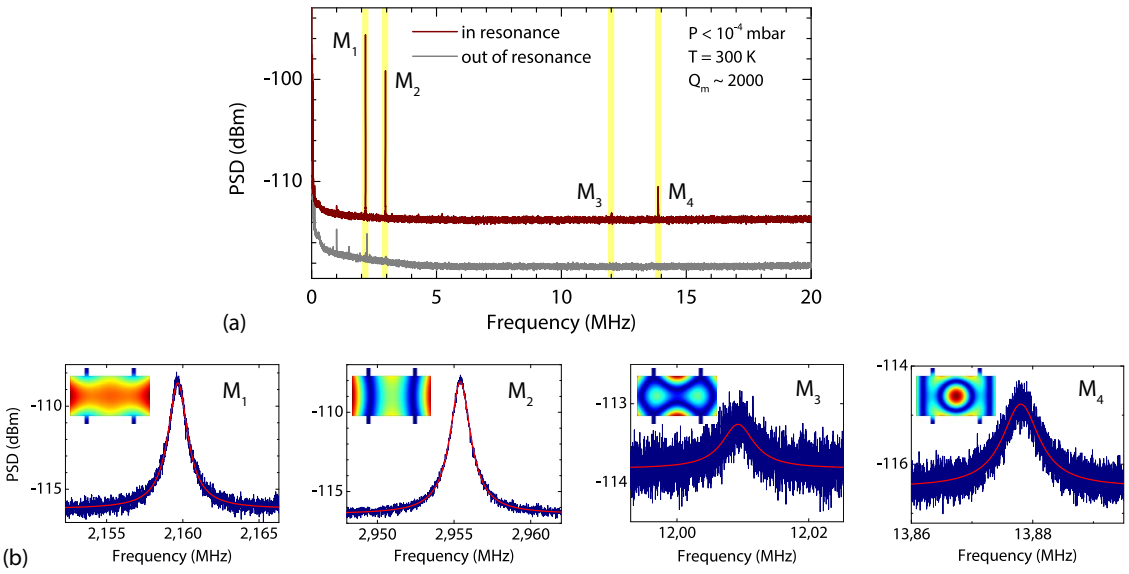

Figure 4.10: (a) Power spectral density (PSD) of the transmitted optical signal for the probe laser tuned in (red curve) and out of (grey curve) the optical resonance of the cavity, embedded into a suspended PhC membrane (dimensions: $m_x = 20$ μm, $m_y = 10$ μm, $t = 260$ nm, $b_x = 1$ μm, $b_y = 2$ μm, $b_d = 5.9$ μm). (b) PSD of detected mechanical resonances, taken with a better resolution around each of the four eigenfrequencies (blue – data, red – Lorentzian fit). Corresponding simulated displacement field $\vec{Q}(\vec{r})$ distributions are given in insets.

This technique of amplitude modulation detection of a probe laser, coupled to the detected cavity resonance (e.g., like the one in Figure 4.8), would typically give a mechanical spectrum, as shown in Figure 4.10a (red trace). Experiment is performed in the vacuum chamber at low pressure P $< 10^{-4}$ mbar in order to avoid air damping, which is considerable for the flexural membrane modes. In this study, we used the L3 defect cavity with a resonance around $\lambda_0 \sim 1560$ nm, embedded inside a 20×10 μm^2 membrane, suspended with four 1×2 μm bridges.

Power spectral density of a transmitted signal in MHz range reveals few resonance peaks, corresponding to the mechanical modes of the suspended membrane, as simulated in Section 2.16. The modes present in the low-frequency spectrum correspond to the ones which exhibit the most prominent amplitudes in the numerical spectroscopy (Section 2.16). An additional measurement is performed with a probe laser tuned completely out of cavity resonance (i.e., $\Delta = 3 - 5$ nm). This allows to detect any spurious modes, present in the current set-up due to the electrical noise sources not related to the mechanical motion of the device under study (grey curve in Fig. 4.10a).

Contrary to the forced oscillation experiment, described in Section 4.1, here we measure the Brownian motion, whose amplitude, in particular, is much weaker compared to the

actuated membrane movement. As the mode energy is directly proportional to the oscillator temperature, the measurements were carried out at room temperature $T_b = 300$ K. Close-up PSD spectra of the four detected modes are given in Figure 4.10b with their Lorentzian fits and the corresponding simulated displacement field profiles. Each of the four measured modes have similar mechanical quality factors Q_m between 2000 and 3000, showing no significant dependency on the mode index or displacement field distribution. This compares well with the quality factors, measured for the modes M_1 and M_2 in Section 4.1. Low power of probe laser is used in order to not impact the mechanical properties and thus the mode shapes and frequencies via the thermomechanical or other thermally induced effects. The latter will be studied in the Section 4.3.6.

4.2.4 Determination of the optomechanical vacuum coupling rate

The vacuum optomechanical coupling rate g_0, as introduced in Section 2.3.4.3, is a common figure of merit describing an optomechanical interaction between two specific modes (optical and mechanical). We experimentally determine its value by using the frequency modulation technique [Schliesser 2009; Gorodetsky 2010]. Previously shown set-up scheme was modified (Fig. 4.11) to include the following phase modulation. The probe laser light is phase-modulated via a fibred $LiNbO_3$ electro-optical modulator (EOM; Thorlabs LN65SFC) in order to calibrate the detected mechanical motion, as it will be described in more details below. A harmonic signal from the function generator (Agilent 81150A) is fed to the electro-optical modulator at a frequency close to the one of the mechanical resonance to be calibrated. Since the electro-optical modulator has a polarization dependent operation, the linear polarization of the output laser light is adjusted with a fibre polarization controller (FPC). Another FPC is used after the EOM in order to match the polarization of the defect cavity mode.

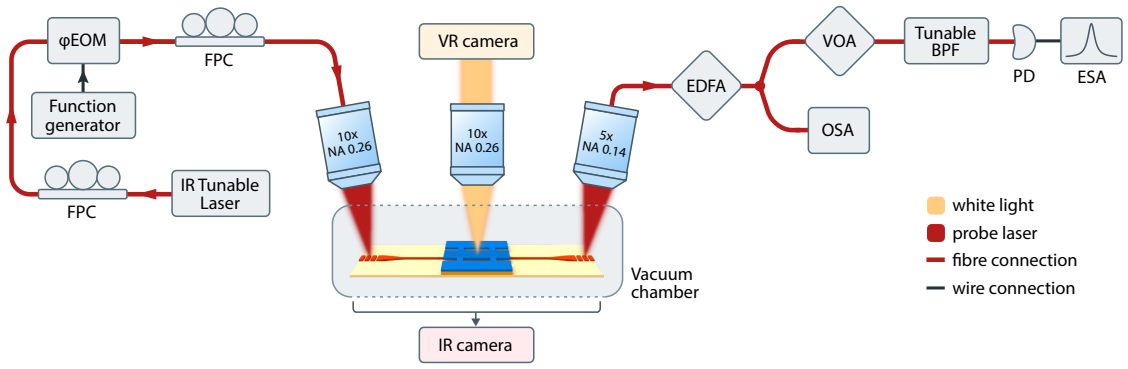

Figure 4.11: Schematic of the set-up for measuring of the optomechanical vacuum coupling rate. Corresponding free space, fibred and wired signal paths are indicated. (IR - infrared, φEOM – phase electro-optical modulator, FPC – fibre polarization controller, VR – visible range, NA – numerical aperture, EDFA – erbium doped fibre amplifier, VOA – variable optical attenuator, OSA – optical spectrum analyzer, BPF – bandpass filter, PD – photodiode, ESA – electric spectrum analyzer.)

To calibrate the detected power spectrum in frequency units using the phase modulation technique, a known phase modulation at a given frequency Ω_{mod} is applied through the electro-optical modulator to the laser carrier before its coupling into the cavity. The time evolution of the modulated carrier phase can be written as

$$\Phi(t) = \omega t + \tilde{\beta}\cos(\Omega_{\mathrm{mod}} t) \tag{4.2}$$

where t is the time, $\omega/2\pi$ – the laser frequency, $\tilde{\beta}$ – the phase shift factor, induced by EOM in the probe signal. The transmitted laser signal after amplification and spectral filtering is detected with a fast photodiode and its spectrum is recorded with the ESA (Fig. 4.11). Alongside with a Lorentzian profile of mechanical mode (Fig. 4.10b) the spectrum exhibits a Gaussian-shaped calibration peak (Fig. 4.12), resulting from the carrier phase modulation [Schliesser 2008a; Schliesser 2008b]. From [Gorodetsky 2010], for a modulation frequency Ω_{mod} close (a couple of mechanical linewidths Γ) to the resonance frequency Ω_{m} of the mechanical mode, g_0 can be expressed as

$$g_0 \approx \sqrt{\frac{1}{2\bar{n}} \frac{\tilde{\beta}^2 \Omega_{\mathrm{mod}}^2}{2} \frac{\Gamma}{4\,\mathrm{RBW}} \frac{S_{\omega\omega}(\Omega_{\mathrm{m}})}{S_{\omega\omega}(\Omega_{\mathrm{mod}})}}, \tag{4.3}$$

where $\bar{n} \approx k_{\mathrm{B}} T_b / \hbar\Omega_{\mathrm{m}}$ (cf. Section 2.4) is the average phonon occupancy of the mechanical mode to be calibrated, RBW is the resolution bandwidth of the ESA, $S_{\omega\omega}(\Omega_{\mathrm{m}})$ is the double-sided frequency spectral noise density evaluated at the mechanical resonance frequency and $S_{\omega\omega}(\Omega_{\mathrm{mod}})$ is the double-sided frequency noise spectral density evaluated at the frequency of modulation. We can directly obtain the ratio $S_{\omega\omega}(\Omega_{\mathrm{m}})/S_{\omega\omega}(\Omega_{\mathrm{mod}})$ from the power spectral density values, measured by ESA at the corresponding frequencies. For the powers P_{m} and P_{mod}, measured at the peak of the mechanical Lorentzian and of the modulation Gaussian, respectively, and expressed in dBm (usual logarithmic units for PSD used through this work), the following relationship holds

$$S_{\omega\omega}(\Omega_{\mathrm{m}})/S_{\omega\omega}(\Omega_{\mathrm{mod}}) = 10^{(P_{\mathrm{m}} - P_{\mathrm{mod}})/10}. \tag{4.4}$$

Figure 4.12 illustrates an example of such calibration measurement for a particular mechanical mode at $\Omega_{\mathrm{m}}/2\pi = 94.92$ MHz with the phase-modulated carrier at $\Omega_{\mathrm{mod}}/2\pi = 95.05$ MHz, from where the peak powers P_{m} and P_{mod} can be extracted. Spectrum calibration, performed in such a manner, is valid for the frequency range to be calibrated, which is close enough (of the order of few mechanical resonance linewidths) to the resonance frequency of the modulation peak.

When working with the spectra of signals from various sources – random and coherent – specific corrections should be made when comparing their measured PSD values [Agilent 2012]. By averaging the spectral response of the ESA, expressed in logarithmic dBm units, one gets an average of the logarithmic power, which is not equal to the logarithmic expression of the averaged power – the value that is of significance in the measurements. Discrepancy would be different for random signals, such as background noise and the

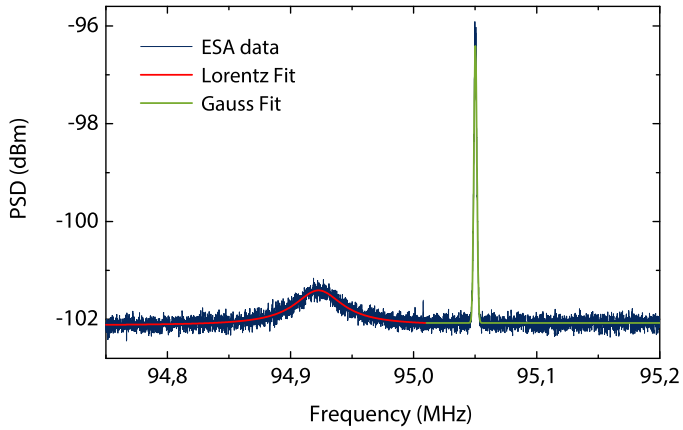

Figure 4.12: ESA power spectrum of a mechanical mode with a calibration peak (blue) including the respective Lorentzian (red) and Gaussian (green) fits.

mechanical oscillations (which is a result of thermal motion), and for coherent signals, such as the one used for the calibration peak with a large enough signal-to-noise ratio. It is known [Agilent 2012], that for random signals the measured value is about 2.5 dB below the actual one, whereas for truly coherent sources the measured signal corresponds to the real one. Some of existing equipment are able to compensate this discrepancy internally, however, as this function was not applied during our experiments, we need to use the above-mentioned value for the correction of the measured signal. A thorough explanation and derivation of this correction factor can be found in supplementary material of [Gavartin 2011].

The phase shift factor $\tilde{\beta}$ from Eq. 4.3 is experimentally determined for a particular EOM as

$$\tilde{\beta} = \pi \cdot V/V_\pi = \pi\sqrt{2P_{\mathrm{rf}}Z}/V_\pi, \tag{4.5}$$

where V is the voltage, applied to the EOM, V_π is the characteristic voltage needed to induce a phase shift of π of the modulated signal, P_{rf} is the input power of the function generator (see Fig. 4.11), Z is the impedance between the EOM and the function generator. Actual voltage V, applied to the EOM, depends on the transmittance characteristics of the cable, linking the EOM with the function generator, and on the reflectance of the EOM itself, while the last two parameters are in addition frequency-dependent. Details on the calibration of these characteristics for the equipment used during these experiments and the corresponding Eq. 4.5 modification are described in Appendix B.

An important role in the calibration procedure is played by the optical bandpass filter, included in our experimental set-up scheme (Fig. 4.11). If we look at the output optical spectrum of the probe laser (blue trace in Fig. 4.13), it contains a linearly increasing background level, mainly related to the gain spectral properties of the used active medium. Passing through an EOM, all of the wavelengths get modulated, however, only the one at the desired probe wavelength will be used to calibrate the strength of optomechanical

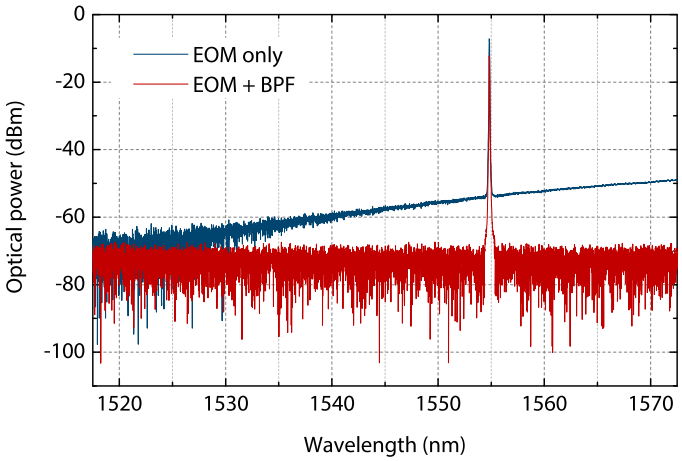

Figure 4.13: OSA power spectrum of the optical mode of the probe laser at nominal power of $P_0 = 1$ mW, after passing through the EOM only (blue) and EOM with BPF (red). Linear polarization of the laser mode was adjusted to match the one of the EOM with an intermediate FPC.

coupling g_0. The wavelengths out of the cavity resonance will not be affected by the optomechanical interaction within the resonator. Therefore, their transmission factors through the access waveguide, will be higher. This can bring a part of the modulated light to the detection system and thus alter the values of the modulation peak power P_{mod}. To overcome this issue, we employ an optical BPF, set to the narrow band filtering around the probe wavelength. As it can be seen from Fig. 4.13 (red trace), it gives a low uniform background with signal-to-noise ratio of about 60 dBm. The calibrations of the mechanical responses of our devices were thus performed in such configuration with narrow-band filtering.

Mode index	M_1	M_2	M_3	M_4	M_{95M}
$\Omega_m/2\pi$ (MHz)	2.17	2.96	12.03	13.88	94.75
Q_m	2120	2950	2650	2400	2690
$g_0/2\pi$ (kHz)	0.20	0.18	0.81	2.10	45.5

Table 4.1: Vacuum optomechanical coupling rate g_0, determined experimentally with the frequency modulation technique for several flexural modes of a suspended 10×20 μm^2 InP membrane (other parameters: $b_x = 1$ μm, $b_y = 2$ μm, $b_d = 5.9$ μm, $t = 260$ nm).

The values of the vacuum optomechanical coupling rate $g_0/2\pi$, determined using the frequency modulation technique, are specified in Table 4.1. Together we provide the frequency of the mechanical modes $\Omega_m/2\pi$ and the corresponding quality Q_m factors, measured at the same optical probe power and detuning. Comparing with the experiment on a non-integrated system [Gavartin 2011], the present values show good agreement, including the higher frequency mode (M_{95M}). Mechanical quality factors in our experiment,

however, show higher values: in [Gavartin 2011] the highest measured quality factor was $Q_{\mathrm{m}} = 890$ for the fundamental mode, rapidly decreasing at higher frequencies (e.g., a mode at 56 MHz had $Q_{\mathrm{m}} = 40$), which can be explained by the unoptimized suspension geometry of the device in that work[4]. In our case, using the four suspension bridges, we measure that all the modes have resembling quality factors ranging between 2000 and 3000, including the one for mode at 95 MHz. Current optomechanical set-up, nevertheless, employs simple detection of laser probe modulation and for the moment permitted us to detect considerably lesser mechanical resonances compared to tapered fibre technique used in the non-integrated configuration. This can be related as well to the amount of probe light, coupled inside the PhC defect cavity, which in our set-up and probing configuration is about $P_c \leqslant 300$ μW due to the relatively low coupling efficiency between microscope objectives and grating couplers of the access waveguide. Increasing the coupled powers in order to enhance sensitivity and resolve more mechanical resonances would lead to thermally induced effects, as described in Section 4.3.6, which in turn may affect the optical and mechanical properties of device and result in false determination of optomechanical coupling strengths.

Comparing with the state of the art optomechanical systems [Oudich 2014; Balram 2014], the highest $g_0/2\pi$ values attain up to ~ 4 MHz, however, reached within devices with mechanical frequencies of the order of few GHz. In the MHz range [Wilson 2014] the $g_0/2\pi$ values are of order of few tens of kHz.

4.3 Optomechanical effects within integrated platform

Heterogeneous integration as a way to precisely control the optical access to our device, introduces two additional mechanisms (referred to as external couplings) alongside with the conventional optomechanical interactions within the membrane body. Chapter 2 described the theoretical estimations of strengths of above-mentioned effects; current Section aims to experimentally measure them and infer each of the components separately, if possible. In order to experimentally extract such data, we employ the wavelength dependencies of optomechanical responses of different types, derived in Section 2.3.2, as a fitting model for the performed experiment and extract the quantities of interest. Experimental verification of four different optomechanical coupling mechanisms will be demonstrated. Finally, the particularities of optically probing a semiconductor cavity will be addressed together with their impact on the mechanical operation of the system.

4.3.1 Dynamical backaction: optical spring effect measurement

In optomechanics, a dynamical backaction – mechanical oscillator response to an external optical force within a device – in the presence of optomechanical coupling leads to the optical spring effect [Aspelmeyer 2013]. It consists in the change of principal mechani-

[4] In these experiments, the membranes were fully clamped along two sides.

cal properties of the oscillator (frequency and damping rate), strongly dependent on the detuning $\Delta = \omega - \omega_0$ of the driving laser carrier with respect to the cavity resonance ω_0.

Measurement of this effect consists in examination of the mechanical response, as introduced in Fig. 4.10, while the pump laser is swept across the optical cavity resonance. In the experiments with optical readout of the Brownian motion, described in Sections 4.2.3 and 4.2.4, the motion is being transduced to an electronic signal of time-varying voltage $V(t)$ from a photodiode, detecting the optical field transmitted through the access waveguide. The voltage $V(t)$ consists of the contribution $V_{\mathrm{OM}}(t)$, generated by the optomechanical interaction with the existing mechanical modes, and of the contribution $V_{\mathrm{n}}(t)$, arising from various optical end electronic noises present in the measurement scheme: $V(t) = V_{\mathrm{OM}}(t) + V_{\mathrm{n}}(t)$. Temporal evolution of the power spectral density of the optomechanical contribution $V_{\mathrm{OM}}(t)$, sampled by the ESA (cf. Fig. 4.14), for the given laser probe nominal power P_0 and its detuning Δ with respect to the cavity mode frequency ω_0, can be described as

$$V_{\mathrm{OM}}(t) = P_0 \xi \beta^2 \eta^{\dagger} g_{\mathrm{ti}} \cdot T\left[\Delta, x(t)\right], \tag{4.6}$$

where the corresponding coefficients, related to the specific set-up components, are illustrated in Figure 4.14; $T\left[\Delta, x(t)\right]$ is the waveguide transmission spectrum and $x(t)$ is the general displacement of the membrane mechanical resonator.

The frequency calibration part, including the polarization controllers and the EOM, is characterized by an attenuation ξ, which by default includes the optical losses at their interconnections, so that the total laser power, incident on the input grating coupler, is $P_0\xi$. Coupling efficiency of a single coupler is β, assumed to be equal for both input and output gratings. Intracavity optical power is thus $P_c \propto P_0\beta$, additionally relying on the coupling efficiency η between waveguide and cavity optical modes, as studied in detail in Section 2.1.3.4, and the laser – cavity detuning, denoted Δ. Optical amplification and filtering block modify the signal power by a factor $\eta^{\dagger}$. Finally, g_{ti} is the photodetector transimpedance gain ($g_{\mathrm{ti}} = 1400$ V/W, as calibrated for our example of New Focus 1592 photodiode).

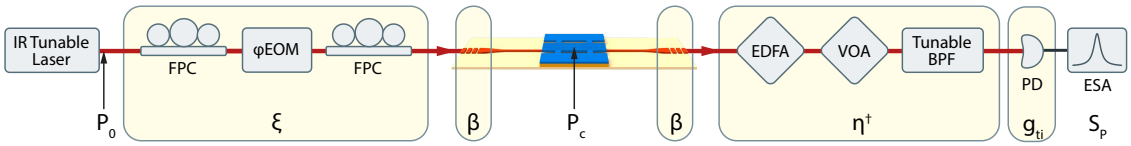

Figure 4.14: Schematic of used transmission and transduction coefficients in the experimental set-up for the thermomechanical calibration, as introduced in Figure 4.11 (cf. caption of Fig. 4.11 for acronyms). Arrows indicate the quantities, measured at specific place of the signal pathway; variables within rounded rectangles refer to the signal multiplier, which corresponds to the elements within a specified group.

Generally speaking, the transmission $T(t)$ of the access waveguide changes depending on the general displacement $x(t)$ and the impact of x on the optical response of the PhC

defect cavity, coupled to the waveguide. In the case of device operation in the sideband-unresolved regime ($\Omega_{\rm m} \ll \gamma_t$) the electromagnetic field of cavity mode can adiabatically follow the membrane oscillations. Hence Equation 4.6 can be written as

$$V_{\rm OM}(t) = P_0 \xi \beta^2 \eta^{\dagger} g_{\rm ti} \cdot \left[T_0 + \frac{dT(\Delta)}{dx} x(t) \right]. \tag{4.7}$$

The two-sided PSD of the optomechanical contribution $V_{\rm OM}(t)$, obtained from the demodulation by ESA of the $V(t)$ and further Fourier transform of the resulting time-series data, writes as

$$S_{\rm VV}^{\rm OM}(\Omega) = |V_{\rm OM}(\Omega)|^2 / \delta t, \tag{4.8}$$

with δt representing the acquisition time of ESA time series, so that $V(\omega) = \int_0^{\delta t} V(t)\, e^{-i\Omega t} dt$. The DC component of V is ignored in the following discussion for clarity. Substituting Equation 4.7 in the frequency domain into Equation 4.8, we relate the two-sided PSD $S_{\rm VV}^{\rm OM}$ to the stochastically varying displacement $x(t)$ of the membrane resonator:

$$\begin{aligned} S_{\rm VV}^{\rm OM}(\Omega) &= \left(P_0 \xi \beta^2 \eta^{\dagger} g_{\rm ti} \frac{dT(\Delta)}{dx} \right)^2 \frac{1}{\delta t} \left| \int_0^{\delta t} x(t)\, e^{-i\Omega t} dt \right|^2 = \\ &= \frac{G^2}{\delta t} \int_0^{\delta t} dt' \int_{-t'}^{\delta t - t'} x^*(t+t')\, x(t')\, e^{-i\Omega t}\, dt, \end{aligned} \tag{4.9}$$

where $G(\Delta) = P_0 \xi \beta^2 \eta^{\dagger} g_{\rm ti} \cdot dT(\Delta)/dx$ describes the optomechanical and detection scheme response. For the acquisition times of the ESA $\delta t \gg 2\pi/\Gamma$, used in current experiment, and assuming the stationary nature of $x(t)$ displacement, meaning that $\langle x^*(t+t')\, x(t) \rangle = \langle x^*(t')\, x(0) \rangle$, we therefore can rewrite the Equation 4.9 as

$$S_{\rm VV}^{\rm OM}(\Omega) = G^2 \int_0^{\delta t} \left\langle x^*(t+t')\, x(t') \right\rangle e^{-i\Omega t}\, dt' = G^2(\Delta)\, S_{xx}(\Omega), \tag{4.10}$$

where $S_{xx}(\Omega)$ is the displacement-noise spectral density of the mechanical resonator. The ESA measures and displays single-sided power spectral densities, hence the total single-sided PSD will write

$$\bar{S}_{\rm VV}(\Delta, \Omega) = \bar{S}_{\rm VV}^{\rm OM}(\Delta, \Omega) + \bar{S}_{\rm VV}^{\rm n}(\Delta, \Omega) = G^2(\Delta)\, \bar{S}_{xx}(\Omega) + \bar{S}_{\rm VV}^{\rm n}(\Delta, \Omega), \tag{4.11}$$

where the technical noise contribution, coming from $V_{\rm n}(t)$ photodetector output component, is denoted $\bar{S}_{\rm VV}^{\rm n}(\Delta, \Omega)$. The displacement noise $\bar{S}_{xx}(\Omega)$ of a thermally driven mechanical mode from Equation 4.11, can be derived from the fluctuation-dissipation theorem [Cleland 2002] and is written as

$$\bar{S}_{xx}(\Omega) = \frac{4k_B T_b \Omega_\mathrm{m}}{m_\mathrm{eff} Q_\mathrm{m}} \left[\left(\Omega^2 - \Omega_\mathrm{m}^2\right)^2 + \left(\frac{\Omega\Omega_\mathrm{m}}{Q_\mathrm{m}}\right)^2 \right]^{-1} \tag{4.12}$$

where k_B is Boltzmann's constant; T_b is the temperature, at which experiment is being conducted ($T_b = 294$ K for all measurements, related to the optical spring effect, carried out in this Chapter); $\Omega_\mathrm{m}/2\pi$ and Q_m are the resonance frequency and quality factor of the studied mechanical mode and m_eff – its effective mass, as introduced before.

If we now evaluate Equation 4.11 on mechanical resonance ($\Omega = \Omega_\mathrm{m}$), the dependence of peak PSD value on the laser – cavity detuning writes

$$\bar{S}_\mathrm{VV}(\Delta)\big|_{\Omega=\Omega_\mathrm{m}} = G^2(\Delta) \frac{4x_\mathrm{rms}^2 Q_\mathrm{m}(\Delta)}{\Omega_\mathrm{m}(\Delta)} + \bar{S}_\mathrm{VV}^\mathrm{n}(\Delta), \tag{4.13}$$

where $x_\mathrm{rms} = \langle x^2 \rangle^{1/2} = \sqrt{k_B T_b / m_\mathrm{eff} \Omega_\mathrm{m}^2}$ is the mean thermal displacement of the membrane resonator. As mentioned in Equation 4.13, the backaction effects should be taken into account, namely the dependencies of the mechanical mode frequency Ω_m and quality factor Q_m on the relative probe laser detuning Δ. We express the single-sided PSD as true power over a load resistance Z (equal to 50 Ohms for the above-described set-up), such that $\bar{S}_\mathrm{P} = \bar{S}_\mathrm{VV}/Z$ in units of dBm/Hz or W/Hz – the ones used by default through the measurements performed in this work. Finally, from Equations 4.13 and 2.5 we obtain

$$\begin{aligned} \bar{S}_\mathrm{P}(\Delta)\big|_{\Omega=\Omega_\mathrm{m}} = {} & \frac{\left(2x_\mathrm{rms} P_0 \xi \beta^2 \eta^\dagger g_\mathrm{ti}\right)^2}{Z} \frac{Q_\mathrm{m}(\Delta)}{\Omega_\mathrm{m}(\Delta)} \times \\ & \times \left| g_{\omega,e} \frac{\partial T}{\partial \Delta} + g_{\gamma,e} \frac{\partial T}{\partial \gamma_e} + g_{\omega,i} \frac{\partial T}{\partial \Delta} + g_{\gamma,i} \frac{\partial T}{\partial \gamma_i} \right| + \bar{S}_\mathrm{P}^\mathrm{n}(\Delta), \end{aligned} \tag{4.14}$$

where the corresponding partial derivatives of T are given by Equations 2.6–2.8. The dispersive g_ω and dissipative g_γ optomechanical coupling strengths and for both external and intrinsic couplings are extracted from the experimental ESA data by fitting the $\bar{S}_\mathrm{P}(\Delta, \Omega = \Omega_\mathrm{m})$ dependence to Equation 4.14. The noise floor $\bar{S}_\mathrm{P}^\mathrm{n}(\Delta)$ can also be found from the corresponding fitting, which allows to calibrate the spectrum and express it as displacement noise spectral density (in units of m^2/Hz) even without using the frequency calibration procedure, described in Section 4.2.4. In the following Sections we study the optomechanical couplings within our devices by measuring the optical spring effect and fitting the experimental data with the model, introduced above.

4.3.2 Optomechanical coupling with constant phase-matching conditions

In this Section we present the measurements and comparison of the optomechanical coupling components, performed for two different mechanical modes, introduced previously

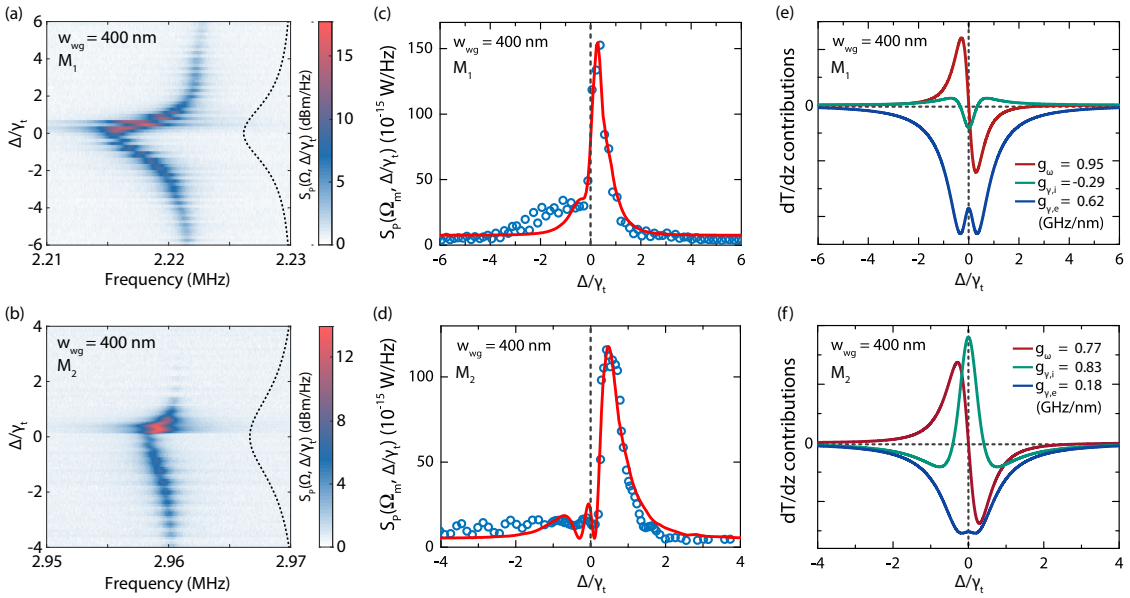

Figure 4.15: Power spectral density $S_{\mathrm{P}}(\Omega, \Delta/\gamma_t)$ for the mechanical modes (a) M_1 and (b) M_2, measured for the device with access waveguide of $w_{\mathrm{wg}} = 400$ nm. The Lorentzian fit of the cavity mode resonance is displayed in black dashed line for reference. Probe laser detuning Δ is normalized with respect to total linewidth γ_t of the optical cavity. Power spectral density at mechanical resonance $S_{\mathrm{P}}(\Omega_{\mathrm{m}}, \Delta/\gamma_t)$ (open circles) as a function of the normalized detuning Δ/γ_t for modes (c) M_1 and (d) M_2 and for the same w_{wg}. The solid lines represent the fits to the theoretical model. Contributions to the transmission spectrum noise (in arbitrary units; red: total dispersive coupling; green: intrinsic dissipative coupling; blue: external dissipative coupling) for (e) M_1 and (f) M_2 versus Δ/γ_t. The inferred optomechanical coupling rates are indicated.

as M_1 and M_2. These modes belong to the same membrane oscillator, therefore the comparison can be made without accounting for the changing geometry of the device or the varying phase-matching conditions between the cavity and the waveguide optical modes.

To do so, we measure the spectral density $\bar{S}_{\mathrm{P}}(\Omega, \Delta)$ evolution around the chosen mechanical resonance frequency Ω_{m} with a certain span. In Figures 4.15a,b the $\bar{S}_{\mathrm{P}}(\Omega, \Delta)$ values are colour-coded and plotted versus the probe laser detuning and within the same frequency span for the two modes. Laser – cavity detuning Δ is normalized to the total cavity linewidth γ_t in order to be able to compare the detuning range for different mechanical modes within one or several devices (as the cavity linewidth varies depending on the fabrication imperfections and the phase-matching conditions with the waveguide mode). As an additional reference for Δ/γ_t, Figures 4.15a,b include the Lorentzian fit of the cavity mode resonance (black dashed line). An optical spring measurement, represented as the one in Figs. 4.15a, gives us a quick overview on the three main mechanical parameters change while the laser probe is swept across the cavity resonance: mode frequency Ω_{m}, intensity of the resonance peak α and the mechanical linewidth Γ.

It should be noted that the oscillations, that can be seen on the experimental de-

pendence, are in fact the optical interference pattern due to mixing of the propagating waveguide mode with its small fraction, reflected from the cavity and/or the waveguide termination. The period of these oscillations out of cavity resonance corresponds to an equivalent Fabry-Pérot cavity of the length equal to the one of the SOI waveguide, with the refractive index of silicon. The oscillations become twice faster when the probe laser is close to cavity resonance, which corresponds to the length shortening of Fabry-Pérot by a factor of 2; this can be explained by the partial light reflection from the PhC cavity, thus forming a shorter Fabry-Pérot resonator between it and one of the waveguide terminations.

Therefore, comparing the fundamental membrane mode M_1 and the higher-order one M_2 from Figs. 4.15a,b, we can state the following. First, the frequency Ω_m evolution of both modes clearly follows the Lorentzian shape of the cavity optical resonance, pointing out the thermomechanical tuning via the change in temperature-dependent Young's modulus of the membrane material (see the discussion in Section 4.3.6). The optically induced frequency shift of the mechanical mode attains the maximum at zero detuning $\Delta = 0$ and is more pronounced for the fundamental M_1 mode, which can be explained by their respective spatial distributions. The effective mode mass m_{eff} is 117.2 pg for M_1 and 61.8 pg for M_2, which means that twice less "amount" of membrane material is put in motion in the latter case and therefore the thermomechanical impact should be less pronounced.

Second, the mechanical linewidth Γ, which can be roughly estimated from Figs. 4.15a,b, increases when the laser probe approaches the cavity resonance $\Delta = 0$, whereas far from resonance its value converges to a certain constant value for both of modes. In addition, Γ broadening is more pronounced at the red-detuned side of cavity resonance.

Last, the amplitudes of both M_1 and M_2 modes show similar trends with clear asymmetry – the PSD spectra taken with the red-detuned probe laser demonstrate higher intensity α compared to ones taken with the blue-detuned probe. Mechanical amplitude dependence α versus detuning Δ is next fitted using Equation 4.14 in order to extract the different optomechanical coupling strengths. Figures 4.15c,d show the experimental data (blue circles) for the two mechanical modes, extracted from Figs. 4.15a,b with the corresponding fits (red lines) to our theoretical model. Zero detuning reference is marked with a dashed grey line. As can be seen, the intensity $\alpha = \bar{S}_P(\Omega = \Omega_m, \Delta)$ demonstrates striking asymmetry with respect to this line, and only the absolute values of the maxima differ between two modes. Theoretical model gives a reasonably fitted curve with the maxima of amplitude at $\Delta \approx +\gamma_t/4$ detuning.

The theoretical fit allows to extract independently the cavity transmission dependencies on different optomechanical coupling mechanisms (see Figs. 4.15e,f). As mentioned before, external and intrinsic dispersive interactions can not be distinguished experimentally, therefore we present only the total dispersive contribution with the corresponding g_ω. Figures 4.15e,f thus represent for each mode the optomechanical transduction $dT(\Delta)/dz$ (or $dT(\Delta)/d\vec{r}$) terms from Eq. 2.5, which correspond to the terms between the absolute value vertical bars in Equation 4.14. Each of the partial derivatives has a weight coefficient

g, or the corresponding optomechanical coupling strength, which is indicated for each of contributions. Two modes, M_1 and M_2, were studied within the same device; the external optomechanical coupling components are thus expected to display equal strengths for these two modes. Although g_ω refers to a total dispersive coupling, we also expect the external part to be dominant. Measured values of 0.95 GHz/nm for M_1 mode and 0.77 GHz/nm for M_2 within the imprecision of fits show thus a good agreement. External dissipative strengths $g_{\gamma,e}$ show a greater difference, which can be explained regarding the amplitude $\alpha(\Delta)$ dependencies from Figs. 4.15c,d. In the case of M_1, the mechanical amplitude at the optical resonance is non-zero, suggesting a strong contribution of the dissipative coupling mechanism (Fig. 4.15e). For M_2, though, the amplitude signal is negligible at $\Delta = 0$, suggesting a relatively larger dispersive contribution to the overall optomechanical response compared to M_1, as the opposite signs of the two dissipative contributions shown in Fig. 4.15f. A similar dependence of the mechanical amplitude $\bar{S}_P(\Omega = \Omega_m, \Delta)$ as a function of the probe laser detuning is exhibited for modes M_3 and M_4 (not shown here), slightly differing from one another for the laser detuning at which the mechanical amplitude peak is observed.

In addition, we observe in general a decreasing maximum mechanical peak amplitude as the mode index increases, which in consequence provides lesser range for the mode detection across the span of laser – cavity detuning. This can be observed by comparing the PSD amplitudes of modes M_1 and M_2 in Figures 4.15a-d – the maximum intensity of M_1 is about 3 dBm higher compared to the one of M_2 for the same probe laser power. Such tendency is also extended to the case of detection range for different mechanical modes: higher order (frequency) modes are detected within the lesser range of probe detuning (compare $\Delta = -6\gamma_t \,..\, +6\gamma_t$ for M_1 and $\Delta = -4\gamma_t \,..\, +2\gamma_t$ for M_2 in Figs. 4.15a,b).

4.3.3 Optomechanical coupling with varying phase-matching conditions

The flexibility of the sample design, permitted by the employed integrated approach, enables us to perform a detailed examination of the optomechanical coupling mechanisms as a function of phase-matching conditions between the propagating waveguide mode and the localized one of the PhC cavity. The variation of the latter conditions, as introduced in Section 2.1.3.4b, is achieved through the change in access waveguide width w_{wg}, while the separation h_{air} between the suspended PhC membrane and the waveguide circuit layer is kept constant.

Figure 4.16 illustrates three characteristic waveguide widths w_{wg} within the fabricated sample, which provide qualitatively different dependencies of optomechanical transduction as a function of the probe laser detuning Δ. From the mechanical spectra $\bar{S}_P(\Omega, \Delta)$ of M_1 mode we extract the mode amplitude in the way it was introduced in Section 4.3.2 with subsequent fitting using Equation 4.14. In all cases, the strong non-zero optomechanical signal at optical resonance ($\Delta = 0$) confirms the important contribution of the dissipative coupling mechanism for our optomechanical devices. For the narrower waveguide of $w_{wg} =$ 350 nm (see Fig. 4.16a) the maximum value of mode M_1 amplitude is reached when

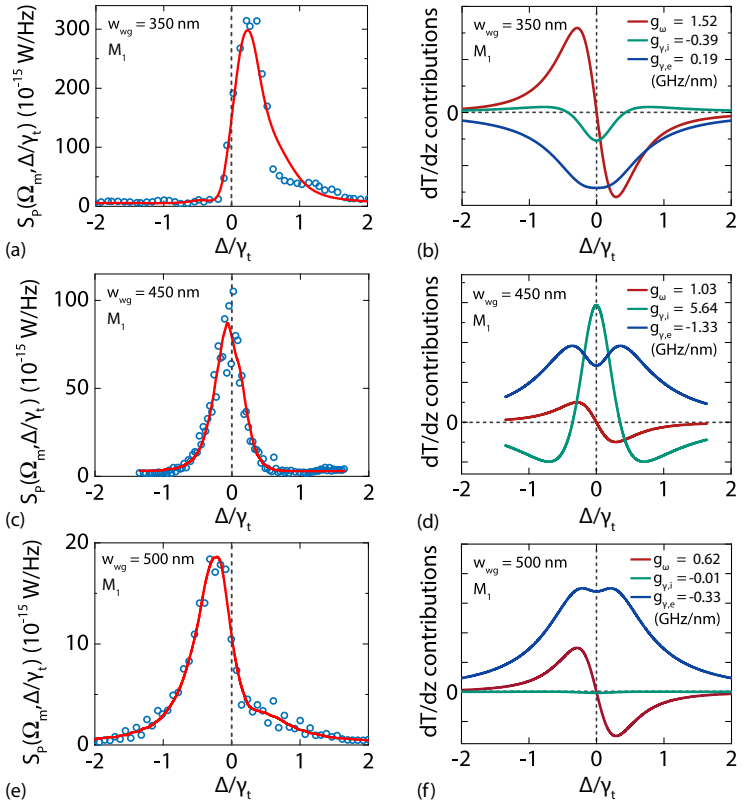

Figure 4.16: Power spectral density $S_{\mathrm{P}}(\Omega_{\mathrm{m}}, \Delta/\gamma_t)$ at the mechanical resonance (experimental data – open circles, fits to the theoretical model – solid line) for the fundamental mode M_1, measured on the devices with different access waveguide widths of (a) $w_{\mathrm{wg}} = 350$ nm, (c) $w_{\mathrm{wg}} = 450$ nm and (e) $w_{\mathrm{wg}} = 500$ nm. Probe laser detuning Δ is normalized with respect to total linewidth γ_t of the optical cavity. Corresponding optomechanical transduction contributions (b,d,e) to transmission spectrum noise (in arbitrary units; red: total dispersive coupling; green: intrinsic dissipative coupling; blue: external dissipative coupling) versus Δ/γ_t. The inferred optomechanical coupling rates are indicated.

the probe laser is red-detuned $\Delta \sim +\gamma_t/4$ with respect to the PhC cavity resonance, resembling the previously discussed case of $w_{\mathrm{wg}} = 400$ nm waveguide (cf. Fig. 4.15). Such a strong mechanical amplitude asymmetry alongside with the weak α values, measured for a blue-detuned probe laser, suggest a relatively high contribution of the dispersive coupling mechanism. Respective fitting (Fig. 4.16b) confirms this analysis, giving $g_\omega = 1.52$ GHz/nm for dispersive and $g_{\kappa,i} = -0.39$ GHz/nm with $g_{\kappa,e} = 0.19$ GHz/nm for dissipative coupling coefficients. As can be clearly seen from Figure 4.16b, the detected red-shifted mechanical amplitude maximum is a result of relative signs of the two main contributions, as measured $\bar{S}_{\mathrm{P}}(\Omega, \Delta)$ is proportional to the squared sum of their values.

In the second case, featuring an access waveguide of $w_{\mathrm{wg}} = 450$ nm width, the optomechanical response (Fig. 4.16c) is more symmetric with respect to the PhC cavity resonance wavelength, reaching the maximum about $\Delta \sim 0$ detuning. This is a signa-

ture of the predominant coupling mechanism in the device being of dissipative nature, which is as well confirmed by the fitted coupling coefficients ($g_{\kappa,i} = 5.64$ GHz/nm with $g_{\kappa,e} = -1.33$ GHz/nm versus $g_\omega = 1.03$ GHz/nm) and extracted respective optomechanical transduction components (Fig. 4.16d), where both dissipative terms are maximized.

In the third device, illustrated in Figures 4.16e,f, with the $w_{\mathrm{wg}} = 500$ nm, we measured the largest optomechanical response with a blue-detuned laser probe. Despite its asymmetry with respect to zero detuning, the optomechanical amplitude shows a significant shoulder on the red-detuned side of the optical resonance. This results (see Fig. 4.16f) from a larger contribution of the external dissipative coupling mechanism, as compared to the first case of $w_{\mathrm{wg}} = 350$ nm wide waveguide (Fig. 4.16b), yielding a predominantly external dissipative coupling operation for this device ($g_{\kappa,e} = -330$ MHz/nm, $g_{\kappa,i} = -10$ MHz/nm and $g_\omega = 620$ MHz/nm). Contrary to the first ($w_{\mathrm{wg}} = 350$ nm) case, the two major contributions – dispersive and external dissipative – have the opposite signs, which explains the mechanical amplitude maximum switch to the blue-detuned side of the optical resonance.

The variability of the intrinsic cavity Q factor, or the loss rate κ_i, which have an impact on the transduction spectral dependencies, can be attributed to the defects introduced within the material during its epitaxial growth or during the fabrication process of the optomechanical devices. Therefore the PhC cavities of identical initial design can demonstrate a slightly different additional intrinsic loss rate due to the scattering on the mentioned local defects.

4.3.4 Comparison with simulations

From the measurements, carried out in two previous Sections, we extract the values of total dispersive g_ω and external dissipative $g_{\gamma,e}$ coupling strengths as a function of waveguide width w_{wg} for the subsequent comparison with the previously computed values (cf. Section 2.3.3.2). Completed experiments, covering both M_1 and M_2 modes on devices with w_{wg} from 350 to 550 nm, are summarized in Figures 4.17a,b.

The higher values of the dispersive coupling coefficient for both M_1 and M_2 modes, observed for $w_{\mathrm{wg}} = 450$ nm access waveguide width, arise from the large optical γ_t, exhibited by this device. As a result, a significant non-zero mechanical amplitude α over a wide span of probe laser detunings Δ around the cavity mode wavelength was detected. The largest dispersive coupling for M_1 coefficient ($g_\omega = 1.52$ GHz/nm) was observed for $w_{\mathrm{wg}} = 350$ nm waveguide, owing to the strong asymmetry of the optomechanical response for this mode (see Fig. 4.16a). The largest external dissipative coupling for the same mode ($g_{\kappa,e} = -1.32$ GHz/nm) was observed in the configuration of $w_{\mathrm{wg}} = 450$ nm, as a consequence of relatively large cavity linewidth γ_t, combined with better phase-matching between the cavity and waveguide modes. Consequently, these effects result in the broad detuning interval, over which the mechanical amplitude is observed, centred with respect to zero Δ detuning, in connection with the symmetry of the optomechanical response for this mode, highlighted in Fig. 4.16c.

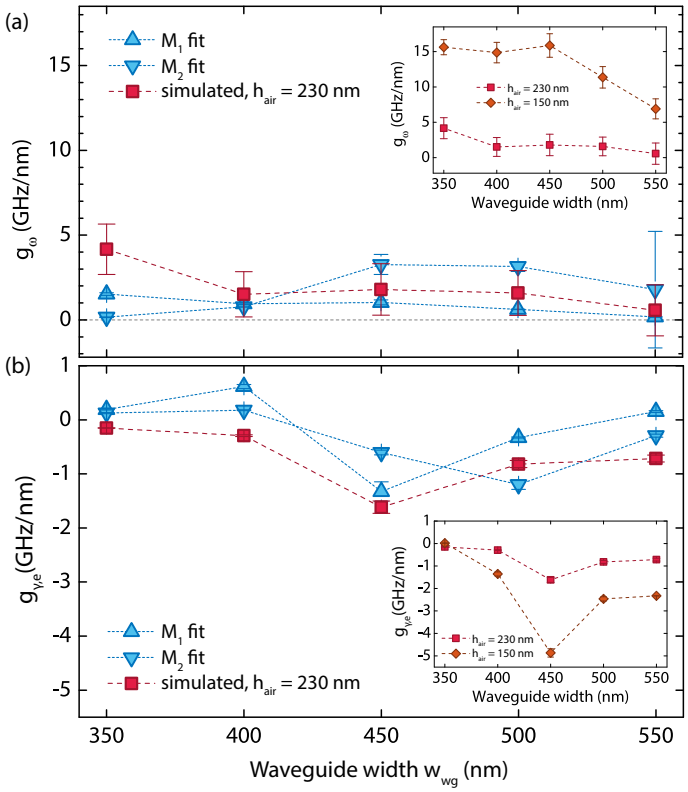

Figure 4.17: (a) Dispersive coupling coefficient g_ω (total) and (b) external dissipative coupling coefficient $g_{\gamma,e}$, plotted versus waveguide width w_{wg}. Blue up-pointing triangles correspond to the coefficients extracted from theoretical fit of M_1 mode data. Blue down-pointing triangles correspond to the coefficients extracted from theoretical fit of M_2 mode data. Red squares: values, computed with static 3D FDTD approach for the air gap thickness of $h_{\mathrm{air}} = 230$ nm. Orange diamonds: computed coupling strengths for $h_{\mathrm{air}} = 150$ nm. Insets: computed g_ω and $g_{\gamma,e}$ versus w_{wg}.

Figure 4.17 compares the coupling strengths, obtained via optical spring effect measurements (blue triangles), with the ones predicted by a complete 3D FDTD simulations (red squares), which was chosen to be the best way of numerical estimation of these quantities, as described in detail in Section 2.3.3.2. As mentioned before, the real devices could exhibit some defects created during the fabrication process, affecting the intrinsic losses γ_i of the cavity optical mode and thus its total linewidth γ_t in the way that differs from the respective computed values. To correct the simulated dissipative coupling coefficient, accounting for this discrepancy, the computed static γ_t versus h_{air} dependencies (as the ones in Fig. 2.26b) were renormalized. Keeping the same field decay length of the PhC cavity mode in the out-of-plane (z) direction, we adapt the above-mentioned dependencies such that they pass through the experimentally determined γ_t values at $h_{\mathrm{air}} = 230$ nm for each of the measured cavities. The external dispersive coupling coefficients $g_{\kappa,e}$ are next found by evaluating the numerical derivatives in the same manner, as introduced previously. As can be observed from Figure 4.17b, the $g_{\kappa,e}$ trend, computed in this way, is

very similar to the experimentally determined dependency for M_1 mode. The largest computed $g_{\kappa,e}$ value, renormalized to the real device linewidth, corresponds to $w_{\mathrm{wg}} = 450$ nm geometry, resulting from the interplay between the experimental γ_t, as detailed above, and the increasing evanescent tail of the guided mode for a decreasing w_{wg}, which should lead to a higher computed $g_{\kappa,e}$ for smaller waveguide widths. The latter effect is related to an increased length of the evanescent tail of the guided move (hence its overlap with the PhC cavity mode) for a decreasing w_{wg} dimension, owing to the spatial squeezing of the guided optical mode in the lateral direction (y).

Concerning the dispersive coupling, values of experimentally determined g_ω coefficients for M_1 resonance fall within the error bars of the computed trend (cf. Fig. 4.17a), except for $w_{\mathrm{wg}} = 350$ nm. A good agreement between the simulated g_ω and the experimental g_ω trends for M_2 is also observed, although M_1 is the mechanical mode, whose displacement pattern mainly resembles the simulated translation of the InP membrane in along the out-of-plane direction.

Another degree of freedom, brought by our heterogeneous integration approach, is the possibility to vary the separation distance h_{air} between the SOI circuit and the membrane layers. We do so by properly adjusting the thickness of the sacrificial SiO_2 layer (see Section 3.2.3 for more details), allowing to achieve a predefined optomechanical coupling. All of the experimental studies of coupling strength were carried out on the sample with $h_{\mathrm{air}} = 230$ nm, as indicated in Fig. 4.17. As predicted by the simulations (cf. Fig. 2.27), further reduction of this distance may lead to the enhancement of both external dispersive and dissipative interaction strengths. Insets in Figs. 4.17a,b provide a comparison between the actual $h_{\mathrm{air}} = 230$ nm membrane suspension height (red squares) and the one, reduced by 80 nm: $h_{\mathrm{air}} = 150$ nm (orange diamonds). The estimation of dissipative coupling coefficients in this case accounts for the optical linewidths γ_t, measured for the real devices. Significantly stronger dispersive and dissipative optomechanical interactions may be therefore expected in such resonators, however, at the expenses of a broader PhC cavity mode.

As mentioned in Chapter 2, the two degrees of freedom, brought by the heterogeneous integration of our devices, allow to tailor the strengths of the different optomechanical coupling mechanisms, as well as their ratio $\Gamma = g_\omega/g_\kappa$. This relaxes somewhat stringent requirements (the operation in sideband-resolved regime with $\Omega_{\mathrm{m}} \gg \gamma_t$), imposed for the applications such as optical ground state cooling in the case of a purely dispersive coupling [Marquardt 2007]. In our case of non-zero dissipative coupling, cooling in the unresolved-sideband regime ($\Omega_{\mathrm{m}} \ll \gamma_t$) is permitted [Weiss 2013]. Further, the varying asymmetry of the optomechanical response of our devices $\bar{S}_{\mathrm{P}}(\Omega_{\mathrm{m}}, \Delta/\gamma_t)$ as a function of w_{wg} stems from a change in the relative signs of the optomechanical coupling coefficients. This tailored coupling makes our optomechanical system potentially capable of reaching the optimal mixed coupling Γ ratio, including their correct relative sign, which ultimately yields the minimal phonon number $\bar{n}_{\mathrm{min}}$ (cf. Section 2.4), paving the way to an optimal mechanical mode cooling to its ground state.

4.3.5 Spectral dependence of mechanical damping

Figures 4.15a,b present a clear manifestation of mechanical linewidth Γ_m dependence on the probe laser detuning Δ with respect to the cavity resonance. In this Section we quantify this effect and study on the example of the fundamental mechanical mode how such dependence varies with the changing phase-matching conditions between the cavity and waveguide modes.

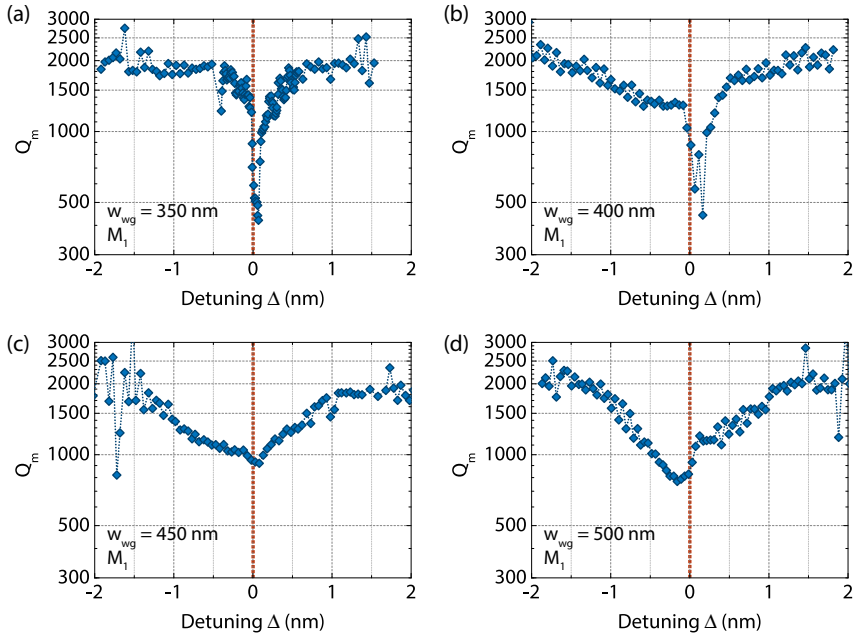

Figure 4.18: Mechanical quality factor Q_m of the fundamental flexural membrane mode (M_1) on laser-cavity detuning for identical devices with only one varying parameter – the access waveguide width w_{wg}: (a) 350 nm, (b) 400 nm, (c) 450 nm and (d) 500 nm. The measurements were performed using the same input optical power P_0.

Experimentally measured Q_m trends are illustrated in Figure 4.18 for the devices, studied in Sections 4.3.2 and 4.3.3. Detuning range of the probe laser covers a larger range in the current study to include the relevant data. For all the four devices we can observe the fundamental mode within the region, covering about ± 2 nm detunings from the cavity resonance λ_0, which is shown in Fig. 4.18. For the same constant nominal power P_0 of the probe laser, corresponding to about 200 μW of intra-cavity power P_c (at resonance $\Delta = 0$) and allowing to work in the linear regime of its operation, we observe peculiar trends of laser cooling between different mechanical devices.

As a general rule we observe a Q_m factor value saturation approximately between 2000 and 2500 when the probe laser is tuned far away from the cavity resonance linewidth (Fig. 4.18), which allows to determine the value of the intrinsic[5] quality factor without influence

[5]As the device temperature defines the intrinsic mechanical losses within the material, here by the intrinsic quality factor we intend its value at the current environment temperature $T_b \approx 300$ K.

from dynamical backaction effects. Looking independently at each of dependencies for different widths w_{wg} of access waveguide, one can identify the trends that reflect the inverted mode PSD, as studied in Section 4.3.3. Therefore, the optomechanical cooling of mechanical modes of our device can be as well performed and tailored according to the respective strength of dispersive and dissipative couplings. The cooling dependencies on probe detuning for different geometries of the access waveguide reflect the corresponding mechanical device responses (peak amplitude $\alpha_{\mathrm{m}} = f(\Delta)$), as shown in Figures 4.15c and 4.16a,c,e. In the case of dominant dispersive coupling ($w_{\mathrm{wg}} = 350$ and 400 nm) the most efficient cooling is observed for $\Delta = \pm\gamma_t/4$ detunings, corresponding to the maximum strength of the total optomechanical coupling (see Section 2.3.2 for details). In the case of cooling in dominant dissipative regime, as suggested in Section 2.4, the most effective cooling is expected at $\Delta = -\Omega_{\mathrm{m}}$ detuning, which in the present measurement could not be resolved ($\Omega_{\mathrm{m}} \ll \gamma_t$), requiring a precise locking to the optical cavity resonance and much finer control of the probe laser detuning. When the mechanical resonance is probed at high optical input power, the induced thermal effects will reflect the cooling efficiency dependence, shown here for a low input power. This is discussed in more details in the following Section.

4.3.6 Thermally induced effects at high coupled probe powers

Optical absorption of the probe laser in the semiconductor cavity may lead to material heating at high input powers of the laser probe. Generally speaking, the electrostatic forces holding atoms together in bonds would decrease as the bond length increases, which happens during the thermal expansion of material. These forces are at the origin of the macro-scale elastic moduli, including the Young's modulus E. The change in E, resulting in the modification of the mode frequencies of the mechanical resonator, is thus considered as a thermomechanical effect.

Experiment in [Wachtman 1961], performed on several single crystal and polycrystalline oxides, proposes a following E dependence from temperature T:

$$E = E_0 - BT\exp(-T_0/T), \tag{4.15}$$

where E_0 is the Young's modulus at $T = 0$ K, T_0 is an empirical parameter, so that at high temperatures E follows a constant slope B, which decreases as the temperature lowers and becomes zero when $T \to 0$ K as required by third law of thermodynamics. As mechanical eigenfrequency is proportional to the Young's modulus of material, we can directly verify the dependency suggested by Eq. 4.15 by recording the eigenmode frequency $\Omega_{\mathrm{m}}/2\pi$ versus input optical power P_{in} using the experimental set-up (Fig. 4.9) for the readout of Brownian motion.

Taking into account the weak amplitude of M_3 mode (cf. Fig. 4.10), the study of the thermomechanical effects was carried out on the M_1, M_2 and M_4 resonances in order to have enough dynamics over a large span of input optical powers. The tunable laser from

our experimental set-up (Fig. 4.9) has a limited range of output powers in stable working regime ($1 - 14$ mW), therefore an additional EDFA (Keopsys CEFA-C-PB-HP-SM-30, 30 dBm maximum output) was included for its amplification (placed before FPC in the scheme) in order to enlarge the span of accessible probe powers towards higher values. From another side, a 10 dBm optical attenuator was used to achieve the probe range extension towards lower powers (instead of setting the laser source to the output powers close or less than its threshold, that would degrade its output spectrum purity by adding an ASE component). These modifications allowed us to work within the range from 0.1 mW to 1 W of probe power P_0, whereas the intracavity power P_c typically equals $1 - 10$ % of P_0 amount, depending on the coupling objective alignment, used grating couplers and coupling strength η between cavity and SOI waveguide.

Figure 4.19 shows the evolution of main characteristic mechanical parameters versus intracavity optical power P_c. Each type of measurement is shown for both linear and logarithmic power scales, which helps to reveal the characteristic regions and the corresponding trends in the evolution of the parameters of interest. Measurements were performed in the system thermal equilibrium state, i.e., on the time scale much bigger compared to the thermal diffusion time in our structures of the order of microseconds [Brunstein 2009]. Due to the changes of laser probe relative position with respect to the cavity resonance, we can only consider a linear dependence $P_c \propto P_0$ for the power range not highlighted in yellow in Fig. 4.19, i.e., for $P_c > 1$ mW. The mechanical frequency $\Omega_\mathrm{m}/2\pi$ (Fig. 4.19a, b) shift is negative for all three modes, which corresponds to material softening, or decrease of its Young's modulus. $\Omega_\mathrm{m}/2\pi$ in Fig. 4.19a shows a similar monotonic trends with two characteristic regions: $P_c < 1$ mW and $P_c > 1$ mW.

As was demonstrated in [Bazin 2013], material temperature is directly proportional to the coupled optical power $T \propto P_c$. From the numerical simulations of the mechanical eigenfrequency Ω_m dependence on material Young's modulus, we found that $\Omega_{\mathrm{m},1}/\Omega_{\mathrm{m},2} = \sqrt{E_1/E_2}$, or, $\Omega_\mathrm{m} \propto \sqrt{E}$. Figure 4.19b shows the experimental evolution of the mechanical frequencies for three different modes, linearly scaled with coupled power. Fitting with the function, derived from Eq. 4.15, didn't give any satisfying results. However, for $P_c >$ 1 mW region, the given trends were fitted quite well using a simple decaying exponential dependency

$$\Omega_\mathrm{m} = \Omega_{\mathrm{m},0} + A\exp(-T/T_0), \tag{4.16}$$

where $\Omega_{\mathrm{m},0}/2\pi$ is the mechanical mode frequency in the absence of laser probe, A and T_0 are the parameters of exponential fit. With the above-stated considerations for the frequency evolution versus intracavity power, we can now write the thermomechanical relation, describing the Young's modulus dependence on material temperature in our system

$$\Delta E = B\exp(-T/2T_0), \tag{4.17}$$

where $B = \sqrt{A}$ and T_0 are the parameters found from the corresponding fit of frequency trend in Fig. 4.19b.

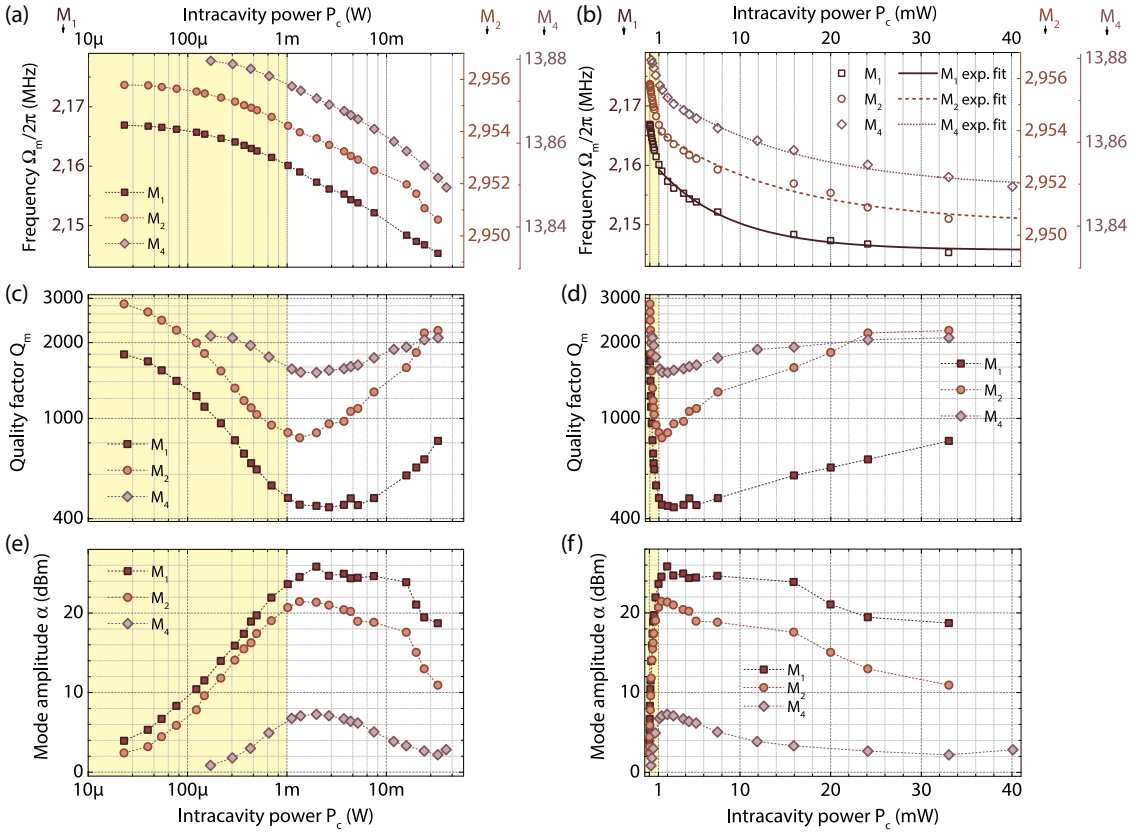

Figure 4.19: Study of thermally induced effects for mechanical modes M_1, M_2 and M_4 (cf. Fig. 4.10) as a function of intracavity power P_c. (a,b) Mechanical frequency $\Omega_m/2\pi$ (scales for each of modes are given in the corresponding colour). (c,d) Mechanical quality factor Q_m. (e,f) Amplitude α of the mode in PSD spectrum. Yellow-highlighted range ($P_c \leqslant 1$ mW) corresponds to the part of experimental data, where linear dependence between incident laser power P_0 and the intracavity power P_c is distorted due to thermo-optical effects. Due to the latter effects (with increasing intracavity power cavity resonance shifts to the greater wavelengths and acquires a triangular profile instead of Lorentzian) and the fact that the laser probe fixed to a certain initial wavelength and not locked to the cavity resonance, the yellow-highlighted region approximately corresponds to the red-detuned pump configuration ($\Delta > 0$) and the $P_c > 1$ mW region – to the blue-detuned one ($\Delta < 0$).

Impact of intracavity power on damping of the mechanical modes is represented in Figures 4.19c,d. We point out, however, that the observed dependencies are the result of mainly combined thermo-optical and optical spring effect for each particular waveguide – cavity coupling conditions. This study is carried out by fixing the laser probe on the rising edge of the cavity Lorentzian in waveguide transmission, i.e., laser is red-detuned ($\Delta = +0.05$ nm) with respect to the cavity wavelength λ_0. The system studied in Figure 4.19 includes a waveguide with $w_{wg} = 500$ nm, therefore, the coupled P_c dependence should be combined with the cooling efficiency of the mechanical resonance, as measured

for linear optical spring effect (Fig. 4.18d). Considering that initial Q_{m} (i.e., estimated for the lowest probe power) is not affected by the thermomechanical effects, we observe about a factor of 4 damping for first two flexural modes and a similar trend for M_4, but with less effective cooling. Local minima, present on all three trends, can originate from the change in coupling conditions to the cavity. As a matter of fact, when feeding an increasing optical power inside a semiconductor cavity, one can expect a red-shift of its resonance together with an apparition of bi-stable spectral response [Shankar 2011] while the symmetry of the Lorentzian shape gets broken, allowing the laser probe locking exclusively to the blue-detuned side. Taking into account such behaviour, our initially (at the lowest P_c power) red-shifted (compared to the cavity resonance) laser probe will become blue-shifted as the input power increases and shifts the λ_0 (while probe laser remains at its initial wavelength), and at some moment match the resonance wavelength $\lambda_0^{'}$ of the heated cavity (this zero detuning corresponds also to the best coupling efficiency from waveguide to cavity, compared to any other detuning). We expect this particular point to correspond to the mentioned local minima of Q_{m} trends. When the coupled power is further increased, the cavity resonance will experience even bigger red-shift, leading to the constant laser probe withdrawal from the best coupling position and therefore a lower fraction of the incident power coupled into the cavity. The passage from red-detuned to blue-detuned pump configuration in this way explains the decreasing efficiency of mechanical mode cooling, as can be seen in Fig. 4.19c. The two characteristic regions can be easily spotted from the linear trends of the Q_{m} factor in Fig. 4.19d. Different values of local minima can be explained by corresponding optomechanical coupling strengths between the optical and different mechanical modes.

The last parameter we investigated in this experiment is the amplitude α of mechanical mode in recorded PSD spectrum (Figs. 4.19e,f). This study confirms the hypothesis about rising thermo-optical effects at high coupled P_c powers, superimposed with the optomechanical coupling efficiency versus laser-cavity detuning (cf. Fig. 4.18), which have to be simultaneously taken into account. Value of α in a general way is related to the modulation of the probe signal by the mechanical oscillations within the probed device, that is, which amount of laser power circulating in the set-up scheme is reaching the active part of our device and gets coupled to its movement. The suggestions considering the cavity resonance red-shift due to thermo-optical effects and related changes in the efficiency of probe laser coupling into the cavity, expressed above, are fully confirmed by the trends in Figs. 4.19e,f. First, for the rising P_c powers up to $1-2$ mW, the probed amplitude α increases monotonically due to both increase in the total optical power in the circuit and increase of the coupling efficiency from access waveguide into the cavity, since the probe approaches its shifted wavelength $\lambda_0^{'}$. In the second regime (P_c powers within $1-10$ mW) amplitude α slowly decreases as a result of interplay between increasing incident laser power and coupling efficiency decrease while the laser – cavity blue detuning increases. Finally, a the highest powers investigated in this study, the probe laser is shifted considerably far from the cavity resonance, which decreases the coupling efficiency, leading

to a considerably smaller fraction of incident power taking part in the optomechanical interaction (i.e., being modulated).

All the experiments described in the previous Sections were performed at low coupled P_c powers, so that to have sufficient dynamics over a measured parameters range and to avoid interference with the thermally induced optical and mechanical effects, described above.

4.4 Non-linearities in optical and mechanical device responses

In this Section we present the ongoing part of experimental studies on the integrated platform, aimed at a better understanding of the role of the active medium, embedded in our device, and of the thermo-optical properties of used semiconductor materials, on the optomechanical or mixed response of our devices.

4.4.1 Thermo-optical behaviour of semiconductor cavity

Coupling high amounts of optical power inside a semiconductor even above its band gap may lead to its partial absorption by the material via different mechanisms and consequently leading to its heating. The refractive index of bulk semiconductors, including InP, is dependent on temperature, therefore the effective mode index n_{eff} of a PhC cavity mode shows a temperature dependence as well. Because of such n_{eff} dependence, when slowly scanning a laser probe over a cavity resonance at high laser power with the laser wavelength coming from the blue-detuned side ($\Delta < 0$), this resonance is progressively red-shifted as the power increase induces rising temperature in the PhC slab membrane. It was shown [Almeida 2004] that such thermo-optical shift is the origin of the optical bi-stability in the semiconductor devices, usually manifested by a triangular optical resonance profile instead of the traditional Lorentzian shape, recorded at low probe laser power.

The semiconductor cavities in our devices demonstrate such triangular resonance shape, as shown in Figure 4.20a. Probe laser powers, coupled inside the cavity (P_c), as indicated in the legends of Fig. 4.20, are calculated with the same coupling conditions assumptions as the ones for data set in Figure 4.19. Figure 4.20a demonstrates slow probe laser scans over the resonance of the same cavity, performed from lower towards higher wavelengths (hereinafter designated as "sweep up") with a constant scanning speed of 2 nm/sec. The cavity response shows clear non-linearity, progressively changing the symmetric Lorentzian shape of resonance (Fig. 4.20a, 10 μW) to asymmetric triangular (Fig. 4.20a, 1.4 mW) as the intracavity power P_c increases. For high powers, such triangular resonance profiles can be extended to the red-detuned spectrum region by amount of several initial cavity linewidths (Fig. 4.20a, 4.9 mW). The cavity response modulation, as observed on all

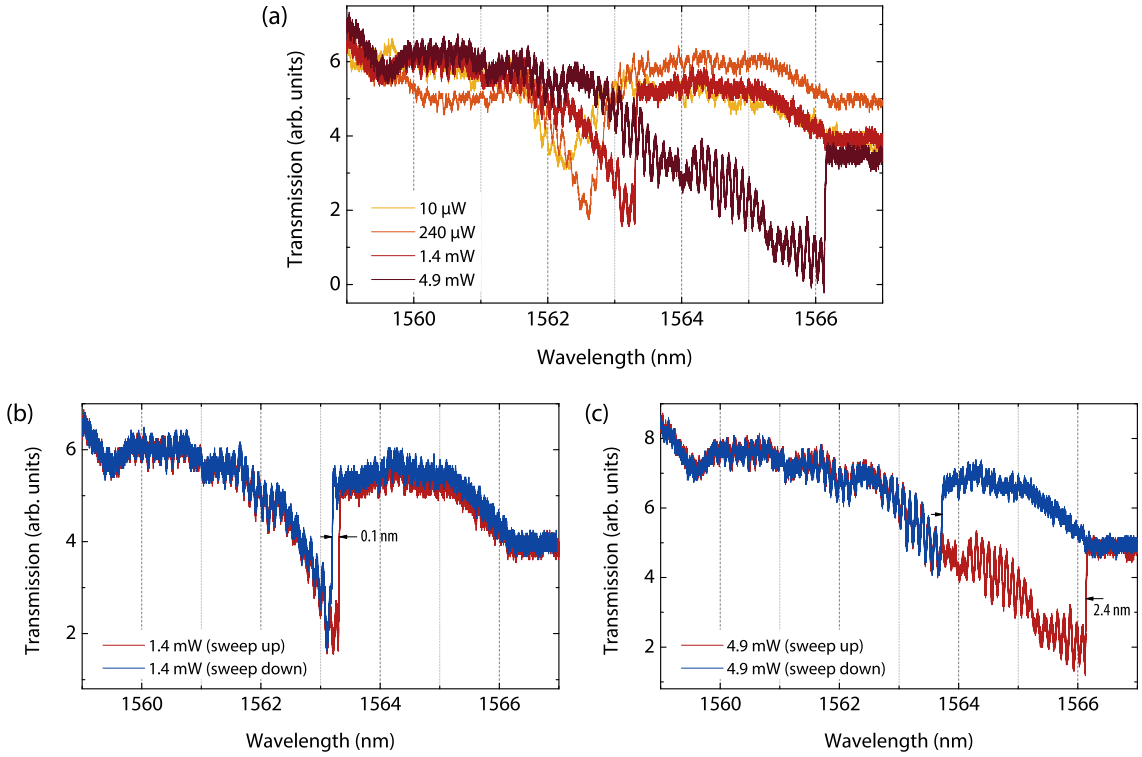

Figure 4.20: Recorded response of the PhC cavity, probed through the integrated access waveguide at different intracavity powers P_c (indicated in the legends). (a) Probe laser scanned from blue-detuned to red-detuned side. (b,c) For a constant P_c power, laser is scanned from lower to higher wavelengths ("sweep up") and in the opposite direction ("sweep down"). The wavelength scan speed in all the experiments shown was 2 nm/sec with the laser operating in CW regime.

traces, is due to the interference of incident probe wave with the one, reflected from the cavity or the waveguide terminations, as described in more details in Section 4.3.2.

We characterized the optical bi-stability in these cavities by performing forward ("sweep up") and backward ("sweep down") probe laser scans over their resonances, as shown in Figures 4.20b,c. For two intracavity power values, for which in Figure 4.20a an asymmetric cavity response was observed (1.4 mW and 4.9 mW), we observe a strong increase of the bi-stable region with increasing intracavity power P_c, mainly due to the greater thermo-optical shift in the red-detuned direction. Backward laser scan ("sweep down"), in turn, would generally result in a similar responses of the cavity with for different input powers. As the sweep direction is opposite to the non-linearity pulling one, the laser probe can not encounter the right-side hop far from the initial (probed at low power) cavity resonance, where it occurs during the forward scanning. Both scanning directions were examined at different speeds of laser sweep from 0.01 nm/sec to 10 nm/sec, accessible within the current set-up. It was observed that non-linear cavity response is perfectly reproduced at low speeds (up to $4-5$ nm/sec), whereas for higher speeds the features in

transmission spectrum, coming from the above-described interference effects, start to flatten. For a continuous wave operation of the laser probe it is known that such non-linearly responding optical system allows to memorize the history of laser scanning direction and consequently follow the forward or backward curve in the hysteresis loop, which describes the above-mentioned fidelity property for low scanning speeds.

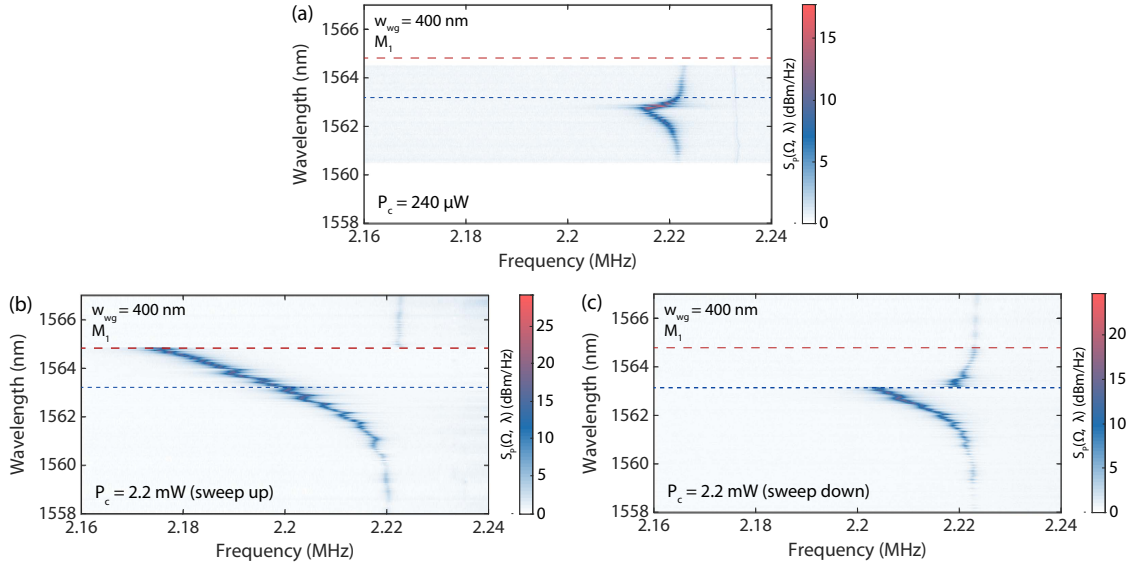

Figure 4.21: Power spectral density $S_{\mathrm{P}}(\Omega, \lambda)$ for the mechanical modes M_1, measured for the device with access waveguide of $w_{\mathrm{wg}} = 400$ nm at two different probe laser powers and scanning directions with respect to the cavity resonance. Optical spring response, measured in (a) linear regime of optical cavity ($P_c = 240$ μW; data from the experiment in Fig. 4.15a) and bi-stable regime ($P_c = 2.2$ mW) for forward (b) and backward (c) laser scanning directions. Dashed red and blue lines indicate the mechanical frequency jumps for "sweep up" (b) and "sweep down" (c) responses of the system.

Having characterized the optical response cavity to high-power scans of the probe laser, we next look at the mechanical response, recorded while device is working in the non-linear optical regime. As a reference for the linear regime of optical cavity we take one of the previous measurements (with intra-cavity power $P_c = 240$ μW) of the optical spring response of the fundamental mechanical mode (M_1), represented in Fig. 4.15a and rescaled in Fig. 4.21a. Figure 4.21 compares the optical spring measurement in the linear regime of the optical cavity with two characteristic measurements carried out with the probe powers which result in its bistable optical response. Taking into account the performed characterization of the bi-stable region spectral width change for different intra-cavity powers (Fig. 4.20), we choose a P_c for the current experiment to have this region comparable (about $1.5 - 2$ nm wide) to the linewidth of the cavity mode in linear regime ($P_c = 2.2$ mW). For the mechanical responses, recorded versus laser – cavity detuning at this power following two scanning directions (Fig. 4.21b,c), we clearly observe that the mechanical system state follows the optical cavity response, which can be explained by thermomechanical effects

(cf. Section 4.3.6), eventually combined with the optical spring effect, modified in view of cavity resonance shape distortion. For qualitative comparison between three different mechanical tuning curves, in Figures 4.21a-c we indicate the respective wavelengths for mechanical frequency jumps during forward (b) and backward (c) laser scanning directions, which gives us about 2 nm large region where two mechanical states exist for the same incident laser power. As demonstrated in Figures 4.21b,c, the mechanical mode shifts by amount of tens of its linewidths from its initial state ($\Gamma_m \sim 1$ kHz for $\Omega_m = 2.22$ MHz), which allows the two mechanical states in the bi-stable region to be well identified and spectrally distinguishable.

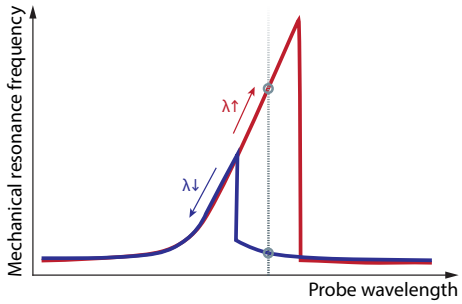

Figure 4.22: Sketch illustrating a proposal for exploring the optically induced mechanical bi-stability. Schematically traced mechanical state dependencies on probe laser detuning with respect to the cavity resonance for forward (red trace) and backward (blue trace) scanning directions. Dotted grey curve indicates an example probe detuning, corresponding to two different mechanical states depending on the scanning history.

Further exploring of this feature of our optomechanical system is schematically illustrated in Figure 4.22. We trace the approximate mechanical state evolution from the last two experiments (Figs. 4.21b,c) versus probe laser wavelength, indicated as $\lambda\uparrow$ and $\lambda\downarrow$, respectively. Therefore, for a certain range of probe wavelengths we are able to put the system into one of the stable states, depending on the probe scanning history. However, since the mechanical state directly follows the optical response of the cavity in its bi-stable regime, in order to achieve a switching between two existing mechanical states it is necessary to do so for the optical switching. The latter is ensured upon condition to exceed a certain threshold (as characterized in Fig. 4.20a) and providing that the detuning between the injection beam and the cold resonance is larger than $\sim \sqrt{3}\gamma_t/2$ (in absolute value) [Brunstein 2009], where γ_t is the total linewidth of the optical cavity.

4.4.2 Optical modulation transduction by active medium

The InAs(P) quantum dots layer in the middle of our PhC slab membranes was until now only used for the alignment of the sample with respect to the set-up for transmission measurements (cf. Section 4.2.2). For this purpose, the QDs are suited for efficient non-resonant pumping at 600–800 nm (1.5–2 eV) below the InP gap ($\sim$ 900 nm) with subsequent broadband emission in the near IR range, filtered by the defect PhC cavity.

From another side, these QDs show some optical absorption at 1550 nm (0.8 eV), e.g., by two-photon absorption mechanism, which increases the optical cavity losses and thus broadens its resonance linewidth while its probed by a ~ 1.55 μm laser in the optomechanics experiments. By saturating the active medium it is possible to cancel such absorption; this mechanism is investigated in the current Section.

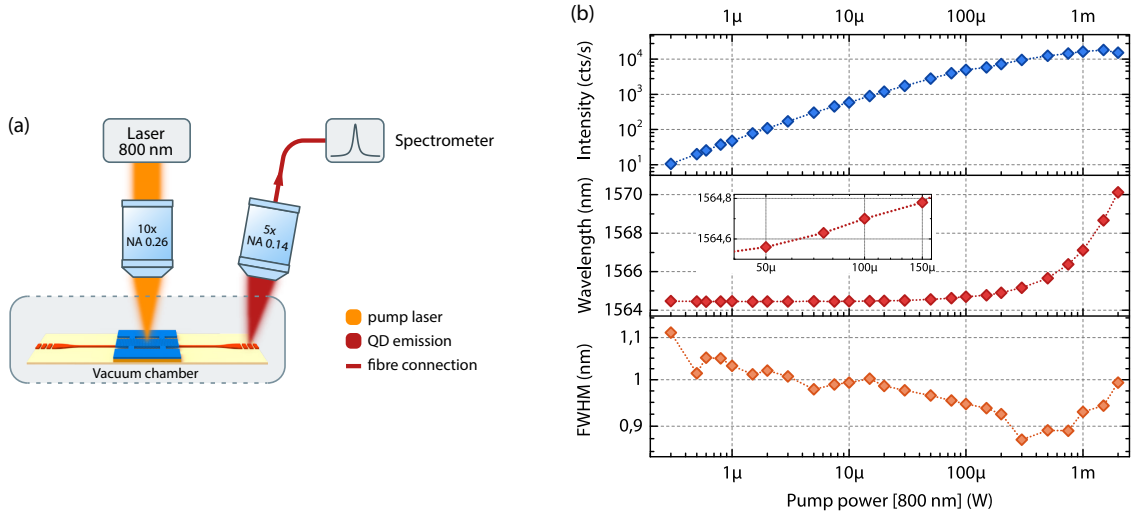

Figure 4.23: Emission properties of the QDs, filtered by the L3 cavity (PhC parameters: $a = 420$ nm, $r = 100$ nm, membrane size 4.8×8.5 μm^2; $w_{\mathrm{wg}} = 350$ nm, $h_{\mathrm{air}} = 230$ nm) under non-resonant (~ 800 nm) pumping (laser operates in CW regime). Experimental set-up is depicted in (a); fitted intensity I, wavelength λ_0 and linewidth γ_t of the collected emission are plotted versus pump power in (b).

Figure 4.23a describes the optical set-up, where the continuous wave (CW) pump laser ($\lambda_{\mathrm{pump}} \sim 800$ nm) is focused on the membrane surface with the microscope objective. The QDs luminescence, filtered by the cavity and partially guided thorough the SOI waveguide, is read out by the spectrometer after being collected from one of the waveguide grating couplers by another microscope objective. The equipment used is described in Section 4.2.1.

Although the lasing from similar structures was demonstrated at room temperature [Hostein 2010], we did not observe any kink in the light-in–light-out (L-L) curve under CW excitation (top graph in Fig. 4.23b), suggesting that no laser threshold exists in the current configuration, and the measured signal consists exclusively of the spontaneous emission of the active medium. This can be explained by strong losses of the optical cavity mode, induced by the presence of the access waveguide in its evanescent field, therefore the system gain is not sufficient to compensate it. The linewidth of the cavity resonance shows a non-negligible decrease (bottom graph in Fig. 4.23b) as the pump power becomes more important, demonstrating the progressive saturation of the QDs and consequently the decrease of the optical losses, associated with the two-photon absorption. At high pump powers (middle graph in Fig. 4.23b) the emission wavelengths shift toward the

longer wavelength, owing to important thermal effects. Finally, a thermal degradation of the QDs emission is observed at a pump powers higher than 1 mW with a simultaneous increase of the emission linewidth (bottom graph in Fig. 4.23b), which is most probably due to important thermal fluctuations.

These measurements indicate that within a certain range of laser pump powers P_{pump} the derivatives $g_{\omega,\mathrm{QD}} = d\omega_0/dP_{\mathrm{pump}}$ and $g_{\gamma,\mathrm{QD}} = d\gamma_t/dP_{\mathrm{pump}}$ are non-zero (e.g., see the inset in Fig. 4.23b), therefore we can establish an analogy with dispersive and dissipative coupling coefficients, where modulation of the membrane coordinate is replaced by the modulation of P_{pump} power. To put some numbers, we estimate the modulation coefficients around $P_{\mathrm{pump}} = 100$ μW value, where the thermal effects do not degrade the QD emission, which results in $g_{\omega,\mathrm{QD}} \approx 275$ MHz/μW and $g_{\gamma,\mathrm{QD}} \approx 33.5$ MHz/μW. Using the device in this region of ω_0 and γ_t trends as a function of P_{pump}) we should be able to detect the dispersive and dissipative impacts of pump laser modulation on the cavity optical parameters.

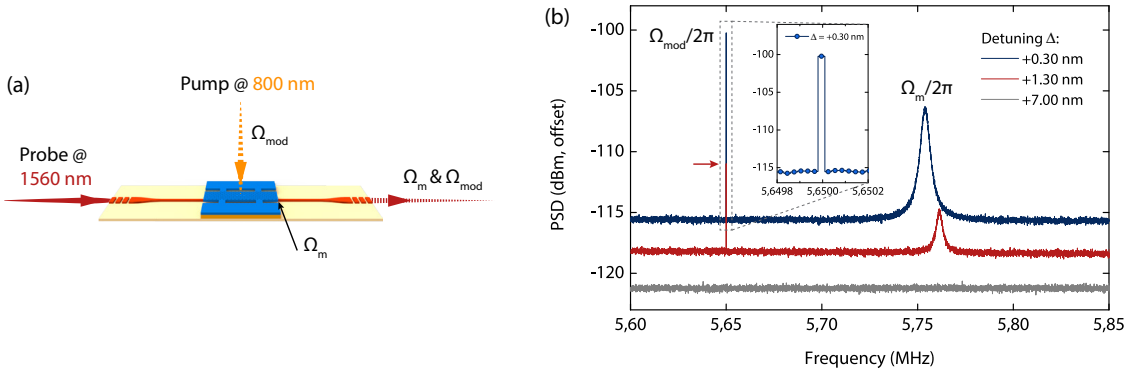

Figure 4.24: (a) Schematic of the experimental set-up for the characterization of optical/optomechanical transduction of non-resonant pump ($\lambda_{\mathrm{pump}} \sim 800$ nm) to resonant probe ($\lambda_{\mathrm{probe}} \sim 1.56$ μm). (b) ESA spectra of the probe light, coupled to the defect cavity inside a PhC slab membrane with a layer of quantum dots in the middle, pumped non-resonantly at normal incidence. Pump laser power is modulated at $\Omega_{\mathrm{mod}}/2\pi$ through the modulation of diode current (AC component is $< 3\%$ of DC one). Shown curves are taken at different laser – cavity detunings $\Delta = \lambda_{\mathrm{probe}} - \lambda_0$, where cavity resonance is $\lambda_0 \sim 1563$ nm. Lorentzian-shaped peak at $\Omega_{\mathrm{m}}/2\pi$ corresponds to the fundamental mechanical mode of the membrane (dimensions: $m_x = 8.5$ μm, $m_y = 4.8$ μm, $t = 260$ nm, $b_x = 0.5$ μm, $b_y = 2$ μm, $b_d = 5.9$ μm) Brownian motion. Inset: close-up of the modulation peak showing its resolution-limited detection (ESA resolution bandwidth is 10 Hz).

To detect such effects, we employ the side of the fringe technique (intracavity power $P_{\mathrm{c}} \sim 100$ μW), used previously for the detection of Brownian motion (cf. Section 4.2.3). The experimental set-up, sketched in Figure 4.24a, is identical with the one depicted in Fig. 4.9; in addition the cavity is pumped with $\lambda_{\mathrm{pump}} \sim 800$ nm CW laser whose output power is $P_{\mathrm{pump}} = 34$ μW. A small P_{pump} modulation with a sine function is performed via the current modulation input in pump laser diode controller (ILX Lightwave LDC-

3724C) by a function generator. Taking into account the modulation depth and respective transduction parameters (amplitude of 20 V_{pp} from function generator; controller transduction 20 mA/V ; calibrated laser diode responsivity $\sim$ 4.67 mW/A within the range of used P_{pump} powers), the approximative power output of the 800 nm pump laser is $P_{pump} \approx 34.00 \pm 0.93$ μW.

Examining the noise spectra of the transmitted probe light, coupled to the defect PhC cavity resonance, at different laser – cavity detunings Δ and close to the fundamental mode frequency of the membrane Brownian motion we observe (see Fig. 4.24b) two resonance peaks: the one corresponding to the mechanical mode at $\Omega_m/2\pi$ and the other to the modulation frequency $\Omega_{mod}/2\pi$ of non-resonant pump laser. As can be seen, both resonances disappear when the probe laser is not coupled to the cavity resonance (grey curve in Fig. 4.24b), confirming that the optomechanical interaction and the one due to the present active medium are impacting the cavity mode (i.e., its resonance frequency and linewidth) and therefore this modulation is imprinted into the resonant probe laser. For the mechanical mode at $\Omega_m/2\pi$ we observe the optical spring effect in the same way it was described in Section 4.3.2: the mechanical mode amplitude α_m, linewidth Γ_m and frequency Ω_m are changing when the laser probe is swept across the cavity optical resonance. Concerning the modulation peak, the fact that the detected resonance doe not come from direct modulation of the probe laser carrier, but in a certain way is transferred to it through an intermediate, which in our case is the active medium inside the PhC membrane, does not allow to affirm that the modulation peak frequency, linewidth and amplitude should not change since defined via the settings of the used equipment (pump laser and function generator). From Figure 4.24b, neither the detected modulation frequency of the pump laser $\Omega_{mod}/2\pi$ nor its linewidth [6] change during such sweep of the probe laser (at least such changes are not detectable with the used resolution); only its amplitude α_{mod} changes – this effect is investigated in the following.

We compare such amplitude change for the pump modulation peak, read out by the probe laser, with the evolution of the mechanical amplitude of the fundamental membrane mode by performing the optical spring effect measurement as introduced in Sections 4.3.1 – 4.3.3. To confirm that the cavity resonance is not influenced by the resonance pumping effects, described in Section 4.4.1, we compare the mechanical response of the M_1 resonance for two scanning direction of the probe laser (Fig. 4.25a) for the P_{probe} power, used for the present experiments (corresponding to $P_c \sim 100$ μW). Two responses are almost identical with no abrupt jumps (the discrepancies are related to slight fluctuations of the sample position with respect to the incident probe beam during the measurement series: acquisition time of a single curve from Fig. 4.25 is about few hours), which confirms that no optical bi-stability is induced for a used probe laser. The recorded mechanical responses $\alpha_m = f(\lambda_{probe})$ are similar to those measured previously for the same geometry of the access waveguide (see Fig. 4.16a). At the same time we measured the evolution of

[6] Showed to be extremely narrow; current detection scheme with the ESA resolution bandwidth of 10 Hz was not sufficient to resolve the modulation peak – see inset in Figure 4.24b.

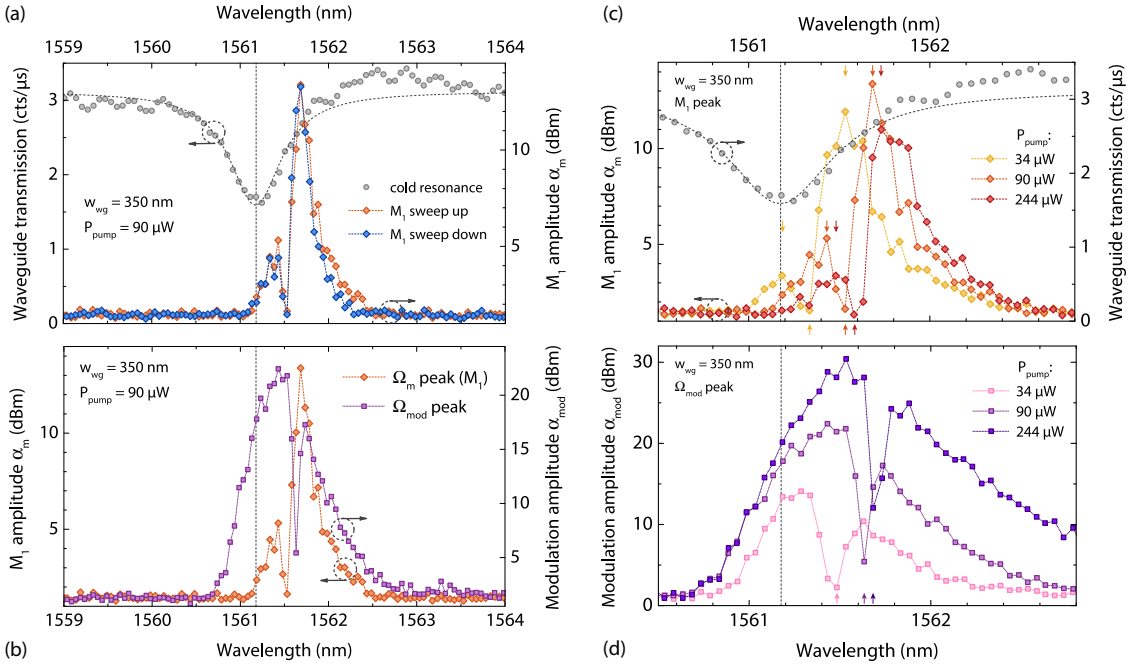

Figure 4.25: Amplitude dependencies of mechanical resonance (at $\Omega_m/2\pi$; membrane parameters correspond to the ones indicated in Fig. 4.24) and transduced modulation peak (at $\Omega_{mod}/2\pi$), as demonstrated in Fig. 4.24b, versus probe laser detuning. Cold resonance response of the optical cavity with its Lorentz fit in (a,c) refers to the cavity probing at very low power (see details in text). Except this reference cavity measurement, all studies in this Figure were performed at the same probe laser power, corresponding to the intracavity power $P_c \sim 100$ μW; at room temperature $T_b = 294$ K and at low pressure $P < 10^{-4}$ mbar. (a) Mechanical M_1 mode response, acquired for the probe laser forward (sweep up) and backward (sweep down) scanning direction. (b) Evolution of the mechanical mode and modulation peak amplitude for the forward scanning direction of the probe laser. Response of the mechanical mode (c) and modulation peak (d) for a set of different pump laser powers P_{pump} (as indicated in legends).

the modulation peak intensity $\alpha_{mod} = f(\lambda_{probe})$, which exhibits a mirror-like symmetry compared to α_m trend, however, with a broader response (at the probe laser detuning scale) (Fig. 4.25b). This symmetry was measured and exists for another access waveguide geometries as well. The response broadening in the case of modulation peak is not yet explained and has to be further investigated.

According to the experiment in Fig. 4.23b, an increasing pump power results in a red-shift of the cavity resonance (although its shape is still a symmetric Lorentzian). We study the impact of such red-shift on the responses of the mechanical mode (Fig. 4.23c) and modulation peak (Fig. 4.23d) for several P_{pump} values (the amplitude of pump laser modulation is kept constant). As can be seen from the corresponding graphs, both quantities, α_m and α_{mod}, shift their trends towards the bigger wavelengths from the reference cold resonance (grey circles with Lorentzian fits in Figs. 4.25a,c, refer to the measurement

of the cavity resonance wavelength in ASE regime of the probe laser, as detailed in Section 4.2.2, showing the cavity response not affected by either resonant or non-resonant pumping).

To get a better insight into the physical phenomenon in the origin of the modulation transduction from non-resonant pump to resonant probe carrier, the evolution of the modulation amplitude α_{mod} can be studied as a function of the modulation frequency Ω_{mod}. Two possible mechanisms can be the thermal effects with the characteristic times of the order of microseconds ($\sim$ MHz modulation frequencies) [Usami 2012] or the absorption and re-emission from quantum dots with the characteristic times in the nanosecond range ($\sim$ GHz modulation frequencies). Radiation pressure is not considered as this effect is too weak for low-reflecting structure at the pump wavelength and in the absence of the external cavity.

4.5 Summary

We presented the experimental mode mapping to the simulated displacement profiles by examining the eigenfrequency and mechanical Q factor evolution on different geometrical parameters of the suspension structure geometry compared with the respective simulations. Intrinsic material losses decrease with the environment temperature, providing a mechanical quality factor enhancement by approximately a factor of 3 for the passage from $T_b = 300$ K to 4.4 K. Additional reduction of the clamping losses and the enhancement of Q_{m} by about a factor of 5 for the fundamental mechanical mode was demonstrated by elongating the suspension bridges, experimentally realized up to the length of $b_y = 12$ μm while incorporating a 10/20 nm thin layer of InGaAs into the InP membrane, allowing to enhance its stiffness and therefore achieve a correct device suspension without collapsing to substrate.

These results were further used in the implementation of the integrated platform (Section 4.2), confirming the expected control over the mutual coupling conditions and efficiency between the access waveguide and an embedded optical cavity. Optical and mechanical spectroscopy on such devices, using conventional side-of-the-fringe technique, showed good performances in the detection of Brownian motion of the photonic crystal slab membrane. Vacuum optomechanical coupling rates were determined for the detected mechanical modes in the frequency range up to 100 MHz via the frequency modulation techniques, giving the values of $g_0/2\pi$ from 0.1 to 45 kHz. Comparing with the state of the art optomechanical systems [Oudich 2014; Balram 2014], the highest $g_0/2\pi$ values attain up to $\sim$ 4 MHz, however, reached within the devices with mechanical frequencies of the order of few GHz. In MHz range [Wilson 2014] the $g_0/2\pi$ values are of order of few tens of kHz. In this vein, by enhancing the experimental set-up in order to achieve a stable detection of GHz range localized modes, we can expect to measure higher corresponding $g_0/2\pi$ coupling rates as well.

The experimental technique to separately measure the strengths of different optome-

chanical coupling mechanisms was implemented (Section 4.3) by examining the mechanical mode amplitude variation from the measurements of optical spring effect. Obtained values showed a good agreement with the corresponding theoretically estimated ones and confirmed the predicted possibility to tailor the absolute and relative external optomechanical coupling strengths by tuning the geometry of the integrated optical access channel and the separation between this channel and the suspended membrane. Optical spring effect, combined with such tailored couplings within devices on waveguides of different widths was characterized and showed several characteristic dependencies of optomechanically induced damping of mechanical mode on laser – cavity detuning. Finally, the thermally induced effects resulting the modification of optical and mechanical properties of the modes of our devices were studies, eventually proposing a mechanism of implementation of bi-stable mechanical switching by exploiting the thermo-optical bi-stability.

Chapter 5

Conclusions and outlook

Contents

5.1 General summary

In this work we proposed and studied a new realization of a hybrid optomechanical platform comprising an InP PhC optomechanical resonator and an integrated silicon-on-insulator waveguide with low optical losses, which allowed for the flexibility in the material choice for the optomechanical resonator. This technology was developed during this thesis in the frame of optomechanical application and provides a full control over the mutual optical coupling strength, demonstrated a tailored optomechanical coupling and interesting perspectives such as non-linear optomechanics and coupling a two-level system (quantum dots) to an optomechanical system.

Contrary to the traditional in-plane designs of the access channels, the optomechanical resonator is vertically stacked over the waveguiding circuit and coupled via an evanescent tail to a propagating mode. This hybrid geometry has two principal advantages: first, the 'active' part of the device (i.e., where the optomechanical interaction occurs) and the access waveguide can be made of two different materials. This allows to choose the material with the optimized properties for each of these components. In order to efficiently feed light into and from the cavity we designed an integrated access waveguide in silicon-on-insulator, having all advantages of silicon photonics and among them lower optical losses compared to the membrane material. Second, in the in-plane access design high efficiency coupling is possible when the optical mode is situated in the close proximity of the waveguide, i.e., at

or close to the edge of the optomechanical resonator, whereas our addressing configuration allows to address an arbitrary cavity location (or multiple locations) and gives full control over the mutual optical coupling and allows for flexible design of the 'active' device part.

In the developed device, the resonator is represented by a photonic crystal slab membrane made of InP, a III-V semiconductor material, allowing to embed a defect optical cavity to confine light. This material choice, featuring a direct band gap allowed in addition to have an active medium inside our device, such as quantum dots or quantum wells, for the integrated broadband light source, whose emission properties such as wavelength and linewidth can be widely tuned by the means of the optical cavity design. Mechanical motion of both the membrane and the cavity core impact the optical properties of the defect cavity via different optomechanical effects. A sacrificial layer between the InP and SOI levels was employed for the membrane suspension; a precise control over its thickness using the standard fabrication techniques allowed to master both light coupling between the waveguide and the cavity and the strength of the external optomechanical interactions, occurring while the latter coupling is modulated by the membrane motion.

In Chapter 2, we introduced the particularities of optical and mechanical designs and their complete simulation, first considering optics and mechanics separately and next tackling the optomechanical characterization of the hybrid system. For the optical part, two configurations have been investigated: either formed by a perfect PhC slab membrane acting as a deformable mirror or containing a line defect photonic crystal cavity embedded inside it and heterogeneously integrated with a SOI waveguide. In both optical geometries, the mechanical design of the resonator has been studied allowing to clearly investigate the optomechanical coupling. Two distinct families of mechanical modes were considered, corresponding to flexural membrane motion (with eigenfrequencies in the MHz range) and to the vibrations localized in the core of the defect PhC cavity (Ω_{m} in GHz range). In the integrated configuration two types of simultaneously existing optomechanical couplings – dispersive and dissipative – were studied both in case of intra-cavity interaction mechanisms ('moving interfaces' and photoelastic effects) and in case of interaction with the external waveguide. Further we focused on the first mode family for a thorough study of optomechanical effects, involving in particular the strong external couplings. Overall dispersive intrinsic interaction strength showed to be less pronounced compared to the external coupling effects at small membrane suspension heights ($\leqslant 300$ nm). Dependence of the external couplings on different opto-geometric parameters of the integrated system, such as the membrane – waveguide vertical separation and the waveguide width were examined, and the possibility to achieve a tailoring of both effect strength and relative weight via these parameters was demonstrated. The implementation of an optimized ground state cooling of our mechanical resonator was examined by bringing the system into the regime of dominance of dissipative coupling while introducing different relative strengths of the dispersive optomechanical interaction.

Chapter 3 is focused on the fabrication of the designed heterogeneously integrated optomechanical platform. Crucial steps were discussed, including adhesive bonding of the

SOI and III-V semiconductor substrates, preparation of high-contrast alignment markers for electron beam lithography, patterning of optical (photonic crystal lattice) and mechanical (mesa structures) device components and removal of the sacrificial layer in order to suspend the PhC membrane. Many features have been implemented into the process flow in order to solve the major issues. Employed adhesive bonding technique with precise control of the sacrificial layer thickness allowed for the respective precision of the SOI and III-V levels separation of $\leqslant$ 10 nm (in the out-of-plane direction). Through the introduction of alignment markers, the alignment of the InP suspended photonic crystal cavities with respect to SOI circuit was achieved with precision $\leqslant$ 40 nm in the in-plane directions. The InP layer patterning was optimized by making use of positive tone PMMA and negative tone HSQ resists, allowing to satisfy different requirements for the optical and mechanical device parts, correspondingly, resulting in particular in obtention of high-Q optical cavities. Standard deviation of the resonant wavelength between PhC cavities with the same geometrical parameters is about 2 – 3 nm on the whole sample (typically several hundreds of devices). Last, the critical point drying technology has permitted us to achieve the suspension yield of 100 % for the air gaps about 200 nm high and for the PhC slab membranes of 10×20 μm^2 lateral dimensions.

In Chapter 4, we described first the experimental characterisation of the mechanical properties of our devices, where the experimental mode mapping to the simulated displacement profiles was performed by examining the eigenfrequency and mechanical Q_{m} factor evolution on different geometrical parameters of the suspension structure geometry compared with the respective simulations. Measured intrinsic material losses showed to decrease with the environment temperature, providing a mechanical quality factor enhancement by approximately a factor of 3 for the passage from room ($T_b = 300$ K) to liquid helium (4.4 K) environment temperature. Additional reduction of the clamping losses and the enhancement of Q_{m} by about a factor of 5 for the fundamental mechanical mode was demonstrated by elongating the suspension bridges, experimentally realized up to a length of 12 μm while incorporating a 10/20 nm thin layer of InGaAs into the InP membrane, allowing to enhance its stiffness and therefore achieve a correct device suspension without collapsing to substrate.

These results were further used in the implementation of the integrated platform, confirming the expected control over the mutual coupling conditions and efficiency between the access waveguide and an embedded optical cavity. Optical and mechanical spectroscopy on such devices, using conventional side-of-the-fringe technique, showed good performances in the detection of Brownian motion of the photonic crystal slab membrane. Vacuum optomechanical coupling rates were determined for the detected mechanical modes in the frequency range up to 100 MHz via the frequency modulation techniques, giving the values of $g_0/2\pi$ from 0.1 to 45 kHz, comparable with the state of the art optomechanical systems in this frequency range [Wilson 2014].

The experimental technique to separately measure the strengths of different optomechanical coupling mechanisms was implemented by examining the mechanical mode am-

plitude variation from the measurements of the optical spring effect. Obtained values showed a good agreement with the corresponding theoretically estimated ones. This confirmed the predicted possibility to tailor the absolute and relative external optomechanical coupling strengths by tuning the geometry of the integrated optical access channel and the separation between this channel and the suspended membrane. Several characteristic dependencies of optomechanically induced damping of mechanical mode on the geometry of access waveguide were also observed. Finally, the thermally induced effects resulting in the modification of optical and mechanical properties of the modes of our devices were studied, eventually proposing a mechanism for implementing bi-stable mechanical switching by exploiting the thermo-optical bi-stability. We discovered and performed preliminary studies of the transduction mechanism between the modulation of non-resonant pump and resonant probe laser carriers using the active medium as an intermediate.

In Appendix A, we presented the design and fabrication of two-side accessible tensile strained membranes for "membrane-in-the-middle" optomechanical experiment, featuring mechanical properties controllable via the used alloy composition and allowing potentially for the strong enhancement of mechanical quality factors of such devices. Added tensile strain values achieved are 350 MPa for $In_{0.45}Ga_{0.55}P$ alloy and 240 MPa for $GaAs_{0.95}P_{0.05}$ with the room for further improvement. Such semiconductor membranes are good candidates for the implementation of photothermal cooling, unavailable for the widely used dielectric silicon nitride membranes, allowing to overcome the fundamental limit of the optomechanical cooling mechanisms based on the radiation pressure interaction.

5.2 Main prospects

Described optomechanical system can be subsequently used for the implementation of various functionalities for fundamental and applied physics; in the following we present two mainstreams for each domain.

5.2.1 Towards hybrid cooling of an optomechanical system coupled to a single quantum object

Our semiconductor membrane allowed for the implementation of embedded active medium, represented by a monolayer of quantum dots, which to a certain extent can be seen as a two-level system. Such active medium, embedded in a semiconductor cavity, has been extensively studied in the frame of light-matter interaction, e.g., for single photon emission [Laurent 2005]. Coupling to such kind of two-level systems within an optomechanical devices has been barely explored experimentally [Arcizet 2011], however, it provides a promising direction for implementing hybrid cooling schemes [WilsonRae 2004].

Following the preliminary studies described in Chapter 4, to get a better insight into the physical phenomenon in the origin of the modulation transduction from non-resonant pump to resonant probe carrier by active medium, modulation behaviours in different frequency ranges will be investigated. On another side, the optomechanics of the mechanical

modes localized inside the cavity, will be studied. These modes lie in the GHz frequency range and for this reason are more attractive for the cooling purposes, as described in Chapter 2. For the same reason, another optomechanical mechanism, resulting in the generation of the high-frequency (GHz) phonons inside the defect cavity via the photostriction effect, could be an interesting possibility to explore. Next, in the mid-term perspective, the investigation of optomechanical cooling of such GHz modes will be carried out; further enhancement of photon–phonon interaction can be achieved with the implementation of phononic/phoxonic crystal lattices to reduce the clamping mechanical losses, following the studies in Chapter 2. Last, in the long-term perspective, the results of both studies might be combined to investigate the hybrid coupling between a high-frequency mechanical mode in its fundamental state and a two-level quantum system and to explore the influence of a mechanical degree of freedom on a non-classical photon emitter.

5.2.2 Towards integrated high-frequency microwave optomechanical oscillator

Exploration and use of the localized modes of our optomechanical oscillator in GHz frequency range can be pursued towards the implementation of applied domain functionalities, such as on-chip high-frequency microwave source or logic elements [Chang 2011; SafaviNaeini 2011b], interconnect-free circuits [Mahboob 2011] and memory [Mahboob 2014]. Frequency and phase of such sources have to be referenced, which is achieved through different synchronization protocols. In addition, the non-electronic nature of optomechanical devices makes them unsusceptible to any electromagnetic interferences and good candidates for all-optical systems, also in view of experimental demonstration of such devices, compatible with CMOS platform [Luan 2014].

Already existing experimental realizations [HosseinZadeh 2008; Zheng 2013] demonstrate that the frequency and phase of an optomechanical oscillator (OMO) within certain lock range can be locked to those of an external electronic oscillator, or any other signal that can modulate the power of input optical field. Injection locking of an optomechanical to an electronic RF oscillator enables combination of OMO with electronic devices and may have interesting applications in certain RF photonics and micro-optoelectromechanical systems. We propose to increase the number of functionalities, provided by our hybrid device, including the self-referencing and synchronization to an external source, by implementing different excitation and tuning mechanisms; the main of them are described in the following.

Future work on the current system in a short-term perspective will aim to pursue the preliminary studies described in Chapter 4 concerning the exploration of the non-linearities in optical and mechanical responses. As proposed, the optical bi-stability, transduced by the optomechanical interaction and creating two well-distinguished stable mechanical states for one probe laser wavelength within a certain range, can be used to explore the possibility to operate our device in a bi-stable mechanical regime, allowing for further implementation as logic or memory component.

Mechanical parametric instabilities can as well be used in such applications [Mahboob 2014], but require an electromechanical resonator with an external drive. For this purpose we propose to combine the efficient optical readout of the mechanical motion, demonstrated in this work, together with the electrostatic actuation of the membrane resonator by the means of metal electrodes, fabricated at a given distance below the InP membrane. To adapt this method to the particular geometry of our device and achieve a more homogeneously distributed actuation force while not introducing an additional mechanical losses compared to the existing solutions [Unterreithmeier 2009; Bagci 2014], already used in an optomechanical system, a proposition would be to introduce a comb drive actuators [Legtenberg 1996]. Three-dimensional integration, demonstrated in this work, will allow for the easier further integration while, for instance, not impacting the membrane mechanical losses since it does not have to be deposited directly on top of the resonator.

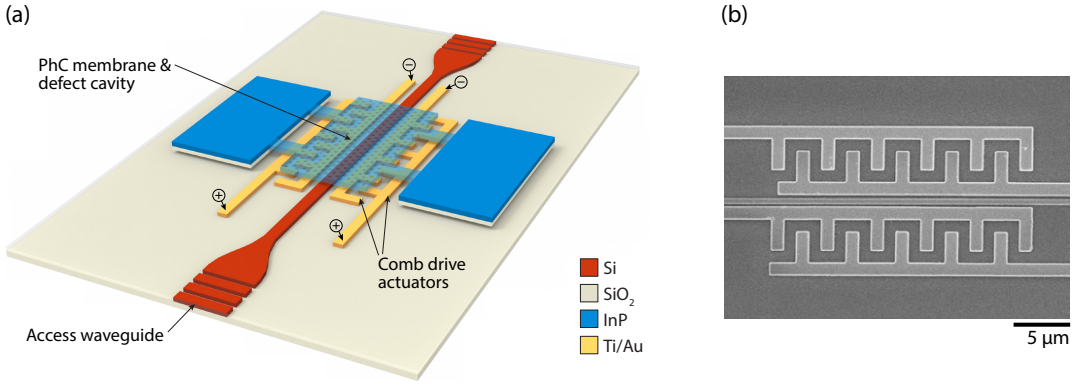

Figure 5.1: (a) Conceptual view of proposed device architecture including the comb drive electrostatic actuators. (b) SEM image of the fabricated SOI wafer with metal electrodes integrated at the same level with Si waveguide.

The device conceptual view is depicted in Figure 5.1a. Such actuation scheme will allow to study various mechanical non-linear effects, such as the mechanical bi-stability for strongly driven resonator and to evidence the sub- and super-harmonic excitation with injection locking. In both ways the mechanical oscillator can be locked to the phase of the external reference, used for resonant or non-resonant pumping, resulting in an on-chip integrated phase-reference device.

The demonstrated super-harmonics can be further used to achieve a parametric amplification of mechanical signals [Shim 2007] from our device. It allows to achieve a gain in the mechanical response of resonance (at eigenfrequency Ω_m) while an electrostatic field is used for the parametric modulation (pumping) at one of the super-harmonic frequencies ($\Omega_\mathrm{m} \times N$, $N \in \mathbb{N}$, $N \geqslant 2$). In such way one of the mechanical oscillator parameters, for instance, its spring constant, can be modulated and depending on pumping phase and strength one can achieve a desired degree of amplification or attenuation of a chosen mechanical mode of the membrane, allowing for a creation of a logic gate [Mahboob 2014]. In addition, thermomechanical noise squeezing of the involved mechanical state can be

obtained [Rugar 1991], thus increasing the displacement sensitivity of the optomechanical device [Mahboob 2014].

Second path of mid-range perspective experiments includes the synchronization of two or more optomechanical resonators, including frequency and phase synchronization protocols. This can be implemented either by optical [Shah 2015] (including the possibility to get more than two synchronized oscillators [Holmes 2012; Zhang 2015]), mechanical [Shim 2007] or electrical [Matheny 2014] connection channels. Moreover, similar to the system theoretically studied in [Heinrich 2011], our hybrid device allows to simultaneously access several spatially separated optical modes, coupled to the same or different mechanical modes, which by design can be coincident or separated spatially. In such way of coupling several OMOs, fundamental aspects of array synchronization and pattern formation [Lauter 2015] can be also studied.

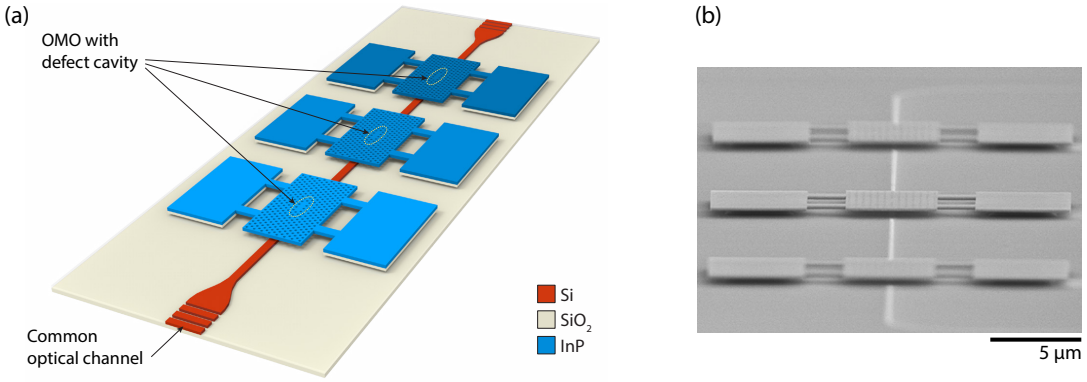

Figure 5.2: (a) Conceptual view of proposed device architecture including for studying mechanical synchronization between different optomechanical oscillators (OMO) coupled via common optical channel. (b) SEM image of the fabricated devices with three resonators coupled to the one access waveguide.

Device design, relative to such application, is shown in Figure 5.2a, with the fabricated sample in Figure 5.2b. The main fabrication challenge still remains the high fidelity of the etched photonic crystal lattices, which defines how well the three (in the shown example) resonant wavelengths will match (currently obtained precision is of the order of $2-3$ nm.). An considerable margin is given by the designed linewidth of the coupled cavity, relaxing the precision condition to $1-2$ nm in the case of samples, studied in this work; this margin can be extended via changing the coupling strength between the waveguide and the cavity to eventually find an optimum solution where all the cavities, coupled via a common waveguide, can be addressed using the same probe laser wavelength, allowing for further mechanical synchronization of the membranes' modes.

In a long-term perspective, having studied the above-mentioned effects exploiting the mechanical non-linearities within the system, one can envisage to further extend the investigation of these effects to the second family of mechanical modes in the current device configurations – localized within the core of the defect cavity (in GHz range). Contrary to

the excitation and driving of the flexural membrane modes using electrostatic field from the comb drives (Fig. 5.1a), the localized modes require another solution, for example, employing a surface acoustic waves (SAW) transducer.

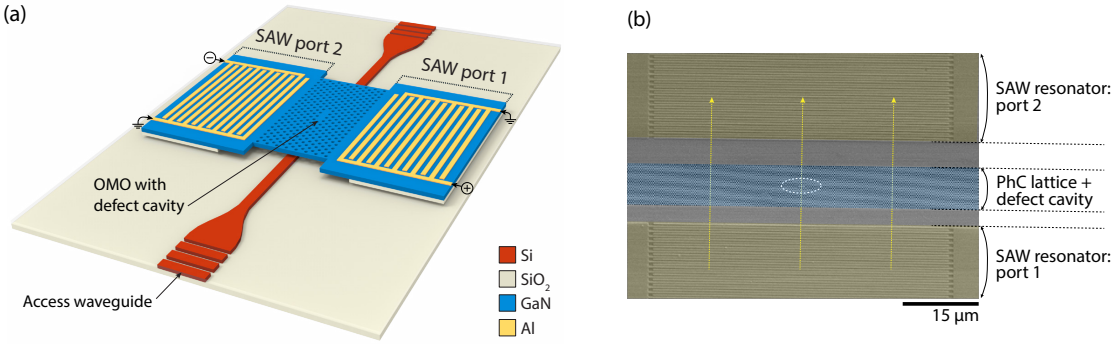

Figure 5.3: (a) Schematic of integrated optomechanical device featuring an excitation of the surface acoustic waves transducer in the GHz range via interdigitated combs. Readout of the mechanical device response can be performed simultaneously using optical access channel and SAW transducers (via S_{21} parameter in the shown two-port configuration). (b) SEM image of the fabricated defect PhC cavity (marked with white ellipse) with two-port SAW resonator; yellow arrows indicate the propagation direction of the excited surface acoustic wave.

Still using a pair of interdigitated combs, it is possible to excite an acoustic wave propagating on the surface of the layer below the electrodes. Such devices consisting of chirped interdigital transducers demonstrate a broad excitation band (covering our frequency range of interest) and a possibility to directly measure the acoustic transmission when using a two-port SAW resonator [Benchabane 2015]. The electrodes have to be fabricated on top of a piezoelectric material, therefore the semiconductor material we used through this work, InP, would require an intermediate layer of piezoelectric. Simpler option consists in using a suitable semiconductor material with good piezoelectric properties, such as GaAs or, even better, GaN/AlN, for the resonator part. An example of fabricated device where the suspended PhC with a defect cavity made of GaN and aluminum (Al) electrodes deposited directly on top of this layer, is shown in Figure 5.3b.

Optomechanical oscillators, featuring direct coupling to continuous-wave light field input from one side and attainable high operation frequency and high quality factor, are a good candidates for frequency reference in radio-frequency-photonic architectures. Such developments of high-quality optomechanical resonators will finally allow for their implementation as on-chip integrated RF oscillators with high spectral purity, covering both MHz and more interestingly GHz frequency ranges.

Two different implementations of on-chip integrated RF oscillators can be used: phase-locking to an external frequency reference and self-referenced optomechanical microwave oscillators. In the first case, the frequency of an OMO is read optically by examining either the phase or the amplitude of a probe laser, coupled to its optical mode. The measured

frequency is then stabilized through a feedback scheme, in which the feedback error signal is obtained by comparing the phase of the optomechanical oscillator with the one of the external reference signal. The feedback scheme then relies on a control of the mechanical frequency via a tuning of the pump laser power or its frequency. An alternative scheme for the localized modes exploits direct acoustic or optical carrier injection via the SAW transducers (Fig. 5.3a,b) [Weigel 2002] or an optical waveguide. In the second case, a self-stabilization of the oscillator is achieved through a use of a system enabling to self-sustain mechanical motion [Gavartin 2011; Villanueva 2013]. It consists in applying a force proportional to the displacement of the oscillator driven by high actuation power. This scheme could also be combined with an injection of the RF signal via the modulation of the laser and optical injection, while the acoustic and optical delays may be introduced to reduce the phase noise of the oscillator. Pursuing such system further in this context, an injection locking can be used to lock two and more optomechanical resonators and improve the frequency stability and noise performance of the driven oscillator(s) similar to what is done in the optical domain with lasers.

Appendix A

Tensile-strained membranes on GaAs substrate

One of the commonly employed configurations in experimental cavity optomechanics is a high-finesse Fabry-Pérot optical cavity embedding a mechanical oscillator. This oscillator can either be one of the end-mirrors of the cavity or a thin membrane inserted inside the optical resonator. The later configuration benefits from a separate tailoring of the mechanical resonator and the optical cavity. These membranes usually consist of extremely thin (few tens to few hundreds of nm) and large (hundreds of microns to few millimeters lateral dimensions) semi-transparent membranes, coupled dispersively to the optical mode of the Fabry-Pérot high-finesse resonator (also referred to as "membrane-in-the-middle" experiment).

Pioneer experiment realizations [Thompson 2007; Sankey 2010] employed dielectric Si_3N_4 (silicon nitride) membranes. Commercially available (e.g., from Norcada[1]) *dielectric* Si_3N_4 devices made from tensile-strained amorphous films have demonstrated a mechanical quality factors greater than 10^7 [Thompson 2007; Purdy 2012] and made possible number of developments in the field of cavity optomechanics, such as the demonstration of radiation-pressure quantum backaction [Purdy 2013a] and ponderomotive squeezing [Purdy 2013b].

More recent developments consider semiconductor (gallium arsenide (GaAs) [Liu 2011] and indium gallium phosphide (InGaP) [Cole 2014]) membranes, allowing to implement hybrid cooling schemes [WilsonRae 2004] in such optomechanical systems. Free-standing *semiconductor* films have demonstrated excellent optomechanical properties [Liu 2011], allowing further for exciton-mediated[2] photothermal cooling [Usami 2012; Xuereb 2012] (in those experiments, by making use of photothermal effect, one can overcome the fundamental limit encountered by any optomechanical cooling mechanism based on the radiation-

[1] http://www.norcada.com/products/silicon-membranes/

[2] Quantum-electronic systems (such as quantum wells and quantum dots) embedded in GaAs enable strong coupling between a photon and a confined exciton (see [Yoshie 2004]). The cooling of membrane's mechanical mode is possible as a result of electron-hole pair generation caused by the absorption of (external) cavity photons by an interband transition in the semiconductor [Fox 2001, p. 77].

pressure interaction; see, for ex. [Pinard 2008]). The implementation of such photon-exciton coupling for cooling requires both low operating temperatures [Fox 2001] together with embedded quantum dot/well structure, in order to successfully create and maintain exciton bonds.

A.1 Device concept

Basic design here with respect to technological feasibility is represented in Fig. A.1. A tensile-strained single-crystal membrane is realized via lattice mismatch in epitaxial growth, through variations of the alloy composition of a ternary $In_xGa_{1-x}P$ (hereinafter InGaP) or $GaAs_yP_{1-y}$ (hereinafter GaAsP) layer, which is detailed below.

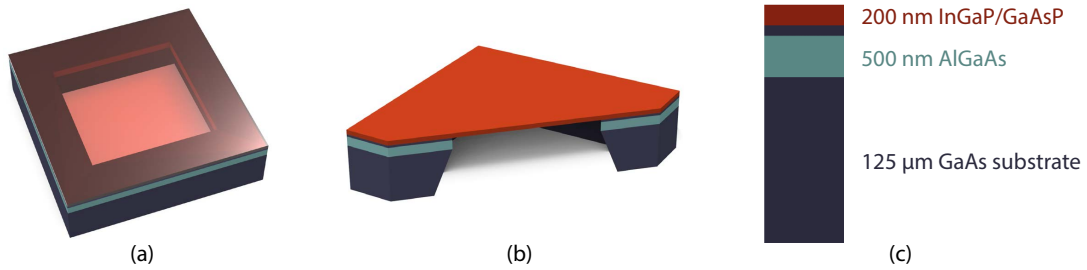

Figure A.1: Sketch of a designed device (not to scale): a concept view (a) and its cut (b) showing the undercut profile for supporting frame; (c) composition of the epitaxial structure.

The main fabrication stages include metalorganic chemical vapour deposition (MOCVD) of the membrane and etch-stop layer stack, preparation of the two sides of the sample and patterning of the etching mask on the backside, wet etching of the host substrate and final removal of all the complementary layers.

Backside etching techniques, which provide two-side access to the membrane, require usually to insert an etch-stop layer in order to protect the top layer (here InGaP/GaAsP) during etching process. For this purpose we employ a few hundred nm thick $Al_xGa_{1-x}As$ (hereinafter AlGaAs) layer with high aluminium concentration (x = 85 %), for better resistance against chosen wet etching solution [Hays 1999; Baca 2005]. It should be noticed that at the same time the use of too high aluminium ratios, while exposed to atmospheric gases, would lead to oxide creation in vicinity of membrane's bottom edges, which impacts in turn mechanical properties. The few nm thick intermediate layer of GaAs between the etch-stop and a top layer (also shown in Fig. A.1c) is introduced due to epitaxy requirements. It allows for a better control over membrane's lattice mismatch one wants to introduce and better quality interface with the InGaP/GaAsP layer.

Whole structure is grown by MOCVD method on top of 125 μm-thick GaAs wafer. In contrast with traditional 350 μm wafers the thinner option both reduces the etching time and preserves better the initial mask shape.

A.2 Strained membrane design

Moving further to InGaP or GaAsP alloys brings essentially two advantages compared to GaAs. First, considering the optical properties, the higher bandgap (around 1.9 eV[3] for both alloys comparing to 1.42 eV for GaAs) lowers the wavelength limit for transparent optical operation to about 650 nm (870 nm for GaAs) at room temperature. Non-linear absorption effects at high optical intensities, including two-photon absorption, become negligible as well. Second, by varying the alloy composition, one introduces a lattice mismatch with the substrate (GaAs is usually used), which in turn brings tensile stress into membrane's layer. The latter fact, while considering free-standing membranes, via the impact on material strain tensor, increases the frequencies of mechanical modes as well as their quality factors, hence favouring the obtention of ground-state cooling by improving the $Q_m \times f_m$ product – a common figure of merit in view of reaching this limit [Liu 2015], as introduced in Chapter 1.

A.2.1 Control of strain via alloy composition

Some of III-V compounds, and in particular GaAs, InGaP and GaAsP, form crystals with the zinc blende arrangement. Such compounds are the simplest crystals lacking a center of symmetry and, hence, capable of exhibiting piezoelectric and relating effects [Adachi 1992].

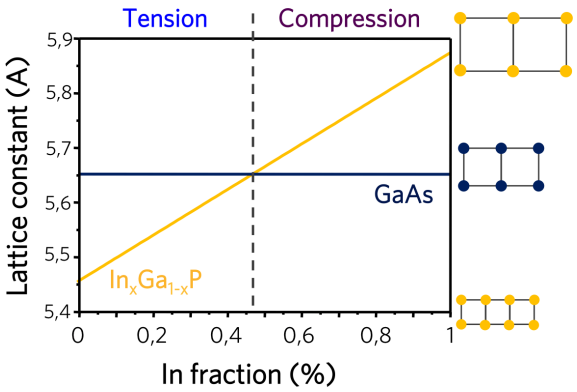

Figure A.2: Lattice constant a_0 dependence on indium concentration for $In_xGa_{1-x}P$ alloy (yellow line). Lattice-matched case to GaAs occurs at the intersection between the black dashed and solid blue lines.

The crystal lattice parameter, or lattice constant a_0 is known to obey empirical Vegard's law [Denton 1991], that is, varies linearly with the concentration(s) of alloy constituent element(s). Such is the case for the ternary alloys considered here. Using this law, the lattice a_0 dependence from the composition fractions x and y of $In_xGa_{1-x}P$ and $GaAs_yP_{1-y}$ respectively, can be written as:

[3] Value may vary depending on alloy composition.

$$a_{\mathrm{InGaP}} = (5.4508 + 0.4182 \cdot x)\ \text{Å} \tag{A.1}$$

$$a_{\mathrm{GaAsP}} = (5.4508 + 0.2025 \cdot y)\ \text{Å} \tag{A.2}$$

That is, one gets the $In_xGa_{1-x}P$ lattice-matched to GaAs with $x \simeq 0.4842$ (as illustrated on Fig. A.2).

When lattice-mismatched, the ternary alloy layer can be either in compression or in tension (Fig. A.2), depending on relative lattice dimensions with the substrate. During the epitaxy stage, the a_0 value is fixed (in plane) and equal to the one of the host substrate. This will lead to the elongation or compression of the lattice cells exclusively in the out of plane direction, with respect to the material Poisson's ratio.

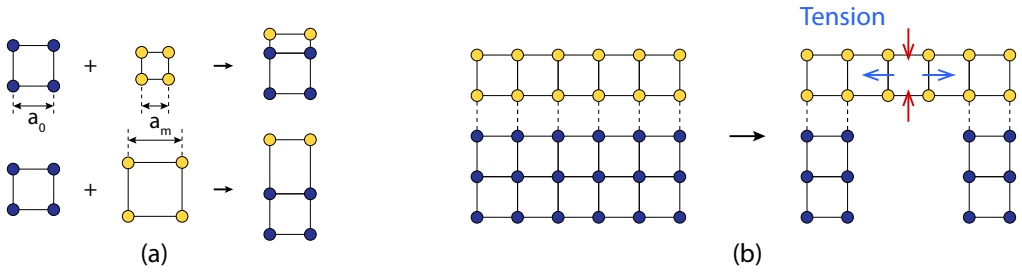

Figure A.3: (a) Case of lattice-matched growth for the membrane lattice constant smaller (top) and bigger (bottom) comparing to the host substrate one. (b) A sketch illustrating the principle of tensile stress release on an example of a free-standing membrane.

Growing membrane layer with a lattice parameter smaller than the one of substrate $a_m < a_0$ forces its in-plane lattice dimensions to fit the underlying layer (that is, to stretch along both axes in substrate plane, see Fig. A.3a). At the same time, due to volume conservation law, the cell is compressed along the growth direction where no constraints exist, i.e. along the vertical axis in the case shown. In such a way one can introduce tension (compression) within the film layer by choosing relative mismatch to be negative (positive) (as denoted on Fig. A.2, with tension case illustrated on Fig. A.3a,b).

The local substrate removal will release the stress, induced during the membrane growth. In consequence, its lattice constant will tend to its natural value, creating a compressive or tensile strained membrane according to the chosen mismatch. The lattice mismatch introduced during MOCVD epitaxy of ternary film is controlled via the concentration of the corresponding gas. The calibration procedure consists of depositing a film of desired thickness directly on GaAs substrate (without AlGaAs layer), and than measuring precisely the resulting concentration via X-rays diffraction spectroscopy. The obtained value is further used to calculate induced stress values.

As an example we took a sample consisting of 200 nm thick $In_xGa_{1-x}P$ membrane MOCVD-grown directly on a GaAs substrate. The calibration spectrum (see Fig. A.4) reveals two distinct peaks corresponding to the GaAs substrate (on the left) and to one of the tensiled membrane layer. The angular position of the latter allows to determine

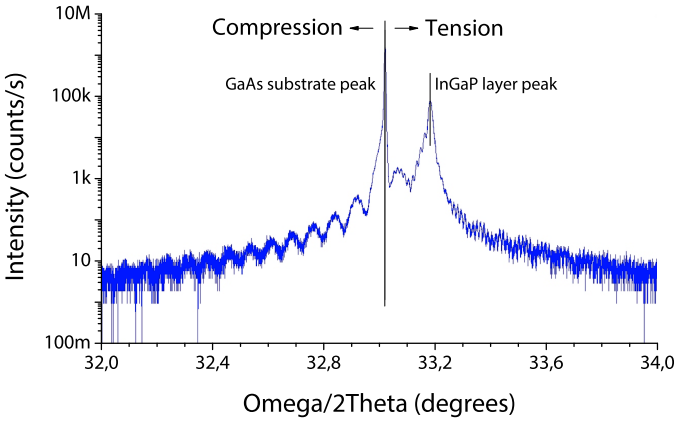

Figure A.4: An example of calibration spectrum (X-ray diffraction), obtained for an InGaP membrane deposited directly on top of a GaAs wafer.

its contents. Fits of this data give $x = 0.45$, hence a $In_{0.45}Ga_{0.55}P$ membrane has been obtained. The concentration value is further used for the calculation of the induced tensile stress.

We assume that the thin film membrane has an interface, perfectly matched with the host substrate (Fig. A.3), i.e., the crystal lattices in film and substrates line up perfectly. Then, for the residual stresses being epitaxial stresses the misfit strain in membrane (assuming two-dimensional misfit in cubic symmetry lattice and relatively small ($\lesssim 3\%$) lattice mismatch) is given by [Vlassak 2004]:

$$\varepsilon_{\mathrm{xx}} = \varepsilon_{\mathrm{yy}} = \frac{a_0 - a_m}{a_{\mathrm{m}}} = \varepsilon_{mf}, \tag{A.3}$$

where a_{m} and a_0 are the lattice constants of the membrane and substrate correspondingly. Given equation holds in case when the membrane lattice would adjust to the substrate one.

Then, the nonzero components on the misfit stress tensor are:

$$\sigma_{\mathrm{xx}} = \sigma_{\mathrm{yy}} = \frac{E\,\varepsilon_{\mathrm{mf}}}{1-\nu}, \qquad \sigma_{\mathrm{zz}} = \nu\,\sigma_{\mathrm{xx}}, \tag{A.4}$$

where E is the substrate Young's modulus, ν – Poisson's ratio, x and y – in-plane membrane's axes, z – direction of membrane epitaxial growth. By applying equations A.3 and A.4 we trace the expected induced stress values versus In (respective As) fractions for two types of fabricated membranes (dark red curves in Fig. A.5a,b).

A.2.2 Critical layer thickness

A critical layer thickness for the lattice-mismatched membrane layer refers to a thickness which can be epitaxially grown without any defects and dislocations. As larger misfits

will result in larger induced strain values, this quantity is important to be known when designing the strained membranes. Few approaches exist for estimation of this quantity. Initially it was calculated on the basis of energy considerations [Van Der Merwe 1963] or considering the mechanical equilibrium theory [Matthews 1974].

When applied to our case of small misfits ($< 1\%$), both theories give critical thicknesses of the order of few nanometers for $\varepsilon_{\mathrm{mf}} = 0.2\%$, while our current successfully grown layers are two orders of magnitude thicker for the same misfits (for two types of membranes we studied, $\varepsilon_{\mathrm{mf}} \simeq 0.25\%$ for $In_{0.45}Ga_{0.55}P$ and $\varepsilon_{\mathrm{mf}} \simeq 0.18\%$ for $GaAs_{0.95}P_{0.05}$). The theory that has the best correspondence to our experiments assumes that misfit dislocation generation is determined solely by the energy balance at the epitaxial interface [People 1985; People 1986]. In this case, critical thickness is given by

$$h_c \simeq \left(\frac{1-\nu}{1+\nu}\right)\left(\frac{1}{16\pi\sqrt{2}}\right)\left[\frac{b^2}{a\,(x)}\right]\left[\left(\frac{1}{\varepsilon_{\mathrm{mf}}^2}\right)\ln\left(\frac{h_c}{b}\right)\right], \tag{A.5}$$

where b is the slip distance (i.e., b = magnitude of the Burger's vector) and $a(x)$ is the alloy's lattice constant dependence from corresponding element fraction, as given for our case by Eq. A.1 and A.2.

Assuming a slip distance $b = 4$ Å [People 1985; People 1986], the solutions of Eq. A.5 are plotted (blue lines) on Fig. A.5a,b for two studied alloys. It reveals that increasing the strain values would require smaller membrane thickness. The maximum grown thickness for the two kinds of membranes studied in this work (with $x = 0.45$ [respectively $y = 0.95$] for $In_xGa_{1-x}P$ [respectively $GaAs_yP_{1-y}$]) is indicated by empty circles. It shows that the lattice mismatch allows to improve the tensile stress up to 460 MPa for GaAsP alloy (compared to 240 MPa), while for InGaP alloy the maximum possible stress (350 MPa) is already attained for current misfit parameter and thickness. The latter could be still improved in case of thinner membrane device (e.g., up to 450 MPa for 200 nm thick InGaP layer).

A.3 Fabrication

This section is devoted to the description of the sample preparation and processing for the fabrication of two types of tensile-strained membranes grown on GaAs substrate. Two available wafer types of 125 and 350 μm thickness have been considered in terms of etching time and quality of mask shape transfer. The process flow is illustrated in Figure A.6.

The processing starts with a polishing of the substrate backside, on which the etching mask will be deposited. The roughness of the mask layer employed for backside etching (in case of non-planarizing material) reflects directly the one of substrate. Such roughness will degrade the etching profile and transfer during the etching step. One may thus consider backside mechanical polishing in order to reduce this impact and hence improve the etching profile homogeneity across the opening surface.

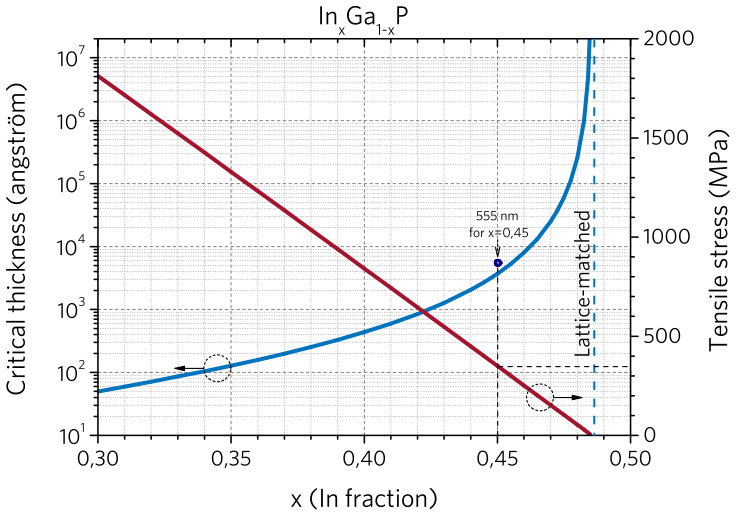

(a)

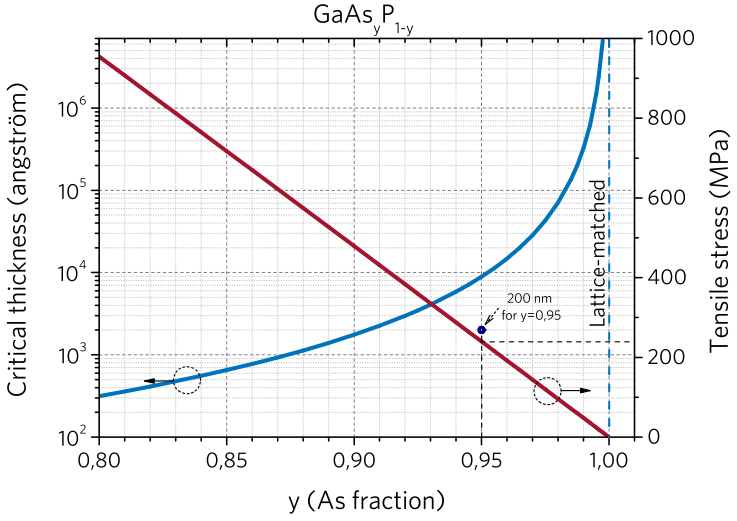

(b)

Figure A.5: Analytical solutions for the critical thickness grown without defaults for both membrane compositions studied in this chapter. Straigth lines give correspondance between the induced tensile stress and the element concentration. Points refer to the devices that have been succesfully fabricated.

Standard single-side polished GaAs wafer has an average (RMS) backside surface roughness R_q of around 600-800 nm. This measurements were performed with Dektak 8 profilometer, assuming

$$R_q = \sqrt{\frac{1}{L}\int_0^L h^2(x)dx}, \tag{A.6}$$

where L is the length of scan, h is the absolute height, measured at x coordinate of scanning tip. Mechanical polishing with colloid solution of aluminium particles of 3 μm diameter and water (1:10 by weight) gave us in best case a reduction of RMS roughness

down to $R_q \gtrsim 300$ nm. Such sample would still require the additional use of planarizing photoresist layer on top of mask for backside etching, moreover, the polishing procedure can degrade the mechanical durability of the sample. In order to minimize the impact of backside surface irregularities on the etching results, we therefore have decided to mainly work with 125 μm–thick GaAs substrates.

A.3.1 Process flow

The established fabrication sequence (Fig. A.6) for the tensile-strained suspended membranes goes as follows (it applies for both InGaP and GaAsP compositions). The membrane layer (standard thickness 200 nm) and an AlGaAs etch-stop layer (standard thickness 500 nm) are deposited via MOCVD epitaxy on top of a 125 μm 2-inch GaAs wafer. A few nm thick GaAs buffer layer is used as an interface between membrane and AlGaAs layer and allows for better (more sharp) interfaces (1). The membrane is then protected with a AZ 5214 E[4] photoresist layer (2) (spin-coating at 2000 rpm speed, 1000 rpm acceleration for 30 s; postbake on a hotplate during 2 min at 80 °C; resulting thickness about 2 μm), as further we operate our sample in upside-down position for a number of processing stages hence some protection from mechanical damage is necessary.

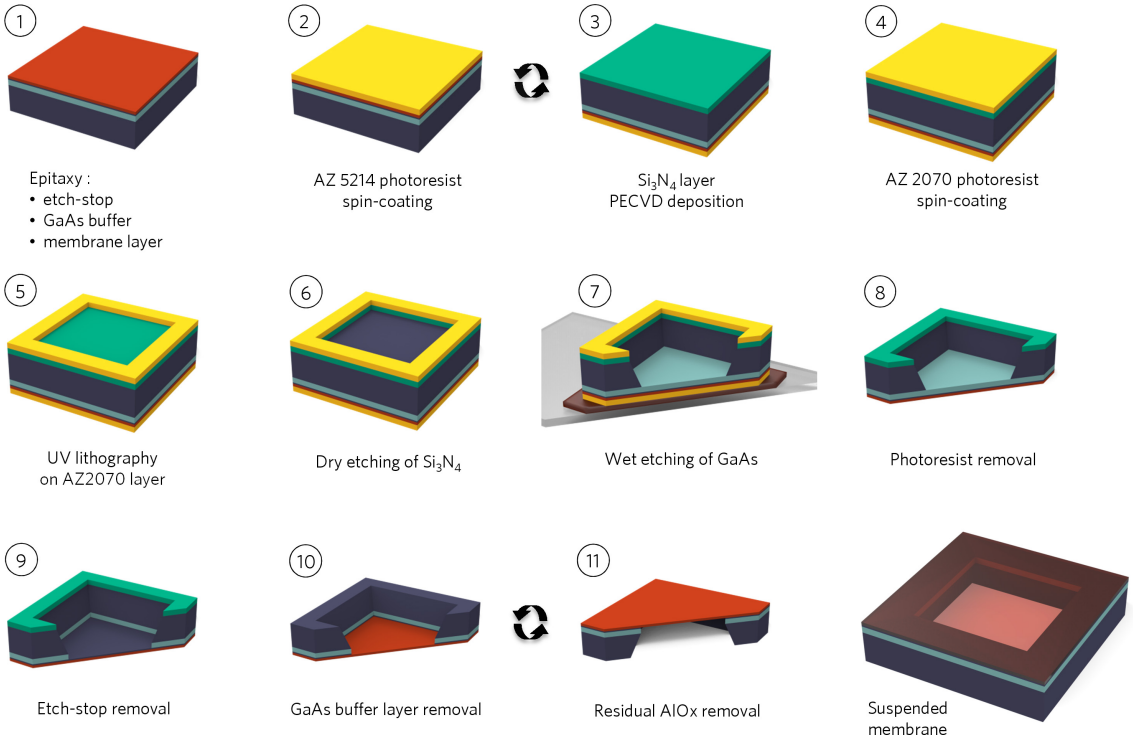

Figure A.6: Process flow of a suspended tensile-strained membrane. The black curved arrows indicate the change of the side being currently processed.

[4]http://www.microchemicals.com/products/photoresists/az_5214e.html

A 500 nm thick Si_3N_4 layer is deposited by PECVD (plasma-enhanced chemical vapour deposition) (3) and will serve as a part of mask for substrate etching. Substrate's backside is relatively rough (RMS roughness R_q vary between 600 and 900 nm) and the silicon nitride layer reproduces well its pattern, eventually resulting in small (few μm) openings though which the wet etching solution can penetrate outside of designed mask opening. To prevent this we employ a second mask layer consisting of thick planarizing photoresist AZ nLOF 2070[5] (4) (spin-coating at 2000 rpm speed, 1000 rpm acceleration for 30 sec; postbake on a hotplate during 5 min at 80 °C; resulting thickness about 7 μm). Resulting double-layer mask is then etched in two stages. First (5), with an UV lithography through the Ni-Cr negative mask (as we work with the negative photoresist) we transfer the mask pattern into the photoresist layer. Then a dry R.I.E. etching (SF_6 plasma) using the AZ nLOF 2070 patterned layer as a mask replicates the pattern into the Si_3N_4 layer (6).

Our developments and trials on wet etching of large openings in GaAs substrate showed that the best results in terms of resulting shape, speed and reproducibility were obtained in the following configuration. The front side of the sample is glued on a glass plate (wax glue, hotplate, $80 - 90$ °C), which allows to maintain the horizontal position while immersed into the etching solution. Moreover, as the ultrasound (US) bath is employed, this protects the membrane during strong mechanical agitation. Substrate wet etching (7) is carried out in an US bath (frequency 80 Hz, 50 % of nominal power) in H_2O_2 : NH_4OH (20:1 by volume) solution. It requires around 25-30 min to etch through 125 μm substrate with a 500 $\times$ 500 μm^2 opening. Thicker substrate (usually a standard 350 μm one) results in longer etching times and less accurate mask shape transfer and can only appear advantageous in terms of handling ease. The end of this etching step is identified by the change of colour within the mask opening: GaAs is grey, while AlGaAs with high aluminium content, exposed to oxygen from hydrogen peroxide dissociation, shows rainbow oxidation (see Fig. A.7a). The sample is then unglued from its glass

[5] http://www.microchemicals.com/products/photoresists/az_nlof_2070.html

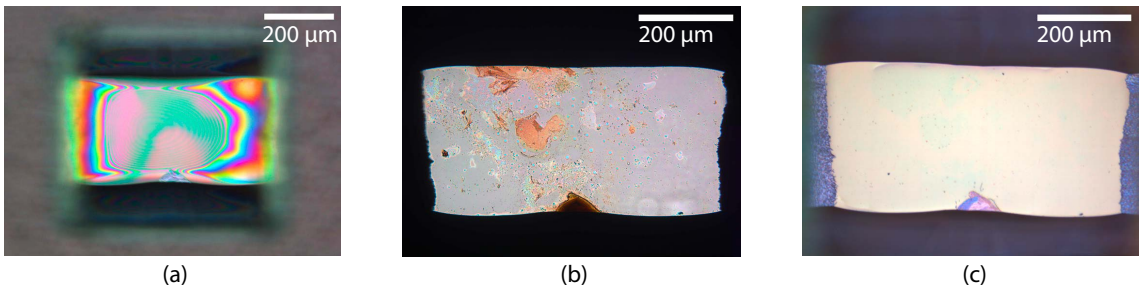

Figure A.7: Optical microscope images of the device at fabrication stages of backside-etched InGaAs membrane. (a) After the GaAs substrate etching; etch-stop layer with high Al content is quickly oxidized with the O_2 from hydrogen peroxide. (b) Some AlOH/AlOx residuals appear after etch-stop layer removal. (c) Membrane surface after cleaning in KOH solution.

plate (trichloroethylene (C_2HCl_3), heated up to 80 °C, dissolves the residues of wax) and photoresist layers are removed by gentle soaking in an acetone bath (8). Ammonium fluoride (NH_4F) solution is then used for AlGaAs etch-stop layer removal (9), followed by a deep in $C_6H_8O_7$: H_2O_2 (4:1 by volume; citric acid is dissolved 1:1 by weight in water) solution to remove the thin GaAs buffer layer.

Optionally, an additional photoresist soft bake (the sample is put into a pre-heated oven without direct contact with a hotplate) at the end of stage (2) makes the protective layer resistant to acetone bath, which could be employed to keep this layer after the membrane's release from the backside at stage (8). This prevents the membrane from mechanical damage during wet etching stages (9) – (11), and the protective layer is removed finally by dry etching (O_2 plasma).

Step (9) of AlGaAs removal could produce some residual AlOH or aluminium oxide, present in a form of flakes (sized tens of micrometers), which eventually introduces additional unwanted mechanical losses (see Fig. A.7b). It can be removed by alternating KOH 10% solution (by weight) and deionized water baths (see Fig. A.7c).

A.4 Summary

In this chapter we presented the design and fabrication of two-side accessible tensile strained membranes for "membrane-in-the-middle" optomechanical experiments, targeting the implementation of hybrid cooling schemes. Different fabrication stages were developed in order to answer the related requirements for mechanical device quality and optimize the transfer of the etching mask profile to membrane shape. Added tensile strain values achieved are 350 MPa for $In_{0.45}Ga_{0.55}P$ alloy and 240 MPa for $GaAs_{0.95}P_{0.05}$. For the designed membrane thicknesses the latter can be improved up to 460 MPa in order to achieve higher mechanical quality factors. Analytical estimation of critical thickness versus lattice mismatch parameter showed a good agreement with the parameters of fabricated samples.

Appendix B

S-parameters for equipment used in mechanical spectrum calibration

Experimental implementation of the mechanical spectrum calibration and measurements of the optomechanical vacuum coupling rate g_0 require the knowledge of the transmittance and reflectance properties of the equipment, used in this purpose. The phase shift factor $\tilde{\beta}$, which characterises the modulation of the laser carrier phase, induced by the electro-optical modulator (EOM), is calculated as $\tilde{\beta} = \pi \cdot V/V_\pi$, where V is the voltage being applied from an external signal generator to the EOM and V_π is the voltage necessary to induce the carrier phase shift of π. The applied voltage is calculated as $V = \sqrt{2P_{\mathrm{rf}}Z}$ with P_{rf} denoting the input power of the function generator and Z is the impedance between the EOM and the function generator. In the real system two additional factors should be accounted for: (a) the reflectance of the system consisting of the EOM and the cable linking it to the signal generator and (b) the transmittance through the linking cable.

In order to include the above-mentioned factors into $\tilde{\beta}$, we directly measure the corresponding S-parameters using a network analyzer (Agilent E5071C). First, we characterize the BNC cable linking the two devices by measuring its S_{21} and S_{11} parameters with the network analyzer. Figure B.1 shows the fraction of power T_{BNC} transmitted to the EOM by the BNC cable as a function of the output frequency of the signal generator. In the same way, Figure B.2 gives the fraction of power being reflected R_{BNC} by the cable. These two parameters may considerably vary from one cable to another, therefore requiring their careful testing prior to implementation into the set-up scheme. As can be seen, the power loss becomes stronger at high frequencies, which is explained by the radiation losses in the BNC cable.

After choosing the linking cable with the lowest losses and the best transmittance (in particular in the MHz range), we characterize the reflectance of the EOM, linking cable and the necessary connector adapters set (BNC to SMA and SMA to GPO). Figure B.3 shows the fraction of power R_{EOM} being reflected by this system and corresponds well to the given specifications. The EOM used in this experiment (Thorlabs LN65SFC, also known as Covega Mach-10 053/065), according to the datasheet, has S_{11} (DC to 10 GHz)

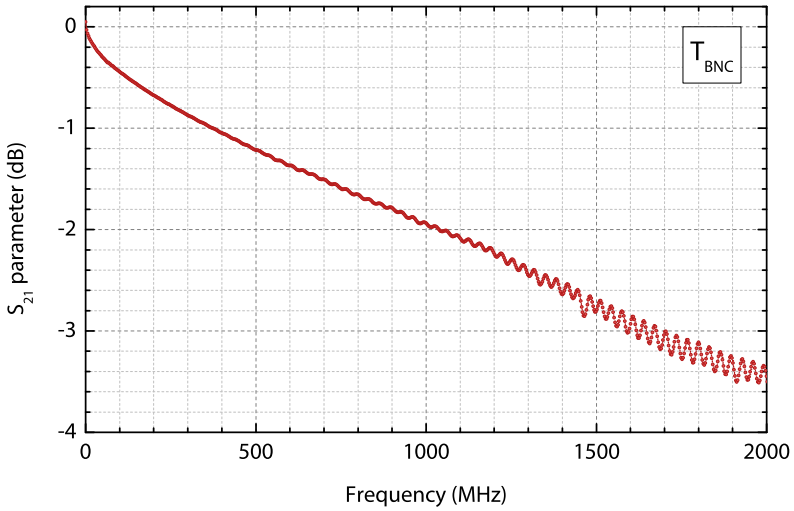

Figure B.1: Transmission coefficient T_{BNC} versus frequency of the power being transmitted through the BNC cable linking the signal generator and the EOM. Incident electrical power at port 1 of the network analyzer is set to 0 dB.

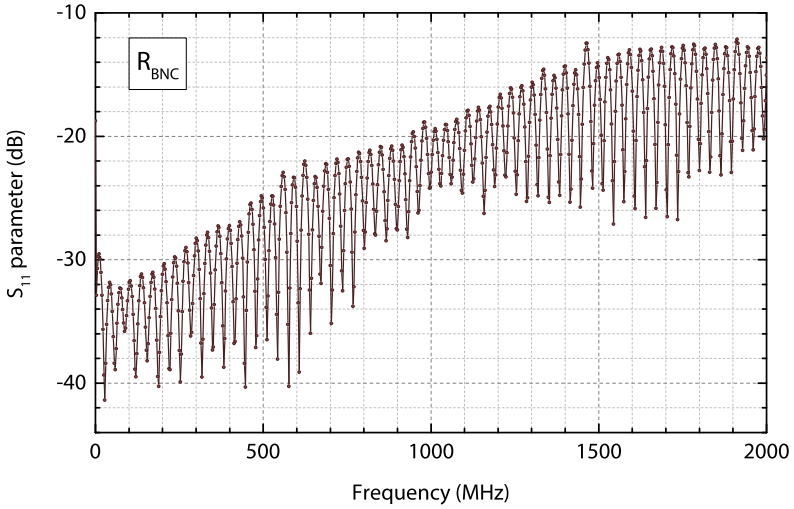

Figure B.2: Reflection coefficient R_{BNC} versus frequency of the power being received by the BNC cable linking the signal generator and the EOM. Incident electrical power at port 1 of the network analyzer is set to 0 dB.

parameter of -12 dB (max -10 dB), which fairly corresponds to our tests (Fig. B.3). Now, the corrected value of the phase shift factor $\tilde{\beta}$ can be determined as

$$\tilde{\beta} = \pi \sqrt{2 P_{\mathrm{rf}} Z_{\mathrm{out}} \cdot 10^{\mathrm{T_{BNC}}/10} \left(1 - 10^{\mathrm{R_{EOM}}/10}\right)} / V_{\pi}, \tag{B.1}$$

According to the device specifications, typical V_π is 3.5 V at DC, which increases to 4 V at 10 GHz. In order to verify this parameter, we set up the Mach-Zender interferometer using the EOM in one arm while another is left free. The phase modulator is fed with

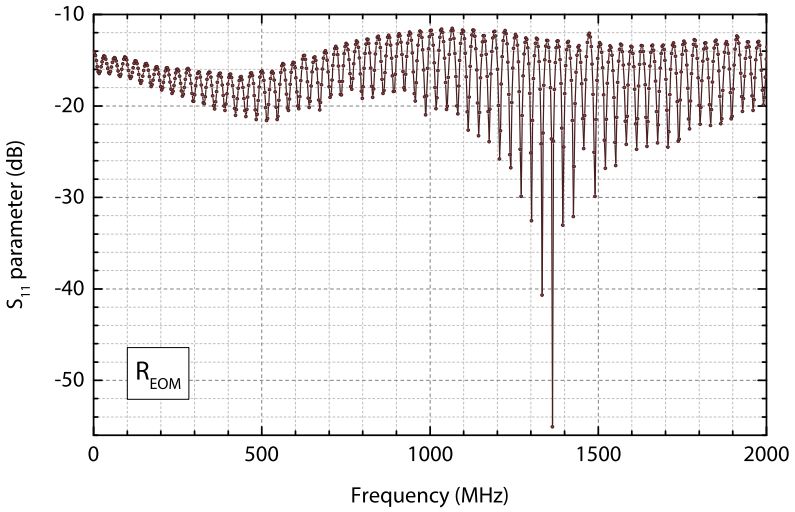

Figure B.3: Reflection coefficient R_{BNC} versus frequency of the power being received by the combined BNC cable and EOM circuit, including the set of necessary connector adapters. Incident electrical power at port 1 of the network analyzer is set to 0 dB.

the RF signal at the test frequency of 1 MHz from the function generator with known voltage and the resulting response at the interferometer output was analysed. We work in the linear regime of the interferometer and analyse the amplitude of the transduced signal with varying input voltage. In this manner the value of $V_\pi = 3.5$ V was obtained, corresponding to the device specifications at DC.

Appendix C

Synthèse en français

La motivation générale de cette thèse repose sur le développement d'une plateforme optomécanique répondant aux enjeux des domaines tant fondamentaux (mécanique quantique, information quantique) qu'appliqués (photonique sur puce, photonique RF, métrologie). Ces enjeux requirent des dispositifs intégrés à couplage optomécanique contrôlé. De fait, l'objectif premier de cette thèse est le développement et la validation expérimentale d'un système optomécanique intégré de manière hétérogène permettant de façonner la nature du couplage lumière – mécanique. Ce système se compose d'une membrane optomécanique suspendue, reportée au-dessus d'un guide d'onde d'accès en silicium. Cette approche tri-dimensionnelle hybride peut être étendue à une grande variété de matériaux employés pour former la partie active de dispositif (ici en semi-conducteurs III-V) ; elle peut aussi tirer partie de la versatilité du circuit optique silicium intégré, réalisant ici un canal d'accès optique compact, efficace, entièrement contrôlé et flexible sur puce. L'intégration d'un cristal photonique dans la membrane optomécanique apporte encore plus de versatilité à notre système, conférant à la membrane à la fois des propriétés optiques et mécaniques. La compréhension fine du système est obtenue par simulations numériques, permettant de quantifier les caractéristiques mécaniques et optiques pertinentes et de les optimiser ; les designs obtenus sont ensuite validés par la caractérisation expérimentale des dispositifs réels. Le système conçu offre de grandes capacités de mise à l'échelle, tout en étant aisément intégrable au sein des circuits plus grands et plus complexes ; ceci ouvre la voie vers des effets de couplage multi-cavités et multi-résonateurs, la mise en œuvre de mécanismes de synchronisation et des expériences optomécaniques multi-modes.

C.1 Optomécanique

Le domaine de l'optomécanique explore l'interaction entre la lumière, ou les ondes électromagnétiques, et le mouvement mécanique d'un objet macroscopique oscillant. L'optomécanique en cavité quant à elle [Kippenberg 2007 ; Aspelmeyer 2013] englobe l'étude et l'utilisation des interactions de lumière avec un résonateur mécanique placé à l'intérieur d'une cavité (par exemple, optique), la présence de la cavité permettant une exaltation de

cette interaction.

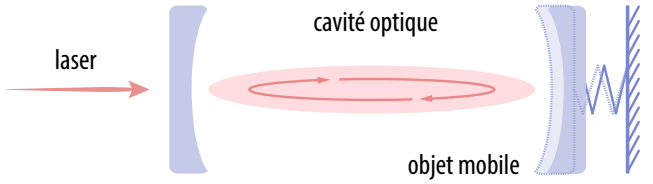

FIGURE C.1 : Illustration schématique d'un résonateur optomécanique générique dans le domaine optique constitué d'une cavité Fabry-Pérot pompée par un laser, où l'un des miroirs est fixe (à gauche) et l'autre est monté sur un ressort (à droite) et libre de se mouvoir.

Le système canonique en optomécanique en cavité est celui d'une cavité Fabry-Pérot avec un miroir mobile (Fig. C.1), mettant en jeu des effets de couplage par pression de radiation. Le domaine de l'optomécanique en cavité s'étend cependant à une grande variété de systèmes, de géométries diverses et réalisant d'autres types de couplage lumière – matière à l'intérieur des cavités monolithiques (par exemple, par la force de gradient, l'effet photo-élastique, la photostriction etc.). Une telle interaction devient considérable à l'échelle micro- et nanométrique, où la masse effective de l'oscillateur mécanique m_{eff} peut être considérablement réduite.

L'effet essentiel du couplage optomécanique est le fait qu'un déplacement mécanique de la cavité induit un changement dans l'état de la lumière. En retour, le changement d'état de la lumière modifie le mouvement de l'oscillateur. Les champs potentiels d'applications de ce domaine couvrent d'une part les études fondamentales de la physique ; on peut ainsi citer le régime quantique d'un oscillateur macroscopique ou bien l'interaction hybride entre un oscillateur mécanique et des systèmes à deux niveaux (atomes, centres NV, boîtes quantiques…). Ainsi, les systèmes optomécaniques sont aujourd'hui envisagés pour les applications dans le traitement quantique de l'information, servant comme une interface cohérente entre les qubits de la lumière et de la matière. D'autre part, l'étude expérimentale des systèmes optomécaniques est étroitement liée aux enjeux métrologiques, en particulier la mesure de très faible déplacements et plus largement de la masse, de la force, de l'accélération, etc. ; ils sont aussi envisagés dans des dispositifs radiofréquences en tant qu'horloges intégrées.

Quel que soit le domaine (fondamental ou appliqué) envisagé, la tendance générale vise à augmenter la fréquence mécanique de fonctionnement f_{m}, ce qui passe par la diminution de la taille de l'oscillateur et au passage la réalisation de cavités monolithiques optiques atteignant la limite de diffraction ; cet enjeu est de fait naturellement associé à celui plus général du couplage de telles cavités monolithiques à l'espace libre. Plusieurs systèmes optomécaniques fonctionnant à la limite de diffraction ont été conçus, parmi lesquels les membranes à cristaux photoniques, qui permettent de contrôler efficacement la propagation de la lumière et son confinement à l'échelle micro- et nanométrique ; ces membranes ont été ainsi choisies dans le cadre de ce travail.

C.2 Cristaux photoniques pour l'optomécanique

Les cristaux photoniques (CP) forment un système naturel ou créé artificiellement, capable de contrôler localement la propagation de la lumière [Joannopoulos 2011]. En général, ce sont des matériaux qui présentent une périodicité dans la constante diélectrique ε dans une ou plusieurs dimensions. Une telle variation, introduite à l'échelle de longueur d'onde optique, peut permettre de contrôler la propagation de la lumière dans une telle structure périodique selon la(les) direction(s) choisie(s). Par analogie avec la bande interdite pour les électrons dans un réseau cristallin de semi-conducteur, les bandes interdites photoniques des CP peuvent également être conçues pour interdire la propagation des photons avec certaines énergies. Ces bandes d'énergie ou plage des longueurs d'onde correspondantes, représentent une bande interdite photonique [Yablonovitch 1987 ; John 1987]. Si on crée un défaut au sein d'un tel milieu périodique, on peut créer une cavité présentant un mode optique dont la fréquence ν_0 est située à l'intérieur de bande interdite photonique. Ce mode ne pourra se propager dans le cristal alentour. Il sera ainsi très confiné avec une durée de vie des photons élevée. Ce système a été intensivement utilisé dans divers domaines et applications en nanophotonique, s'étendant des sources de photons uniques [Laurent 2005] jusqu'à l'optique non-linéaire [Bazin 2014]. Ce n'est que récemment, en 2009, qu'il a été utilisé dans le cadre de l'optomécanique [Eichenfield 2009a ; Eichenfield 2009b]. Ce concept de CP est généralement utilisé dans les systèmes optomécaniques pour créer une cavité optique incorporée dans un dispositif optomécanique. Plusieurs designs des cavités à cristaux photoniques existent ; ils se distinguent par le nombre de dimensions présentant une périodicité de l'indice de réfraction. Pour les applications optomécaniques des systèmes périodiques uni-dimensionnel (1D) et bi-dimensionnel (2D) sont utilisés, le confinement du mode optique dans les directions restantes étant obtenu par réflexion totale interne (la structure est généralement suspendue dans l'air). Dans le cadre de ce travail de thèse, la membrane suspendue est percée par un cristal photonique 2D intégrant une cavité optique à défaut L3 (trois trous manquants en ligne). Notons que le cristal photonique peut être aussi utilisé dans différentes configurations, créant un miroir à incidence normale ou une cavité à défaut dans un cristal parfait.

C.3 Vers l'intégration des résonateurs optomécaniques

La plupart des dispositifs dans les expériences d'optomécanique englobent une cavité optique dont le mode participe dans l'interaction optomécanique. Traditionnellement, cette cavité (dans sa réalisation monolithique) est alimentée avec de la lumière provenant d'un laser de sonde, couplé à une fibre étirée introduite dans le champ évanescent de la cavité. Une telle fibre nécessite une préparation délicate et spécifique (sa partie centrale doit être beaucoup plus mince que celle d'une fibre ordinaire de manière à se coupler au mode de la cavité) ainsi qu'un alignement précis par rapport à l'échantillon sondé dans tous les trois dimensions (dans le plan pour s'accorder avec la cavité et hors plan pour obtenir

un couplage optique) avec une précision jusqu'à quelques dizaines de nanomètres. Cela complique l'expérimentation systématique et avancée sur le dispositif et ajoute plusieurs restrictions importantes : par exemple, il est presque impossible d'adresser deux cavités optiques à la fois ; les conditions de couplage entre la fibre et la cavité sont difficilement reproductibles d'une expérience à l'autre ; l'intégration de tels dispositifs s'avère délicate, etc.

Afin de surmonter ces limitations, certains systèmes existants utilisent un canal d'accès optique intégré, formé par un guide d'onde optique permettant d'adresser de manière efficace le résonateur optomécanique à l'échelle nanométrique. Du point de vue de la fabrication, la solution la plus simple à mettre en œuvre est un guide d'onde ayant un profil rectangulaire fermé par des coupleurs à réseau d'entrée et de sortie pour assurer un couplage à l'espace libre. Toutes les réalisations décrites dans la littérature s'appuient sur un guide d'ondes placé dans le plan d'un résonateur optomécanique (Fig. C.2). Les principales géométries d'accès comprennent des profils de guide d'ondes droits et courbés au point de couplage au mode optique ; éventuellement le résonateur optomécanique peut être conçu comme une partie du guide d'onde d'accès. Tirant parti de périodicité d'un cristal photonique, on peut également intégrer un guide d'onde d'accès à défaut dans une membrane à CP. L'une ou l'autre géométrie ainsi que les dimensions de guides d'ondes sont alors adaptées pour assurer les conditions d'accord de modes optiques et l'efficacité de couplage qu'on souhaite d'atteindre. Une des conséquences de cette intégration planaire du guide d'ondes et du résonateur optomécanique, est que les deux éléments (guide et résonateur) doivent être faits dans la même couche, soit du même matériau. Afin d'assurer un fort confinement de la lumière dans le guide et résonateur, il est nécessaire de recourir à des matériaux de fort indice de réfraction. De fait, la majorité des dispositifs intégrés sont aujourd'hui en silicium (Figures C.2a,d,e), permettant de profiter de l'expertise de fabrication CMOS. Ceci limite la plage de longueur d'onde optique possible (supérieures à 1.1 μm pour limiter les pertes par absorption). Cependant, les dispositifs optiques silicium se heurtent à la forte absorption à deux photons et à l'absorption des porteurs libres dans la gamme des longueurs d'onde télécom, conduisant souvent à des effets thermiques forts limitant la stabilité du dispositif et les performances de son refroidissement par voie optique [Pernice 2011 ; SafaviNaeini 2011a].

Quelques autres matériaux sont apparus récemment dans les expériences d'optomécanique intégrée : on peut citer le diamant [Rath 2013] pour ses propriétés mécaniques exceptionnelles (le module d'Young est d'environ 1 GPa) et le nitrure d'aluminium (AlN) [Xiong 2012 ; Bochmann 2013] pour le couplage électromécanique fort, recherché pour des systèmes optomécaniques accordables électriquement. Afin d'adjoindre des fonctionnalités photoniques actives impossibles avec le silicium, l'arséniure de gallium (GaAs) a aussi trouvé ces dernières années de nouvelles applications dans les systèmes optomécaniques intégrés [Ding 2011 ; Baker 2011]. Tout comme le GaAs, d'autres semi-conducteurs III-V comme le phosphure d'indium (InP) [Gavartin 2011] ou le nitrure de gallium (GaN) peuvent également être utilisés dans des dispositifs optomécaniques. Cependant, pour la

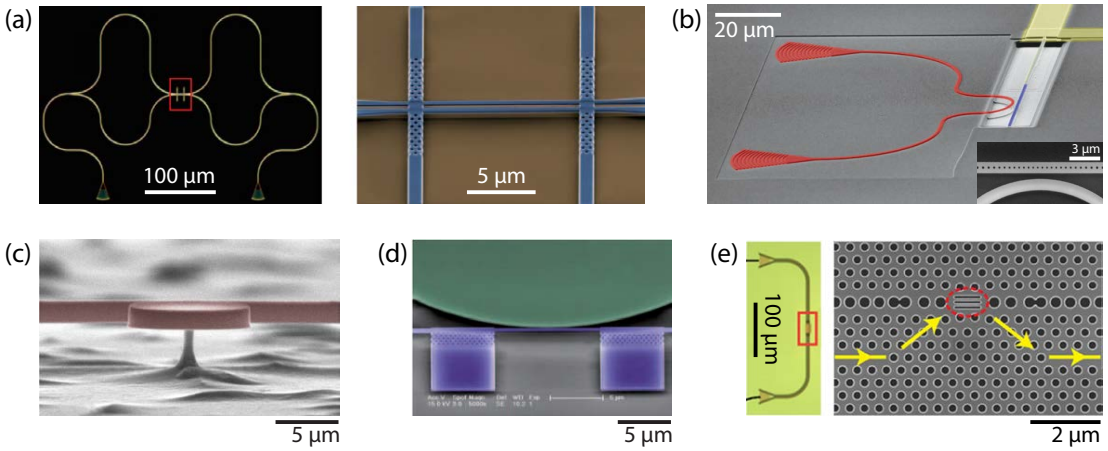

FIGURE C.2 : Quelques réalisations expérimentales de systèmes optomécaniques intégrés comportant un canal d'accès optique. (a) Deux guides d'ondes suspendus mis à proximité [Li 2009a]. (b) Nanopoutre à cristal optomécanique suspendu (bleu) avec un circuit photonique (rouge, guide d'onde et de coupleurs à réseau) [Bochmann 2013]. Microdisque couplé à un guide d'onde suspendu (c) [Baker 2013] ; (d) [Li 2009b]. (e) Cavité L3 – nanopoutre couplée à un guide d'onde à défaut créé dans un cristal photonique [Sun 2012]. Toutes les figures sont adaptées à partir des références correspondantes.

plupart des matériaux précédemment mentionnés (diamant, AIN, GaN, etc.) d'importantes pertes optiques le long des guides d'ondes dans le matériau sont introduites du fait des imperfections de fabrication (la rugosité des parois latérales est plus importante par rapport aux dispositifs en silicium), nécessitant une réduction des dimensions du guide.

La solution retenue dans ce travail de thèse propose d'exploiter l'intégration hétérogène tri-dimensionnelle (3D). Elle permet de séparer la fonctionnalité de guidage et celle de l'oscillateur optomécanique, en les réalisant respectivement sur deux niveaux différents. Cette voie permet une flexibilité totale dans le choix des matériaux pour chacun de ces composants mis en jeu. En outre, elle permet une flexibilité dans la géométrie du dispositif, les cavités optiques pouvant être adressées sur puce quelle que soit leur position. Ceci ouvre la voie à la réalisation de réseaux d'oscillateurs optomécaniques, couplés à la lumière via un unique guide d'onde optique par exemple. Enfin, cette géométrie tridimensionnelle, tout en assurant un couplage optomécanique important, permet de contrôler l'amplitude et la nature de l'interaction, en jouant sur la distance entre le guide d'ondes et la cavité elle-même modifiée par le mouvement mécanique du résonateur. En ayant un contrôle total sur la géométrie du guide d'onde, il est ensuite possible de et mettre en œuvre différents types de couplage optomécanique sur une seule puce.

C.4 Description de la structure étudiée au cours de cette thèse

Plus précisément, ce travail a porté sur une nouvelle réalisation d'une plateforme hybride optomécanique (Fig. C.3), comprenant un guide d'ondes optique intégré en silicium sur isolant à faibles pertes, sur lequel est reporté un résonateur optomécanique ici en semi-conducteur III-V.

Dans la plupart des diapositifs optomécaniques intégrés, les canaux d'accès optiques sont réalisés dans le plan de l'oscillateur. Ici, le résonateur optomécanique est empilé verticalement au dessus du circuit de guidage optique et couplé par ondes évanescentes au mode se propageant dans le guide d'ondes. Cette géométrie hybride a deux avantages principaux : d'une part, la partie "active" du dispositif (c'est-à-dire, celle où se produit l'interaction optomécanique) et le guide d'onde d'accès peuvent être fabriqués de deux matériaux différents. Ceci permet de choisir le matériau avec des propriétés optimisées pour chacun de ces composants. Pour injecter et extraire efficacement la lumière entrant et sortant de la cavité, nous avons conçu un guide d'onde d'accès intégré en silicium sur isolant, présentant tous les avantages de la photonique sur silicium, et parmi eux des faibles pertes optiques par rapport aux guides réalisés dans le matériau de la couche membranaire (ici en semi-conducteur III-V). D'autre part, cette approche tridimensionnelle permet d'accéder à un emplacement arbitraire (ou plusieurs emplacements arbitraires) de la cavité et donne un contrôle total sur le couplage optique mutuel, permettant une conception flexible de la partie "active" du dispositif.

Dans le dispositif développé, le résonateur est formé par une membrane à cristal photonique bidimensionnel en InP et intégrant une cavité optique à défaut pour y confiner la lumière. Ce choix de matériau ayant une bande interdite directe permet d'inclure un milieu actif à l'intérieur de notre dispositif, tel que les boîtes quantiques ou des puits quantiques. Ce milieu actif crée une source de lumière intégrée à large bande des longueurs d'ondes,

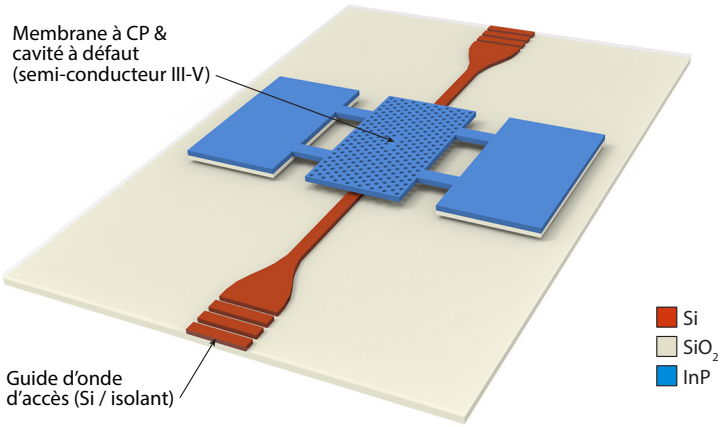

FIGURE C.3 : Représentation schématique de l'architecture du dispositif proposé.

permettant dans ce travail de sonder les propriétés optiques de la cavité telles que la longueur d'onde et largeur de raie d'émission qui peuvent être largement accordées lors de conception du résonateur optique. Le mouvement mécanique à la fois de la membrane et du coeur de la cavité impacte les propriétés optiques de la cavité à défaut par différents effets optomécaniques. Une couche sacrificielle entre les niveaux d'InP et silicium sur substrat SOI (silicium-sur-isolant – *silicon-on-insulator* en anglais) a été utilisée pour la suspension de la membrane. Un contrôle précis de la distance guide-cavité à l'aide des techniques de fabrication classiques a permis de maîtriser à la fois le couplage de la lumière entre le guide d'ondes et la cavité, et la force des interactions optomécaniques induites par la modulation du couplage optique due au mouvement de la membrane.

C.5 Simulations optiques, mécaniques et optomécaniques de la structure

La simulation complète des structures a été menée, tout d'abord en considérant les caractéristiques optiques et mécaniques séparément et ensuite abordant la caractérisation optomécanique du système hybride. L'objectif ici est d'optimiser les paramètres géométriques de la plateforme et extraire les processus d'interaction mis en jeu. Pour la partie optique, deux configurations de membrane à CP bidimensionnel ont été étudiées, soit pour former un miroir déformable parfait soit pour réaliser une cavité à défaut à l'intérieur du cristal photonique et intégrée de manière hétérogène avec un guide d'onde SOI. Dans les deux géométries optiques, le design mécanique du résonateur a été étudié permettant ensuite d'identifier clairement les processus de couplage optomécanique. Deux familles distinctes des modes mécaniques ont été considérées, correspondant (1) au mouvement de flexion de la membrane de type tambour (avec des fréquences propres dans la gamme de MHz) et (2) aux vibrations localisées dans le cœur de la cavité à défaut dans le CP (f_{m} dans la gamme de GHz) .

Le couplage optomécanique dans notre système hybride intégré implique deux types d'effets – dispersif et dissipatif. Ces effets peuvent être produits par deux mécanismes distincts. Ces deux effets sont (i) les effets dits externes, gouvernés par la présence d'un guide d'onde SOI couplé de manière évanescente au voisinage d'une cavité à CP, et (ii) les couplages intrinsèques, qui dépendent exclusivement des processus se produisant dans le cœur de la membrane à CP. Leur impact respectif peut aussi être différent. Le mouvement mécanique des modes de flexion de la membrane modifie l'écart entre la cavité et le guide d'onde h_{air}, ce qui a pour effet de changer le recouvrement mutuel des modes optiques lorsque la distance guide-cavité est suffisamment faible (ce qui est le cas dans nos expériences). Les conséquences sont double. Tout d'abord, tout changement ou modulation de h_{air} modifie les pertes optiques de la cavité, résultant dans un couplage optomécanique dit dissipatif externe [Elste 2009 ; Xuereb 2011] (Fig. C.4b). Ce couplage dissipatif externe est induit par la modulation du recouvrement des queues du champ évanescent – entre modes optiques de la cavité et du guide d'onde, lorsque la membrane se déplace et change

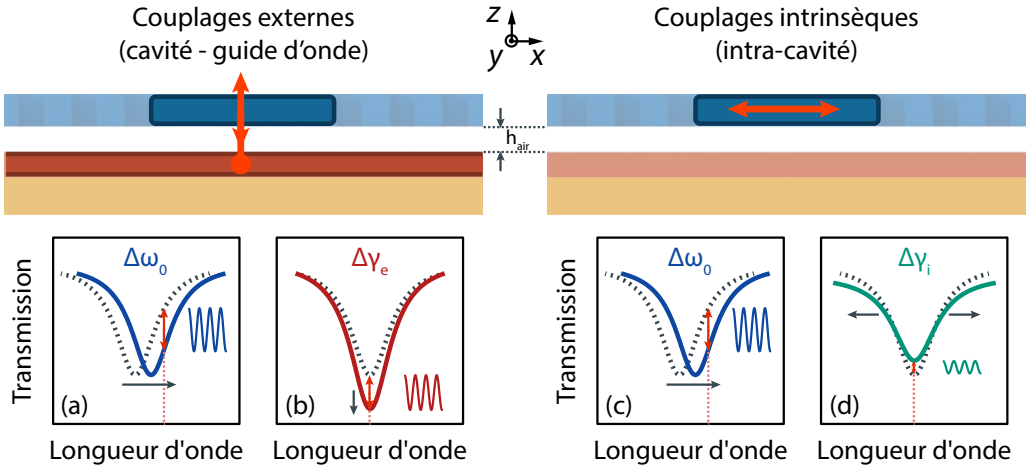

FIGURE C.4 : Illustration de l'effet du déplacement mécanique sur la réponse optique d'une cavité à CP (en surbrillance en bleu) couplée à un guide d'onde SOI (en surbrillance en rouge), après une demi-période d'oscillation mécanique. Est présentée la variation de la forme de la résonance optique détectée après transmission via le guide d'ondes, pour les couplages optomécaniques externes dispersif (a) et dissipatif (b), et ses équivalents intrinsèques (c,d).

la position de la cavité intégrée par rapport au guide d'onde fixe. D'autre part, tout changement ou modulation de h_{air} induit une modification de la fréquence de résonance ω_0 de la cavité optique (Fig. C.4a) en raison de la modification de l'environnement diélectrique autour de cette cavité ; cet effet introduit un couplage optomécanique dit externe dispersif [Kippenberg 2008]. La fréquence de résonance ω_0 du mode de la cavité dépend aussi de la distribution du tenseur diélectrique ε à l'intérieur de la membrane et dans son voisinage. Par conséquent, la modulation de la séparation membrane – guide d'onde h_{air} affectera ω_0 en changeant la distribution de ε dans le champ évanescent du mode.

Deux mécanismes supplémentaires de couplage apparaissent lorsque la déformation de la membrane durant son mouvement mécanique impacte les paramètres optiques intrinsèques de la cavité, tels que son taux de déclin intrinsèque γ_i (correspondant au facteur de qualité Q_0) (Fig. C.4d) et sa fréquence de résonance ω_0 (Fig. C.4c). Ces deux effets sont respectivement dénommés couplages optomécaniques intrinsèques dissipatif et dispersif.

La dépendance des couplages externes en fonction des différents paramètres optogéométriques du système intégré, tels que la séparation verticale membrane – guide d'onde et la largeur du guide d'onde ont été examinés. Les couplages optomécaniques intrinsèques ont été numériquement étudiés pour les deux familles de modes mécaniques, impliquant cette fois les effets photo-élastique et le déplacement des bords de la cavité optique. Ces couplages existeraient aussi dans un système sans un guide d'onde intégré, ainsi ils ont été dénommés intrinsèques.

Les résultats pour les modes de flexion de la membrane à CP (dans la gamme fréquentielle de MHz) sont montrés sur la Figure C.5 ; cette figure présente aussi les distributions du

champ de déplacement associées aux différents modes étudiés, pour lesquels les valeurs des différents couplages sont données dans le Tableau C.1 avec les paramètres caractéristiques principaux. Les simulations pour la famille des modes mécaniques localisés (dans la gamme fréquentielle du GHz) ont également été effectués.

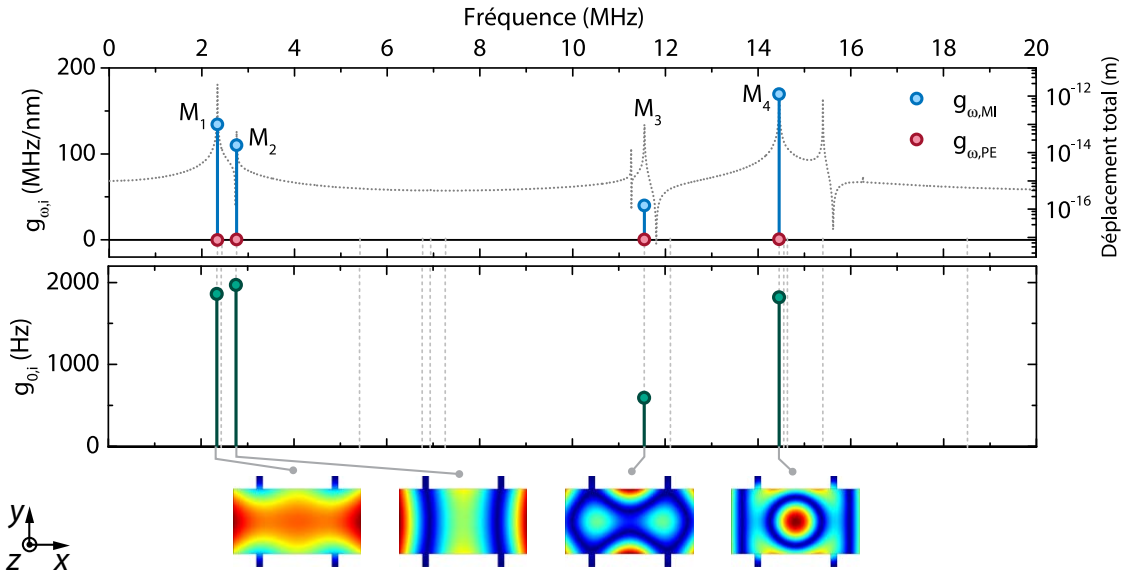

FIGURE C.5 : Valeurs simulées des différentes composantes du couplage optomécanique intrinsèque dispersif $g_{\omega,i}$ (dû aux interfaces mobiles [MI] et dû à l'effet photoélastique [PE]). Les paramètres caractéristiques sont extraits pour plusieurs modes de flexion d'une membrane en InP suspendue ayant les dimensions $m_x = 20$ μm, $m_y = 10$ μm, $b_x = 1$ μm, $b_y = 2$ μm. La courbe grise pointillée (en haut) représente la réponse mécanique suite à l'actionnement externe de la membrane, mesurée au milieu de la cavité ; les profils de $\vec{Q}$ correspondants sont présentés en bas pour les modes d'intérêt.

Mode	$\Omega_m/2\pi$ (MHz)	m_{eff} (pg)	x_{ZPF} (fm)	$g_{\omega,\text{MI}}$ (MHz/nm)	$g_{\omega,\text{PE}}$ (MHz/nm)	$g_{0,i}$ (Hz)
M_1	2.34	117.2	5.54	134.4	-0.27	1858.5
M_2	2.75	61.8	7.14	110.1	0.24	1967.8
M_3	11.54	21.7	5.90	39.8	0.24	590.6
M_4	14.45	32.9	4.28	169.5	0.49	1818.5

TABLE C.1 : Valeurs simulées des couplages optomécaniques intrinsèques dispersifs et des paramètres caractéristiques pour plusieurs modes de flexion d'une membrane 10×20 μm^2 en InP suspendue.

Ces travaux ont aussi révélé la possibilité de façonner à la fois l'amplitude et le poids relatif des effets de couplage dissipatif et dispersif (Figure C.6). Ceci ouvre la voie à la mise en œuvre d'un refroidissement optimisé jusqu'à l'état fondamental de notre résonateur

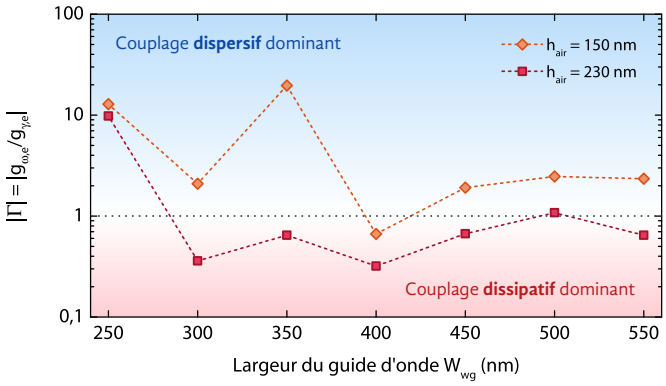

FIGURE C.6 : Rapport entre les forces de couplage optomécanique externe dispersif $g_{\omega,e}$ et dissipatif $g_{\gamma,e}$, obtenues par simulations numériques, en fonction de la largeur du guide d'onde d'accès W_{wg} et pour deux séparations différentes h_{air} entre la membrane à CP et le guide d'onde.

mécanique dans le régime dominé par le couplage dissipatif. Ce régime présente l'avantage de relaxer les contraintes sur les pertes optiques de la cavité, en comparaison au refroidissement en régime de couplage dispersif usuellement employé.

C.6 Procédé de fabrication

La fabrication de la plateforme hétérogène optomécanique intégrée repose sur plusieurs étapes, dont en particulier le collage de substrats SOI et en semi-conducteur III-V, la préparation des marques d'alignement à contraste élevé pour la lithographie électronique, la gravure des composants optiques (réseau du cristal photonique) et mécaniques (structures mesa) ainsi que le retrait de la couche sacrificielle afin de suspendre la membrane à CP. Ces étapes ont nécessité un travail de développement et optimisation. La technique de collage employée avec un contrôle précis de l'épaisseur de la couche sacrificielle a permis d'atteindre une précision sur la séparation entre les niveaux SOI et semi-conducteur III-V de $\leqslant$ 10 nm (dans la direction hors plan). Grâce à l'introduction de marques d'alignement, l'alignement des cavités à cristaux photoniques en InP suspendues par rapport au circuit SOI a été réalisé avec une précision de $\leqslant$ 40 nm dans les directions dans le plan. La structuration de la couche InP a été optimisée en faisant usage des résines positive (PMMA) et négative (HSQ), ce qui a permis de satisfaire les différentes exigences pour les parties optique et mécanique du dispositif ; ce travail d'optimisation se traduit notamment par l'obtention des cavités optiques à haut facteur de qualité Q. L'écart-type de la longueur d'onde de résonance entre les cavités à CP avec les mêmes paramètres géométriques est d'environ $2-3$ nm sur l'ensemble de l'échantillon (typiquement comprenant plusieurs centaines de dispositifs). Enfin, la technologie de séchage supercritique nous a permis d'atteindre un rendement de 100 % pendant la suspension des membranes, pour des distances entre la membrane et le substrat d'environ 200 nm et pour les membranes à CP ayant des

dimensions latérales de 10×20 μm^2.

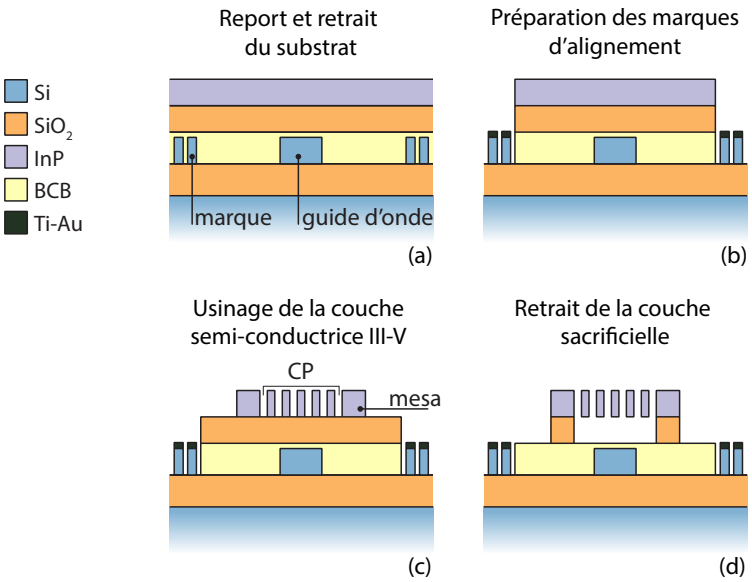

FIGURE C.7 : Étapes principales de fabrication pour la structuration de la membrane suspendue à cristal photonique bidimensionnel en semi-conducteur III-V sur un circuit intégré des guides d'ondes SOI (silicium-sur-isolant).

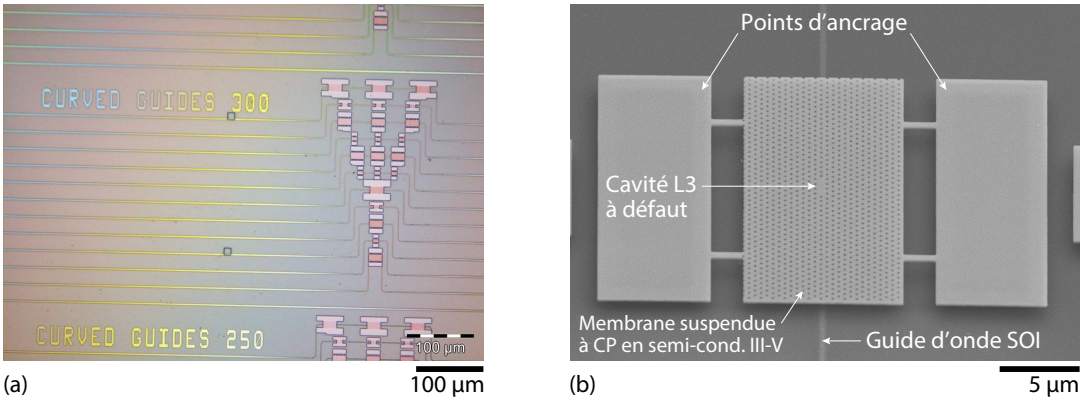

FIGURE C.8 : Dispositifs fabriqués à leur phase finale. (a) Vue de dessus de l'échantillon montrant la partie du réseau des guides d'onde SOI dans le milieu de section effilée ; ces guides permettent d'adresser les membranes suspendues. (b) Cliché du microscope électronique à balayage (MEB) d'une seule membrane suspendue à cristal photonique.

C.7 Mesures optomécaniques avancées

La réponse mécanique des membranes suspendues a été dans un premier étudiée dans un montage interférométrique. Les mesures ont alors été confrontées aux simulations, en examinant l'évolution de la fréquence propre et du facteur de qualité mécanique Q_{m} pour

les différents paramètres géométriques de la structure suspendue. Ces mesures montrent, comme attendu, une diminution des pertes intrinsèques induite par le matériau avec la température de l'environnement ; ainsi le facteur de qualité mécanique augmente d'un facteur 3 environ, en passant de la température ambiante (T_b = 300 K) à celle de l'hélium liquide (4.4 K). Une réduction supplémentaire des pertes dues à l'ancrage sur les mesa permettant de suspendre la membrane a aussi été obtenue en allongeant les ponts entre la membrane et les points d'ancrage. On constate ainsi une amélioration de Q_{m} par un facteur d'environ 5 pour le mode mécanique fondamental, en allongeant les ponts 1 μm à 12 μm. Cette observation a été rendue possible, grâce à l'intégration d'une couche mince d'InGaAs de 10/20 nm d'épaisseur à l'intérieur de la membrane InP, permettant d'améliorer sa rigidité et par conséquent obtenir une suspension correcte du dispositif sans son effondrement au substrat.

Ces résultats ont ensuite été utilisés dans la mise en œuvre de la plateforme intégrée, confirmant le contrôle attendu sur les conditions et l'efficacité du couplage mutuel entre le guide d'onde d'accès et une cavité optique intégrée. La spectroscopie optique et mécanique sur de tels dispositifs conventionnels utilise la technique dite "side of the fringe". Cette technique a déjà montré de bonnes performances dans la détection du mouvement brownien de la membrane à cristal photonique 2D. Le dispositif expérimental employé est illustré dans la Figure C.9. Un faisceau laser accordable est couplé au guide d'onde, lui-même couplé à la cavité optique. La courbe de transmission optique en sortie du guide présente une forme généralement Lorentzienne centrée sur la longueur d'onde de résonance λ_0 de la cavité (voir la Figure C.9, *Optique*). Le résonateur mécanique, oscillant à sa fréquence

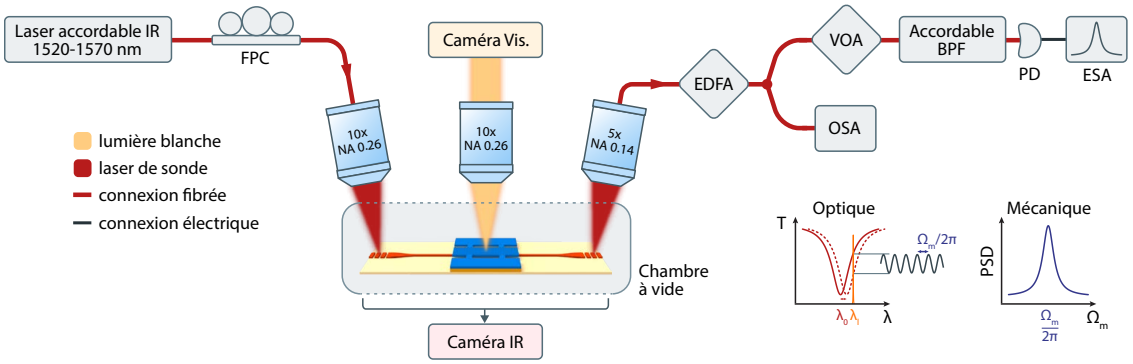

FIGURE C.9 : Schéma du montage expérimental pour les mesures du spectre mécanique du dispositif optomécanique intégré. Les connexions en espace libre, fibrées et électriques sont indiquées. Le mécanisme de transduction du mouvement mécanique sur la sonde laser fixe est illustré sur deux spectres, montrant la transmission du guide d'ondes couplé à la cavité [T(λ)] et la densité spectrale de puissance de la sonde laser transmise [PSD(Ω_{m})], tel qu'il est mesuré par l'ASE (ESA sur le schéma). (IR - infra-rouge, FPC – contrôleur de polarisation fibré, Vis. – visible, NA – ouverture numérique, EDFA – amplificateur en fibre dopée erbium, VOA – atténuateur optique variable, OSA – analyseur de spectre optique, BPF – filtre passe-bande, PD – photodiode, ESA – analyseur de spectre électrique.)

propre $\Omega_m/2\pi$, module la longueur d'onde de résonance et la largeur spectrale de la cavité par l'intermédiaire de mécanismes de couplage dispersif ou dissipatif (voir la Section 2.3.1 pour plus de détails). Par conséquent, une telle modulation de la réponse Lorentzienne de la cavité optique s'imprime sur le laser de sonde (dans le cas où sa largeur de raie est beaucoup plus étroite par rapport à celle de la cavité $\gamma_l \ll \gamma_t$)). La réponse mécanique peut donc être sondée, en désaccordant légèrement le faisceau laser par rapport à la longueur d'onde de résonance et en mesurant le spectre de son bruit d'intensité, comme le montre la Figure C.9. Dans cette configuration, l'intensité de la sonde est modulée à la fréquence de l'oscillation mécanique du résonateur, et ce pour tous les modes mécaniques qui ont un impact sur le mode optique. En examinant le bruit de la sonde transmise par un ASE (analyseur du spectre électrique ; ESA en anglais), on récupère le spectre de(s) mode(s) mécanique(s) de la membrane dans le spectre de densité spectrale de la puissance (PSD, pour *power spectral density* en anglais) (Fig. C.9).

Cette technique de détection donne ainsi le spectre mécanique, dont un exemple est montré sur la Figure C.10a (courbe rouge). L'expérience est réalisée dans une chambre à vide à basse pression P $< 10^{-4}$ mbar afin d'éviter l'amortissement de l'air, qui a un impact considérable pour les modes de flexion d'une membrane. Dans cette étude, nous avons utilisé une cavité à défaut L3 ayant une résonance optique autour de $\lambda_0 \sim 1560$ nm, incorporée dans une membrane des dimensions de 20×10 μm^2, suspendue à l'aide des

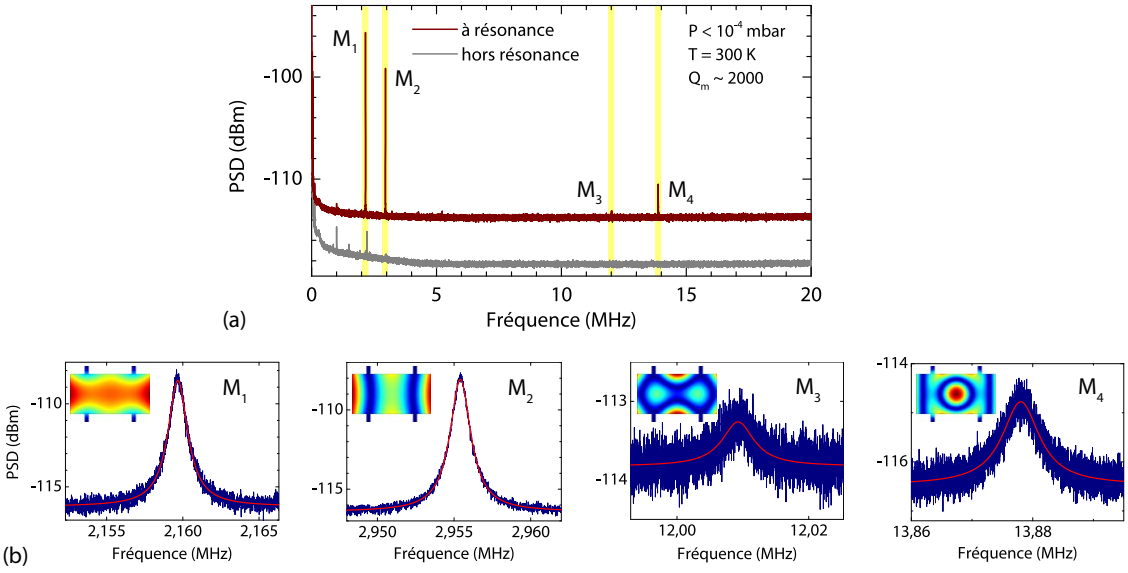

FIGURE C.10 : (a) Densité spectrale de puissance (PSD) du signal optique transmis pour le laser de sonde à résonance (courbe rouge) et hors résonance (courbe grise) optique avec la cavité intégrée dans une membrane suspendue à CP (dimensions : $m_x = 20$ μm, $m_y = 10$ μm, $t = 260$ nm, $b_x = 1$ μm, $b_y = 2$ μm, $b_d = 5.9$ μm). (b) PSD des résonances mécaniques détectées, prise avec une meilleure résolution autour de chacune des quatre fréquences propres (bleu – les données, rouge – ajustement Lorentzien). Les distributions du champ de déplacement $\vec{Q}(\vec{r})$ correspondantes simulées sont données dans les encarts.

quatre ponts 1×2 μm.

La densité spectrale de puissance (PSD) du signal transmis, mesurée dans la gamme de 1 à 100 MHz révèle quelques pics de résonance, correspondant aux modes mécaniques de la membrane suspendue, en accord avec nos simulations. Les modes présents dans le spectre de basse fréquence correspondent à ceux qui manifestent dans la spectroscopie numérique les amplitudes simulées les plus importantes. Une mesure supplémentaire a été effectuée avec un laser de sonde hors de résonance de la cavité (à savoir, avec $\Delta = 3 - 5$ nm), pour détecter tout signal parasite présent dans le montage expérimental, signal dû aux sources de bruit électrique qui ne sont pas liées au mouvement mécanique du dispositif étudié (courbe grise dans la Fig. C.10a).

Les taux de couplage optomécanique sous vide ont été déterminés pour les modes mécaniques détectés dans la gamme des fréquences jusqu'à 100 MHz par l'intermédiaire des techniques de modulation de fréquence, ce qui a donné les valeurs de $g_0/2\pi$ de 0.1 à 45 kHz, comparables à l'état de l'art des systèmes optomécaniques dans cette gamme de fréquences [Wilson 2014].

La technique expérimentale pour mesurer séparément les forces des différents mécanismes de couplage optomécanique, consiste à étudier la variation des caractéristiques des modes mécaniques, variations induites par effet du ressort optique [*optical spring effect* en anglais] (Fig. C.11). Cet effet se traduit par une modification de l'amplitude, fréquence et pertes mécaniques, en fonction du désaccord entre le laser et le mode optique de la cavité. Pour ce faire, nous avons mesuré l'évolution de la densité spectrale de $\bar{S}_{\mathrm{P}}(\Omega, \Delta)$ autour de

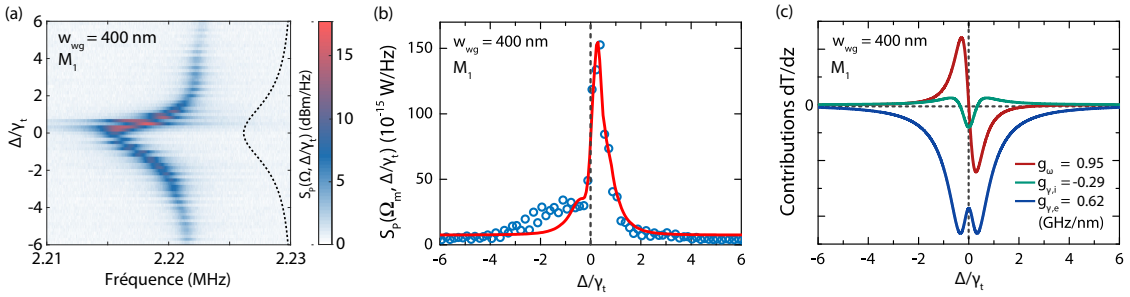

FIGURE C.11 : (a) Densité spectrale de puissance $S_{\mathrm{P}}(\Omega, \Delta/\gamma_t)$ pour le mode mécanique fondamental M_1, mesurée pour le dispositif avec le guide d'ondes d'accès dont la largeur est de $w_{\mathrm{wg}} = 400$ nm. L'ajustement Lorentzien du mode de résonance de la cavité est montré en pointillés noirs pour référence. Le désaccord du laser de sonde Δ est normalisé par rapport à la largeur de raie totale γ_t de la cavité optique. (b) Densité spectrale de puissance à résonance mécanique $S_{\mathrm{P}}(\Omega_{\mathrm{m}}, \Delta/\gamma_t)$ (cercles vides) en fonction du désaccord normalisé du laser de sonde Δ/γ_t pour le mode mécanique fondamental M_1 [données extraites à partir de (a)]. La ligne continue représente l'ajustement du modèle théorique. (c) Contributions au bruit du spectre de transmission (en unités arbitraires ; rouge : couplage dispersif total, vert : couplage dissipatif intrinsèque ; bleu : couplage dissipatif externe) obtenu par ajustement de la courbe expérimentale dans (b). Les taux de couplage optomécanique déduits sont indiqués.

la fréquence de résonance mécanique Ω_{m} du mode considéré, en fonction de la longueur d'onde du laser sonde. La Figure C.11a rassemble ces différents spectres en fonction du désaccord du laser de sonde (ce désaccord est normalisé par rapport à la largeur de raie γ_t de la cavité optique intégrée).

Cette mesure de ressort optique nous donne un aperçu rapide sur le changement des trois principaux paramètres mécaniques lorsque la longueur d'onde de la sonde laser varie autour de la résonance de la cavité : la fréquence du mode Ω_{m}, l'intensité du pic de résonance α et la largeur de raie mécanique Γ sont modifiées.

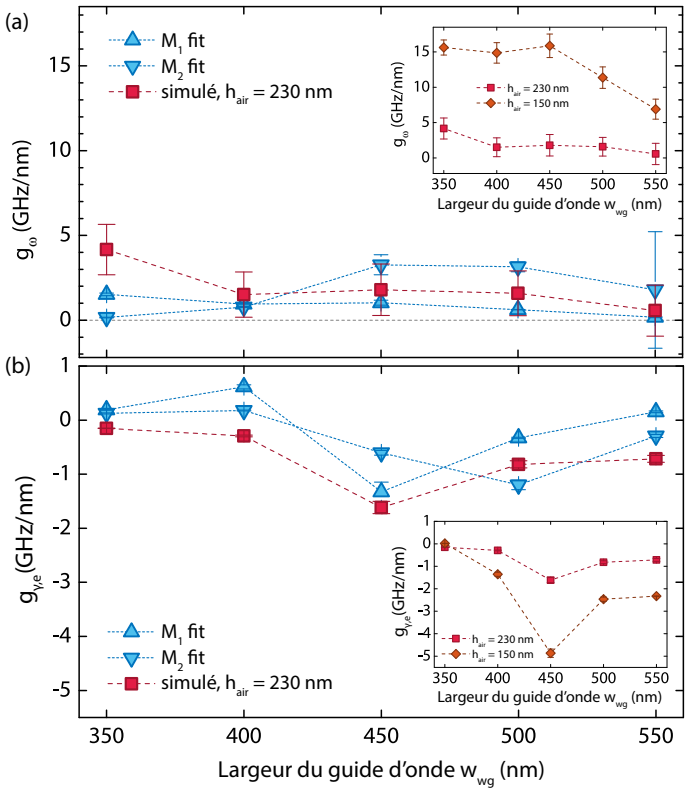

FIGURE C.12 : (a) Coefficient de couplage dispersif g_ω (total) et (b) externe dissipatif $g_{\gamma,e}$, tracés en fonction de la largeur du guide d'onde w_{wg}. Les triangles bleus pointant vers le haut correspondent aux coefficients extraits de l'ajustement théorique des données mesurées pour le mode M_1. Les triangles bleus pointant vers le bas correspondent aux coefficients extraits de l'ajustement théorique des données mesurées pour le mode M_2. Les carrés rouges correspondent aux valeurs calculées avec l'approche 3D FDTD statique pour l'épaisseur d'espace d'air de $h_{\mathrm{air}} = 230$ nm. Les diamants oranges représentent les forces de couplage optomécanique calculées pour $h_{\mathrm{air}} = 150$ nm. Encadrés : valeurs calculées de g_ω et $g_{\gamma,e}$ en fonction de w_{wg}.

La dépendance de l'amplitude mécanique α comparativement au désaccord du laser sonde Δ est ensuite ajustée avec un modèle analytique, permettant d'extraire les différentes forces de couplage optomécanique. La Figure C.11b montre les données expérimentales (cercles bleus) pour le mode mécanique fondamental, extraites de la Figure C.11a avec

l'ajustement correspondant (ligne rouge) à notre modèle théorique. La référence de désaccord nul est marquée par une ligne en pointillés gris. Comme on peut le voir, pour la géométrie donnée du guide d'accès ($w_{\mathrm{wg}} = 400$ nm), l'intensité $\alpha = \bar{S}_{\mathrm{P}}(\Omega = \Omega_{\mathrm{m}}, \Delta)$ présente une forte asymétrie par rapport à cette ligne de référence. Le modèle théorique donne une courbe raisonnablement bien ajustée avec des maxima d'amplitude à la valeur du désaccord de $\Delta \approx +\gamma_t/4$. L'ajustement théorique permet également d'extraire le poids des différents mécanismes de couplage optomécanique (voir la Figure C.11c). Les valeurs obtenues sont en bon accord avec celles correspondantes estimées théoriquement.

Nous avons expérimentalement estimé les composantes dispersives et dissipatives de couplage optomécanique pour différentes dimensions du guide d'onde d'accès. Les résultats sont rassemblés sur la Figure C.12. Des simulations supplémentaires ont aussi inclus l'impact de la variation de la distance entre la membrane et le guide d'onde d'accès. L'ensemble de résultats (mesures et simulations) confirme la possibilité d'adapter les valeurs absolues et relatives des forces de couplage optomécanique externes en accordant la géométrie du canal d'accès optique intégré et la séparation entre ce canal et la membrane suspendue.

Enfin, les effets induits thermiquement ont été étudiés, proposant par la suite un mécanisme de mise en œuvre d'une commutation (*switching* en anglais) mécanique bi-stable, en exploitant la bi-stabilité thermo-optique. Nous avons aussi réalisé des études préliminaires sur le mécanisme de transduction entre la modulation du laser de pompe non-résonant et du laser de sonde résonant en utilisant le milieu actif (boîtes quantiques à l'intérieur de la membrane à CP) en tant qu'intermédiaire.

C.8 Annexe A. Développement des membranes semi-conductrices accessibles par les deux faces pour l'optomécanique

Des membranes contraintes, accessibles optiquement par les deux faces pour des expériences optomécaniques de type "membrane-au-milieu" (*"membrane-in-the-middle"* en anglais), ont d'autre part été conçues et fabriquées. Ces membranes présentent des propriétés mécaniques contrôlables via la composition d'alliage ternaire de semi-conducteur utilisé ; d'autre part, la contrainte induite permet partiellement une forte amélioration des facteurs de qualité mécaniques. Les valeurs de la contrainte ajoutée obtenues sont de 350 MPa pour l'alliage $\mathrm{In_{0.45}Ga_{0.55}P}$ et 240 MPa pour $\mathrm{GaAs_{0.95}P_{0.05}}$ avec une marge de progression. Les deux alliages sont fabriqués par l'épitaxie en phase vapeur aux organométalliques sur des substrats d'arséniure de gallium (GaAs).

C.9 Perspectives principales

Le système optomécanique étudié dans ces travaux ouvre la voie à la mise en œuvre de diverses fonctionnalités pour la physique fondamentale et appliqué ; dans ce qui suit, nous

présentons deux voies possible.

À titre d'exemple, les modes qui occupent la gamme GHz, sont attractifs pour les applications de refroidissement, la température permettant d'atteindre le régime quantique étant plus élevée que pour les modes dans la gamme MHz. Cependant, il reste néanmoins nécessaire d'adjoindre des techniques de refroidissement optique, jusqu'à présent mises en œuvre dans le régime de couplage dispersif. Ce régime est très exigent sur les pertes optiques de la cavité. Or, il a été récemment démontré que le refroidissement peut être mis en œuvre en régime dissipatif, qui relaxe les contraints sur les pertes optiques. Ces plateformes, à couplage optomécanique contrôlé, constituent au fait des dispositifs prometteurs.

D'autre part, la membrane en semi-conducteur III-V permet ici l'incorporation de milieu actif formé par une monocouche des boîtes quantiques, qui peuvent être considérées comme des systèmes à deux niveaux sous faible excitation et basse température. Ce milieu actif, intégré dans une cavité semi-conductrice, a été largement étudié dans le cadre d'interaction lumière-matière, par exemple, pour l'émission des photons uniques [Laurent 2005]. Le couplage à ce genre de systèmes à deux niveaux dans des dispositifs optomécaniques a été peu exploré expérimentalement [Arcizet 2011], cependant, il offre une direction prometteuse pour la mise en œuvre des mécanismes de refroidissement hybrides [WilsonRae 2004]. À plus long terme, il permet d'envisager l'étude du couplage hybride entre un mode mécanique à haute fréquence dans son état quantique fondamental et un système quantique à deux niveaux.

La plupart des enjeux du domaine (fondamentaux et appliqués) requièrent un couplage optomécanique important, qui pourrait être exalté par la réalisation des réseaux à cristal phononique/photonique (dit phoxonique) afin de réduire les pertes mécaniques par ancrage. Soulignons qu'un autre mécanisme optomécanique, la photostriction, est susceptible d'entraîner la génération des phonons de haute fréquence (GHz) à l'intérieur de la cavité à défaut. L'existence d'un tel mécanisme reste encore à démontrer.

Ces modes de haute fréquence présentent un intérêt pour les applications métrologiques ou photonique RF. Cependant, celles-ci requirent une stabilisation en fréquence de l'oscillateur. Les réalisations expérimentales déjà existantes [HosseinZadeh 2008 ; Zheng 2013] montrent que la fréquence et la phase d'un oscillateur optomécanique (OOM) peuvent en effet être verrouillées à celles d'un oscillateur électronique externe. Des techniques de verrouillage par injection d'un oscillateur optomécanique à un oscillateur électronique radio-fréquence (RF) ont aussi été mises en oeuvre. Ces dispositifs bénéficieraient fortement d'une augmentation du nombre de fonctionnalités intégrées, permettant d'élargir les outils de contrôle de la réponse mécanique et donc des techniques de verrouillage telles que les techniques d'auto-référencement. Un tel défi peut être relevé dans notre dispositif hybride, en mettant en œuvre des mécanismes d'excitation et d'accordabilité différents.

Dans cette perspective, les travaux futurs sur le système actuel viseront à poursuivre l'exploration des non-linéarités optiques et mécaniques, pour atteindre le régime d'auto-oscillation. D'autres outils d'actionnement des vibrations mécaniques dans la gamme

MHz seront intégrées, tels que l'actionnement électrostatique via un peigne d'électrodes métalliques intégrées sous la membrane en InP [Legtenberg 1996] (voir Figure C.13a).

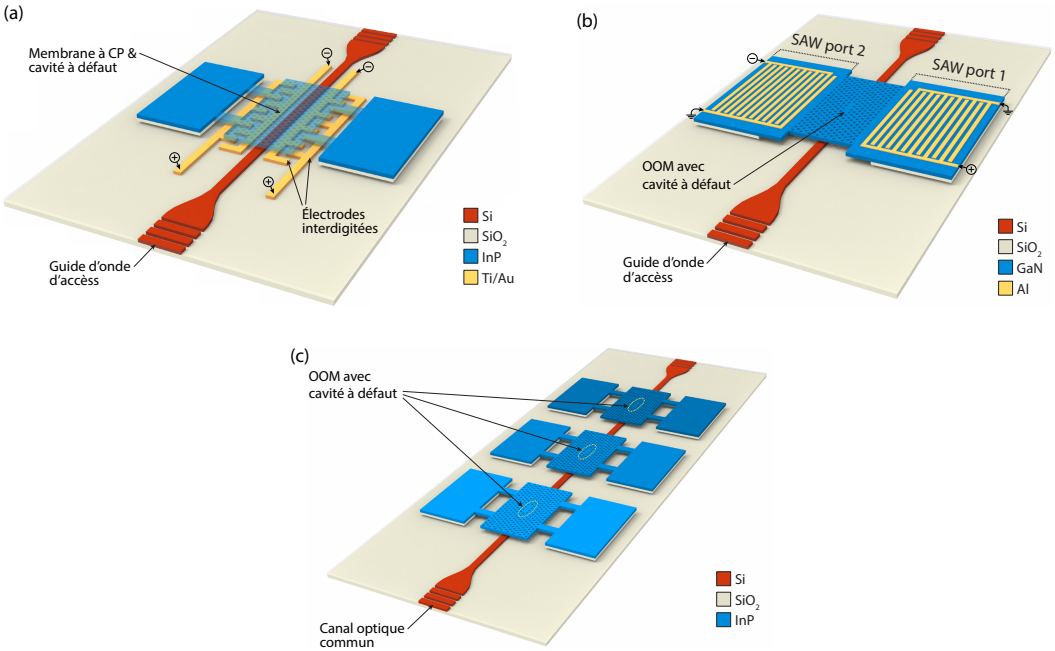

FIGURE C.13 : (a) Vue conceptuelle de l'architecture du dispositif proposé comprenant les actuateurs. (b) Représentation schématique du dispositif optomécanique comportant une excitation intégrée des ondes acoustiques de surface dans la plage des GHz via des transducteurs à ondes de surface (SAW pour *surface acoustic waves* en anglais). La lecture de la réponse mécanique du dispositif peut être effectuée simultanément en utilisant un canal d'accès optique et les transducteurs SAW (via le paramètre S_{21} dans la configuration à deux ports représentée). (c) Vue conceptuelle de l'architecture du dispositif proposé pour l'étude de la synchronisation mécanique entre les différents oscillateurs optomécaniques couplés via un canal optique commun.

Les perspectives à moyen terme étendront ces travaux à la deuxième famille de modes mécaniques présents dans la configuration du résonateur actuel, les modes localisés dans le cœur de la cavité à défaut (correspondant à la gamme fréquentielle du GHz). Contrairement à l'excitation et l'actionnement des modes de flexion de la membrane utilisant le champ électrostatique provenant des électrodes interdigitées (Fig. C.13a), les modes localisés nécessitent une autre solution, par exemple, en utilisant des transducteurs à ondes acoustiques de surface (SAW), formés de peignes interdigitées (Fig. C.13b). Ce processus de transduction peut être large bande en recourant à des peignes à pas variables et pourrait permettre de lire le spectre mécanique en utilisant un résonateur SAW à deux ports [Benchabane 2015]. Cependant, le processus de transduction ici, s'appuie sur la piézoélectricité du matériau. On peut imaginer ainsi d'incorporer une couche piézoélectrique intermédiaire entre le peigne et la couche d'InP. Une option plus simple consiste à utiliser un matériau semi-conducteur approprié ayant de bonnes propriétés piézoélectriques, tel que le GaAs

ou, encore mieux, le GaN/AlN, pour réaliser le résonateur optomécanique.

La deuxième voie d'expériences en perspective à long terme inclut la synchronisation de deux ou plusieurs résonateurs mécaniques. Ceci peut être réalisé par les canaux de connexion optiques [Shah 2015] (voir Figure C.13c), permettant d'obtenir plus de deux oscillateurs synchronisés [Holmes 2012 ; Zhang 2015]), mécaniques [Shim 2007] ou électriques [Matheny 2014]. Ce dispositif hybride intégré permettra ainsi d'accéder simultanément à plusieurs modes optiques spatialement séparés, couplés à un ou plusieurs (différents) modes mécaniques, qui par conception peuvent être coïncidents ou séparés spatialement. Ce couplage de plusieurs oscillateurs optomécaniques, ouvre la voie à l'exploration d'effets optomécaniques multimodes, comme la synchronisation en réseau et la formation de motifs (*pattern formation* en anglais) [Lauter 2015].

Bibliography

[Acernese 2008] F Acernese et al. "The Virgo 3 km interferometer for gravitational wave detection". In: *Journal of Optics A: Pure and Applied Optics* 10.6 (June 2008), p. 064009. DOI: 10.1088/1464-4258/10/6/064009.

[Adachi 1992] Sadao Adachi. *Physical Properties of III-V Semiconductor Compounds*. Vol. 1992. Wiley, 1992, p. 318. ISBN: 0471573299.

[Adams 2014] Thomas S. Adams. "Detector Characterisation and Searches for Gravitational Waves Using GEO 600". PhD thesis. Cardiff University, 2014, p. 203.

[Agilent 2012] Agilent. *Spectrum and Signal Analyzer Measurements and Noise: Application Note 1303*. Agilent Technologies, 2012, p. 31.

[Akahane 2003] Yoshihiro Akahane, Takashi Asano, Bong-Shik Song, and Susumu Noda. "High-Q photonic nanocavity in a two-dimensional photonic crystal." In: *Nature* 425.6961 (Oct. 2003), pp. 944–7. DOI: 10.1038/nature02063.

[Akahane 2005] Yoshihiro Akahane, Takashi Asano, Bong-Shik Song, and Susumu Noda. "Fine-tuned high-Q photonic-crystal nanocavity". In: *Optics Express* 13.4 (2005), p. 1202. DOI: 10.1364/OPEX.13.001202.

[Almeida 2004] Vilson R. Almeida and Michal Lipson. "Optical bistability on a silicon chip". EN. In: *Optics Letters* 29.20 (Oct. 2004), p. 2387. DOI: 10.1364/OL.29.002387.

[Arcizet 2006a] O Arcizet, P-F Cohadon, T Briant, M Pinard, and A Heidmann. "Radiation-pressure cooling and optomechanical instability of a micromirror." In: *Nature* 444.7115 (Nov. 2006), pp. 71–4. DOI: 10.1038/nature05244.

[Arcizet 2006b] O. Arcizet, P.-F. Cohadon, T. Briant, M. Pinard, A. Heidmann, J.-M. Mackowski, C. Michel, L. Pinard, O. Français, and L. Rousseau. "High-Sensitivity Optical Monitoring of a Micromechanical Resonator with a Quantum-Limited Optomechanical Sensor". In:

Physical Review Letters 97.13 (Sept. 2006), p. 133601. DOI: 10.1103/PhysRevLett.97.133601.

[Arcizet 2011] O. Arcizet, V. Jacques, A. Siria, P. Poncharal, P. Vincent, and S. Seidelin. "A single nitrogen-vacancy defect coupled to a nanomechanical oscillator". In: *Nature Physics* 7.11 (Sept. 2011), pp. 879–883. DOI: 10.1038/nphys2070.

[Aspelmeyer 2013] Markus Aspelmeyer, Tobias J. Kippenberg, and Florian Marquardt. "Cavity Optomechanics". In: (Mar. 2013), p. 65. arXiv: 1303.0733.

[Aspelmeyer 2014] Markus Aspelmeyer, Tobias J. Kippenberg, and Florian Marquardt, eds. *Cavity Optomechanics*. Berlin, Heidelberg: Springer Berlin Heidelberg, 2014. ISBN: 978-3-642-55311-0. DOI: 10.1007/978-3-642-55312-7.

[Aspelmeyer 2012] Markus Aspelmeyer, Pierre Meystre, and Keith Schwab. "Quantum optomechanics". In: *Physics Today* 65.7 (2012), p. 29. DOI: 10.1063/PT.3.1640.

[Baca 2005] Albert G. Baca and Carroll I. H. Ashby. *Fabrication of GaAs Devices*. Vol. 2005. 2005, p. 350. ISBN: 0863413536.

[Bagci 2014] T Bagci, A Simonsen, S Schmid, L G Villanueva, E Zeuthen, J Appel, J M Taylor, A Sørensen, K Usami, A Schliesser, and E S Polzik. "Optical detection of radio waves through a nanomechanical transducer." In: *Nature* 507.7490 (Mar. 2014), pp. 81–5. DOI: 10.1038/nature13029.

[Bagheri 2011] Mahmood Bagheri, Menno Poot, Wolfram Pernice, and Hong Tang. "Nonvolatile optomechanical memory enabled by dynamic optical backaction". In: *Advanced Photonics*. Optical Society of America, 2011, IMB2. DOI: 10.1364/IPRSN.2011.IMB2.

[Baker 2011] C. Baker, C. Belacel, A. Andronico, P. Senellart, A. Lemaitre, E. Galopin, S. Ducci, G. Leo, and I. Favero. "Critical optical coupling between a GaAs disk and a nanowaveguide suspended on the chip". In: *Applied Physics Letters* 99.15 (Oct. 2011), p. 151117. DOI: 10.1063/1.3651493.

[Baker 2013] Christopher Baker. "On-chip nano-optomechanical whispering gallery resonators". PhD Thesis. Université Paris-Diderot - Paris VII, 2013.

[Balram 2014] Krishna C. Balram, Marcelo Davanço, Ju Young Lim, Jin Dong Song, and Kartik Srinivasan. "Moving boundary and photoelastic coupling in GaAs optomechanical resonators". EN. In: *Optica* 1.6 (Dec. 2014), p. 414. DOI: 10.1364/OPTICA.1.000414.

[Barish 1999] Barry C. Barish and Rainer Weiss. "LIGO and the Detection of Gravitational Waves". en. In: *Physics Today* 52.10 (Jan. 1999), p. 44. DOI: 10.1063/1.882861.

[Bazin 2013] Alexandre Bazin. "III-V Semiconductor Nanocavitieson Silicon-On-Insulator Waveguide : Laser Emission, Switching and Optical Memory". en. PhD thesis. Université Paris-Diderot - Paris VII, July 2013.

[Bazin 2014] Alexandre Bazin, Rama Raj, and Fabrice Raineri. "Design of Silica Encapsulated High-Q Photonic Crystal Nanobeam Cavity". In: *Journal of Lightwave Technology* 32.5 (Mar. 2014), pp. 952–958. DOI: 10.1109/JLT.2013.2295267.

[Benchabane 2015] Sarah Benchabane, Olivier Gaiffe, Roland Salut, Gwenn Ulliac, Vincent Laude, and Kimmo Kokkonen. "Guidance of surface waves in a micron-scale phononic crystal line-defect waveguide". In: *Applied Physics Letters* 106.8 (Feb. 2015), p. 081903. DOI: 10.1063/1.4913532.

[Berenger 1994] Jean-Pierre Berenger. "A perfectly matched layer for the absorption of electromagnetic waves". In: *Journal of Computational Physics* 114.2 (Oct. 1994), pp. 185–200. DOI: 10.1006/jcph.1994.1159.

[Bluestein 1970] L. Bluestein. "A linear filtering approach to the computation of discrete Fourier transform". English. In: *IEEE Transactions on Audio and Electroacoustics* 18.4 (Dec. 1970), pp. 451–455. DOI: 10.1109/TAU.1970.1162132.

[Bochmann 2013] Joerg Bochmann, Amit Vainsencher, David D. Awschalom, and Andrew N. Cleland. "Nanomechanical coupling between microwave and optical photons". In: *Nature Physics* 9.11 (Sept. 2013), pp. 712–716. DOI: 10.1038/nphys2748.

[Bose 1997] S. Bose, K. Jacobs, and P. L. Knight. "Preparation of nonclassical states in cavities with a moving mirror". In: *Physical Review A* 56.5 (Nov. 1997), pp. 4175–4186. DOI: 10.1103/PhysRevA.56.4175.

[Braginskii 1977] V. B. Braginskii and A. B. Manukin. *Measurement of weak forces in physics experiments*. 1977.

[Braginsky 1992] Vladimir B Braginsky, Farid Ya Khalili, and Kip S Thorne. *Quantum Measurement*. Cambridge University Press, 1992. ISBN: 9780511622748.

[Braive 2009] R. Braive, S. Barbay, I. Sagnes, A. Miard, I. Robert-Philip, and A. Beveratos. "Transient chirp in high-speed photonic-crystal quantum-dot lasers with controlled spontaneous emission". In: *Optics Letters* 34.5 (Feb. 2009), p. 554. DOI: 10.1364/OL.34.000554.

[Bruel 1997] Michel Bruel, Bernard Aspar, and Andre-Jacques Auberton-Hervé. "Smart-Cut: A New Silicon On Insulator Material Technology Based on Hydrogen Implantation and Wafer Bonding". In: *Japanese Journal of Applied Physics* 36.Part 1, No. 3B (Mar. 1997), pp. 1636–1641. DOI: 10.1143/JJAP.36.1636.

[Brunstein 2009] M Brunstein, R Braive, R Hostein, A Beveratos, I Rober-Philip, I Sagnes, T J Karle, A M Yacomotti, J A Levenson, V Moreau, G Tessier, and Y De Wilde. "Thermo-optical dynamics in an optically pumped Photonic Crystal nano-cavity." EN. In: *Optics express* 17.19 (Sept. 2009), pp. 17118–29. DOI: 10.1364/OE.17.017118.

[Burek 2014] Michael J Burek, Yiwen Chu, Madelaine S Z Liddy, Parth Patel, Jake Rochman, Srujan Meesala, Wooyoung Hong, Qimin Quan, Mikhail D Lukin, and Marko Lončar. "High quality-factor optical nanocavities in bulk single-crystal diamond." en. In: *Nature communications* 5 (Jan. 2014), p. 5718. DOI: 10.1038/ncomms6718.

[Camerer 2011] Stephan Camerer, Maria Korppi, Andreas Jöckel, David Hunger, Theodor W. Hänsch, and Philipp Treutlein. "Realization of an Optomechanical Interface Between Ultracold Atoms and a Membrane". In: *Physical Review Letters* 107.22 (Nov. 2011), p. 223001. DOI: 10.1103/PhysRevLett.107.223001.

[Canal 1979] F. Canal, M. Grimsditch, and M. Cardona. "Piezobirefringence in GaP and InP". In: *Solid State Communications* 29.7 (Feb. 1979), pp. 523–526. DOI: 10.1016/0038-1098(79)90349-1.

[Chan 2011] Jasper Chan, T. P. Mayer Alegre, Amir H. Safavi-Naeini, Jeff T. Hill, Alex Krause, Simon Gröblacher, Markus Aspelmeyer, and Oskar Painter. "Laser cooling of a nanomechanical oscillator into its quantum ground state". In: *Nature* 478.7367 (Oct. 2011), pp. 89–92. DOI: 10.1038/nature10461.

[Chan 2012] Jasper Chan, Amir H. Safavi-Naeini, Jeff T. Hill, Seán Meenehan, and Oskar Painter. "Optimized optomechanical crystal cavity with acoustic radiation shield". In: *Applied Physics Letters* 101.8 (2012), p. 081115. DOI: 10.1063/1.4747726.

[Chang 2011] D E Chang, A H Safavi-Naeini, M Hafezi, and O Painter. "Slowing and stopping light using an optomechanical crystal array". In: *New Journal of Physics* 13.2 (Feb. 2011), p. 023003. DOI: 10.1088/1367-2630/13/2/023003.

[Cleland 2002] Andrew N. Cleland. *Foundations of Nanomechanics: From Solid-State Theory to Device Applications*. 2002, p. 436. ISBN: 3540436618.

[Cohadon 1999] P. F. Cohadon, A. Heidmann, and M. Pinard. "Cooling of a Mirror by Radiation Pressure". In: *Physical Review Letters* 83.16 (Oct. 1999), pp. 3174–3177. DOI: 10.1103/PhysRevLett.83.3174.

[Cole 2011] Garrett D Cole, Ignacio Wilson-Rae, Katharina Werbach, Michael R Vanner, and Markus Aspelmeyer. "Phonon-tunnelling dissipation in mechanical resonators." In: *Nature communications* 2 (Jan. 2011), p. 231. DOI: 10.1038/ncomms1212.

[Cole 2014] Garrett D. Cole, Pen-Li Yu, Claus Gärtner, Karoline Siquans, Ramon Moghadas Nia, Jonas Schmöle, Jason Hoelscher-Obermaier, Thomas P. Purdy, Witlef Wieczorek, Cindy a. Regal, and Markus Aspelmeyer. "Tensile-strained InxGa1-xP membranes for cavity optomechanics". In: *Applied Physics Letters* 104.20 (May 2014), p. 201908. DOI: 10.1063/1.4879755. arXiv: 1404.0029.

[Courant 1928] R. Courant, K. Friedrichs, and H. Lewy. "Über die partiellen Differenzengleichungen der mathematischen Physik". In: *Mathematische Annalen* 100.1 (Dec. 1928), pp. 32–74. DOI: 10.1007/BF01448839.

[Denton 1991] A. Denton and N. Ashcroft. "Vegard's law". In: *Physical Review A* 43.6 (Mar. 1991), pp. 3161–3164. DOI: 10.1103/PhysRevA.43.3161.

[Ding 2011] L. Ding, C. Baker, P. Senellart, A. Lemaitre, S. Ducci, G. Leo, and I. Favero. "Wavelength-sized GaAs optomechanical resonators with gigahertz frequency". In: *Applied Physics Letters* 98.11 (Mar. 2011), p. 113108. DOI: 10.1063/1.3563711.

[Dong 2014] B. Dong, J. G. Huang, H. Cai, P. Kropelnicki, A. B. Randles, Y. D. Gu, and A. Q. Liu. "Nano-opto-mechanical memory based on optical gradient force induced bistability". English. In: *2014 IEEE 27th International Conference on Micro Electro Mechanical Systems (MEMS)*. IEEE, Jan. 2014, pp. 1091–1094. ISBN: 978-1-4799-3509-3. DOI: 10.1109/MEMSYS.2014.6765835.

[Eichenfield 2009a] Matt Eichenfield, Ryan Camacho, Jasper Chan, Kerry J Vahala, and Oskar Painter. "A picogram- and nanometre-scale photonic-crystal optomechanical cavity." In: *Nature* 459.7246 (May 2009), pp. 550–5. DOI: 10.1038/nature08061.

[Eichenfield 2009b] Matt Eichenfield, Jasper Chan, Ryan M. Camacho, Kerry J. Vahala, and Oskar Painter. "Optomechanical crystals". In: *Nature* 462.7269 (Oct. 2009), pp. 78–82. DOI: 10.1038/nature08524.

[Eichenfield 2009c] Matt Eichenfield, Jasper Chan, Amir H Safavi-Naeini, Kerry J Vahala, and Oskar Painter. "Modeling dispersive coupling and losses of localized optical and mechanical modes in optomechanical crystals." In: *Optics express* 17.22 (Oct. 2009), pp. 20078–98. DOI: 10.1364/OE.17.020078. arXiv: 0908.0025.

[Ellis 2011] Bryan Ellis, Marie A. Mayer, Gary Shambat, Tomas Sarmiento, James Harris, Eugene E. Haller, and Jelena Vučković. "Ultralow-threshold electrically pumped quantum-dot photonic-crystal nanocavity laser". en. In: *Nature Photonics* 5.5 (Apr. 2011), pp. 297–300. DOI: 10.1038/nphoton.2011.51.

[Elste 2009] Florian Elste, S. M. Girvin, and A. A. Clerk. "Quantum Noise Interference and Backaction Cooling in Cavity Nanomechanics". In: *Physical Review Letters* 102.20 (May 2009), p. 207209. DOI: 10.1103/PhysRevLett.102.207209.

[Emmons 1992] R.M. Emmons and D.G. Hall. "Buried-oxide silicon-on-insulator structures. II. Waveguide grating couplers". English. In: *IEEE Journal of Quantum Electronics* 28.1 (1992), pp. 164–175. DOI: 10.1109/3.119511.

[Fabre 1994] C. Fabre, M. Pinard, S. Bourzeix, A. Heidmann, E. Giacobino, and S. Reynaud. "Quantum-noise reduction using a cavity with a movable mirror". In: *Physical Review A* 49.2 (Feb. 1994), pp. 1337–1343. DOI: 10.1103/PhysRevA.49.1337.

[Fox 2001] Mark Fox. *Optical Properties of Solids*. Vol. 2001. 2001, p. 305. ISBN: 0198506139.

[Gavartin 2011] Emanuel Gavartin, Remy Braive, Isabelle Sagnes, Olivier Arcizet, Alexios Beveratos, and Isabelle Robert. "Optomechanical coupling in a two dimensional photonic crystal cavity". In: *Physical Review Letters* 106.20 (May 2011), pp. 2011–2012. DOI: 10.1103/PhysRevLett.106.203902.

[GomisBresco 2014] J Gomis-Bresco, D Navarro-Urrios, M Oudich, S El-Jallal, A Griol, D Puerto, E Chavez, Y Pennec, B Djafari-Rouhani, F Alzina, A Martinez, and C M Sotomayor Torres. "A one-dimensional optomechanical crystal with a complete phononic band gap." en. In: *Nature communications* 5 (Jan. 2014), p. 4452. DOI: 10.1038/ncomms5452.

[Gorodetsky 2010] M. L. Gorodetsky, A. Schliesser, G. Anetsberger, S. Deleglise, and T. J. Kippenberg. "Determination of the vacuum optomechanical coupling rate using frequency noise calibration". In: *Optics Express* 18.22 (Oct. 2010), p. 23236. DOI: 10.1364/OE.18.023236.

[Gosset 2006] C. Gosset, K. Merghem, A. Martinez, G. Moreau, G. Patriarche, G. Aubin, J. Landreau, F. Lelarge, and A. Ramdane. "Subpicosecond pulse generation at 134 GHz and low radiofrequency spectral linewidth in quantum dash-based Fabry-Perot lasers emitting at 1.5 [micro sign]m". In: *Electronics Letters* 42.2 (2006), p. 91. DOI: 10.1049/el:20063868.

[Gröblacher 2009] Simon Gröblacher, Jared B. Hertzberg, Michael R. Vanner, Garrett D. Cole, Sylvain Gigan, K. C. Schwab, and Markus Aspelmeyer. "Demonstration of an ultracold micro-optomechanical oscillator in a cryogenic cavity". In: *Nature Physics* 5.7 (June 2009), pp. 485–488. DOI: 10.1038/nphys1301.

[Haus 1984] Hermann A. Haus. *Waves and fields in optoelectronics*. 1984, p. 402. ISBN: 0139460535.

[Hays 1999] David C Hays. "Selective Etching of Compound Semiconductors". Master Thesis. University of Florida, 1999.

[Hechenblaikner 1998] Gerald Hechenblaikner, Markus Gangl, Peter Horak, and Helmut Ritsch. "Cooling an atom in a weakly driven high- Q cavity". In: *Physical Review A* 58.4 (Oct. 1998), pp. 3030–3042. DOI: 10.1103/PhysRevA.58.3030.

[Heinrich 2011] Georg Heinrich, Max Ludwig, Jiang Qian, Björn Kubala, and Florian Marquardt. "Collective Dynamics in Optomechanical Arrays". In: *Physical Review Letters* 107.4 (July 2011), p. 043603. DOI: 10.1103/PhysRevLett.107.043603.

[Hennessy 2003] K. Hennessy, C. Reese, A. Badolato, C. F. Wang, A. Imamoglu, P. M. Petroff, E. Hu, G. Jin, S. Shi, and D. W. Prather. "Square-lattice photonic crystal microcavities for coupling to single InAs quantum dots". In: *Applied Physics Letters* 83.18 (Oct. 2003), p. 3650. DOI: 10.1063/1.1623319.

[Holmes 2012] C. A. Holmes, C. P. Meaney, and G. J. Milburn. "Synchronization of many nanomechanical resonators coupled via a common cavity field". In: *Physical Review E* 85.6 (June 2012), p. 066203. DOI: 10.1103/PhysRevE.85.066203.

[HosseinZadeh 2008] Mani Hossein-Zadeh and Kerry J. Vahala. "Observation of injection locking in an optomechanical rf oscillator". In: *Applied Physics Letters* 93.19 (Nov. 2008), p. 191115. DOI: 10.1063/1.3028024.

[Hostein 2010] R Hostein, R Braive, L Le Gratiet, A Talneau, G Beaudoin, I Robert-Philip, I Sagnes, and A Beveratos. "Demonstration of coherent emission from high-beta photonic crystal nanolasers at room temperature." EN. In: *Optics letters* 35.8 (Apr. 2010), pp. 1154–6. DOI: 10.1364/OL.35.001154.

[Hryciw 2014] Aaron C. Hryciw, Marcelo Wu, Behzad Khanaliloo, and Paul E. Barclay. "Near-field tuning of optomechanical coupling in a split-beam nanocavity". In: (July 2014), p. 5. arXiv: 1407.0106.

[Jacobs 1994] K. Jacobs, P. Tombesi, M. J. Collett, and D. F. Walls. "Quantum-nondemolition measurement of photon number using radiation pressure". In: *Physical Review A* 49.3 (Mar. 1994), pp. 1961–1966. DOI: 10.1103/PhysRevA.49.1961.

[Jallal 2013] Said El-Jallal, Mourad Oudich, Yan Pennec, Bahram Djafari-Rouhani, Vincent Laude, Jean-Charles Beugnot, Alejandro Martinez, José Maria Escalante, and Abdelkader Makhoute. "Analysis of optomechanical coupling in two-dimensional square lattice phoxonic crystal slab cavities". In: *Physical Review B* 88.20 (Nov. 2013), p. 205410. DOI: 10.1103/PhysRevB.88.205410.

[Joannopoulos 2011] John D. Joannopoulos, Steven G. Johnson, Joshua N. Winn, and Robert D. Meade. *Photonic Crystals: Molding the Flow of Light (Second Edition)*. 2011, p. 304. ISBN: 1400828244.

[John 1987] Sajeev John. "Strong localization of photons in certain disordered dielectric superlattices". In: *Physical Review Letters* 58.23 (June 1987), pp. 2486–2489. DOI: 10.1103/PhysRevLett.58.2486.

[Johnson 2002] Steven G Johnson, M Ibanescu, M A Skorobogatiy, O Weisberg, J D Joannopoulos, and Y Fink. "Perturbation theory for Maxwell's equations with shifting material boundaries". In: *Phys. Rev. E* 65.6 (2002), p. 66611. DOI: 10.1103/PhysRevE.65.066611.

[Johnson 2001] Steven Johnson and John Joannopoulos. "Block-iterative frequency-domain methods for Maxwell's equations in a planewave basis". In: *Optics Express* 8.3 (Jan. 2001), p. 173. DOI: 10.1364/OE.8.000173.

[Karagodsky 2012] Vadim Karagodsky and Connie J Chang-Hasnain. "Physics of near-wavelength high contrast gratings." EN. In: *Optics express* 20.10 (May 2012), pp. 10888–95. DOI: 10.1364/OE.20.010888.

[Karle 2010] T. J. Karle, Y. Halioua, F. Raineri, P. Monnier, R. Braive, L. Le Gratiet, G. Beaudoin, I. Sagnes, G. Roelkens, F. van Laere, D. Van Thourhout, and R. Raj. "Heterogeneous integration and precise alignment of InP-based photonic crystal lasers to complementary metal-oxide semiconductor fabricated silicon-on-insulator wire waveguides". In: *Journal of Applied Physics* 107.6 (Mar. 2010), p. 063103. DOI: 10.1063/1.3319667.

[Keyvaninia 2013] S. Keyvaninia, M. Muneeb, S. Stanković, P. J. Van Veldhoven, D. Van Thourhout, and G. Roelkens. "Ultra-thin DVS-BCB adhesive bonding of III-V wafers, dies and multiple dies to a patterned silicon-on-insulator substrate". In: *Optical Materials Express* 3.1 (Dec. 2013), p. 35. DOI: 10.1364/OME.3.000035.

[Kippenberg 2008] T J Kippenberg and K J Vahala. "Cavity optomechanics: back-action at the mesoscale." In: *Science (New York, N.Y.)* 321.5893 (Aug. 2008), pp. 1172–6. DOI: 10.1126/science.1156032.

[Kippenberg 2007] Tobias J Kippenberg and Kerry J Vahala. "Cavity opto-mechanics." In: *Optics express* 15 (2007), pp. 17172–17205. DOI: 10.1364/OE.15.017172. arXiv: 0712.1618.

[Laurent 2005] S. Laurent, S. Varoutsis, L. Le Gratiet, A. Lemaitre, I. Sagnes, F. Raineri, A. Levenson, I. Robert-Philip, and I. Abram. "Indistinguishable single photons from a single-quantum dot in a two-dimensional photonic crystal cavity". In: *Applied Physics Letters* 87.16 (Oct. 2005), p. 163107. DOI: 10.1063/1.2103397.

[Lauter 2015] Roland Lauter, Christian Brendel, Steven J. M. Habraken, and Florian Marquardt. "Pattern phase diagram for two-dimensional arrays of coupled limit-cycle oscillators". In: *Physical Review E* 92.1 (July 2015), p. 012902. DOI: 10.1103/PhysRevE.92.012902. arXiv: 1501.01509.

[Lebedew 1901] Peter Lebedew. "Untersuchungen über die Druckkräfte des Lichtes". In: *Annalen der Physik* 311.11 (1901), pp. 433–458. DOI: 10.1002/andp.19013111102.

[Legtenberg 1996] Rob Legtenberg, A W Groeneveld, and M Elwenspoek. "Comb-drive actuators for large displacements". In: *Journal of Micromechanics and Microengineering* 6.3 (Sept. 1996), pp. 320–329. DOI: 10.1088/0960-1317/6/3/004.

[Li 2009a] Mo Li, W. H. P. Pernice, and H. X. Tang. "Tunable bipolar optical interactions between guided lightwaves". In: *Nature Photonics* 3.8 (July 2009), pp. 464–468. DOI: 10.1038/nphoton.2009.116.

[Li 2009b] Mo Li, Wolfram H. P. Pernice, and Hong X. Tang. "Reactive Cavity Optical Force on Microdisk-Coupled Nanomechanical Beam Waveguides". In: *Physical Review Letters* 103.22 (Nov. 2009), p. 223901. DOI: 10.1103/PhysRevLett.103.223901.

[Li 2010] Ying Li, Jiangjun Zheng, Jie Gao, Jing Shu, Mehmet Sirin Aras, and Chee Wei Wong. "Design of dispersive optomechanical coupling and cooling in ultrahigh-Q/V slot-type photonic crystal cavities." EN. In: *Optics express* 18.23 (Nov. 2010), pp. 23844–56. DOI: 10.1364/OE.18.023844.

[Liu 2011] J. Liu, K. Usami, A. Naesby, T. Bagci, E. S. Polzik, P. Lodahl, and S. Stobbe. "High-Q optomechanical GaAs nanomembranes". In: *Applied Physics Letters* 99.24 (2011), p. 243102. DOI: 10.1063/1.3668092.

[Liu 2012] Victor Liu and Shanhui Fan. "S4 : A free electromagnetic solver for layered periodic structures". In: *Computer Physics Communications* 183.10 (Oct. 2012), pp. 2233–2244. DOI: 10.1016/j.cpc.2012.04.026.

[Liu 2015] Yong-Chun Liu, Rui-Shan Liu, Chun-Hua Dong, Yan Li, Qihuang Gong, and Yun-Feng Xiao. "Cooling mechanical resonators to the quantum ground state from room temperature". In: *Physical Review A* 91.1 (Jan. 2015), p. 013824. DOI: 10.1103/PhysRevA.91.013824.

[Luan 2014] Xingsheng Luan et al. "An integrated low phase noise radiation-pressure-driven optomechanical oscillator chipset." en. In: *Scientific reports* 4 (Jan. 2014), p. 6842. DOI: 10.1038/srep06842.

[Mahboob 2011] I Mahboob, E Flurin, K Nishiguchi, A Fujiwara, and H Yamaguchi. "Interconnect-free parallel logic circuits in a single mechanical resonator." In: *Nature communications* 2 (Jan. 2011), p. 198. DOI: 10.1038/ncomms1201.

[Mahboob 2014] I Mahboob, M Mounaix, K Nishiguchi, A Fujiwara, and H Yamaguchi. "A multimode electromechanical parametric resonator array." en. In: *Scientific reports* 4 (Jan. 2014), p. 4448. DOI: 10.1038/srep04448.

[Makles 2015] K. Makles, T. Antoni, A. G. Kuhn, S. Deléglise, T. Briant, P.-F. Cohadon, R. Braive, G. Beaudoin, L. Pinard, C. Michel, V. Dolique, R. Flaminio, G. Cagnoli, I. Robert-Philip, and A. Heidmann. "2D photonic-crystal optomechanical nanoresonator". In: *Optics Letters* 40.2 (Jan. 2015), p. 174. DOI: 10.1364/OL.40.000174.

[Maldovan 2013] Martin Maldovan. "Sound and heat revolutions in phononics." In: *Nature* 503.7475 (Nov. 2013), pp. 209–17. DOI: 10.1038/nature12608.

[Maldovan 2006] Martin Maldovan and Edwin L. Thomas. "Simultaneous localization of photons and phonons in two-dimensional periodic structures". In: *Applied Physics Letters* 88.25 (June 2006), p. 251907. DOI: 10.1063/1.2216885.

[Malitson 1965] I. H. Malitson. "Interspecimen Comparison of the Refractive Index of Fused Silica". In: *Journal of the Optical Society of America* 55.10 (Oct. 1965), p. 1205. DOI: 10.1364/JOSA.55.001205.

[Mancini 1997] S. Mancini, V. I. Man'ko, and P. Tombesi. "Ponderomotive control of quantum macroscopic coherence". In: *Physical Review A* 55.4 (Apr. 1997), pp. 3042–3050. DOI: 10.1103/PhysRevA.55.3042.

[Mancini 1994] S. Mancini and P. Tombesi. "Quantum noise reduction by radiation pressure". In: *Physical Review A* 49.5 (May 1994), pp. 4055–4065. DOI: 10.1103/PhysRevA.49.4055.

[Manolatou 1999] C. Manolatou, M.J. Khan, S. Fan, P.R. Villeneuve, H.A. Haus, and J.D. Joannopoulos. "Coupling of modes analysis of resonant channel add-drop filters". English. In: *IEEE Journal of Quantum Electronics* 35.9 (1999), pp. 1322–1331. DOI: 10.1109/3.784592.

[Marcatili 1969] E. A. J. Marcatili. "Dielectric Rectangular Waveguide and Directional Coupler for Integrated Optics". In: *Bell System Technical Journal* 48.7 (Sept. 1969), pp. 2071–2102. DOI: 10.1002/j.1538-7305.1969.tb01166.x.

[Marquardt 2007] Florian Marquardt, Joe Chen, A. Clerk, and S. Girvin. "Quantum Theory of Cavity-Assisted Sideband Cooling of Mechanical Motion". In: *Physical Review Letters* 99.9 (Aug. 2007), p. 093902. DOI: 10.1103/PhysRevLett.99.093902.

[Matheny 2014] Matthew H. Matheny, Matt Grau, Luis G. Villanueva, Rassul B. Karabalin, M. C. Cross, and Michael L. Roukes. "Phase Synchronization of Two Anharmonic Nanomechanical Oscillators". In: *Physical Review Letters* 112.1 (Jan. 2014), p. 014101. DOI: 10.1103/PhysRevLett.112.014101.

[Matsumoto 2013] Nobuyuki Matsumoto, Kentaro Komori, Yuta Michimura, Gen Hayase, Yoichi Aso, and Kimio Tsubono. "5-mg suspended mirror driven by measurement-induced back-action". In: (Dec. 2013), p. 4. arXiv: 1312.5031.

[Matthews 1974] J.W. Matthews and A.E. Blakeslee. "Defects in epitaxial multilayers". In: *Journal of Crystal Growth* 27 (Dec. 1974), pp. 118–125. DOI: 10.1016/S0022-0248(74)80055-2.

[Merghem 2008] K. Merghem, A. Akrout, A. Martinez, G. Moreau, J.-P. Tourrenc, F. Lelarge, F. Van Dijk, G.-H. Duan, G. Aubin, and A. Ramdane. "Short pulse generation using a passively mode locked single InGaAsP/InP quantum well laser". In: *Optics Express* 16.14 (July 2008), p. 10675. DOI: 10.1364/OE.16.010675.

[Mohammadi 2010] Saeed Mohammadi, Ali A Eftekhar, Abdelkrim Khelif, and Ali Adibi. "Simultaneous two-dimensional phononic and photonic band gaps in opto-mechanical crystal slabs." EN. In: *Optics express* 18.9 (Apr. 2010), pp. 9164–72. DOI: 10.1364/OE.18.009164.

[Namatsu 1998] Hideo Namatsu, Yasuo Takahashi, Kenji Yamazaki, Toru Yamaguchi, Masao Nagase, and Kenji Kurihara. "Three-dimensional siloxane resist for the formation of nanopatterns with minimum linewidth fluctuations". In: *Journal of Vacuum Science & Technology B: Microelectronics and Nanometer Structures* 16.1 (Jan. 1998), p. 69. DOI: 10.1116/1.589837.

[Nawrodt 2008] R Nawrodt, A Zimmer, T Koettig, C Schwarz, D Heinert, M Hudl, R Neubert, M Thürk, S Nietzsche, W Vodel, P Seidel, and A Tünnermann. "High mechanical Q-factor measurements on silicon bulk samples". In: *Journal of Physics: Conference Series* 122.1 (July 2008), p. 012008. DOI: 10.1088/1742-6596/122/1/012008.

[Neben 2012] Abraham R Neben, Timothy P Bodiya, Christopher Wipf, Eric Oelker, Thomas Corbitt, and Nergis Mavalvala. "Structural thermal noise in gram-scale mirror oscillators". en. In: *New Journal of Physics* 14.11 (Nov. 2012), p. 115008. DOI: 10.1088/1367-2630/14/11/115008.

[Nichols 1901] E. F. Nichols and G. F. Hull. "A Preliminary Communication on the Pressure of Heat and Light Radiation". In: *Physical Review (Series I)* 13.5 (Nov. 1901), pp. 307–320. DOI: 10.1103/PhysRevSeriesI.13.307.

[Okano 2010] M Okano, T Yamada, J Sugisaka, N Yamamoto, M Itoh, T Sugaya, K Komori, and M Mori. "Analysis of two-dimensional photonic crystal L-type cavities with low-refractive-index material cladding". In: *Journal of Optics* 12.7 (July 2010), p. 075101. DOI: 10.1088/2040-8978/12/7/075101.

[Olynick 2010] D. L. Olynick, B. Cord, A. Schipotinin, D. F. Ogletree, and P. J. Schuck. "Electron-beam exposure mechanisms in hydrogen silsesquioxane investigated by vibrational spectroscopy and in situ electron-beam-induced desorption". In: *Journal of Vacuum Science & Technology B: Microelectronics and Nanometer Structures* 28.3 (May 2010), p. 581. DOI: 10.1116/1.3425632.

[Oudich 2014] Mourad Oudich, Said El-Jallal, Yan Pennec, Bahram Djafari-Rouhani, Jordi Gomis-Bresco, Daniel Navarro-Urrios, Clivia M. Sotomayor Torres, Alejandro Martinez, and Abdelkader Makhoute. "Optomechanic interaction in a corrugated phoxonic nanobeam cavity". In: *Physical Review B* 89.24 (June 2014), p. 245122. DOI: 10.1103/PhysRevB.89.245122.

[Painter 1999] O. Painter. "Two-Dimensional Photonic Band-Gap Defect Mode Laser". en. In: *Science* 284.5421 (June 1999), pp. 1819–1821. DOI: 10.1126/science.284.5421.1819.

[Pandithage 2012] Ruwin Pandithage. "Brief Introduction to Critical Point Drying". In: *http://www.leica-microsystems.com/science-lab/brief-introduction-to-critical-point-drying/* (Dec. 2012).

[People 1985] R. People and J. C. Bean. "Calculation of critical layer thickness versus lattice mismatch for GexSi1-x/Si strained-layer heterostructures". In: *Applied Physics Letters* 47.3 (Aug. 1985), p. 322. DOI: 10.1063/1.96206.

[People 1986] R. People and J. C. Bean. "Erratum: Calculation of critical layer thickness versus lattice mismatch for GexSi1-x/Si strained-layer heterostructures [Appl. Phys. Lett. 47, 322 (1985)]". In: *Applied Physics Letters* 49.4 (July 1986), p. 229. DOI: 10.1063/1.97637.

[Pernice 2011] Wolfram H P Pernice, Carsten Schuck, Mo Li, and Hong X Tang. "Carrier and thermal dynamics of silicon photonic resonators at cryogenic temperatures." EN. In: *Optics express* 19.4 (Feb. 2011), pp. 3290–6. DOI: 10.1364/OE.19.003290.

[Pettit 1965] G. D. Pettit and W. J. Turner. "Refractive Index of InP". In: *Journal of Applied Physics* 36.6 (1965), p. 2081. DOI: 10.1063/1.1714410.

[Pinard 2008] M Pinard and A Dantan. "Quantum limits of photothermal and radiation pressure cooling of a movable mirror". en. In: *New Journal of Physics* 10.9 (Sept. 2008), p. 095012. DOI: 10.1088/1367-2630/10/9/095012.

[Pinard 1995] M. Pinard, C. Fabre, and A. Heidmann. "Quantum-nondemolition measurement of light by a piezoelectric crystal". In: *Physical Review A* 51.3 (Mar. 1995), pp. 2443–2449. DOI: 10.1103/PhysRevA.51.2443.

[Purdy 2010] T. P. Purdy, D. W. C. Brooks, T. Botter, N. Brahms, Z.-Y. Ma, and D. M. Stamper-Kurn. "Tunable Cavity Optomechanics with Ultracold Atoms". In: *Physical Review Letters* 105.13 (Sept. 2010), p. 133602. DOI: 10.1103/PhysRevLett.105.133602.

[Purdy 2013a] T P Purdy, R W Peterson, and C A Regal. "Observation of radiation pressure shot noise on a macroscopic object." In: *Science (New York, N.Y.)* 339.6121 (Feb. 2013), pp. 801–4. DOI: 10.1126/science.1231282.

[Purdy 2012] T P Purdy, R W Peterson, P. -L. Yu, and C A Regal. "Cavity optomechanics with Si3N4 membranes at cryogenic temperatures". en. In: *New Journal of Physics* 14.11 (Aug. 2012), p. 19. DOI: 10.1088/1367-2630/14/11/115021. arXiv: 1208.6560.

[Purdy 2013b] T. P. Purdy, P. -L. Yu, R. W. Peterson, N. S. Kampel, and C. A. Regal. "Strong Optomechanical Squeezing of Light". In: *Physical Review X* 3.3 (June 2013), p. 12. DOI: 10.1103/PhysRevX.3.031012. arXiv: 1306.1268.

[Rabiner 1975] Lawrence R. Rabiner and Bernard Gold. *Theory and application of digital signal processing*. 1975, p. 762. ISBN: 0139141014.

[Rath 2013] Patrik Rath, Svetlana Khasminskaya, Christoph Nebel, Christoph Wild, and Wolfram H.P. Pernice. "Diamond-integrated optomechanical circuits". en. In: *Nature Communications* 4 (Apr. 2013), p. 1690. DOI: 10.1038/ncomms2710.

[Regal 2008] C. A. Regal, J. D. Teufel, and K. W. Lehnert. "Measuring nanomechanical motion with a microwave cavity interferometer". In: *Nature Physics* 4.7 (May 2008), pp. 555–560. DOI: 10.1038/nphys974.

[Reichmanis 1989] Elsa Reichmanis and Larry F. Thompson. "Polymer materials for microlithography". In: *Chemical Reviews* 89.6 (Sept. 1989), pp. 1273–1289. DOI: 10.1021/cr00096a001.

[Roelkens 2006] G. Roelkens, J. Brouckaert, D. Van Thourhout, R. Baets, R. Nötzel, and M. Smit. "Adhesive Bonding of InP/InGaAsP Dies to Processed Silicon-On-Insulator Wafers using DVS-bis-Benzocyclobutene". en. In: *Journal of The Electrochemical Society* 153.12 (Dec. 2006), G1015. DOI: 10.1149/1.2352045.

[Roelkens 2008] G. Roelkens, L. Liu, D. Van Thourhout, R. Baets, R. Nötzel, F. Raineri, I. Sagnes, G. Beaudoin, and R. Raj. "Light emission and enhanced nonlinearity in nanophotonic waveguide circuits by III–V/silicon-on-insulator heterogeneous integration". In: *Journal of Applied Physics* 104.3 (Aug. 2008), p. 033117. DOI: 10.1063/1.2967832.

[Roels 2009] Joris Roels, Iwijn De Vlaminck, Liesbet Lagae, Bjorn Maes, Dries Van Thourhout, and Roel Baets. "Tunable optical forces between nanophotonic waveguides." In: *Nature nanotechnology* 4.8 (Aug. 2009), pp. 510–3. DOI: 10.1038/nnano.2009.186.

[Rolland 2012] Q. Rolland, M. Oudich, S. El-Jallal, S. Dupont, Y. Pennec, J. Gazalet, J. C. Kastelik, G. Léveˆque, and B. Djafari-Rouhani. "Acousto-optic couplings in two-dimensional phoxonic crystal cavities". In: *Applied Physics Letters* 101.6 (Aug. 2012), p. 061109. DOI: 10.1063/1.4744539.

[Rönnow 1998] D. Rönnow, P. Santos, M. Cardona, E. Anastassakis, and M. Kuball. "Piezo-optics of InP in the visible-ultraviolet range". In: *Physical Review B* 57.8 (Feb. 1998), pp. 4432–4442. DOI: 10.1103/PhysRevB.57.4432.

[Rugar 1991] D. Rugar and P. Grütter. "Mechanical parametric amplification and thermomechanical noise squeezing". In: *Physical Review Letters* 67.6 (Aug. 1991), pp. 699–702. DOI: 10.1103/PhysRevLett.67.699.

[SafaviNaeini 2011a] A H Safavi-Naeini, T P Mayer Alegre, J Chan, M Eichenfield, M Winger, Q Lin, J T Hill, D E Chang, and O Painter. "Electromagnetically induced transparency and slow light with optomechanics." In: *Nature* 472.7341 (Apr. 2011), pp. 69–73. DOI: 10.1038/nature09933.

[SafaviNaeini 2013] Amir H Safavi-Naeini, Simon Gröblacher, Jeff T Hill, Jasper Chan, Markus Aspelmeyer, and Oskar Painter. "Squeezed light from a silicon micromechanical resonator." In: *Nature* 500.7461 (Aug. 2013), pp. 185–9. DOI: 10.1038/nature12307.

[SafaviNaeini 2014] Amir H. Safavi-Naeini, Jeff T. Hill, Seán Meenehan, Jasper Chan, Simon Gröblacher, and Oskar Painter. "Two-Dimensional Phononic-Photonic Band Gap Optomechanical Crystal Cavity". In: *Physical Review Letters* 112.15 (Apr. 2014), p. 153603. DOI: 10.1103/PhysRevLett.112.153603.

[SafaviNaeini 2011b] Amir H Safavi-Naeini and Oskar Painter. "Proposal for an optomechanical traveling wave phonon–photon translator". In: *New Journal of Physics* 13.1 (Jan. 2011), p. 013017. DOI: 10.1088/1367-2630/13/1/013017.

[Salzberg 1957] Calvin D. Salzberg and John J. Villa. "Infrared Refractive Indexes of Silicon Germanium and Modified Selenium Glass". In: *Journal of the Optical Society of America* 47.3 (Mar. 1957), p. 244. DOI: 10.1364/JOSA.47.000244.

[Sankey 2010] J. C. Sankey, C. Yang, B. M. Zwickl, A. M. Jayich, and J. G. E. Harris. "Strong and tunable nonlinear optomechanical coupling in a low-loss system". In: *Nature Physics* 6.9 (June 2010), pp. 707–712. DOI: 10.1038/nphys1707.

[Sar 2011] T. van der Sar, J. Hagemeier, W. Pfaff, E. C. Heeres, S. M. Thon, H. Kim, P. M. Petroff, T. H. Oosterkamp, D. Bouwmeester, and R. Hanson. "Deterministic nanoassembly of a coupled quantum emitter–photonic crystal cavity system". In: *Applied Physics Letters* 98.19 (May 2011), p. 193103. DOI: 10.1063/1.3571437.

[Sauvan 2005] C. Sauvan, P. Lalanne, and J. P. Hugonin. "Slow-wave effect and mode-profile matching in photonic crystal microcavities". In: *Physical Review B* 71.16 (Apr. 2005), p. 165118. DOI: 10.1103/PhysRevB.71.165118.

[Sawadsky 2015] Andreas Sawadsky, Henning Kaufer, Ramon Moghadas Nia, Sergey P. Tarabrin, Farid Ya. Khalili, Klemens Hammerer, and Roman Schnabel. "Observation of Generalized Optomechanical Coupling and Cooling on Cavity Resonance". In: *Physical Review Letters* 114.4 (Jan. 2015), p. 043601. DOI: 10.1103/PhysRevLett.114.043601.

[Schliesser 2008a] A Schliesser, G Anetsberger, R Rivière, O Arcizet, and T J Kippenberg. "High-sensitivity monitoring of micromechanical vibration using optical whispering gallery mode resonators". In: *New Journal of Physics* 10.9 (Sept. 2008), p. 095015. DOI: 10.1088/1367-2630/10/9/095015.

[Schliesser 2009] A. Schliesser, O. Arcizet, R. Rivière, G. Anetsberger, and T. J. Kippenberg. "Resolved-sideband cooling and position measurement of a micromechanical oscillator close to the Heisenberg uncertainty limit". In: *Nature Physics* 5.7 (June 2009), pp. 509–514. DOI: 10.1038/nphys1304.

[Schliesser 2008b] A. Schliesser, R. Rivière, G. Anetsberger, O. Arcizet, and T. J. Kippenberg. "Resolved-sideband cooling of a micromechanical oscillator". In: *Nature Physics* 4.5 (Apr. 2008), pp. 415–419. DOI: 10.1038/nphys939.

[Schnabel 2010] Roman Schnabel, Nergis Mavalvala, David E McClelland, and Ping K Lam. "Quantum metrology for gravitational wave astronomy." In: *Nature communications* 1 (Jan. 2010), p. 121. DOI: 10.1038/ncomms1122.

[Selvaraja 2009] S.K. Selvaraja, P. Jaenen, W. Bogaerts, D. Van Thourhout, P. Dumon, and R. Baets. "Fabrication of Photonic Wire and Crystal Circuits in Silicon-on-Insulator Using 193-nm Optical Lithography". English. In: *Journal of Lightwave Technology* 27.18 (Sept. 2009), pp. 4076–4083. DOI: 10.1109/JLT.2009.2022282.

[Shah 2015] Shreyas Y. Shah, Mian Zhang, Richard Rand, and Michal Lipson. "Master-Slave Locking of Optomechanical Oscillators over a Long Distance". In: *Physical Review Letters* 114.11 (Mar. 2015), p. 113602. DOI: 10.1103/PhysRevLett.114.113602.

[Shankar 2011] Raji Shankar, Irfan Bulu, Rick Leijssen, and Marko Lončar. "Study of thermally-induced optical bistability and the role of surface treatments in Si-based mid-infrared photonic crystal cavities." EN. In: *Optics express* 19.24 (Nov. 2011), pp. 24828–37. DOI: 10.1364/OE.19.024828.

[Shim 2007] Seung-Bo Shim, Matthias Imboden, and Pritiraj Mohanty. "Synchronized oscillation in coupled nanomechanical oscillators." In: *Science (New York, N.Y.)* 316.5821 (Apr. 2007), pp. 95–9. DOI: 10.1126/science.1137307.

[Shkarin 2014] A. B. Shkarin, N. E. Flowers-Jacobs, S. W. Hoch, A. D. Kashkanova, C. Deutsch, J. Reichel, and J. G. E. Harris. "Optically Mediated Hybridization between Two Mechanical Modes". In: *Physical Review Letters* 112.1 (Jan. 2014), p. 013602. DOI: 10.1103/PhysRevLett.112.013602.

[Stepanova 2011] Maria Stepanova and Steven Dew. *Nanofabrication: Techniques and Principles*. Vol. 2011. 2011, p. 352. ISBN: 3709104246.

[Sun 2012] Xiankai Sun, Jiangjun Zheng, Menno Poot, Chee Wei Wong, and Hong X Tang. "Femtogram doubly clamped nanomechanical resonators embedded in a high-Q two-dimensional photonic crystal nanocavity." In: *Nano letters* 12.5 (May 2012), pp. 2299–305. DOI: 10.1021/nl300142t.

[Taillaert 2002] D. Taillaert, W. Bogaerts, P. Bienstman, T.F. Krauss, P. Van Daele, I. Moerman, S. Verstuyft, K. De Mesel, and R. Baets. "An out-of-plane grating coupler for efficient butt-coupling between compact planar waveguides and single-mode fibers". English. In: *IEEE Journal of Quantum Electronics* 38.7 (July 2002), pp. 949–955. DOI: 10.1109/JQE.2002.1017613.

[Taillaert 2006] Dirk Taillaert, Frederik Van Laere, Melanie Ayre, Wim Bogaerts, Dries Van Thourhout, Peter Bienstman, and Roel Baets. "Grating Couplers for Coupling between Optical Fibers and Nanophotonic Waveguides". In: *Japanese Journal of Applied Physics* 45.8A (Aug. 2006), pp. 6071–6077. DOI: 10.1143/JJAP.45.6071.

[Takano 2004] Hitomichi Takano, Yoshihiro Akahane, Takashi Asano, and Susumu Noda. "In-plane-type channel drop filter in a two-dimensional photonic crystal slab". In: *Applied Physics Letters* 84.13 (Mar. 2004), p. 2226. DOI: 10.1063/1.1689742.

[Taylor 1973] H. F. Taylor. "Optical switching and modulation in parallel dielectric waveguides". In: *Journal of Applied Physics* 44.7 (1973), p. 3257. DOI: 10.1063/1.1662743.

[Teufel 2011] J D Teufel, T Donner, Dale Li, J W Harlow, M S Allman, K Cicak, A J Sirois, J D Whittaker, K W Lehnert, and R W Simmonds. "Sideband cooling of micromechanical motion to the quantum ground state." In: *Nature* 475.7356 (July 2011), pp. 359–63. DOI: 10.1038/nature10261.

[Thompson 2007] J D Thompson, B M Zwickl, A M Jayich, Florian Marquardt, S M Girvin, and J G E Harris. "Strong dispersive coupling of a high finesse cavity to a micromechanical membrane". In: *Nature* 452.7183 (July 2007), p. 25. DOI: 10.1038/nature06715. arXiv: 0707.1724.

[Unterreithmeier 2009] Quirin P Unterreithmeier, Eva M Weig, and Jörg P Kotthaus. "Universal transduction scheme for nanomechanical systems based on dielectric forces." In: *Nature* 458.7241 (Apr. 2009), pp. 1001–4. DOI: 10.1038/nature07932.

[Usami 2012] K. Usami, A. Naesby, T. Bagci, B. Melholt Nielsen, J. Liu, S. Stobbe, P. Lodahl, and E. S. Polzik. "Optical cavity cooling of mechanical modes in a semiconductor nanomembrane". In: *Nature Physics* 8.2 (Nov. 2012), p. 5. DOI: 10.1038/nphys2196. arXiv: 1011.3974.

[Van Der Merwe 1963] J. H. Van Der Merwe. "Crystal Interfaces. Part II. Finite Overgrowths". In: *Journal of Applied Physics* 34.1 (June 1963), p. 123. DOI: 10.1063/1.1729051.

[Verbridge 2008] Scott S. Verbridge, Harold G. Craighead, and Jeevak M. Parpia. "A megahertz nanomechanical resonator with room temperature quality factor over a million". In: *Applied Physics Letters* 92.1 (Jan. 2008), p. 013112. DOI: 10.1063/1.2822406.

[Villanueva 2013] L. G. Villanueva, E. Kenig, R. B. Karabalin, M. H. Matheny, Ron Lifshitz, M. C. Cross, and M. L. Roukes. "Surpassing Fundamental Limits of Oscillators Using Nonlinear Resonators". In: *Physical Review Letters* 110.17 (Apr. 2013), p. 177208. DOI: 10.1103/PhysRevLett.110.177208.

[Vlassak 2004] Joost Vlassak. *Thin Film Mechanics*. Harvard University, Boston, MA, 2004.

[Wachtman 1961] J. B. Wachtman, W. E. Tefft, D. G. Lam, and C. S. Apstein. "Exponential Temperature Dependence of Young's Modulus for Several Oxides". In: *Physical Review* 122.6 (June 1961), pp. 1754–1759. DOI: 10.1103/PhysRev.122.1754.

[Weigel 2002] R. Weigel, D.P. Morgan, J.M. Owens, A. Ballato, K.M. Lakin, K. Hashimoto, and C.C.W. Ruppel. "Microwave acoustic materials, devices, and applications". In: *IEEE Transactions on Microwave Theory and Techniques* 50.3 (Mar. 2002), pp. 738–749. DOI: 10.1109/22.989958.

[Weiss 2013] Talitha Weiss and Andreas Nunnenkamp. "Quantum limit of laser cooling in dispersively and dissipatively coupled optomechanical systems". In: *Physical Review A* 88.2 (Aug. 2013), p. 023850. DOI: 10.1103/PhysRevA.88.023850.

[Wilson 2014] D. J. Wilson, V. Sudhir, N. Piro, R. Schilling, A. Ghadimi, and T. J. Kippenberg. "Measurement and control of a mechanical oscillator at its thermal decoherence rate". In: (Oct. 2014), p. 24. arXiv: 1410.6191.

[WilsonRae 2004] I. Wilson-Rae, P. Zoller, and A. Imamoglu. "Laser Cooling of a Nanomechanical Resonator Mode to its Quantum Ground State". In: *Physical Review Letters* 92.7 (Feb. 2004), p. 075507. DOI: 10.1103/PhysRevLett.92.075507.

[Wu 2014] Marcelo Wu, Aaron C. Hryciw, Chris Healey, David P. Lake, Harishankar Jayakumar, Mark R. Freeman, John P. Davis, and Paul E. Barclay. "Dissipative and Dispersive Optomechanics in a Nanocavity Torque Sensor". In: *Physical Review X* 4.2 (June 2014), p. 021052. DOI: 10.1103/PhysRevX.4.021052.

[Xiong 2012] Chi Xiong, Wolfram H P Pernice, Xiankai Sun, Carsten Schuck, King Y Fong, and Hong X Tang. "Aluminum nitride as a new material for chip-scale optomechanics and nonlinear optics". In: *New Journal of Physics* 14.9 (Sept. 2012), p. 095014. DOI: 10.1088/1367-2630/14/9/095014.

[Xuereb 2011] André Xuereb, Roman Schnabel, and Klemens Hammerer. "Dissipative Optomechanics in a Michelson-Sagnac Interferometer". In: *Physical Review Letters* 107.21 (Nov. 2011), p. 213604. DOI: 10.1103/PhysRevLett.107.213604.

[Xuereb 2012] André Xuereb, Koji Usami, Andreas Naesby, Eugene S Polzik, and Klemens Hammerer. "Exciton-mediated photothermal cooling in GaAs membranes". en. In: *New Journal of Physics* 14.8 (Aug. 2012), p. 085024. DOI: 10.1088/1367-2630/14/8/085024.

[Yablonovitch 1987] Eli Yablonovitch. "Inhibited Spontaneous Emission in Solid-State Physics and Electronics". In: *Physical Review Letters* 58.20 (May 1987), pp. 2059–2062. DOI: 10.1103/PhysRevLett.58.2059.

[Yasumoto 2005] Kiyotoshi Yasumoto. *Electromagnetic Theory and Applications for Photonic Crystals*. CRC Press, 2005, p. 464. ISBN: 1420026623.

[Yee 1966] Kane Yee. "Numerical solution of initial boundary value problems involving maxwell's equations in isotropic media". In: *IEEE Transactions on Antennas and Propagation* 14.3 (May 1966), pp. 302–307. DOI: 10.1109/TAP.1966.1138693.

[Yoshie 2004] T Yoshie, A Scherer, J Hendrickson, G Khitrova, H M Gibbs, G Rupper, C Ell, O B Shchekin, and D G Deppe. "Vacuum Rabi splitting with a single quantum dot in a photonic crystal nanocavity." In: *Nature* 432.7014 (Nov. 2004), pp. 200–3. DOI: 10.1038/nature03119.

[Yoshie 2002] T. Yoshie, O.B. Shchekin, H. Chen, D.G. Deppe, and A. Scherer. "Quantum dot photonic crystal lasers". In: *Electronics Letters* 38.17 (2002), p. 967. DOI: 10.1049/el:20020650.

[Zhang 2015] Mian Zhang, Shreyas Shah, Jaime Cardenas, and Michal Lipson. "Synchronization and Phase Noise Reduction in Micromechanical Oscillators Arrays Coupled through Light". In: (May 2015). arXiv: 1505.02009.

[Zheng 2013] Jiangjun Zheng, Ying Li, Noam Goldberg, Mickey McDonald, Xingsheng Luan, Archita Hati, Ming Lu, Stefan Strauf, Tanya Zelevinsky, David A. Howe, and Chee Wei Wong. "Feedback and harmonic locking of slot-type optomechanical oscillators to external low-noise reference clocks". In: *Applied Physics Letters* 102.14 (Apr. 2013), p. 141117. DOI: 10.1063/1.4801473.

[Zheng 2012] Jiangjun Zheng, Xiankai Sun, Ying Li, Menno Poot, Ali Dadgar, Norman Nan Shi, Wolfram H P Pernice, Hong X Tang, and Chee Wei Wong. "Femtogram dispersive L3-nanobeam optomechanical cavities: design and experimental comparison." EN. In: *Optics express* 20.24 (Nov. 2012), pp. 26486–98. DOI: 10.1364/OE.20.026486.